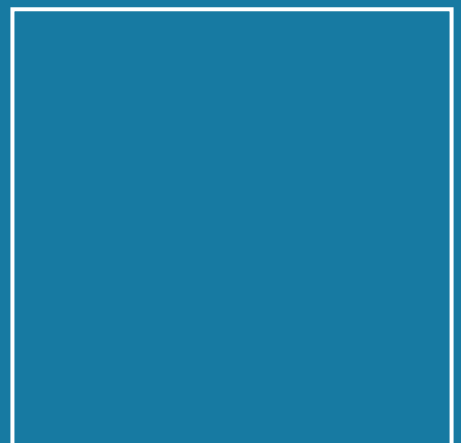
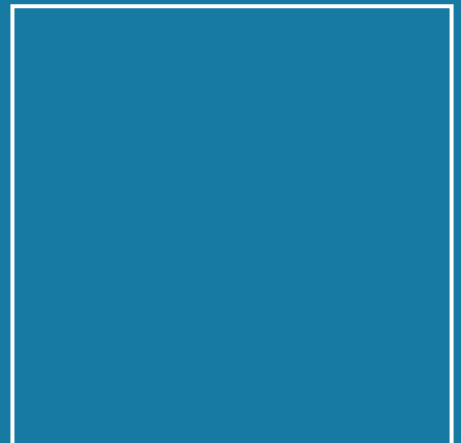




Dissertation

Tim Käseberg

Optical Metrology for Resolving Topological Information of Nanoscale Structures via Modified Mueller Matrix Ellipsometry



DOI 10.7795/110.20240308

ISSN 2941-1297

ISBN 978-3-944659-33-6

Physikalisch-Technische Bundesanstalt

Dissertationen

PTB-Diss-4

Braunschweig, März 2024

Tim Käseberg

Optical Metrology for Resolving Topological Information of Nanoscale Structures via Modified Mueller Matrix Ellipsometry

DOI 10.7795/110.20240308

ISSN 2941-1297

ISBN 978-3-944659-33-6

<https://doi.org/10.7795/110.20240308>

Empfohlene Zitierweise/recommended citation

Käseberg, T., 2024. *Optical Metrology for Resolving Topological Information of Nanoscale Structures via Modified Mueller Matrix Ellipsometry*.

Dissertation, Technische Universität Carolo-Wilhelmina zu Braunschweig.

Braunschweig: Physikalisch-Technische Bundesanstalt.

PTB-Bericht Diss-4. ISBN 978-3-944659-33-6.

Verfügbar unter: <https://doi.org/10.7795/110.20240308>

Herausgeber:

Physikalisch-Technische Bundesanstalt

ISNI: 0000 0001 2186 1887

Presse und Öffentlichkeitsarbeit

Bundesallee 100

38116 Braunschweig

Telefon: (05 31) 592-93 21

Telefax: (05 31) 592-92 92

www.ptb.de

<https://doi.org/10.7795/110.20240308>

Optical Metrology for Resolving Topological Information of Nanoscale Structures via Modified Mueller Matrix Ellipsometry

Von der Fakultät für Elektrotechnik, Informationstechnik, Physik
der Technischen Universität Carolo-Wilhelmina zu Braunschweig

zur Erlangung des Grades eines
Doktors der Naturwissenschaften (Dr. rer. nat.)

genehmigte Dissertation

von Tim Käseberg
aus Wolfsburg

Eingereicht am: 15.09.2023

Mündliche Prüfung (Disputation) am: 18.12.2023

1. Referentin: Prof. Dr. Stefanie Kroker
2. Referent: Prof. Dr. Uwe Zeitner

Druckjahr: 2024

Dissertation an der Technischen Universität Braunschweig,
Fakultät für Elektrotechnik, Informationstechnik, Physik

On wings of hope, you rise up through the night higher, oh higher
Carrying our song, cradled fast within your arms
That its chorus might ring for all

Masayoshi Soken – Endwalker - Footfalls

Abstract

With the on-going progress in nanotechnology, the necessary metrology to characterize fabricated structures struggles to keep pace. Indirect optical methods like ellipsometry are promising for this task, being highly accurate and at the same time non-invasive, fast, and flexible. In conventional ellipsometry, results are integrated over the whole illumination spot, making it applicable only on larger measurement fields and periodic structures. While imaging ellipsometry enables a more local evaluation of polarizing properties, it is not widely used in metrology yet. Measured images are usually evaluated like conventional measurements, neglecting useful information from inhomogeneous areas. These are only fully accessible using 3D simulations, which are computationally highly expensive. In this thesis, I investigate approaches to enhance the performance of imaging MUELLER matrix ellipsometry to establish it for nanometrology. Using specially designed nanostructures, I examine the influence of subwavelength scale structure form and size on MUELLER matrix images, observable in both, measurements and simulations. With these samples, I explore possibilities to advance MUELLER matrix ellipsometry. This includes ways to evaluate MUELLER matrix images without the need for 3D simulations, using techniques inspired by machine learning that provide information exceeding microscopy images alone. In addition, this thesis covers the problem of usually disregarded thermal drifts, proving that they are a potential source of uncertainty in imaging ellipsometry by performing experiments on moving samples. I also offer an algorithmic solution for handling drifts to improve even already existing setups. Apart from that, I explore the applicability of plasmonic lenses for the advancement of ellipsometric methods. Conventional plasmonic lenses are challenging to fabricate with common lithographic methods. Therefore, I developed a new design scheme, so-called inverted plasmonic lenses. They keep the same functionality while complying with fabrication conditions, enabling higher fabrication rates for possible future applications. Plasmonic lenses were designed, optimized, and their parameters systematically examined with numerical simulations. Then, lenses were fabricated with varying parameters and examined using microscopy and imaging ellipsometry. Fabricated lenses produced expected focal spots and showed dispersion. Design schemes to enhance the performance of plasmonic lenses in terms of throughput maximization and dispersion reduction are compared and discussed. I present an approach to merge plasmonic lens designs for different wavelengths, which successfully reduces dispersion, albeit at the cost of focal spot intensity. Numerical simulations showed that plasmonic lenses focusing the illumination on a sample enhances the sensitivity of ellipsometric measurements to subwavelength sized structures significantly. The contributions from this thesis will help to establish imaging ellipsometry as a tool in optical nanometrology, pushing it further beyond its limits to ultimately help bridging the gap towards nanotechnology.

Zusammenfassung

Mit dem anhaltenden Fortschritt der Nanotechnologie kann die Metrologie zur Charakterisierung gefertigter Strukturen nur schwer Schritt halten. Indirekte, optische Verfahren wie die Ellipsometrie sind dafür vielversprechend, da sie hochgenau und gleichzeitig nicht-invasiv, schnell und flexibel sind. In der konventionellen Ellipsometrie wird das Messergebnis über den gesamten Beleuchtungsfleck integriert. Daher ist sie nur bei größeren Messfeldern und periodischen Strukturen anwendbar. Abbildende Ellipsometrie ermöglicht eine lokalere Betrachtung der Polarisations-eigenschaften, ist in der Metrologie allerdings noch nicht weit verbreitet. Für gewöhnlich werden nur gemittelte Werte der aufgenommenen Bilder mit herkömmlichen Verfahren ausgewertet, wobei wertvolle Informationen aus ungleichmäßigen Bereichen der Probe verloren gehen. Solche Informationen ließen sich nur mit aufwendigen 3D-Simulationen vollständig nutzen. In dieser Arbeit untersuche ich Ansätze zur Verbesserung der Leistung abbildender Ellipsometrie mit dem Ziel, sie für die Nanometrologie zu etablieren. Mithilfe spezieller Nanostrukturen untersuche ich den Einfluss von Strukturform und -größe im Subwellenlängenbereich auf MUELLER-Matrix-Bilder experimentell und in Simulationen. Unter anderem betrachte ich Möglichkeiten zur Bild-Auswertung in Anlehnung an Methoden des maschinellen Lernens ohne 3D-Simulationen zur Erschließung von Informationen, die über Mikroskopbilder allein hinausgehen. Zudem befasst sich diese Arbeit mit thermischen Drifts, die in der Ellipsometrie sonst vernachlässigt werden. Ich zeige auf, dass Drifts eine Unsicherheitsquelle in der abbildenden Ellipsometrie darstellen, und biete eine algorithmische Behandlung selbst in bestehenden Aufbauten an. Des Weiteren untersuche ich die Eignung plasmonischer Linsen zur Sensitivitätssteigerung ellipsometrischer Methoden. Konventionelle plasmonische Linsen sind mit üblichen Lithographie-Verfahren allerdings umständlich herzustellen. Daher habe ich ein neues Design entwickelt, die sogenannte invertierte plasmonische Linse. Ohne Abzüge in der Funktionalität kommt sie den Herstellungsbedingungen entgegen, was höhere Produktionsraten für zukünftige Anwendungen ermöglicht. Verschiedene plasmonische Linsen wurden entworfen, optimiert und ihre Parameter in Simulationen untersucht. Anschließend wurden Linsen mit unterschiedlichen Parametern hergestellt und mittels Mikroskopie und abbildender Ellipsometrie evaluiert. Die hergestellten Linsen erzeugten die erwarteten Brennpunkte und zeigten Dispersion. Ansätze zur Verbesserung ihrer Leistung im Hinblick auf Durchsatzmaximierung und Dispersionsreduzierung werden verglichen und diskutiert. Die Zusammenführung von Linsendesigns verschiedener Wellenlängen reduziert erfolgreich die Dispersion, beeinträchtigt aber auch die Brennpunkt-Intensität. Simulationen zeigen, dass die Empfindlichkeit ellipsometrischer Messungen auf Subwellenlängen-Strukturen durch den Einsatz der Linsen deutlich gesteigert wird. Die Ergebnisse dieser Dissertation tragen dazu bei, die abbildende Ellipsometrie in der optischen Nanometrologie zu etablieren und letztendlich die metrologische Lücke zur Nanotechnologie zu schließen.

Contents

Nomenclature	1
1 Motivation	3
2 Light in and around Conductive Media	9
2.1 MAXWELL'S Equations and the Description of Light	9
2.1.1 Wave Equations	10
2.1.2 Solutions of the Wave Equations	10
2.1.3 Evanescent Fields	11
2.2 Polarization of Light	12
2.2.1 The Polarization Ellipse	12
2.2.2 States of Polarization	12
2.2.3 JONES Calculus	14
2.2.4 STOKES Calculus	14
2.2.5 MUELLER JONES Matrices	15
2.3 Plasmonics	16
2.3.1 Plasma Oscillations	16
2.3.2 Surface Plasmon Polaritons	17
2.3.3 Excitation of Surface Plasmon Polaritons	19
3 MUELLER Matrix Ellipsometry	21
3.1 Polarimetry and Ellipsometry	21
3.1.1 Ψ - Δ -Ellipsometry	22
3.1.2 STOKES Polarimetry	22
3.1.3 MUELLER Matrix Ellipsometry	24
3.1.4 Error Compensation	27
3.1.5 Imaging Ellipsometry	28
3.2 Experimental Setups	30
3.2.1 MUELLER Matrix Microscope	30
3.2.2 Commerical Imaging Ellipsometry Setup EP4	33
3.3 Nanoform Structures	34
3.3.1 Sample design	34
3.3.2 Fabrication and SEM Characterization	35
3.3.3 AFM Characterization	39

3.4	Ellipsometric Measurements	41
3.4.1	Measurements at MUELLER Matrix Microscope	41
3.4.2	Measurements at EP4 Setup	44
3.5	Thermal Influences	48
3.5.1	Drift at MUELLER Matrix Microscopy Setup	48
3.5.2	Drift at EP4 Setup	50
3.5.3	Drift Correction Algorithm	51
3.5.4	Intentionally Induced Drift	53
4	Plasmonic Lens Devices	55
4.1	Plasmonic Waveguides	55
4.2	Plasmonic Lenses	57
4.3	Inverted Plasmonic Lenses	59
4.4	Lens Design and Parameter Optimization	61
4.4.1	Waveguide Length and Lens Aperture	62
4.4.2	Coating Thickness	65
4.4.3	Ridge Arrangement	67
4.4.4	Final Designs	68
4.5	Lens Performance Evaluation	71
4.5.1	Tolerances to Deviations from Design	71
4.5.2	Wavelength Dependency	72
4.6	Concepts for Achromatic Plasmonic Lenses	76
4.6.1	Dispersion-Free Meta-Lenses	76
4.6.2	Cylindrical Plasmonic Meta-Atoms	77
4.6.3	Merged Plasmonic Lens Design	80
5	Advanced Methods for Imaging Ellipsometry	85
5.1	MUELLER Matrix Images of Fabricated Plasmonic Lenses	85
5.1.1	MUELLER Matrix Images at Different Wavelengths	86
5.1.2	MUELLER Matrix Images at Different Focus Positions	89
5.2	Numerical Simulations of MUELLER Matrix Images	91
5.2.1	Simulated MUELLER Matrix Images of the Nanoform Sample	92
5.2.2	Plasmonic Lens Supported Ellipsometry Simulations	96
5.3	Machine Learning Concepts for MUELLER Matrix Images	98
5.3.1	Wavelets and Features	98
5.3.2	Application to MUELLER Matrix Images	99
6	Conclusion	103
	Bibliography	107
	List of Figures	120

List of Tables	125
A Mathematical Details and Derivations	127
A.1 Derivation of the Wave Equation and the HELMHOLTZ Equation	127
A.2 MUELLER Matrices	129
A.3 Rotating Retarder MUELLER Matrix Ellipsometry	130
A.3.1 Transition from FOURIER Coefficients to MUELLER Matrix Elements	130
A.3.2 Error Compensation	138
A.4 Fit Parameters	141
A.5 Derivation of the Characteristic Equation for Surface Plasmon Polaritons .	142
A.6 Plasmonic Lens Parameters	146
B Further Figures	155
B.1 MUELLER Matrix Images of the Nanoform Sample	156
B.1.1 Row A, without drift correction	156
B.1.2 Row A, with drift correction	158
B.1.3 Row A, simulated	160
B.1.4 Row C	162
B.2 MUELLER Matrix Images of Plasmonic Lenses	164
B.2.1 OS-00, Measurement at EP4, PCSA	164
B.2.2 OS-00, Measurement at EP4, PCSCA	166
Acknowledgments	169
List of Publications	171

Nomenclature

List of symbols and abbreviations used in this thesis.

Symbol	Meaning	Symbol	Meaning
a	Aperture	N	Number
a_j, b_j	FOURIER coefficients	NA	Numerical aperture
A, B, C, D	Auxiliary variables	p	Dipole moment
A, B, C, D	Rows of the nanoform sample	P	Polarizer
\vec{B}	Magnetic flux density	P_D	Depolarization index
c	Speed of light	Q_{SPP}	Plasmonic quality factor
d	Diameter	r	Radius
d_c	Coating thickness	r_c	Corner radius
d_{min}	Minimum ridge distance	\vec{r}	Position vector
\vec{E}	Electric field (strength)	\underline{R}	Rotation matrix
\vec{E}_0	Electric field amplitude vector	R_s, R_p	Reflection coefficient
E_0	Electric field amplitude	\vec{S}	STOKES vector
E_{0x}, E_{0y}	Electric field amplitude components	S_0, S_1, S_2, S_3	STOKES parameters
E_x, E_y, E_z	Electric field components	$\mathcal{S}_x, \mathcal{S}_y$	SOBEL operators
f	Focal length	t	Time
\vec{g}	Grating vector	\underline{T}	Transformation matrix
h	Helicity	T	Temperature
H	Humidity	u, v	Integers
I	Intensity	w	Width
I_v	Modified BESSEL function of order v	x, y, z	Cartesian coordinates
j	Integer	β	Propagation constant
\vec{j}	Electric current density	γ	Gaussian distribution scale
\vec{J}	JONES vector	Γ	Gamma function
k	Wave number	δ_d, δ_m	SPP penetration depths
k_0	Vacuum wave number	δ_{SPP}	SPP propagation length
\vec{k}	Wave vector	Δ	Ellipsometric phase difference
k_x, k_y, k_z	Wave vector components	ϵ	Permittivity
K_v	Modified BESSEL function of order v	ϵ_r	Relative permittivity
l	Lens thickness / Waveguide length	$\epsilon_1, \dots, \epsilon_5$	Polarizer and retarder deviations
m	Integer	θ	Rotation angle
$m_{a,i}$	PSA MUELLER matrix element	λ	Wavelength
m_{ij}	MUELLER matrix elements	λ_0	Vacuum wavelength
\underline{M}	MUELLER matrix	λ_c	Critical wavelength
\underline{M}_j	JONES matrix	λ_{SPP}	SPP wavelength
\vec{n}	Normal vector	Λ	Period
n	Refractive index	μ	Permeability
n_e	Electron number density		

Symbol	Meaning	Symbol	Meaning
μ_r	Relative permeability	ϕ	Phase
μ_{uv}	Combined PSA-PSG matrix elements	ψ	HAAR wavelet / function
ξ_d, ξ_m	Auxiliary variable	Ψ	Ellipsometric amplitude component
Π	Degree of polarization	ω	Angular frequency
ρ	Electric charge density	ω_p	Plasma frequency
σ	Electric conductivity		

Abbreviations

AFM	Atomic Force Microscopy	PSA	Polarization State Analyzer
ALD	Atomic Layer Deposition	PSG	Polarization State Generator
C	Cylindrical lens	PSO	Particle Swarm Optimization
CAD	Computer-Aided Design	PTB	Physikalisch-Technische Bundesanstalt
CCD	Charge-Coupled Device	RAM	Random-Access Memory
CMI	Czech Metrology Institute	RMSE	Root-Mean-Square Error
FEM	Finite Element Method	ROI	Region Of Interest
FIB	Focused Ion Beam	s	perpendicular (<i>senkrecht</i>)
FWHM	Full Width at Half Maximum	S	Successive
IQR	InterQuartile Range	SEM	Scanning Electron Microscopy
JCM	James Clerk MAXWELL	SiO ₂	Silicon dioxide
LED	Light-Emitting Diode	SNOM	Scanning Near-field Optical Microscopy
O	Spherical lens	SPM	Scanning Probe Microscopy
p	parallel	SPP	Surface Plasmon Polariton
P	Periodic	STED	STimulated Emission Depletion
PCSA	Polarizer, Compensator, Sample, Analyzer	TE	Transverse-Electric
PCSCA	Pol., Comp., Sample, Compensator, Analyzer	TM	Transverse-Magnetic
PMMA	PolyMethylMethAcrylat	TSOM	Through-focus Scanning Optical Microscopy

Constants

Vacuum speed of light	c_0	=	$299792458 \frac{\text{m}}{\text{s}}$
Elementary charge	e	=	$1.60217663 \cdot 10^{-19} \text{ C}$
Electron mass	m_e	=	$9.10938370 \cdot 10^{-31} \text{ kg}$
Vacuum permittivity	ϵ_0	=	$8.85418781 \cdot 10^{-12} \frac{\text{As}}{\text{Vm}}$
Vacuum permeability	μ_0	=	$1.25663706 \cdot 10^{-6} \frac{\text{Vs}}{\text{Am}}$
Pi	π	≈	3.14159265...
EULER's number	e	≈	2.71828183...
Imaginary unit	i	=	$\sqrt{-1}$

Motivation

ONCE, WHEN I WAS LITTLE, I HAD A TAMAGOTCHI. A DIGITAL FRIEND IN FORM OF A little device in my pocket that would beep at me when it needed my attention. Tamagotchis as popular in the 1990s (compare Figure 1.1(a)) contained simple 4-bit single chip microcomputers, running at 2 MHz maximum and bundled with 640 words of RAM [1, 2, 3]. Little has changed since then. I still have a device in my pocket that alerts me when one of my friends wants my attention. Just the numbers are different: Instead of only one digital friend, I now have close to 200 real-life contacts stored in my smartphone (see Figure 1.1(b)). With 8 GB of RAM, it has about as much memory as my laptop, and its Kirin 980 chip features eight cores running at up to 2.6 GHz, while being only half the size of the chip in a Tamagotchi. Its 6.9 billion transistors fit into only 1 cm², thanks to it being fabricated within the scope of the so-called 7 nm process technology node [4, 5, 6, 7]. Even if '7 nm' nowadays is more of a marketing term, transistors made with this technology are as small as a few tens of nanometers only [8]. As of writing this thesis, transistor technologies have even reached the 3 nm node, with the 2 nm node being expected in the near future [9, 10, 11, 12].



(a) Tamagotchi, image from [13].



(b) My current smartphone.

Figure 1.1 – A 1997 Tamagotchi (a) and my current smartphone, a 2019 Huawei P30 Pro (b).

Advances in the fabrication of novel technologies also require the reliable and accurate characterization of the fabricated structures. Thus, nanometrology has to keep pace with the progress in nanotechnology. For measurements at the nanometer scale, atomic force microscopy (AFM) and scanning electron microscopy (SEM), inter alia, have proven themselves. AFM is regarded as a highly accurate technique, but fails to characterize large structured areas due to its low speed. SEM faces the issues of being potentially destructive to the sample while requiring specific measurement conditions [14, 15, 16]. For these reasons, optical techniques are usually preferred. They are faster than tactile methods and at the same time non-invasive and scalable, making them easy to integrate even in large-scale manufacturing environments. Conventional light microscopy is the most common method here, but famously faces ABBE's diffraction limit at roughly half the wavelength of the incident light. Optical imaging systems are incapable of resolving objects that are closer to each other than this limit [17]. Much has been done to overcome this limit, with a famous recent example being the development of stimulated emission depletion microscopy (STED), which was awarded the Nobel Prize in Chemistry in 2014 [18]. Super-resolution methods like STED, however, rely on the presence of fluorescent markers in the structures under investigation. While it is common to use fluorophores in biological applications, they are incompatible with, e.g., semiconductor samples, making these techniques impractical especially in metrology [19, 20, 21]. In contrast to all these stand non-imaging methods, such as ellipsometry, which are indirect optical techniques. Instead of directly measuring for example the thickness of a thin layer, ellipsometry measures the difference of the sample's influence on light polarized in different ways. This difference is then compared to models in order to find the corresponding layer thickness. As this is not limited by diffraction, it is capable of characterizing dimensions down to a few Ångström with high accuracy [22, 23, 24, 25].

When talking to people from outside the optics community about ellipsometry, many struggle to connect the term with the measurement method. Usually, the '-metry' part is obvious, stemming from the ancient Greek word μέτρον (*métron*, measure) [26]. The 'ellipso-' part refers to the polarization ellipse, a general description of light's state of polarization. Alexandre ROTHEN is said to have coined the term 'ellipsometry' in 1945 [27], but the method has been around since the time of Paul DRUDE, and potentially even longer. Its origins are not quite clear, but already in the 19th century, measurements that can be regarded as ellipsometry were conducted [25, 28, 29]. Although it is by far not a new tool, it is still popular today, being used in a wide range of applications from metrology [30, 31, 32] over semiconductor industries [25, 33, 34] to biology [35, 36, 37]. It even played a role in characterizing PTB's monocrystalline silicon spheres used in determining the quantity of the AVOGADRO constant by measuring the thickness of its oxide layer [38].

The appeal of ellipsometry lies in its high accuracy when measuring layer thicknesses or optical constants or when reconstructing the parameters of periodic nanostructures. However, to some extent, it still faces the problem of finite illumination spot size: Dur-

ing a measurement, the sample is illuminated with light and the intensity change of the reflected (or transmitted) light is measured for different states of polarization. In doing so, the result is integrated over the whole illumination spot, the diameter of which is usually in the order of magnitude of 1 mm^2 . Thus, structures smaller than this illumination spot can only be evaluated correctly when they are periodic and when the patterned area is larger than the illuminated area. If the structured field is smaller than the spot size, influences from the surroundings are mixed into the measured signal, affecting the result. Local polarization effects from opposing corners or edges are averaged out and features from non-periodic, individual structures cannot be separated and evaluated. A possible solution for this, which I explored in this work, is the use of imaging ellipsometry. This technique combines ellipsometry with microscopy: Instead of a simple detector, a camera is used to collect the information from the ellipsometry measurement in images of the sample. Together with a magnifying optical system, this allows to measure polarizing effects more locally than conventional ellipsometry is able to. The idea of imaging ellipsometry is not new [39, 40, 41]. Yet, there is currently only one imaging ellipsometry system commercially available, offered by Park Systems / Accurion [42], and it is barely used in a metrological context, despite its advantages. A reason for this might be its evaluation difficulties [43]. By now, results from imaging ellipsometry are usually evaluated by averaging over regions of interest (ROI) in the image and evaluating these mean results like in conventional ellipsometry. Although this allows for an easier evaluation of smaller areas than in conventional ellipsometry, it only makes use of homogeneous areas in the images and completely neglects other topological information from features like structure edges or corners. Reconstructing non-periodic nanostructures using the information from these inhomogeneities would necessitate numerical simulations in three dimensions, which come with considerable computational costs and are thus often evaded. Other methods to access topological information without elaborate simulations are needed to make this method more viable for metrological purposes. For the sake of reliability in metrology, it is also important to consider the thermal stability of imaging ellipsometry. The thermal influence on these kinds of measurements is still widely ignored as it only plays a minor role in conventional ellipsometry and when measurements are conducted in sufficiently short time ranges. Apart from that, typical imaging ellipsometry usually features optical components also used in microscope systems. Replacing these optics with structures from the rapidly developing field of meta-lenses involves many potential advantages, from more compact setups over smaller illumination areas towards the possibility to implement scanning-type or structured-illumination-like measurement schemes. These kinds of enhancements, that are likely to improve the access to subwavelength information, are still pending.

The aim of this thesis was to find ways to enhance the performance of imaging MUELLER matrix ellipsometry for the purpose of establishing it for nanometrological applications and ultimately helping to bridge the gap towards nanotechnology. I explored different possibilities to advance MUELLER matrix ellipsometry for metrological purposes. This en-

compasses ways to evaluate MUELLER matrix images without the need for three-dimensional simulations, using techniques inspired by machine learning and image processing. As a testbed, I designed a set of distinct nanostructures which showed detectable responses in measurements agreeing with simulations, even for feature changes smaller than the illuminating wavelength and even for simple measurements under normal incidence. In addition, this thesis covers the problem of thermal drifts that naturally occur during measurements. While negligible in conventional ellipsometry and thus mostly disregarded, I prove that these drifts are a potential source of uncertainty in imaging ellipsometry by performing experiments on moving samples. I also offer an algorithmic solution for handling drifts to improve even already existing setups. Apart from that, I explored the application of specially designed flat meta-lenses, specifically plasmonic lenses, for the advancement of ellipsometric methods towards more compact and versatile setups.

Plasmonic lenses are based on the extraordinary transmission effect. Usually, light is unable to pass holes which are significantly smaller than the wavelength. However, it was observed that, instead of the transmission dropping steadily towards zero with decreasing hole diameter, there is some transmission enhancement for certain small diameters of metallic holes [44, 45]. This unexpected behavior was called extraordinary transmission. Although not completely understood yet [46], it is regarded by most to be linked to the excitation of surface plasmon polaritons (SPPs) [45, 47], which are oscillations of the surface electron density coupled to the photons that excited them. They were first described in the late 1960s [48]. When light passes as SPPs through such a hole, its phase changes according to the hole size and shape [49, 50, 51]. In the 2000s, when this was examined in more detail and when fabrication techniques for such holes became more available, the first types of focusing plasmonic metasurfaces were developed by arranging slits or similar structures in metal [52, 53, 54, 55, 56, 57]. Concerning the advancement of ellipsometry, this thesis aimed to scrutinize the suitability of these types of structures for the enhancement of measurement sensitivity. Other than normal lenses, plasmonic lenses are flat and can produce small focal spots with much shorter focal lengths. This potentially enables an easier integration of these lenses in ellipsometry, leading to more compact setups. Also, it enables extensions of the method by scanning type measurements, which I approached with numerical simulations at focal distances of a few micrometers. However, plasmonic lenses as they are common in literature are relatively difficult to produce without the right tools. They often require focused ion beam (FIB) milling for their fabrication, which is rather time consuming and unsuited for a large-scale production. This is why I developed a new design, the so-called inverted plasmonic lens, which I present in this thesis. The new design enables an easier fabrication with common lithography methods. Using this, I designed, simulated and, after fabrication, measured a set of inverted plasmonic lenses to characterize their functionality, and created a study about various lens parameters to see their limitations. Part of the new design is an alternative placement scheme for the waveguides these lenses are made of, which maximizes the throughput and thus tackles one of plasmonic lenses' major disadvantages compared to dielectric meta-lenses.

In addition, I characterized their dispersive behavior and discuss different schemes for the realization of achromatic plasmonic lenses compatible with ellipsometric methods at multiple wavelengths.

After this motivation, Chapter 2 starts with a brief introduction concerning MAXWELL's equations and how light behaves when it interacts with conductive media. That gives us the foundation needed to describe the polarization of light in the MUELLER matrix formalism and the link between photons and plasmons. Chapter 3 then goes into detail about ellipsometry, comparing different techniques of polarimetry and ellipsometry and presenting the experimental setups used in this thesis. It also introduces us to the nanoform sample, the set of structures fabricated for the investigations in this thesis. Measurements conducted on this sample revealed thermal drifts, which are characterized and algorithmically accounted for. Continuing from the exposition, Chapter 4 then shows how plasmonic waveguides can be used to build flat lenses. It presents the inverted plasmonic lens design and goes into detail about parameter optimization. After evaluating the performance of the lenses, both numerically and experimentally, it discusses different concepts for the realization of multispectral plasmonic lenses to circumvent the dispersion observed in the evaluation. Afterwards, Chapter 5 characterizes the polarizing properties of the fabricated plasmonic lenses using the setups presented earlier, before discussing numerical simulations of MUELLER matrix images as well as the implementation of plasmonic lenses in ellipsometric setups. Apart from that, it covers an approach for the application of machine learning ideas in an ellipsometric context. In the end, Chapter 6 gives a brief conclusion of the results of this thesis.

2

Light in and around Conductive Media

IN THIS THESIS, WE WILL SEE BOTH LIGHT BEING USED AS AN INFORMATION CHANNEL for nanometrology and light being shaped for this purpose. Therefore, we start by briefly reviewing the theoretical framework necessary to understand how light and its interaction with matter will be described mathematically in what follows. This chapter begins at MAXWELL's equations to establish the wave character of light, before it deals with its subsequent property polarization and how to describe it using STOKES vectors. It then introduces the MUELLER matrix formalism for the influence of optical components on polarization, which is the foundation for MUELLER matrix ellipsometry as described in Chapter 3. Afterwards, we see how light waves interact with electrons in metals in a way to excite surface plasmon polaritons. These will be used in Chapter 4 in the construction of plasmonic lenses.

2.1 MAXWELL's Equations and the Description of Light

The classical description of electromagnetic waves follows from MAXWELL's equations [58]. They represent the interaction and propagation of electric fields \vec{E} and magnetic fields \vec{B} :

$$\nabla \cdot \vec{E} = \frac{\rho}{\varepsilon}, \quad (1a) \quad \nabla \times \vec{E} = -\frac{\partial \vec{B}}{\partial t}, \quad (1c)$$

$$\nabla \cdot \vec{B} = 0, \quad (1b) \quad \nabla \times \vec{B} = \mu \vec{j} + \varepsilon \mu \frac{\partial \vec{E}}{\partial t}. \quad (1d)$$

In these equations, $\varepsilon = \varepsilon_0 \varepsilon_r$ denotes the permittivity and $\mu = \mu_0 \mu_r$ the permeability of the corresponding media. In the uncharged, current-free vacuum case, the equations can be simplified by neglecting the electric charge density ρ and the electric current density \vec{j} as well as ε_r and μ_r [59].

2.1.1 Wave Equations

From MAXWELL's equations follows the wave equation for the behavior of electromagnetic waves in conducting media [60]:

$$\nabla^2 \vec{E} - \frac{\sigma}{\epsilon c^2} \frac{\partial \vec{E}}{\partial t} - \frac{1}{c^2} \frac{\partial^2 \vec{E}}{\partial t^2} = 0, \quad (2)$$

where c is the speed of light in the medium and σ denotes the electric conductivity, which is the proportionality between the current density and the electric field [60]:

$$\vec{j} = \sigma \cdot \vec{E}. \quad (3)$$

An in detail derivation of the wave equation is given in Appendix A.1. An often used case is the wave equation in the absence of electrical currents and charges:

$$\nabla^2 \vec{E} - \frac{1}{c^2} \frac{\partial^2 \vec{E}}{\partial t^2} = 0. \quad (4)$$

Similar equations can be found for the magnetic field and in general, each single component of both fields follows the wave equation [46]. Under the assumption of a harmonic time dependence, we can rewrite the wave equation to the HELMHOLTZ equation with the wave number k_0 [61]:

$$\nabla^2 \vec{E} + k_0^2 \vec{E} = 0. \quad (5)$$

2.1.2 Solutions of the Wave Equations

The simplest and presumably most versatile solution of the wave equation is the plane wave [46]:

$$\vec{E}(\vec{r}, t) = \vec{E}_0 e^{i(\vec{k} \cdot \vec{r} - \omega t)}, \quad (6)$$

where \vec{k} is the so-called wave vector. For simplicity, we often consider plane waves traveling along a certain direction of the Cartesian coordinate system, for example the z -direction:

$$\vec{E}(z, t) = \vec{E}_0 e^{i(kz - \omega t)}. \quad (7)$$

In the case of vacuum, without charges present, the divergence of the electric field has to vanish in accordance with Equation (1a). For a plane wave traveling along the z -direction, this reduces to:

$$\frac{\partial E_z}{\partial z} = 0, \quad (8)$$

as the field does not depend on x or y . This is only fulfilled when $E_z = 0$. Non-trivial solutions would suggest that E_z had a constant value for all t and z , which does not hold for a wave. Hence, the field components of an electromagnetic wave in direction of their propagation are zero and the fields oscillate only in the directions transverse to their propagation [58]. Thus, light is considered a transverse electromagnetic wave.

Apart from plane waves, other solutions for the wave equation exist that are especially useful in specific situations, such as the description of certain light sources like lasers. Important examples for these, which are not further discussed in this thesis, are spherical waves and Gaussian beams [62].

2.1.3 Evanescent Fields

A more general description of complex wave fields usually follows from a decomposition of the field into several plane waves, a so-called angular spectrum [63]. Mathematically, this is described via a FOURIER transform of the components of the electromagnetic fields [46]. Consider the electric field in a plane with constant z -coordinate. The inverse FOURIER transform of this field yields its angular spectrum representation [64]:

$$\vec{E}(x, y, z) = \iint_{-\infty}^{\infty} \tilde{\vec{E}}(k_x, k_y; z) e^{i(k_x x + k_y y)} dk_x dk_y. \quad (9)$$

When we insert this into the HELMHOLTZ equation, we see that, in the angular spectrum, the propagation of the wave along the z -axis is described with a phase factor [46, 64]:

$$\tilde{\vec{E}}(k_x, k_y; z) = \tilde{\vec{E}}(k_x, k_y; 0) e^{\pm i k_z z}. \quad (10)$$

The component k_z which is the wave vector component along the axis of propagation is also called the propagation constant β [61]. The different signs of $e^{\pm i k_z z}$ represent different directions of propagation along the z -axis. For propagating waves, k_z is real and $e^{\pm i k_z z}$ describes an oscillation. However, the wave number k_z might also be imaginary. This leads to a phase factor of $e^{-k_z z}$ which describes a field decaying along the z -axis instead. This case is also referred to as the evanescent field. Generally, it only occurs at inhomogeneities. The most prominent examples for this are interfaces of dielectric media with different indices of refraction, where total internal reflection occurs [46, 64, 65]. Another important case is the excitation of surface plasmons at metal-dielectric-interfaces, which will be discussed in Section 2.3.1.

When considering the wave vector \vec{k} , its components have to describe the surface of a sphere with radius $|\vec{k}| = k$, the so called EWALD sphere [66]:

$$k^2 = k_x^2 + k_y^2 + k_z^2. \quad (11)$$

For propagating waves, k_z is real and therefore $k^2 \geq k_x^2 + k_y^2$. However, evanescent fields deliver solutions for the wave equation where $k^2 < k_x^2 + k_y^2$, which means that the associated wave vector is no longer inside the EWALD sphere [46]. Transformed into the Cartesian space, spatial frequencies outside of the EWALD sphere relate to structures smaller or closer together than the wavelength. Thus, in contrast to propagating waves, evanescent fields carry information from the sub-wavelength domain [46, 67, 68]. Because of the rapidly decaying nature of evanescent fields however, we can't access this information in the far-field. Therefore, we have to rely on means of near-field optics, for example scanning near-field optical microscopy (SNOM) [69].

2.2 Polarization of Light

We have seen in Section 2.1.2 that propagating light is a transverse electromagnetic wave, where the electric and magnetic field vectors oscillate in directions perpendicular to the propagation. The orientation of these oscillations is referred to as polarization. In this section, we discuss the mathematical descriptions of polarization relevant for this work.

2.2.1 The Polarization Ellipse

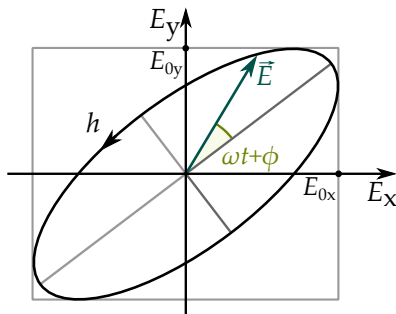


Figure 2.1 – Polarization ellipse. The helicity is denoted by h .

Considering a monochromatic plane wave as introduced in Section 2.1.2:

$$\vec{E}(\vec{r}, t) = \vec{E}_0 \cdot e^{i(\vec{k} \cdot \vec{r} - \omega t + \phi)}, \quad (12)$$

with an arbitrary phase ϕ . The wave travels along the z -direction and the fields oscillate transversely to its direction of propagation in the x - y -plane. Thus, the wave can be decomposed into the Cartesian components [70]:

$$E_x(z, t) = E_{0x} \cos(kz - \omega t + \phi_x), \quad (13a)$$

$$E_y(z, t) = E_{0y} \cos(kz - \omega t + \phi_y), \quad (13b)$$

$$E_z(z, t) = 0. \quad (13c)$$

When these equations are combined, they result in the equation of an ellipse, which is the most general description of the polarization of an electromagnetic wave:

$$\frac{E_x^2}{E_{0x}^2} + \frac{E_y^2}{E_{0y}^2} - 2 \frac{E_x E_y}{E_{0x} E_{0y}} \cos(\phi) = \sin^2(\phi), \quad (14)$$

with the arbitrary phases $\phi = \phi_y - \phi_x$. A schematic of the polarization ellipse is given in Figure 2.1.

2.2.2 States of Polarization

As demonstrated in Section 2.2.1, the polarization of light can generally be described with an ellipse. Consequently, this case is referred to as elliptical polarization. Figure 2.2(a) shows an example for this. From the general case, useful special cases can be derived. If the half-axes of the ellipse are of same length ($E_{0x} = E_{0y} = E_0$) and the phase ϕ is an odd-numbered multiple of $\pi/2$, the ellipse degenerates to a circle, which describes circular polarization:

$$\frac{E_x^2}{E_0^2} + \frac{E_y^2}{E_0^2} = 1. \quad (15)$$

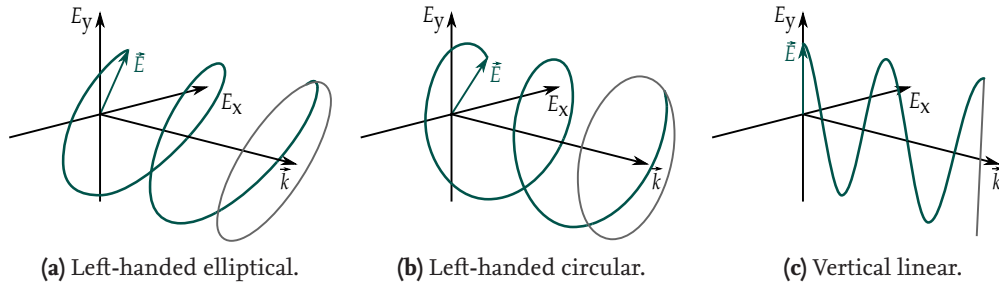


Figure 2.2 – Examples for elliptical (a), circular (b), and linear (c) states of polarization.

In both cases, elliptical and circular polarization, the helicity h of the wave can be either left-handed or right-handed, depending on the phase. An example for left-handed circular polarization is depicted in Figure 2.2(b). If the phase is an integer multiple of π , Equation (14) further simplifies to a linear equation, describing linear polarization:

$$E_y = \pm \left(\frac{E_{0x}}{E_{0y}} \right) E_x . \tag{16}$$

If one of the field components vanishes, this results in linear horizontal ($E_{0y} = 0$) or vertical ($E_{0x} = 0$) polarization. The latter is shown in Figure 2.2(c). If the field components are the same, the equation describes diagonally polarized light [70].

When describing light at oblique incidences, e.g. when dealing with reflection, refraction, or change of propagation, it is more reasonable to describe the state of polarization relative to a plane of incidence instead of an overall coordinate system. We describe light as parallel (p) polarized, if the electric field vector oscillates in the plane of incidence, which is spanned by the wave vector \vec{k} and the normal vector \vec{n} of the surface as depicted in Figure 2.3(a). Likewise, perpendicular (s from German *senkrecht*) polarized light has its electric field vector perpendicular to the plane of incidence, as shown in Figure 2.3(b). In the context of structured fields, when the plane of incidence coincides with the plane spanned by the normal vector \vec{n} and the grating vector \vec{g} , we also refer to these cases as transverse-magnetic (TM) or transverse-electric (TE) polarized, respectively [46].

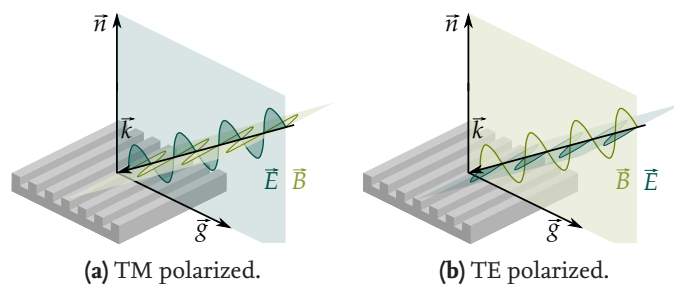


Figure 2.3 – States of polarization depending on the plane of incidence. Examples for TM (a) and TE polarized light (b).

2.2.3 JONES Calculus

A vector based description for completely polarized light was introduced in 1941 by Robert Clark JONES [71]. States of polarization of a plane wave propagating in z -direction are described by a so-called JONES vector \vec{J} :

$$\vec{E} = \vec{J} \cdot e^{i(\vec{k} \cdot \vec{r} - \omega t)}, \quad \vec{J} = \begin{pmatrix} E_{0x} e^{i\phi_x} \\ E_{0y} e^{i\phi_y} \end{pmatrix}. \quad (17)$$

When examining polarization only, JONES vectors are usually normalized with regard to amplitude and phase [58].

If an optical component changes the polarization of light, this transform is mathematically performed via a 2×2 JONES matrix \underline{M}_J :

$$\vec{J}' = \underline{M}_J \cdot \vec{J}. \quad (18)$$

2.2.4 STOKES Calculus

The JONES calculus introduced in Section 2.2.3 describes completely polarized light in a compact manner. The vectorial treatment of only partially polarized light however needs another formalism. In 1852, Sir George Gabriel STOKES introduced the description of polarized light via four parameters, the so-called STOKES parameters, which can be summarized into a STOKES vector [72]:

$$\begin{pmatrix} S_0 \\ S_1 \\ S_2 \\ S_3 \end{pmatrix} = \begin{pmatrix} E_{0x}^2 + E_{0y}^2 \\ E_{0x}^2 - E_{0y}^2 \\ 2E_{0x}E_{0y} \cos(\phi) \\ 2E_{0x}E_{0y} \sin(\phi) \end{pmatrix}. \quad (19)$$

The first parameter, S_0 , denotes the overall intensity I of the light. S_1 contains information about linear horizontal and vertical polarization, S_2 describes linear diagonal polarization, and S_3 stands for circular polarization. Generally, the sum of the squares of the other parameters is less than or equal to the square of S_0 :

$$S_0^2 \geq S_1^2 + S_2^2 + S_3^2. \quad (20)$$

Completely unpolarized light is represented by every parameter except S_0 being zero. For partially polarized light, the degree of polarization Π is defined as [70]:

$$\Pi = \frac{\sqrt{S_1^2 + S_2^2 + S_3^2}}{S_0}. \quad (21)$$

Similar to the JONES calculus, the change of polarization induced by optical components onto a STOKES vector is described with 4×4 MUELLER matrices [73, 74]:

$$\vec{S}' = \underline{M} \cdot \vec{S}, \tag{22a}$$

$$\begin{pmatrix} S'_0 \\ S'_1 \\ S'_2 \\ S'_3 \end{pmatrix} = \begin{pmatrix} m_{00} & m_{01} & m_{02} & m_{03} \\ m_{10} & m_{11} & m_{12} & m_{13} \\ m_{20} & m_{21} & m_{22} & m_{23} \\ m_{30} & m_{31} & m_{32} & m_{33} \end{pmatrix} \cdot \begin{pmatrix} S_0 \\ S_1 \\ S_2 \\ S_3 \end{pmatrix}. \tag{22b}$$

The interaction with multiple components mathematically corresponds to the multiplication of the respective MUELLER matrices. As a helpful example, the rotation of an optical component by an angle of θ is achieved by multiplying the component's MUELLER matrix with a rotation matrix $\underline{R}(\theta)$:

$$\underline{M}(\theta) = \underline{R}(-\theta) \cdot \underline{M} \cdot \underline{R}(\theta), \quad \underline{R}(\theta) = \begin{pmatrix} 1 & 0 & 0 & 0 \\ 0 & \cos(2\theta) & \sin(2\theta) & 0 \\ 0 & -\sin(2\theta) & \cos(2\theta) & 0 \\ 0 & 0 & 0 & 1 \end{pmatrix}. \tag{23}$$

A set of relevant MUELLER matrices is collected in Appendix A.2.

2.2.5 MUELLER JONES Matrices

If the light is completely polarized, the degree of polarization is $\Pi = 1$ and the squares of the STOKES parameters sum up to the square of the intensity:

$$S_0^2 = S_1^2 + S_2^2 + S_3^2. \tag{24}$$

When completely polarized light interacts with a non-depolarizing medium, the MUELLER matrix of this medium is referred to as a pure MUELLER matrix or a MUELLER JONES matrix, because it can also be described by a JONES matrix. Equivalently, each JONES matrix can be transformed into a MUELLER JONES matrix via [75]:

$$\underline{M} = \underline{T}(\underline{M}_j \otimes \underline{M}_j^*)\underline{T}^{-1}, \tag{25}$$

where \underline{T} is the transformation matrix [75]:

$$\underline{T} = \begin{pmatrix} 1 & 0 & 0 & 1 \\ 1 & 0 & 0 & -1 \\ 0 & 1 & 1 & 0 \\ 0 & i & -i & 0 \end{pmatrix}. \tag{26}$$

We can use the depolarization index P_D as a description for the purity of a state of polarization [76]:

$$P_D = \frac{\sqrt{\text{Tr}(\underline{M}^T \underline{M}) - m_{00}^2}}{\sqrt{3} \cdot m_{00}}. \tag{27}$$

A pure MUELLER matrix has a depolarization index of $P_D = 1$ [75].

2.3 Plasmonics

In conductive solids, electromagnetic forces induced by incident light inherently influence the movement of electrons among atomic nuclei, leading to charge imbalances and causing local electric fields. These plasmonic interactions are able to create evanescent fields traveling along the surfaces of solids. This section gives a brief introduction into plasmonics and the properties of surface plasmon polaritons.

2.3.1 Plasma Oscillations

Consider a number of n_e free electrons in a medium being displaced by a distance of x from their quasi-neutral positions, for example due to an external electric field. This displacement creates a net charge imbalance, which, according to MAXWELL's Equation (1a), leads to an electric field itself:

$$E_x = \frac{p}{\epsilon_0} = \frac{en_e x}{\epsilon_0}, \quad (28)$$

where p is the dipole moment caused by the displacement [77, 78]. This electric field creates a retracting force on the electrons:

$$m_e \frac{d^2 x}{dt^2} = -eE_x = -\frac{e^2 n_e x}{\epsilon_0}. \quad (29)$$

This force might cause the electrons to oscillate around the nuclei, so we describe the solution to this differential equation with a periodic movement of the electrons:

$$x(t) = x_0 \cos(\omega_p t), \quad (30)$$

where ω_p is the frequency of this oscillation. With Equation (29), this leads to:

$$m_e \omega_p^2 x = \frac{e^2 n_e x}{\epsilon_0}, \quad (31a)$$

$$\omega_p = \sqrt{\frac{e^2 n_e}{m_e \epsilon_0}}. \quad (31b)$$

Following the description of free electrons in conductive solids as a plasma, this oscillation frequency ω_p of the charge density is usually referred to as the plasma frequency. Likewise, local imbalances of the charge density carry on through the solid as plasma oscillations [77, 79]. These collective, propagating excitations of the free electrons are described via quasi-particles, so-called plasmons. When these electron density waves travel along the surface of a material, we call them surface plasmons [80].

2.3.2 Surface Plasmon Polaritons

As indicated in Section 2.3.1, external electromagnetic fields, for example in the form of photons, can excite plasma oscillations. If plasmons couple to the photons that excited them, they are referred to as plasmon polaritons [77]. We want to focus on the special case of surface plasmon polaritons (SPP), which are oscillations of the surface electron density, excited by and coupled to photons while propagating along the surface [81]. We can excite these evanescent fields deliberately at the interfaces between materials with a positive and a negative permittivity, respectively. In most cases, these materials are a dielectric medium and a metal [82, 83].

Figure 2.4(a) depicts an interface between two arbitrary uncharged media 1 and 2 with permittivities ϵ_1 and ϵ_2 . We assume density charge oscillations inside material 2 coupled to an electric field right at the interface. We describe this field as follows:

$$\vec{E}(\vec{r}, t) = \begin{cases} E_{0,1}e^{-i(\omega t+k_x,1x+k_{z,1}z)}, & z > 0 \\ E_{0,2}e^{-i(\omega t+k_x,2x+k_{z,2}z)}, & z \leq 0 \end{cases} \quad (32)$$

The electric field underlies continuity conditions at the interface [59]:

$$E_{x,1} - E_{x,2} = 0, \quad (33a)$$

$$\epsilon_1 E_{z,1} - \epsilon_2 E_{z,2} = 0, \quad (33b)$$

which together with MAXWELL’S equations lead to the dispersion relation of the wave vector component along the surface [82]:

$$k_x = \frac{\omega}{c} \sqrt{\frac{\epsilon_1 \epsilon_2}{\epsilon_1 + \epsilon_2}}, \quad (34)$$

and the component perpendicular to the surface [82]:

$$k_{z,v} = \sqrt{\epsilon_v \left(\frac{\omega}{c}\right)^2 - k_x^2} = \frac{\omega}{c} \sqrt{\frac{\epsilon_v^2}{\epsilon_1 + \epsilon_2}}, \quad v = 1, 2. \quad (35)$$

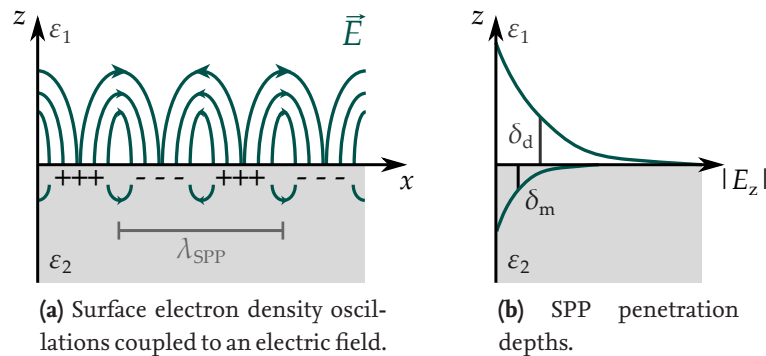


Figure 2.4 – SPPs at the interface between two materials, adapted from [84]. Electric field at the surface (a) and with distance to it (b).

Generally, the electric permittivity is complex-valued: $\varepsilon = \varepsilon' + i\varepsilon''$. Under the assumption that the permittivity of material 1 is real-valued, and when our goal is to describe propagations along the interface, k_x^2 has to be real-valued as well [82]. Thus, the real part of the permittivity of material 2 has to be negative and its absolute value has to be larger than the one of material 1. Usually, metals do have large negative real parts and smaller imaginary parts, so these requirements for the existence of SPPs are fulfilled for metal-dielectric-interfaces. In this case, $k_{z,v}$ is imaginary, which classifies the electromagnetic field associated with SPPs as an evanescent field (see Section 2.1.3). The suitability of a metal for plasmonic excitations is coupled to its permittivity and can be expressed in form of a quality factor [85, 86]:

$$Q_{\text{SPP}} = \frac{\varepsilon_m'^2}{\varepsilon_m''} . \quad (36)$$

For example, pure silver is the metal with the highest quality factor of $Q_{\text{SPP}} \approx 373$ at a wavelength of 532 nm (data from [87]).

From the real part of k_x , we get the wavelength of the SPPs along the surface [88]:

$$\lambda_{\text{SPP}} = \lambda_0 \sqrt{\frac{\varepsilon_d + \varepsilon_m'}{\varepsilon_d \varepsilon_m'}} , \quad (37)$$

where $\lambda_0 = 2\pi/k_0$ is the incident wavelength and $\varepsilon_{m,d} = \varepsilon'_{m,d} + i\varepsilon''_{m,d}$ are the complex permittivities of the metal and the dielectric, respectively. Generally, k_x is complex-valued, which means that the field is also dampened along the interface from its center of origin. From the imaginary part of k_x , we obtain the distance after which the SPPs' intensity decreases by $1/e$ of their initial value, the so-called propagation length [88]:

$$\delta_{\text{SPP}} = \lambda_0 \frac{\varepsilon_m'^2}{2\pi\varepsilon_m''} \left(\frac{\varepsilon_d + \varepsilon_m'}{\varepsilon_d \varepsilon_m'} \right)^{\frac{3}{2}} . \quad (38)$$

Additionally, SPPs penetrate into both media to a certain extent which is considered by the penetration depths illustrated in Figure 2.4(b) [88]:

$$\delta_d = \frac{1}{k_0} \sqrt{\left| \frac{\varepsilon_d + \varepsilon_m'}{\varepsilon_d^2} \right|} , \quad (39a)$$

$$\delta_m = \frac{1}{k_0} \sqrt{\left| \frac{\varepsilon_d + \varepsilon_m'}{\varepsilon_m'^2} \right|} . \quad (39b)$$

2.3.3 Excitation of Surface Plasmon Polaritons

Figure 2.5 illustrates the dispersion curve of SPPs at an interface between a metal (silver) and a dielectric material (SiO_2), following Equation (34). As we see, it always lies at higher wave numbers than the light line, shown for the vacuum case. The excitation of SPPs, however, requires conservation of energy and momentum, but the momentum of a photon is always smaller than that of the SPPs. This momentum mismatch prevents photons to directly excite SPPs. Nevertheless, we can find geometries to compensate this momentum mismatch, for example by using the total internal reflection in prisms or by means of grating couplers [82, 83, 84].

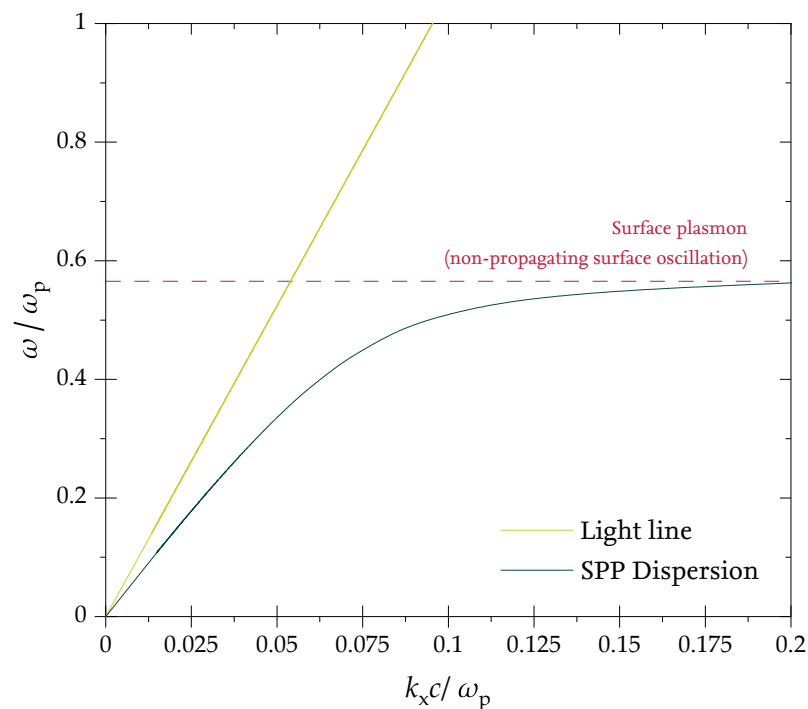


Figure 2.5 – Dispersion of surface plasmon polaritons at an interface between silver and SiO_2 (dark) compared to light in vacuum (light), normalized to the plasma frequency in silver. The dashed red line is the frequency of surface plasmons at the silver- SiO_2 interface.

MUELLER Matrix Ellipsometry

ONE OF THE MOST IMPORTANT PROPERTIES OF LIGHT IS ITS POLARIZATION. ESPECIALLY in nanometrology, it forms a crucial information channel sensitive to geometries as well as materials of samples under investigation. Using the MUELLER matrix formalism introduced in Chapter 2, we now take a look on the polarization-based characterization of nanostructures, from experimental setups to measurements on specific samples. This chapter starts with a brief overview over polarimetric and ellipsometric techniques before presenting the setups used in this thesis. Afterwards, a particular set of samples for systematic investigations on local polarization influences is introduced and characterized. This chapter ends with a treatment of thermal influences in ellipsometric systems.

3.1 Polarimetry and Ellipsometry

Polarimetry is the science of measuring polarization as a property of waves [89]. The terms polarimetry and ellipsometry are often used synonymous and their distinction is not always presented clearly. Ellipsometry is more of a specialized case of polarimetry: While polarimetry measures the state of polarization of a beam of light, ellipsometry measures the polarization ellipse. This is more often used in the scope of thin film or surface characterization in reflection measurements, usually to retrieve layer thicknesses or refractive indices [28, 70, 90, 91]. Nevertheless, both terms are sufficiently congruent and as this thesis deals mainly with measurements of surface nanostructures, I will refer to the procedures used here as ellipsometry. This section gives a brief overview of common polarimetry and ellipsometry techniques that are relevant for this work.

3.1.1 Ψ - Δ -Ellipsometry

Historically speaking, ellipsometry could be divided from polarimetry by performing measurements in reflection. As such, traditional ellipsometry measures the reflection (or transmission) from a sample for two different states of polarization of the illuminating light, s- and p-polarized. The resulting complex reflection coefficient ratio is then described in terms of an amplitude and a phase difference:

$$\frac{R_p}{R_s} = \tan \Psi \cdot e^{i\Delta} . \quad (40)$$

As usual in ellipsometry, the resulting values, Ψ and Δ , are then used to indirectly derive the desired information about the sample by fitting a model to the measurement. This way, film thicknesses or refractive indices can be obtained [25].

3.1.2 STOKES Polarimetry

Sets of optical elements that are used to create a certain state of polarization are called polarization state generators (PSG). Similarly, polarization state analyzers (PSA) are systems to analyze the state of polarization. Both, PSG and PSA, often involve rotating optical elements for the creation or examination of polarization. Rotating element polarimetry uses the intensity modulation created by these rotating polarizing elements to deduce STOKES vectors, which usually involves a truncated FOURIER series over the rotation angle θ . One of the simplest possible PSAs is a single polarizer, shown in Figure 3.1(a). When inserted in a polarized beam of light in front of a detector, rotating the polarizer creates a modulation of the measured intensity, as depicted in Figure 3.2(a). Using the formalism introduced in Section 2.2.4, this enables the measurement of three of the four STOKES parameters [70]:

$$\vec{S}' = \underline{R}(-\theta) \cdot \underline{M}_{\text{pol}} \cdot \underline{R}(\theta) \cdot \vec{S} , \quad (41a)$$

$$\begin{pmatrix} S'_0 \\ S'_1 \\ S'_2 \\ S'_3 \end{pmatrix} = \begin{pmatrix} 1 & 0 & 0 & 0 \\ 0 & \cos(2\theta) & -\sin(2\theta) & 0 \\ 0 & \sin(2\theta) & \cos(2\theta) & 0 \\ 0 & 0 & 0 & 1 \end{pmatrix} \cdot \frac{1}{2} \begin{pmatrix} 1 & 1 & 0 & 0 \\ 1 & 1 & 0 & 0 \\ 0 & 0 & 0 & 0 \\ 0 & 0 & 0 & 0 \end{pmatrix} \cdot \begin{pmatrix} 1 & 0 & 0 & 0 \\ 0 & \cos(2\theta) & \sin(2\theta) & 0 \\ 0 & -\sin(2\theta) & \cos(2\theta) & 0 \\ 0 & 0 & 0 & 1 \end{pmatrix} \cdot \begin{pmatrix} S_0 \\ S_1 \\ S_2 \\ S_3 \end{pmatrix} \quad (41b)$$

$$= \frac{1}{2} \begin{pmatrix} 1 & \cos(2\theta) & \sin(2\theta) & 0 \\ \cos(2\theta) & \cos^2(2\theta) & \sin(2\theta)\cos(2\theta) & 0 \\ \sin(2\theta) & \sin(2\theta)\cos(2\theta) & \sin^2(2\theta) & 0 \\ 0 & 0 & 0 & 0 \end{pmatrix} \cdot \begin{pmatrix} S_0 \\ S_1 \\ S_2 \\ S_3 \end{pmatrix} . \quad (41c)$$

The modulated intensity follows from executing the multiplication for the first STOKES parameter only:

$$S'_0 = I = \frac{S_0}{2} + \frac{S_1}{2} \cos(2\theta) + \frac{S_2}{2} \sin(2\theta) = \frac{a_0}{2} + \frac{a_2}{2} \cos(2\theta) + \frac{b_2}{2} \sin(2\theta) , \quad (42)$$

where a and b are the FOURIER coefficients.

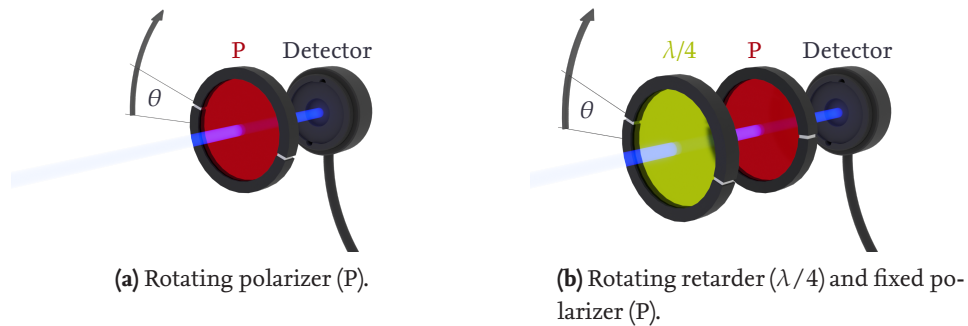


Figure 3.1 – Examples for polarization state analyzers (PSA), consisting of a single polarizer (a) and a combination of polarizer and retarder (b).

The full STOKES vector can already be obtained by adding a retarder, a quarter-wave plate, as a rotating element in front of a fixed polarizer, as visualized in Figure 3.1(b). In this case, the modulated intensity can be obtained in the same way [70] (compare Figure 3.2(b)):

$$I = \frac{a_0}{2} + \frac{1}{2} \sum_{v=1}^2 (a_{2v} \cos(2v\theta) + b_{2v} \sin(2v\theta)) . \tag{43}$$

The STOKES vector follows again from the FOURIER coefficients:

$$\begin{pmatrix} S_0 \\ S_1 \\ S_2 \\ S_3 \end{pmatrix} = \begin{pmatrix} a_0 - a_4 \\ 2a_4 \\ 2b_4 \\ b_2 \end{pmatrix} . \tag{44}$$

In this manner, several different possible combinations of rotating optical elements allow for the characterization of the STOKES parameters.

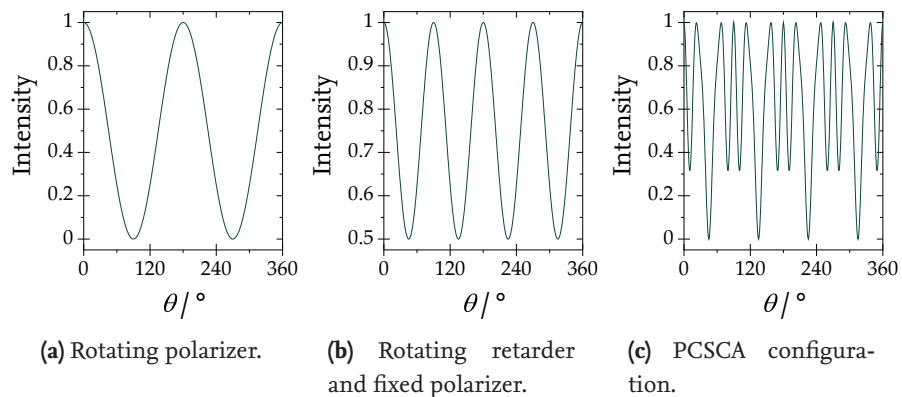


Figure 3.2 – Intensity modulation of linear polarized light due to rotating optical elements. Examples for a rotating polarizer (a), a polarizer and retarder (b), and PCSCA configuration (c).

3.1.3 MUELLER Matrix Ellipsometry

Instead of measuring the sample properties at just two states of polarization, as described in Section 3.1.1, a more generalized approach to ellipsometry is to measure at many different states of polarization. This gives access to the sample's MUELLER matrix, which contains additional information about anisotropy and depolarization [25]. For the measurement of the MUELLER matrix of a sample, we need to modulate both, the polarization of the illumination and of the light coming from the sample. Thus, regarding the rotating element polarimetry from Section 3.1.2, a PSG and a PSA are needed [70]. A common way to accomplish that is the configuration shown in Figure 3.3(a) that uses a fixed polarizer in combination with a rotating retarder as PSG and a rotating polarizer, which is in this case called an analyzer, as PSA. This configuration is abbreviated as PCSA (polarizer, compensator, sample, analyzer) and it is capable of measuring the first three rows of the MUELLER matrix. The complete MUELLER matrix can be obtained with rotating optical elements when both, PSG and PSA, consist of a fixed polarizer and a rotating retarder. This configuration, depicted in Figure 3.3(b), is referred to as dual-rotating retarder configuration or PCSCA (polarizer, compensator, sample, compensator, analyzer) [70, 92, 93].

In general, for any ellipsometric system, the modulated intensity measured at the detector comes from the MUELLER matrix \underline{M} of the sample, the MUELLER matrix of the PSA, and the STOKES vector coming from the PSG. As we are only interested in the intensity, we can omit the other rows and find the intensity as a sum of parameters [70]:

$$\vec{S}' = \underline{M}_{\text{PSA}} \cdot \underline{M} \cdot \vec{S}_{\text{PSG}}, \quad (45a)$$

$$\begin{pmatrix} I \\ \cdot \\ \cdot \\ \cdot \end{pmatrix} = \begin{pmatrix} m_{a,0} & m_{a,1} & m_{a,2} & m_{a,3} \\ \cdot & \cdot & \cdot & \cdot \\ \cdot & \cdot & \cdot & \cdot \\ \cdot & \cdot & \cdot & \cdot \end{pmatrix} \cdot \begin{pmatrix} m_{00} & m_{01} & m_{02} & m_{03} \\ m_{10} & m_{11} & m_{12} & m_{13} \\ m_{20} & m_{21} & m_{22} & m_{23} \\ m_{30} & m_{31} & m_{32} & m_{33} \end{pmatrix} \cdot \begin{pmatrix} S_{g,0} \\ S_{g,1} \\ S_{g,2} \\ S_{g,3} \end{pmatrix}, \quad (45b)$$

$$I = \sum_{u,v=0}^3 m_{a,u} m_{uv} S_{g,v} = \sum_{u,v=0}^3 \mu_{uv} m_{uv}, \quad (45c)$$

with $\mu_{uv} = m_{a,u} S_{g,v}$. For a dual-rotating retarder configuration like in Figure 3.3(b) with two linear polarizers and two rotating quarter-wave plates, we can specify this further:

$$\vec{S}' = \underline{M}_{\text{PSA}} \cdot \underline{M} \cdot \vec{S}_{\text{PSG}} \quad (46a)$$

$$= \underline{M}_{\text{pol}} \cdot \underline{R}(-\theta_A) \cdot \underline{M}_{\lambda/4} \cdot \underline{R}(\theta_A) \cdot \underline{M} \cdot \underline{R}(-\theta_G) \cdot \underline{M}_{\lambda/4} \cdot \underline{R}(\theta_G) \cdot \underline{M}_{\text{pol}} \cdot \vec{S}. \quad (46b)$$

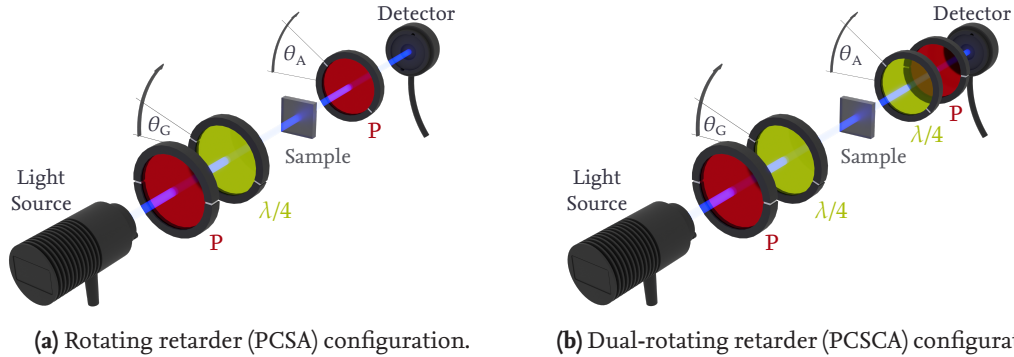


Figure 3.3 – MUELLER matrix ellipsometry configurations with one (a) and two retarders (b).

The retarders of the PSA and PSG need to rotate with different speeds to obtain enough modulation for a FOURIER analysis like discussed in Section 3.1.2. Though many different ratios for their speeds are possible to obtain the MUELLER matrix, we want to consider only the lowest possible one, which is 5:1 [70], so $\theta_G = \theta$ and $\theta_A = 5\theta$. Given that the light source is generally unpolarized and using trigonometric identities, we get:

$$\vec{S}_{PSG} = \underline{R}(-\theta) \cdot \underline{M}_{\lambda/4} \cdot \underline{R}(\theta) \cdot \underline{M}_{pol} \cdot \vec{S} \tag{47a}$$

$$= \frac{1}{2} \begin{pmatrix} 1 \\ \cos^2(2\theta) \\ \sin(2\theta) \cos(2\theta) \\ \sin(2\theta) \end{pmatrix}, \tag{47b}$$

$$\underline{M}_{PSA} = \underline{M}_{pol} \cdot \underline{R}(-5\theta) \cdot \underline{M}_{\lambda/4} \cdot \underline{R}(5\theta) \tag{48a}$$

$$= \frac{1}{2} \begin{pmatrix} 1 & \cos^2(10\theta) & \sin(10\theta) \cos(10\theta) & -\sin(10\theta) \\ 1 & \cos^2(10\theta) & \sin(10\theta) \cos(10\theta) & -\sin(10\theta) \\ 0 & 0 & 0 & 0 \\ 0 & 0 & 0 & 0 \end{pmatrix}. \tag{48b}$$

When we neglect the factors of 1/2 because they are just intensity scaling factors, we get for the respective vectors of PSA and PSG:

$$\begin{pmatrix} m_{a,0} & m_{a,1} & m_{a,2} & m_{a,3} \end{pmatrix} = \begin{pmatrix} 1 & \cos^2(10\theta) & \sin(10\theta) \cos(10\theta) & -\sin(10\theta) \end{pmatrix}, \tag{49}$$

$$\begin{pmatrix} S_{g,0} \\ S_{g,1} \\ S_{g,2} \\ S_{g,3} \end{pmatrix} = \begin{pmatrix} 1 \\ \cos^2(2\theta) \\ \sin(2\theta) \cos(2\theta) \\ \sin(2\theta) \end{pmatrix}. \tag{50}$$

These are now used to calculate the expressions for $\mu_{uv} = m_{a,u}S_{g,v}$, which help to develop the modulated intensity in a FOURIER series:

$$I = \sum_{u,v=0}^3 \mu_{uv} m_{uv} \quad (51a)$$

$$= a_0 + \sum_{j=1}^{12} (a_j \cos(2j\theta) + b_j \sin(2j\theta)) = I(\theta). \quad (51b)$$

From this, we obtain the FOURIER coefficients a_j and b_j as functions of the MUELLER matrix elements m_{uv} and vice versa:

$$a_0 = m_{00} + \frac{1}{2}(m_{01} + m_{10}) + \frac{1}{4}m_{11} \quad (52)$$

$$\begin{array}{llll} a_1 = 0 & a_7 = \frac{1}{4}m_{32} & b_1 = m_{03} + \frac{1}{2}m_{13} & b_7 = -\frac{1}{4}m_{31} \\ a_2 = \frac{1}{2}m_{01} + \frac{1}{4}m_{11} & a_8 = \frac{1}{8}m_{11} + \frac{1}{8}m_{22} & b_2 = \frac{1}{2}m_{02} + \frac{1}{4}m_{12} & b_8 = -\frac{1}{8}m_{12} - \frac{1}{8}m_{21} \\ a_3 = -\frac{1}{4}m_{32} & a_9 = \frac{1}{4}m_{23} & b_3 = -\frac{1}{4}m_{31} & b_9 = -\frac{1}{4}m_{13} \\ a_4 = -\frac{1}{2}m_{33} & a_{10} = \frac{1}{2}m_{10} + \frac{1}{4}m_{11} & b_4 = 0 & b_{10} = \frac{1}{2}m_{20} + \frac{1}{4}m_{21} \\ a_5 = 0 & a_{11} = -\frac{1}{4}m_{23} & b_5 = -m_{30} - \frac{1}{2}m_{31} & b_{11} = \frac{1}{4}m_{13} \\ a_6 = \frac{1}{2}m_{33} & a_{12} = \frac{1}{8}m_{11} - \frac{1}{8}m_{22} & b_6 = 0 & b_{12} = \frac{1}{8}m_{12} + \frac{1}{8}m_{21} \end{array}$$

\Leftrightarrow

$$\begin{array}{ll} m_{00} = a_0 - a_2 + a_8 - a_{10} + a_{12} & m_{20} = -2b_8 + 2b_{10} - 2b_{12} \\ m_{01} = 2a_2 - 2a_8 - 2a_{12} & m_{21} = 4b_8 + 4b_{12} \\ m_{02} = 2b_2 + 2b_8 - 2b_{12} & m_{22} = 4a_8 - 4a_{12} \\ m_{03} = b_1 + b_9 - b_{11} & m_{23} = 2(a_9 - a_{11}) \\ m_{10} = -2a_8 + 2a_{10} - 2a_{12} & m_{30} = b_3 - b_5 + b_7 \\ m_{11} = 4a_8 + 4a_{12} & m_{31} = -2(b_3 + b_7) \\ m_{12} = -4b_8 + 4b_{12} & m_{32} = 2(-a_3 + a_7) \\ m_{13} = 2(-b_9 + b_{11}) & m_{33} = -a_4 + a_6 \end{array}$$

The complete derivation of these expressions is given in Appendix A.3, together with the equations for the PCSA configuration.

We calculate the FOURIER coefficients from the measured intensity signal [58]. As the rotation of the retarders usually happens in discrete steps rather than in continuous motion, we use discrete sum expressions for this:

$$a_0 = \frac{2}{N} \sum_{v=1}^N I(\theta_v), \quad (53a)$$

$$a_j = \frac{4}{N} \sum_{v=1}^N I(\theta_v) \cos(2j\theta_v), \quad (53b)$$

$$b_j = \frac{4}{N} \sum_{v=1}^N I(\theta_v) \sin(2j\theta_v). \quad (53c)$$

3.1.4 Error Compensation

When implementing the methods described in Section 3.1.3, misalignments of the optical elements and imperfections of the retarders proved to be the most crucial sources for errors. We can account for these by introducing error compensation parameters that describe deviations of the polarizing elements from the ideal case. Figure 3.4 depicts these parameters for a dual-rotating retarder configuration. The respective parameters account for deviations in the retardation of the two retarders (ε_1 and ε_2) as well as for differences in the orientation of all optical elements relative to the first polarizer (ε_3 , ε_4 , and ε_5). Repeating the FOURIER analysis (as in Section 3.1.3) under consideration of these errors leads to new relations between the MUELLER matrix elements and the FOURIER coefficients. From a calibration measurement without a sample, we obtain the FOURIER coefficients. Together with the identity matrix as a MUELLER matrix, they deliver the error parameters, which in turn can be used in a measurement of a sample for error compensation. As the corresponding relations are lengthy, you may find them in Appendix A.3.2. An in-depth examination of error compensation can be found in [94, 95]. Other sources of error, like depolarization, detector linearity, or wavelength uncertainty, were accounted for by calibrations of the components and by normalizing the results. More complex influences like beam fluctuations due to wedge errors require a more in-depth examination of the uncertainty budget of these setups, which is beyond the scope of this thesis.

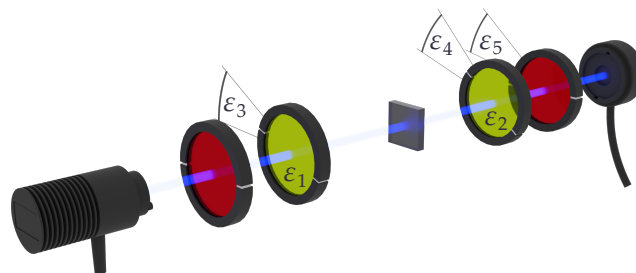


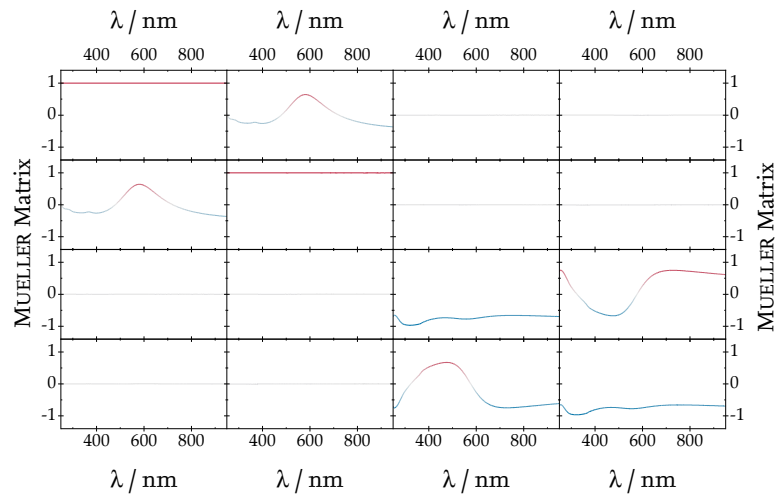
Figure 3.4 – Error compensation parameters.

3.1.5 Imaging Ellipsometry

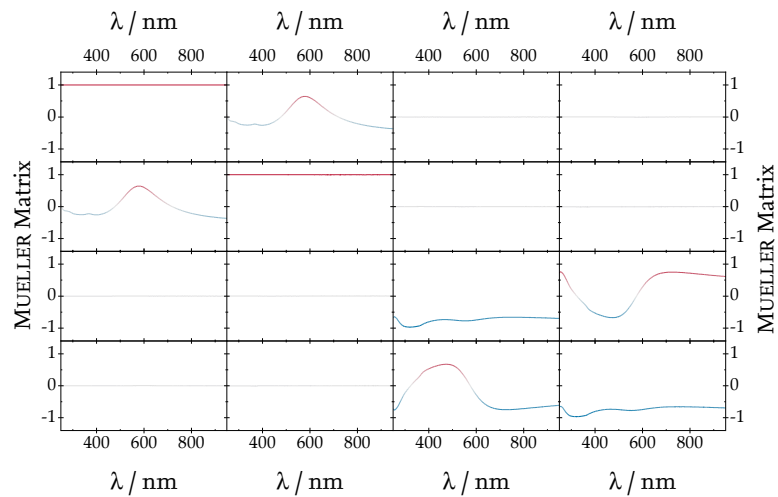
Ellipsometry like described in Sections 3.1.1 - 3.1.4 is a powerful tool. From the measured polarization information, further characteristics of the sample exceeding polarization can be deduced. This encompasses optical parameters, like the refractive index, as well as geometrical parameters, like layer thicknesses, structure sizes or periodicity. The process used for this parameter reconstruction is referred to as solving an inverse problem. First, an ellipsometric measurement of the sample is performed and either Ψ and Δ or the MUELLER matrix are measured. Then, a model of the sample is constructed. For this model, the same ellipsometric values are computed numerically and for different degrees of freedom in the structure. By fitting the numerical model to the measured values, structure parameters can be obtained. This process is highly successful for the parameter reconstruction in various areas [37, 96, 97, 98, 99, 100]. The way homogeneously layered or structured surfaces influence the polarization of transmitted or reflected light and how this effects the MUELLER matrix are already widely examined. However, this is mostly true only for two special cases:

The first case is about homogeneously layered areas. For these kinds of samples, the MUELLER matrix can simply be measured and then used to determine the optical parameters or the thicknesses of the stacked layers.

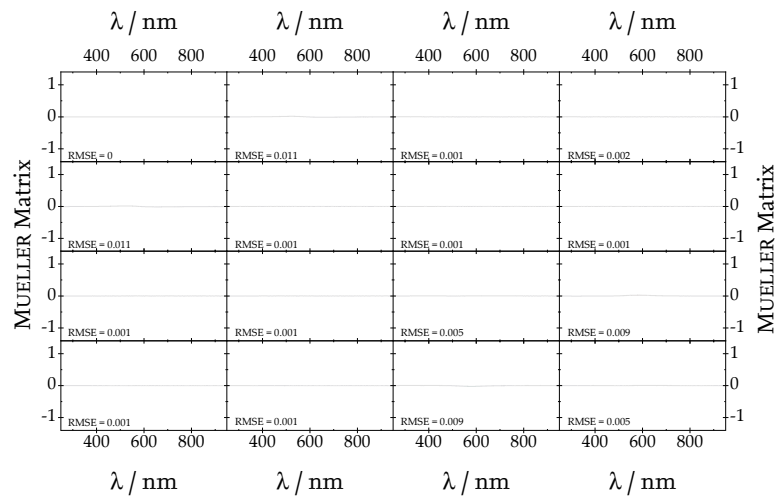
The second case concerns periodic nanostructures, where the influence on the MUELLER matrix stems from the polarizing effect of periodic lattices. When evaluated by solving the inverse problem using numerical simulations, more average information about the periodic structure can be obtained, depending on the number of performed measurements at different wavelengths and angles of incidence. However, conventional ellipsometry has a downside: While it can yield layer thicknesses down to the sub-nanometer regime, since in the detector the response of the sample is integrated over the whole illuminated area, its sensitivity to spatial variations is limited to the spot size of the illumination, which is in the order of magnitude of 1 mm^2 . Thus, when the structured field is smaller than the illumination spot, or when non-periodic samples are examined, additional responses from the surrounding medium might interfere with the result, or information from the actual structures might average out [25, 42]. We see an example for this in Figure 3.5(a). It shows a conventional spectroscopic MUELLER matrix measurement of a square, $5 \times 5 \mu\text{m}^2$ sized structure, performed at PTB's SENTECH SE850 spectroscopic ellipsometer [100, 101] at 70° angle of incidence in reflection. Each graph contains the spectral response of one MUELLER matrix element to a wavelength change between 190 nm and 980 nm. As a comparison, Figure 3.5(b) shows a measurement of the unstructured substrate in the same configuration. As evident from these graphs and clarified in Figure 3.5(c), the structure has no observable influence on the MUELLER matrix elements. In this measurement, the illumination spot diameter is around 200 times the size of the structure under investigation. Therefore, polarizing effects are averaged out at detection.



(a) Measurement of structure.



(b) Measurement of substrate.



(c) Difference between structure and substrate measurement.

Figure 3.5 – Conventional spectroscopic ellipsometry measurement example with (a) and without structure (b) as well as direct comparison (c).

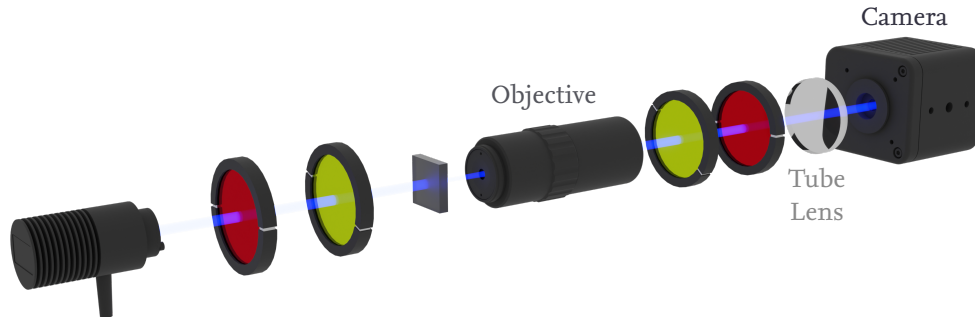


Figure 3.6 – Imaging ellipsometry in PCSCA configuration.

Instead of just reducing the spot size, which also has its limits, a solution for this challenge is imaging ellipsometry. In the analyzing side of the ellipsometer, an objective lens is inserted to collect the light from the sample, and instead of a detector after the PSA, a camera collects the analyzed light and builds an image of the sample. This way, the MUELLER matrix can be measured for each pixel in the resulting microscope image, which in turn leads to 16 individual images of the sample, each representing one element of the MUELLER matrix. These so-called MUELLER matrix images allow for a more local examination of the polarizing properties of the structure, without information loss due to integrating of the spot size [39, 40]. An example for this is shown in Figure 3.6.

3.2 Experimental Setups

For the experiments described in this thesis, two imaging MUELLER matrix ellipsometry setups were used. In this section, both setups and their evaluation procedures are briefly presented.

3.2.1 MUELLER Matrix Microscope

Commercial setups are often closed systems without possibilities for experimental adjustments. Thus, we realized a custom-built imaging MUELLER matrix ellipsometry setup within the framework of a Master's thesis [102]. It is based on a dual-rotating retarder ellipsometry configuration (PCSCA) as described in Section 3.1.3, but horizontally oriented as opposed to the usual vertical orientation. Figures 3.7(a), 3.7(b), and 3.7(c) show a top view sketch, a CAD sketch, and a photography of the setup, respectively. The setup consists of two arms: The arm on the left side of Figure 3.7(a) is fixed to the table and contains the illumination parts of the system, while the arm on the right side is attached to a large aperture rotation stage and contains the analyzing parts.

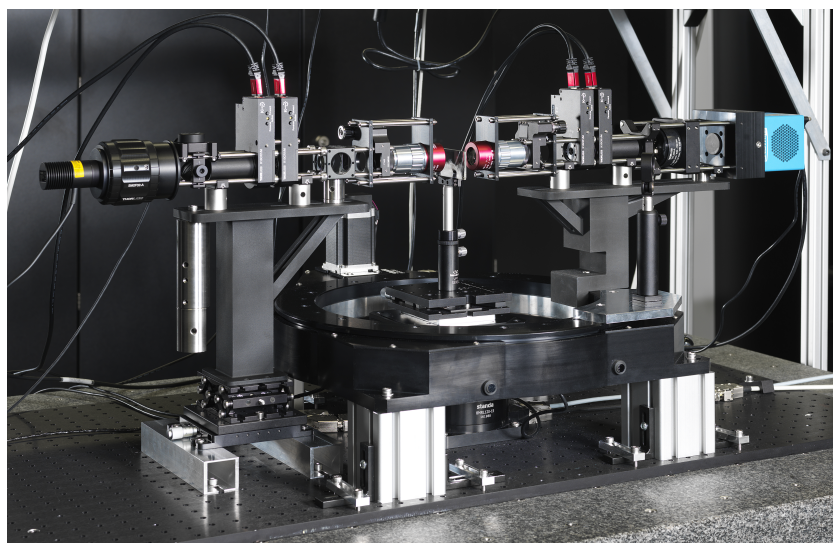
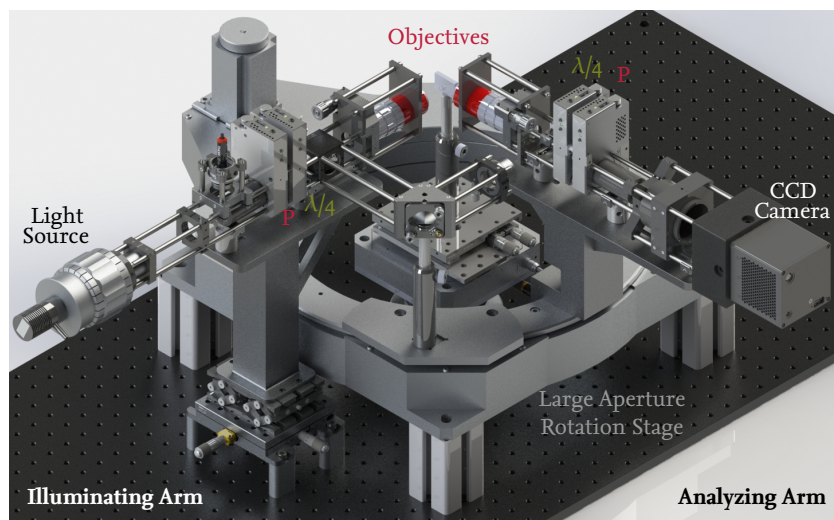
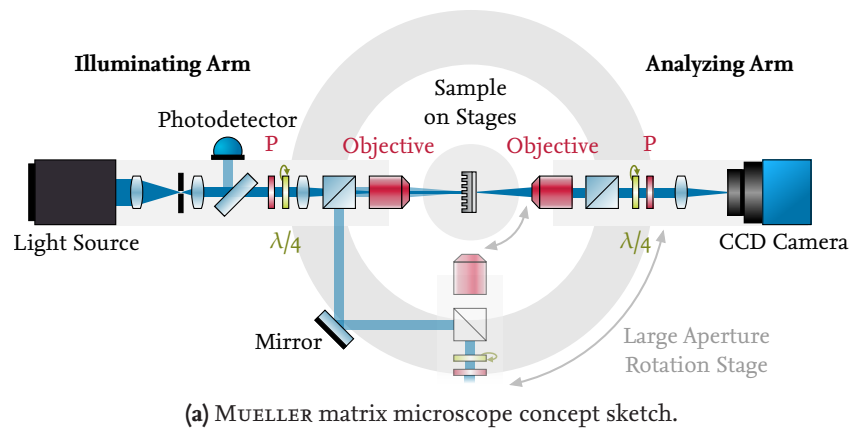


Figure 3.7 – Sketch (a), CAD sketch (b), and photograph (c) of the MUELLER matrix microscope setup. The system can be operated as microscope both in reflection (a, b) and in transmission mode (a, c) as well as in oblique incidence (a, b).

In the illumination arm, light from the light source is collimated and then sent through an aperture to create KÖHLER illumination. For this, two lenses focus the light on the aperture and afterwards collimate it again. Currently, a blue light LED with a wavelength of 455 nm, a bandwidth of 18 nm, and typically 1445 mW power is used as a light source. The short wavelength was chosen to ensure a high resolution in the microscope images. As a reference for the intensity of the light source, 10 % of the light are branched off to a detector using a beam splitter plate, before the remaining light is sent through the polarization state generator system. A GLAN-THOMPSON polarizer and a superachromatic quarter-wave plate, both placed in motorized rotation mounts, control the state of polarization of the illumination. Afterwards, the light is focused to the entrance pupil of an objective, which then illuminates the sample plane with collimated light [103]. Several adjustment stages allow for a linear and rotational positioning of the sample. In the analyzing arm, another objective collects the light reflected from or transmitted through the sample.

Both objectives have a numerical aperture (NA) of 0.42 and a long working distance of 25.5 mm to enable rotations around samples of up to 5 cm diameter. The polarization state analyzer system contains the same parts as the generator system in reverse order: a quarter-wave plate and a polarizer, both in rotation stages. Due to the stepwise rotation of the retarders, measurements take about 7 minutes to complete. After the polarization analysis, a tube lens focuses the light on the chip of a monochromatic CCD camera to create the microscope image. The analyzing arm is mounted on a rotation stage with the sample at the center in the axis of rotation. Together with the rotation stage of the sample, this setup can measure in transmission and in reflection, both at nearly arbitrary angles of incidence and view between 37.5° and 90° , only limited by the finite size of the arms.

A unique feature of this setup is the direct incidence microscopy mode, which can be accessed when the analyzing arm is moved to a position in a 90° angle to the illumination arm as shown in the CAD sketch in Figure 3.7(b). Light reflecting back from the sample into the first objective in the illumination arm is then guided via a beam splitter in that arm over a mirror mounted outside of the rotation stage to the analyzing arm, where a flip mirror brings the light to the polarization state analyzer system and the camera. This way, reflection measurements can be performed even at 0° angle of incidence without major reconstructions of the system. Complete details on the construction and calibration of this setup are elaborated in the Master's thesis by Jana GRUNDMANN [102].

3.2.2 Commercial Imaging Ellipsometry Setup EP4

Figure 3.8 shows a photograph of the imaging ellipsometer *Accurion EP4* (EP4) by the company Park Systems / Accurion [42]. The overall composition is similar to the custom setup, consisting of two arms for the illumination and the analysis, respectively, but in a vertical orientation. A flowbox surrounds this setup which allows for a cleaner measurement environment with a more stable temperature control compared to the experimental MUELLER matrix microscope setup from Section 3.2.1 without a flowbox. Additionally, the EP4 setup is mounted on an active vibration isolation unit. A laser-driven light source with a monochromator enables spectroscopic ellipsometry measurements at the EP4. The objective collecting the light from the sample can be replaced to account for different magnifications from $10\times$ to $50\times$. Two cameras allow for measurements both in the visible as well as in the ultraviolet spectral range. The EP4 usually realizes the PCSA configuration, which allows for the measurement of only 11 elements of the MUELLER matrix (see Section 3.1.3). However, our EP4 also features an additional retarder which can be removed from the setup as desired. Thus, the setup can not only perform measurements in its usual manner, but also in a dual-rotating compensator configuration to measure the complete MUELLER matrix. However, the software accompanying the setup does not include this configuration, yet. Thus, measurements with the additional retarder have to be performed under the control of a Python script which implements the evaluation methods used in the custom setup.



Figure 3.8 – Custom Accurion EP4 imaging ellipsometer.

3.3 Nanoform Structures

In Section 3.1.5, we briefly discussed the advantages of imaging ellipsometry opposed to conventional ellipsometry. To gain better understanding of the relationship between certain elements of the MUELLER matrix and variations in structural properties, I designed a set of test samples for systematic measurements. This section describes these structures, their fabrication, and their characterization with non-optical methods.

3.3.1 Sample design

The set of individual nanostructures designed as reference samples for systematic measurements consists of basic geometrical shapes with varying parameters [104]. Within the scope of this thesis, we will refer to these structures as nanoform structures. A sketch of them is depicted in Figure 3.9. I chose basic square and circle shapes with different sizes (**B** and **C**) as well as squares with varying corner rounding (**A**) to emulate a transition from a square to a circle. Similar investigations of MUELLER matrix images of structures like these have been performed before by using simulations only [105]. The individual structures have 5 mm distance between each other to prevent interactions, even when measured with large beams. In addition, a set of small arrays with only up to 4×4 square structures (**D**) is included for investigations on the influence of structures with low periodicity. The **A** labeled square structures have a width w of $5 \mu\text{m}$ and varying corner radii r_c between 100 nm and 2000 nm. The square structures labeled **B** as well as the circle structures labeled **C** vary in size w or in diameter $d = 2r$, respectively, from 50 nm to 2000 nm. The small arrays labeled **D** are made up of $N \times N$ square structures of width $w = 1 \mu\text{m}$ and with two different pitches Λ between the structures. A detailed list of the structure specifications is given in Table 3.1.

Table 3.1 – Structure specifications of the designed nanoform structures.

	1	2	3	4	5	6	7	8	9	10
A r_c / nm	100	150	200	300	400	500	750	1000	1500	2000
B w / nm	50	70	100	200	250	500	750	1000	1500	2000
C r / nm	25	35	50	100	125	250	375	500	750	1000
D $N, \Lambda / \mu\text{m}$	1, -	2, 10	3, 10	4, 10	-	1, -	2, 20	3, 20	4, 20	-

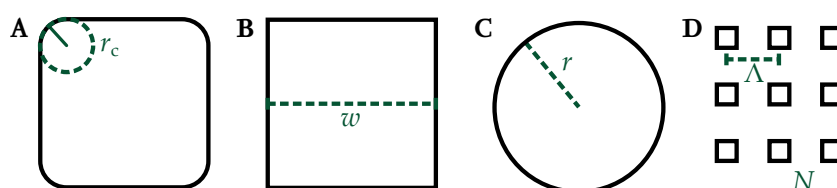


Figure 3.9 – Nanoform structures for investigations on imaging ellipsometry.

3.3.2 Fabrication and SEM Characterization

The nanoform structures were fabricated as holes in 100 nm thick polymethylmethacrylate (PMMA) on a 100 mm silicon wafer using electron beam lithography. The silicon substrate enables ellipsometric measurements in reflection, while the PMMA layer was retained to keep the possibility for etching the structures into the silicon [104].

Before the samples were finalized, a wafer with test structures was produced which is depicted in Figure 3.10. These test structures were the same structures as designed, but fabricated with different dose factors during the electron beam lithography process. The dose factor was varied in 10 steps between 1.0 and 4.3. As the choice of dose factor influences the final shape of the structure, it was necessary to fabricate and evaluate the test structures to find the right dose factor for the required feature sizes. For this evaluation, scanning electron microscopy (SEM) images of all test structures were taken. Examples for these SEM images are given in Figure 3.11. Additional images of the lower two corners of the rounded square structures were taken to control the corner radius.

In the SEM images, I used a CANNY edge detection algorithm for the evaluation [106]. The algorithm identifies pixels belonging to edges of the structures by analyzing gradients in the intensity values and choosing suitable threshold values for these gradients. In circular structures, the pixels associated with an edge were then fitted to a circle to determine the structure radius. The sizes of square structures, their width and height, were determined by performing a HOUGH line transform to detect straight edges in the images and then measuring the distances between edges with the same orientation [107, 108]. In the HOUGH line transform, straight lines are represented in their HESSE normal form with a parameterization over their angle to an axis and their Euclidean distance from the origin,

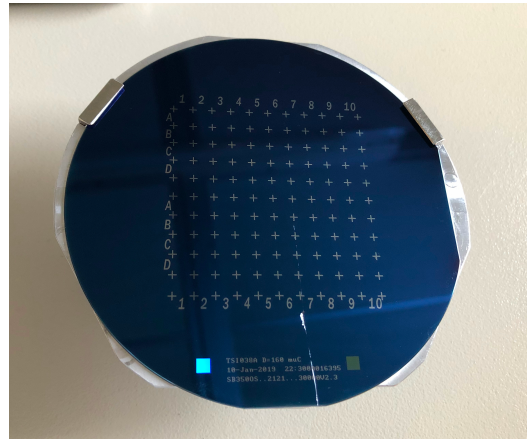


Figure 3.10 – Nanoform sample test wafer. Structures are in the middle of the $5 \times 5 \text{ mm}^2$ sections marked with crosses in the corners. The crack did not damage any structure.

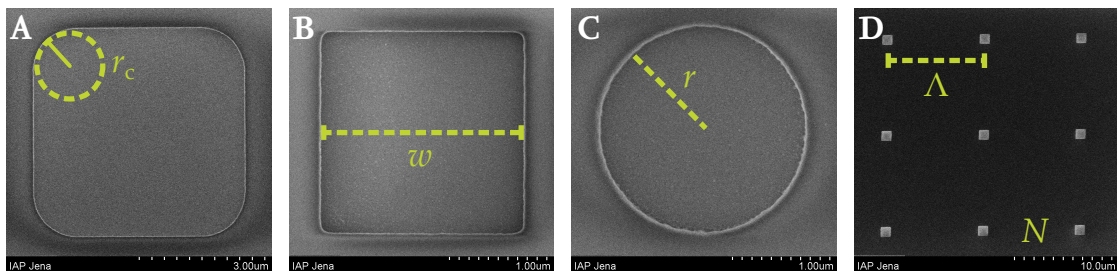


Figure 3.11 – SEM images of nanoform structures.

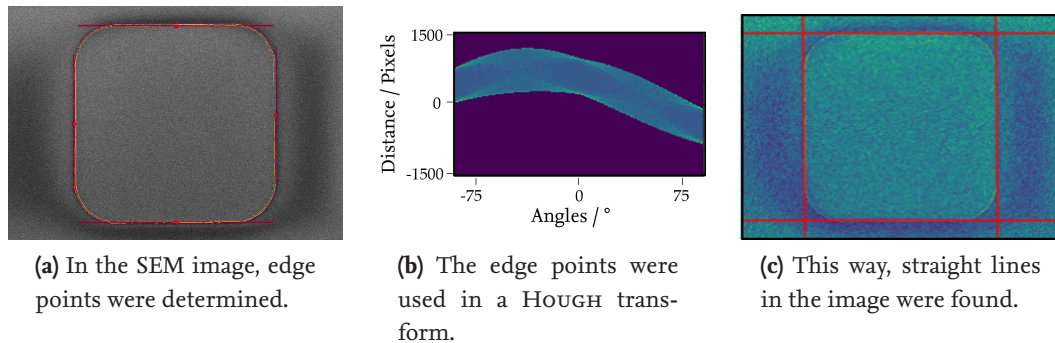


Figure 3.12 – SEM image evaluation example, from edge detection (a), over the HOUGH transform (b), to line identification (c).

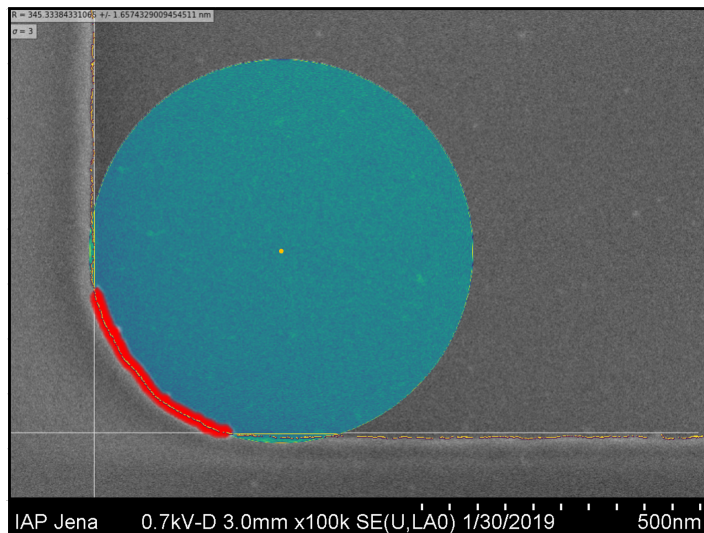
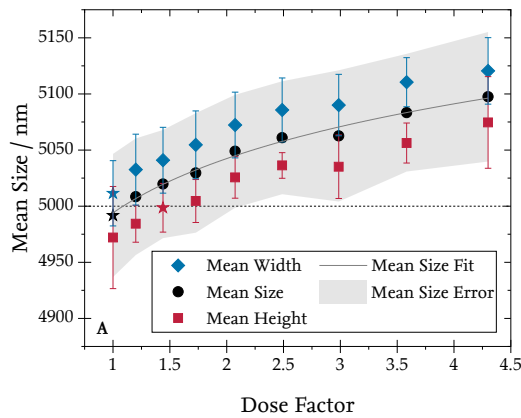
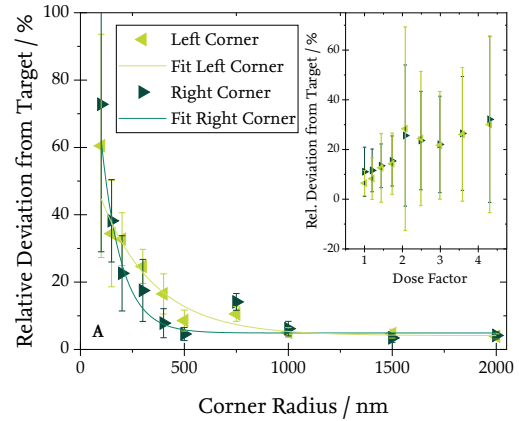


Figure 3.13 – SEM corner evaluation example. From the edges (yellow pixels) found in the SEM image, those pixels associated with the corner (red area) were fitted to a circle (green, with yellow center point) to find the corner radius.

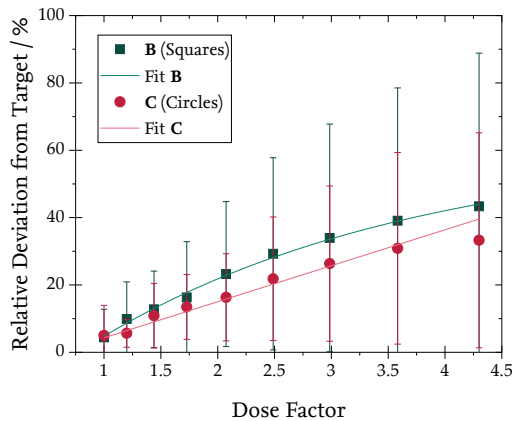
as shown in Figure 3.12. Performing this transform on an edge image leads to accumulation points in the HOUGH space that indicate straight lines in the original image [108, 109]. The corner radii were evaluated using the images of the corners: First, I had to identify pixels associated with the corner. I achieved this by numerically taking the second derivative of the edge pixels over their distance to the edge until a significant deviation was observed. Similar to the circular structures, all pixels belonging to the corner were then fitted to a circle to determine the corner radius, as shown in Figure 3.13. In the small arrays of square structures, sizes were also evaluated by HOUGH line transform and distances by using the FROBENIUS norm [110]. The implementation of these methods was performed in Python using the scikit-image package [111].



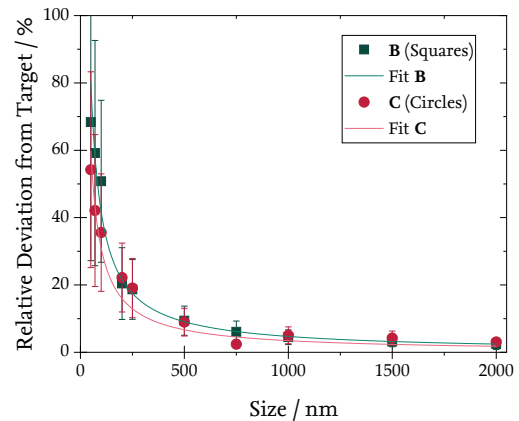
(a) Average sizes of rounded squares in row A for different dose factors. Stars mark values closest to target.



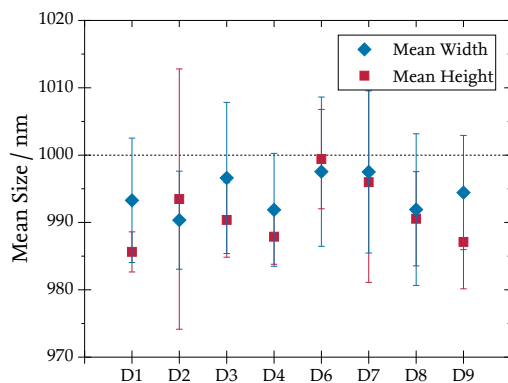
(b) Average deviation of lower corner radius from target value for rounded squares in row A. Inset: Deviation depending on dose factor.



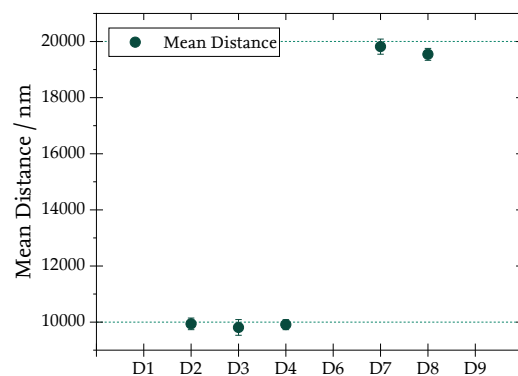
(c) Average deviation of structure size from target value for squares and circles in rows B and C, respectively, for different dose factors.



(d) Average deviation of structure size from target value for squares and circles in rows B and C, respectively, depending on structure size.



(e) Average sizes of squares in row D.



(f) Average distances of squares in row D.

Figure 3.14 – SEM image evaluation results. Structure size (a, c - e) and corner radius (b) as well as structure distance evaluation (f). Fit parameters are given in Appendix A.4

Figure 3.14 collects the averaged results from evaluating the SEM images. Uncertainty bars result from combining a systematic deviation by one pixel size due to the image evaluation process with the statistic deviation coming from averaging results from multiple images. From the evaluations, it is evident that structure sizes as well as corner radii increased with increasing dose factor, as indicated in Figures 3.14(a) and 3.14(c). We also observe a slight asymmetry in the rounded square structures with a mean aspect ratio of 1.0095. From Figures 3.14(b) and (d), we see that larger structures matched the design more often than smaller ones, regardless of the dose factor. Likewise, in Figures 3.14(c) and (d) we see that circular structures had less deviations from the design compared to square ones. Below 100 nm size, squares were likely to degenerate into circles. Overall, the mean dose factor for structures as close to the design as possible was 1.18 with a standard deviation of 0.28.

The evaluation with image processing methods delivered adequate information about the connection between dose factor and structure sizes. This information helped to produce a second sample, shown in Figure 3.15, which was used in all further measurements. Usually, critical dimensions in SEM images are evaluated using more complex edge operators in model-based approaches [112, 113]. However, elaborated methods like these are more efficient when implemented for SEM image evaluations on a regular basis. For the investigations in this thesis, the image processing approach proved to be sufficient, as we will see in Section 3.3.3.

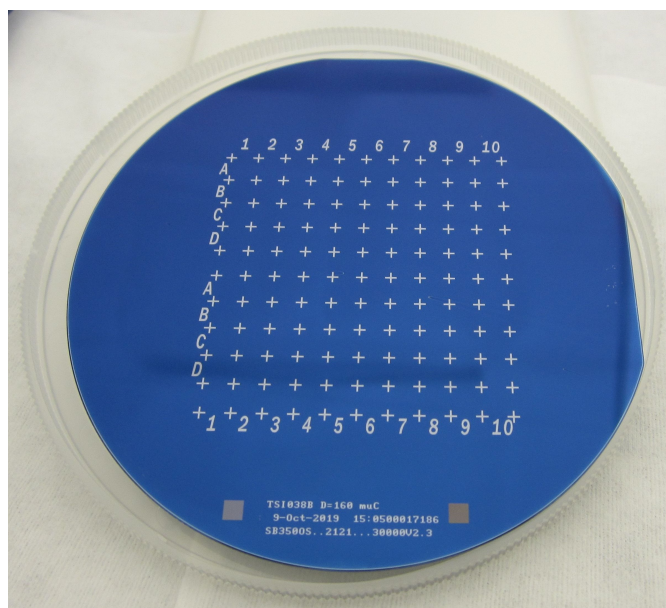


Figure 3.15 – Nanoform sample wafer. Structures are again located in the middle of each $5 \times 5 \text{ mm}^2$ section marked with crosses in their corners.

3.3.3 AFM Characterization

The final sample in Figure 3.15, fabricated with the results from the SEM characterization described in Section 3.3.2, was characterized using traceable AFM. The measurements were performed at a metrological scanning probe microscope (SPM) [114] and a commercial AFM with a high aspect ratio probe, calibrated with the metrological SPM and a transfer standard, at CMI in the Czech Republic [115]. As a tactile method, AFM measurements take considerably longer than optical techniques in general [116]. For this reason, only selected structures were examined. An overview of the selected structures and the measurement results is given in Table 3.2. Figure 3.16 depicts the measured AFM images. The structures were evaluated with the open-source software Gwyddion [117]. Gwyddion's "Fit shape" function was used to fit the structures in row **A** to a square hole with rounded corners. On average, the outer widths of the structures deviate about 1.4 % between measurement and design, while the corner radius deviates by 6.8 %. The larger deviations are explained by a partial damage of structure **A6** during the AFM measurement process as can be seen in Figure 3.16(c). Neglecting the damaged structure, the deviations are 0.33 % for the outer width and 4.38 % for the corner radius. For the other rows, Gwyddion was used to measure structure diameters and pitches. The measured sizes deviate on average by 8 nm from the target in rows **B** and **C** and by 0.4 nm for row **D**. The pitch of the structures in row **D** varies by 0.13 % on average. All deviations are below the uncertainty limit of the measurement system which is estimated to 20 nm [115]. Thus, the structures fabricated with the information from the SEM characterization meet their target values and are suitable for further investigations.

Table 3.2 – Selected structures and AFM measurement results.

	Outer width / μm	Target width / μm	Corner radius / nm	Target radius / nm
A1	5.007	5	111	100
A5	4.967	5	394	400
A6	5.210	5	571	500
A10	4.977	5	2013	2000
	Size / nm	Target size / nm	Pitch / μm	Target pitch / μm
B4	189	200	–	–
B6	499	500	–	–
C4	182	200	–	–
C6	499	500	–	–
D4	1005	1000	10.014	10
D9	1002	1000	20.022	20

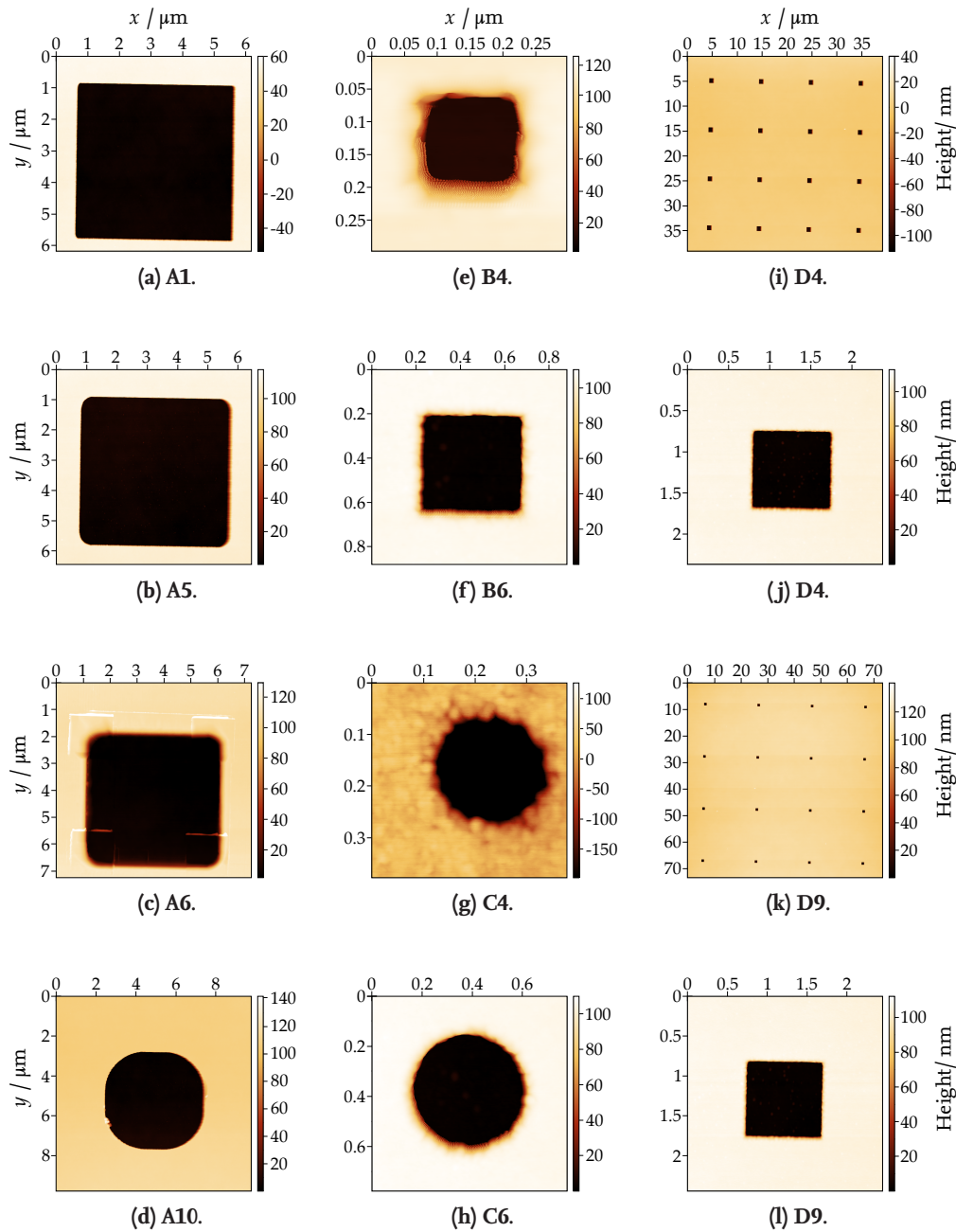


Figure 3.16 – AFM images of selected structures from rows A (a - d), B (e, f), C (g, h), and D (i - l) from the nanoform sample.

3.4 Ellipsometric Measurements

After introducing the measurement systems and the sample in Sections 3.2 and 3.3, respectively, we now take a look on measurements of selected structures from the nanoform sample. The large size of MUELLER matrix images doesn't allow for every measurement to be included in this thesis, so only those reasonable to be discussed are shown here.

3.4.1 Measurements at MUELLER Matrix Microscope

Structures of the nanoform sample (see Section 3.3) were measured using the MUELLER matrix microscope setup (see Section 3.2.1) in the direct incidence reflection mode at 455 nm wavelength. The resulting images for some of the rounded square structures in row **A** are collected in Figure 3.17. The MUELLER matrix images are normalized to the element m_{00} . As this element contains only little information exceeding a pure microscope image, it is given unnormalized and in grayscale [32]. In the raw measurements, a noticeable blur was present in the MUELLER matrix images. This blur, that stems from movement of the sample during the measurement, was already corrected for in Figure 3.17. Details on this drift correction will be discussed in Section 3.5. A collection of further MUELLER matrix images is given in Appendix B.1.1 and B.1.2. The measured MUELLER matrix images in Figure 3.17 show polarization effects in the corners and at the edges of the structures. In conventional, non-imaging ellipsometry, these effects would be averaged over the whole image and therefore not detectable, especially as they have opposite signs depending on the orientation of the edge or corner relative to the image axes. Thus, imaging ellipsometry provides additional information about the structures compared to both microscopy and conventional ellipsometry alone. As the effects are observable in measurements, but rather weak, Figure 3.18 provides a scaled view of certain matrix elements of selected structures in row **A**. The m_{00} elements are barely distinguishable for sub-wavelength changes of the corner radius. Off-diagonal matrix elements, however, show a more pronounced response. As an example for this additional information channel, when the corner radius changes from 100 nm in **A1** to 400 nm in **A5**, the absolute value of the m_{13} element in the corners increases by 15 %. With about 160 %, the change from **A5** with 400 nm to **A10** with 2000 nm corner radius is even more significant. Similar behaviors can be observed in other off-diagonal matrix elements, for example for edges in the m_{23} elements. Therefore, local sub-wavelength sized geometries of the structures under investigation like orientation and curvature of edges have measurable influence on sign and value of the MUELLER matrix image, which is promising for the application of imaging ellipsometry in nanometrology.

The square and circular structures of different sizes in rows **B** and **C** were supposed to be used in the determination of resolution limits in the measurements. Presumably, MUELLER matrix images might have shown polarization effects even for structures too small for microscopy. Unfortunately, because the structures are much smaller than the

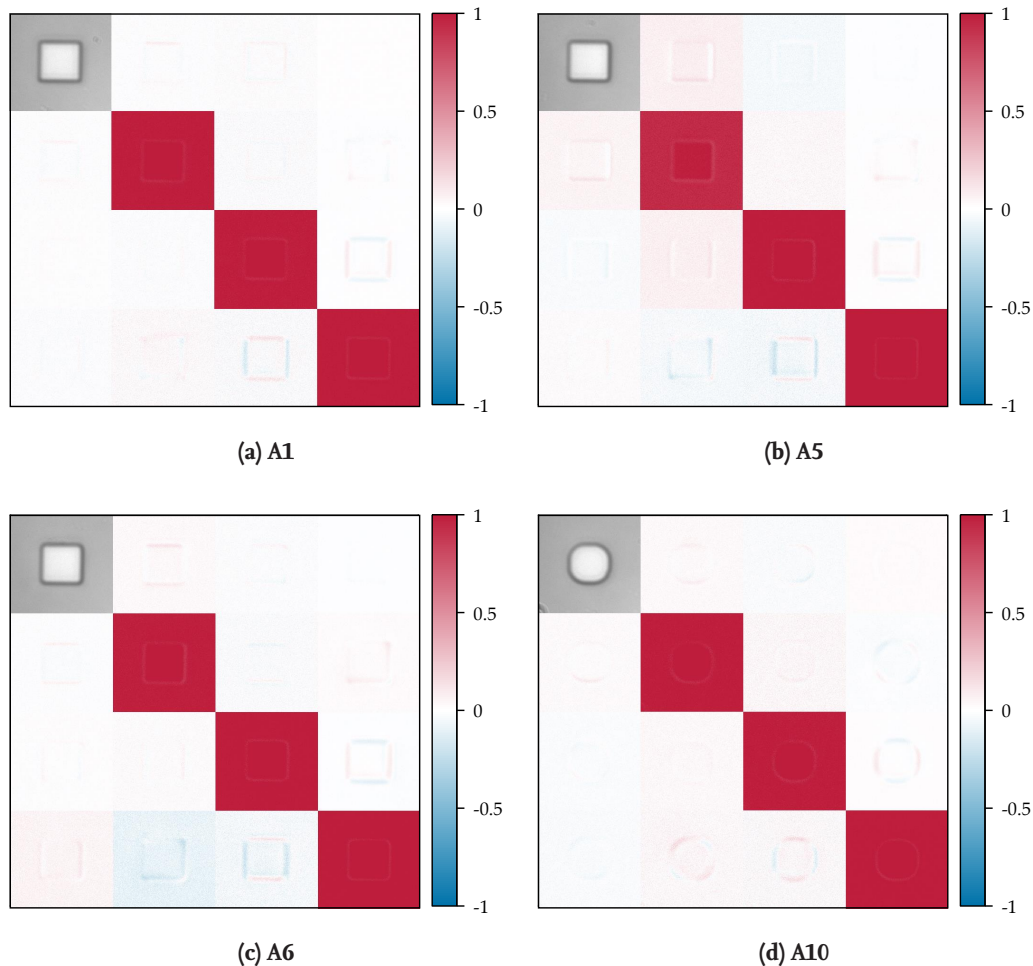


Figure 3.17 – MUELLER matrix images of 5 μm by 5 μm sized structures **A1** (a), **A5** (b), **A6** (c), and **A10** (d) from the nanoform sample measured at the MUELLER matrix microscope setup, corrected for structure drift.

ones in row **A**, they could not be corrected for drifts reliably. For this reason, measuring both rows **B** and **C** did not bring any advantage and in the end, only the circular structures in row **C** were measured. A selection of their MUELLER matrix images is shown in Figure 3.19 and Appendix B.1.4 collects all measurements on the structures in this row. Structures smaller than **C4** with a radius of 100 nm were not visible anymore due to being much smaller than the ABBE diffraction limit [60]. This and the aforementioned drift-related blur made it impossible to find these structures in the images. Even when knowing their exact position, at this size, polarization effects are most likely indistinguishable from noise. Nevertheless, even sub-wavelength sized structures like **C4** still showed measurable polarization effects while being barely visible in the microscope image.

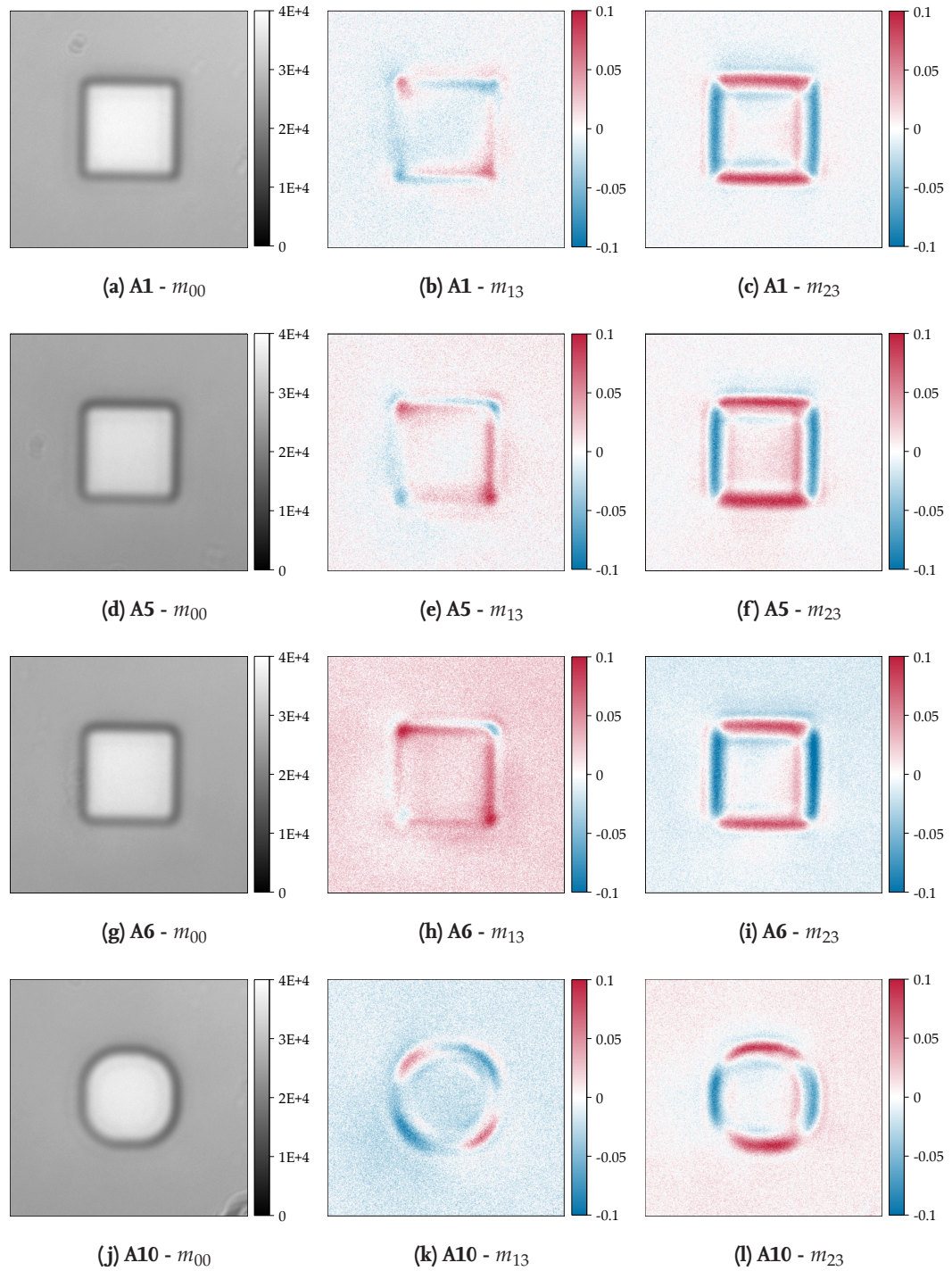


Figure 3.18 – Detailed view of matrix elements m_{00} (a, d, g, j), m_{13} (b, e, h, k), and m_{23} (c, f, i, l) of drift corrected MUELLER matrix images measured at the MUELLER matrix microscope setup.

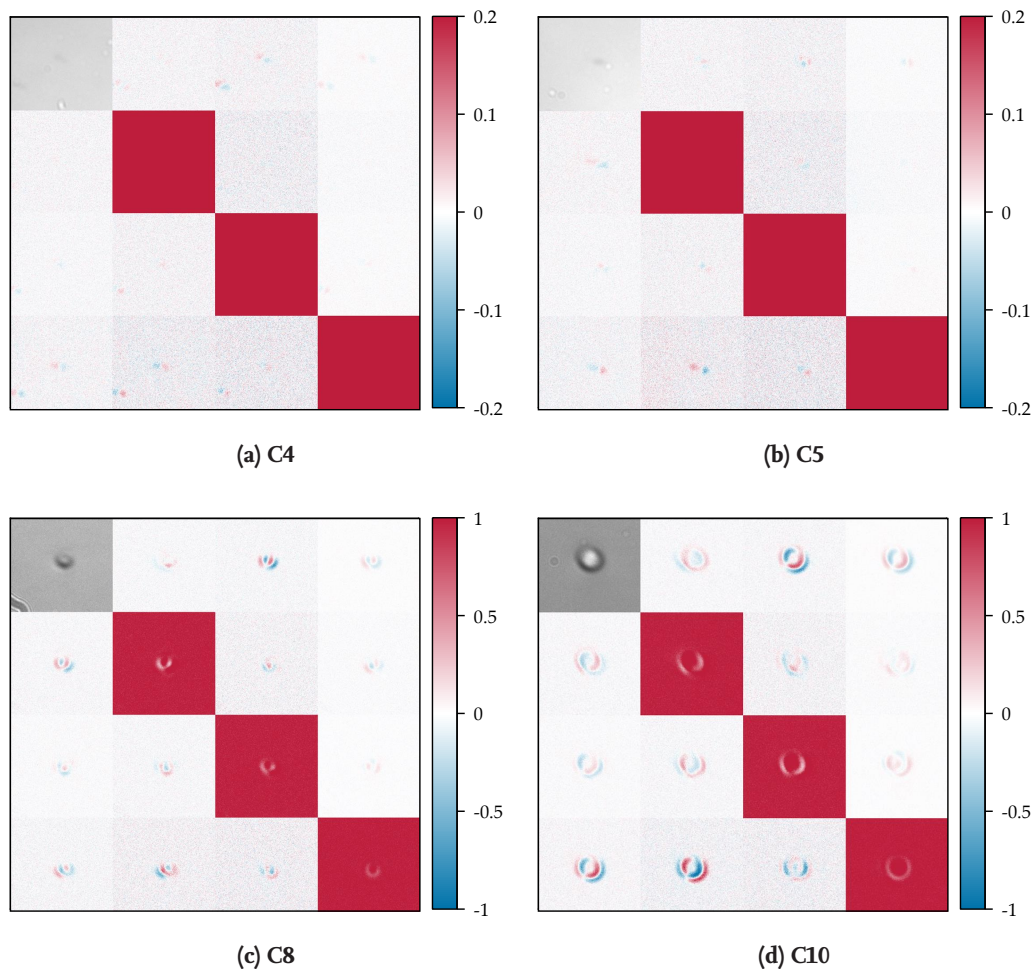


Figure 3.19 – MUELLER matrix images of structures C4 (a), C5 (b), C8 (c), and C10 (d) from the nanoform sample measured at the MUELLER matrix microscope setup.

3.4.2 Measurements at EP4 Setup

Structures of the nanoform sample discussed in Section 3.3 were measured using the EP4 imaging ellipsometry setup described in Section 3.2.2. Measurements were performed for wavelengths between 400 nm and 800 nm in steps of 50 nm with a $50\times$ magnification under 40° angle of incidence in reflection. Due to the different wavelengths, the number of resulting MUELLER matrix images is rather large. Therefore, Figures 3.20 and 3.21 show only some of the measured structures for exemplary wavelengths for both configurations, PCSCA and PCSA, respectively. For measurements at this setup, drift correction is usually not required, as the measurements are performed considerably faster and the environment is more stable than at the other setup. Generally, the average matrices look different from the close to identity matrices measured at the MUELLER matrix microscope, with considerable more retardation showing in the lower right quadrant. Reasons for this are the change from transmission to reflection measurement and the oblique

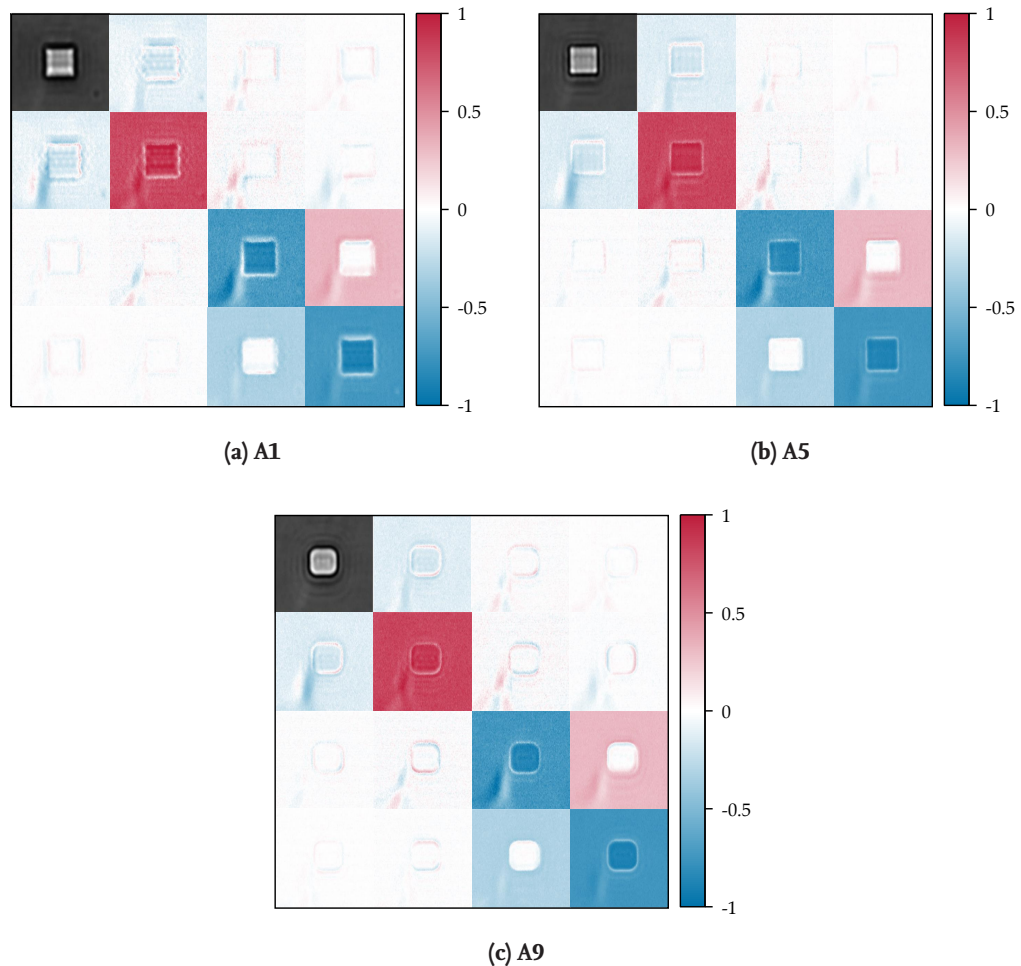


Figure 3.20 – Measurements of structures **A1** (a), **A5** (b), and **A9** (c) at 450 nm at the EP4 setup in PCSCA configuration.

angle of incidence, which influence the polarization according to the FRESNEL equations [63]. Strikingly, structures of row **A** in Figure 3.20 are more pronounced in the MUELLER matrix images than in the microscope image, with clearly highlighted edges and corners as well as less interferences showing up around the structures. In the PCSA measurements, the m_{00} element also gets normalized together with the other matrix elements by the company's own evaluation method, so the microscope image doesn't show up here. Figures 3.21(d) to (g) demonstrate how sensitive spectral measurements of the MUELLER matrix are: They show matrix images on the structures **B4** and **B6**; square structures with 200 nm and 600 nm width, respectively, at two wavelengths, 450 nm and 500 nm. Not only can even the sub-wavelength sized **B4** still be observed in the off-diagonal matrix elements, but also rectangular areas around the structures are visible. These are most likely remnants of the AFM measurements discussed in Section 3.3.3 and their contrast to the surroundings depends strongly on the wavelength.

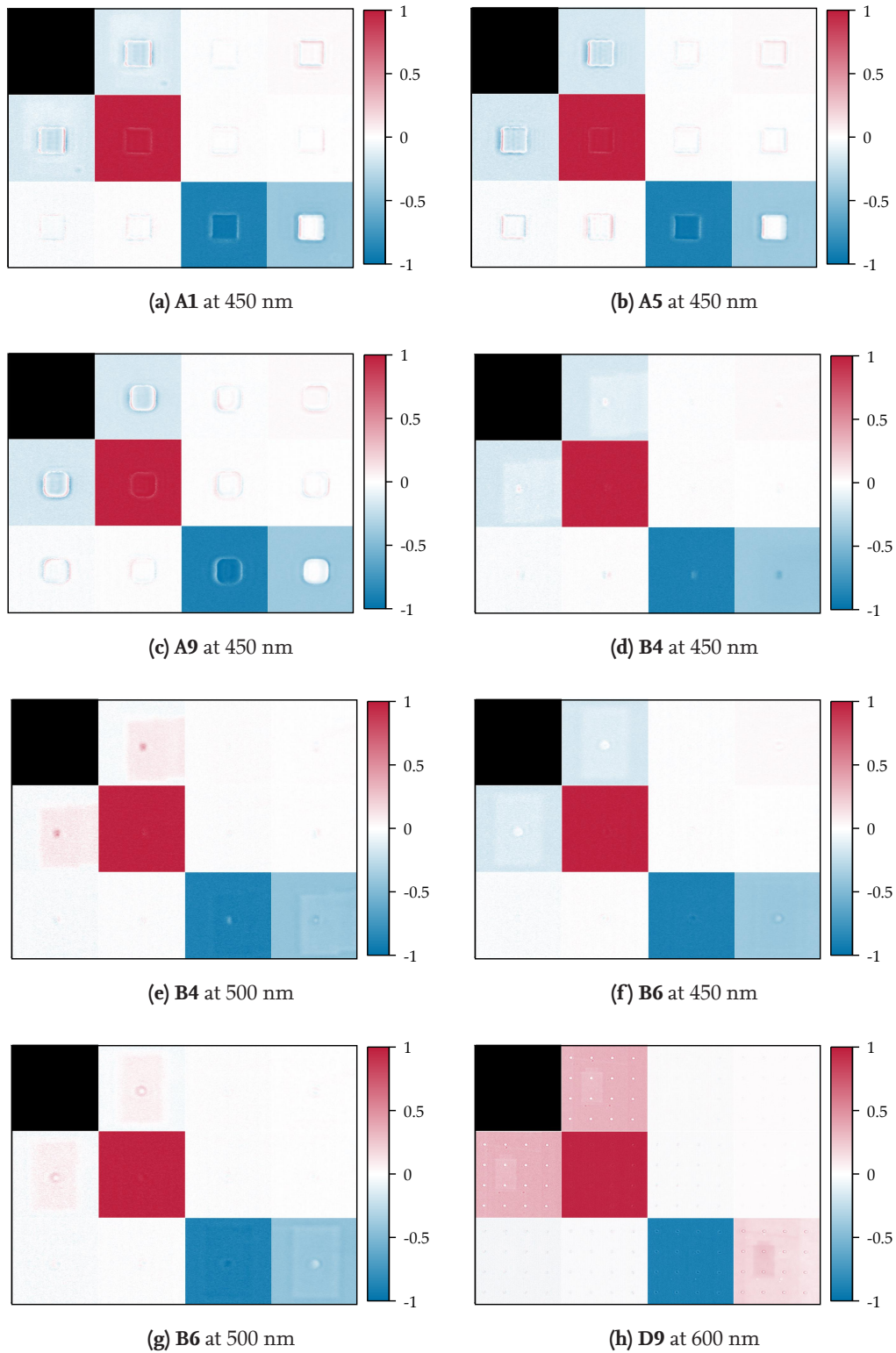


Figure 3.21 – Measurements of structures from rows A (a - c), B (d - g), and (D) (h) from the nanoform sample at the EP4 setup in PCSA configuration.

A measurement of an area from row **D** is shown in Figure 3.21(h). In the images, no major influence from the superstructure is visible, which was expected considering the large pitch of $20\ \mu\text{m}$. Yet, thanks to the imaging system, we can distinguish polarization properties of individual structures, even when they are as close together as several micrometers, which is an advantage over conventional ellipsometry. Figure 3.22 shows the averaged MUELLER matrix images of the nanoform sample in dependence of illumination wavelength and corner radius. As demonstrated in Section 3.1.5, the local polarization effects all vanish in the averaged values and the main influence on the matrix elements visible here stems from the varying wavelength.

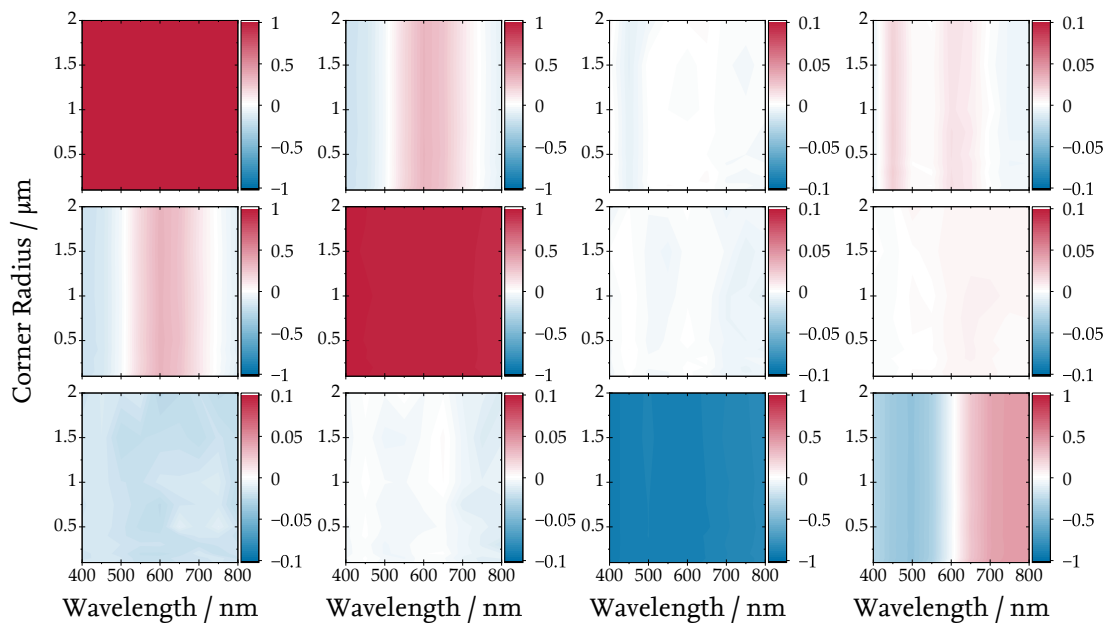


Figure 3.22 – Averaged MUELLER matrices of the nanoform sample over wavelength and corner radius, measured at the EP4 setup in PCSA configuration.

3.5 Thermal Influences

Evaluated measurements from the MUELLER matrix microscope setup contained blur which didn't stem from the imaging system. An example for this is shown in Figure 3.23. In direct comparison, the blurry measured m_{00} element in Figure 3.23(a) looks remarkably similar to Figure 3.23(b), which shows an overlay of the first and the last image of the measurement series. Therefore, the reason for this blur was a drift of the structures during the measurements, most likely due to thermal influences. This drift apparently also affects measured MUELLER matrix images, as indicated from Figure 3.23(c). In this section, we examine the thermal drift at the MUELLER matrix microscope setup. As other setups might suffer from similar issues, we also take a look on drifts at the EP4 setup. In addition, this section includes an analysis of intentionally moving samples to scrutinize the impact of movements on MUELLER matrix images as well as the introduction and discussion of an algorithmic solution for the thermal drift problem.

3.5.1 Drift at MUELLER Matrix Microscopy Setup

For the characterization of drifts at the MUELLER matrix microscopy setup, the position of a structure in the microscope image was tracked for eight hours. Laboratory air temperature T as close to the sample as 3 cm was also measured. Electrical drifts of the controllable rotating components were prevented by disconnecting them from the power supply, as far as they were not needed. The test series was conducted in the late afternoon and evening to reduce disturbances. Images were taken and temperature measured every 10 s. The results are collected in Figures 3.24 and 3.25.

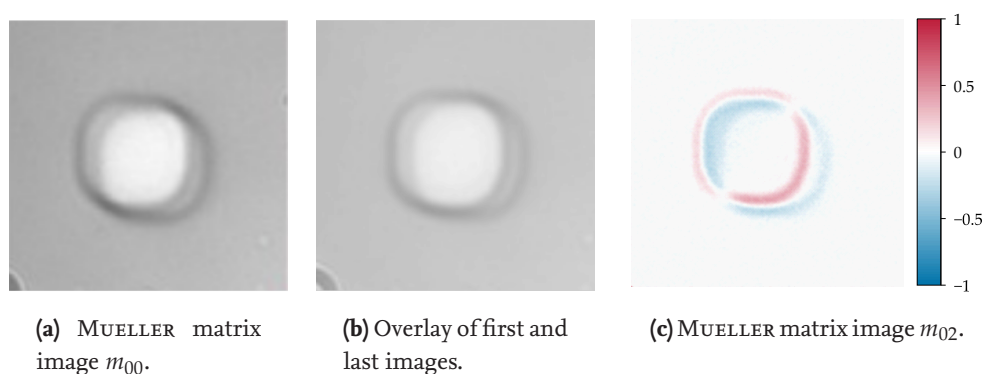


Figure 3.23 – Blur of MUELLER matrix images of elements m_{00} (a) and m_{02} (c) during a measurement at the MUELLER matrix microscope. Compared to an overlay of the first and last images of the measurement series (b), it is evident that the blur stems from sample drift.

An exponential fit of the temperature compensates the digitization due to the temperature sensor visible in Figure 3.25(a). The measured x - and y -coordinates of the structure position in Figure 3.25(b) show an exponential trend, where the structure position follows the temperature change. Figure 3.25(c) illustrates this further. Nearly linearly, the structure moved about $33.5 \frac{\mu\text{m}}{^\circ\text{C}}$ in x -direction and about $46 \frac{\mu\text{m}}{^\circ\text{C}}$ in y -direction. The direct influence of the change in room temperature on the structure position also shows in the correlation between these parameters, visualized in Figure 3.24. All parameters are nearly perfectly correlated to each other. The decreasing temperature is the result of two persons being present in the laboratory during sample adjustment and measurement preparations, heating up the room temperature. After leaving the laboratory for the measurement series, the air cools down, but the air conditioning needs several hours to stabilize the room temperature. Even after five hours, the structure still moved perpetually about 11 nm per minute. During a measurement series, images are taken over the course of several minutes, as described in Section 3.2.1. On these timescales, the observable drift of the structures is crucial for measurement quality.

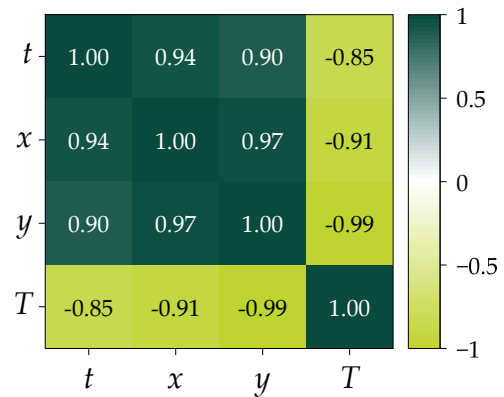
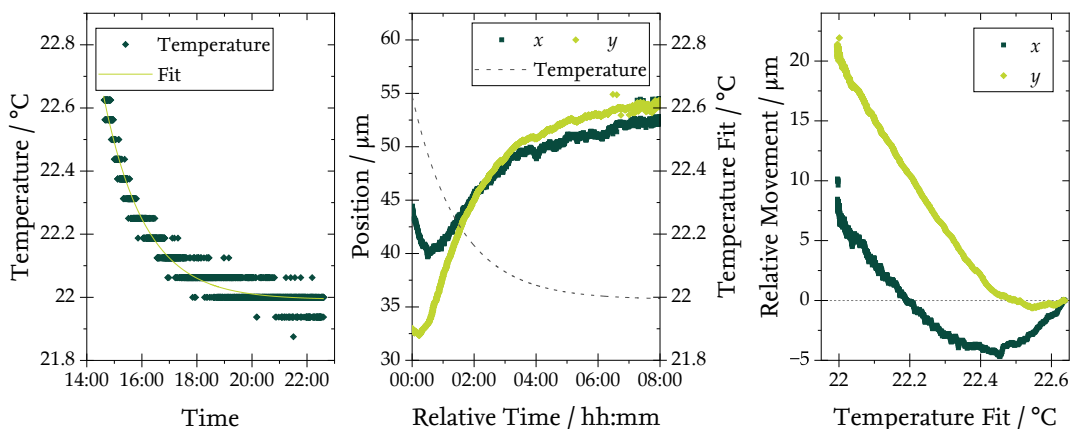


Figure 3.24 – Thermal influences at MUELLER matrix microscope, correlation matrix.



(a) Temperature and exponential fit over time. (b) Movement and temperature fit over time. (c) Movement over temperature.

Figure 3.25 – Characterization of sample movement (b, c) due to temperature changes (a) at MUELLER matrix microscope setup.

3.5.2 Drift at EP4 Setup

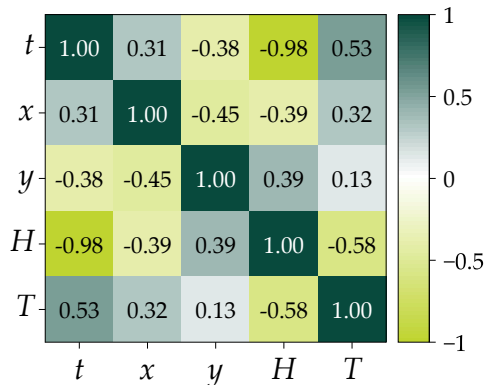
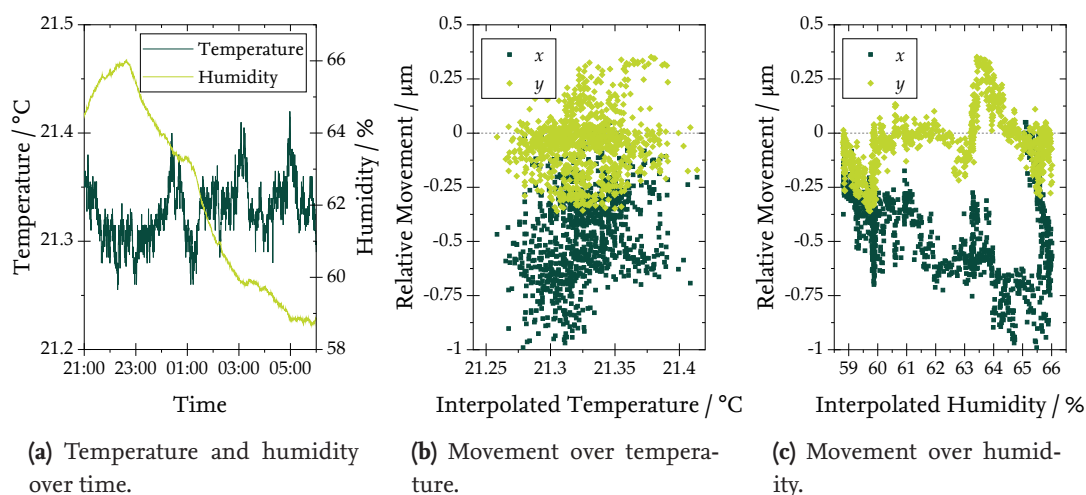


Figure 3.26 – Thermal influences at EP4, correlation matrix.

Thermal influences on the commercial EP4 setup were examined in a way similar to Section 3.5.1. Again, structure position in microscope images was tracked for eight hours together with laboratory air temperature and humidity, this time in steps of 30 s. Figure 3.26 indicates parameter correlation again while Figure 3.27(a) shows temperature T and humidity H over time. Ambient conditions are much better controllable at the EP4 setup compared to the MUELLER matrix microscope, with the temperature only changing in a 0.15°C range. Humidity, which could not be controlled directly and which is heavily influenced

by weather conditions, ranged between about 59 % and 66 %. In Figures 3.27(b) and 3.27(c), structure positions are shown over the measured temperature and humidity, respectively. In contrast to the MUELLER matrix microscope setup, the position shows no direct influence from temperature changes exceeding stochastic movements. Over the course of eight hours, the structure did not move further than $1\ \mu\text{m}$ away from its initial position. Interestingly, the structure moved slightly with the changing humidity, but as seen in the correlation matrix in Figure 3.26, direct influences from both temperature and humidity are negligibly small at this setup for short measurements. However, for long-term measurements over several hours, even a stochastic movement of up to $1\ \mu\text{m}$ is visible in the images and therefore crucial over time.



(a) Temperature and humidity over time.

(b) Movement over temperature.

(c) Movement over humidity.

Figure 3.27 – Characterization of sample movement (b, c) due to temperature and humidity changes (a) at EP4 setup.

3.5.3 Drift Correction Algorithm

During a measurement with the MUELLER matrix microscope setup, the imaged structure might move by several micrometers. When the single images taken during measurement are then evaluated to MUELLER matrix images, intensity values are evaluated by pixel coordinate, leading to a blurring of the resulting images. The best mitigation for this effect would be a complete stabilization of the surrounding climate. However, as discussed in Section 3.5.2, even under the flowbox at the commercial setup, air temperature and humidity can only be controlled to a certain extent, and structure position is still subject to small random movements. A more viable approach is the implementation of an algorithm that counteracts the drift. This section discusses the implementation of a drift correction algorithm optimized to work with structures from the nanoform sample described in Section 3.3. Its concepts are, however, applicable to arbitrary cases. A flowchart for the algorithm is given in Figure 3.28. It detects the structure in the first image of a measurement series and crops a 400×400 pixel area containing this structure to speed up computations. The image is then normalized to an empty reference image and a histogram of its gray values is extracted. Next, SOBEL operators are applied to the image. SOBEL operators are edge detection operators that visualize high local intensity differences as gradients [118]. To calculate this gradient for a certain pixel, the 3×3 area around this pixel is convolved with the SOBEL operators:

$$\mathcal{S}_x = \begin{pmatrix} -1 & 0 & 1 \\ -2 & 0 & 2 \\ -1 & 0 & 1 \end{pmatrix} \quad \text{and} \quad \mathcal{S}_y = \begin{pmatrix} 1 & 2 & 1 \\ 0 & 0 & 0 \\ -1 & -2 & -1 \end{pmatrix}. \quad (54)$$

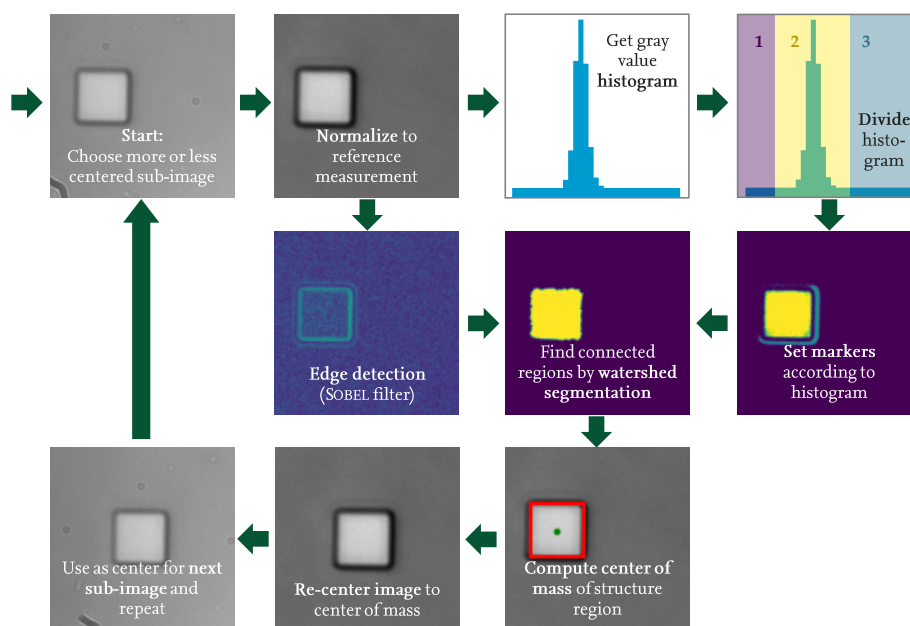


Figure 3.28 – Drift correction algorithm, flow chart.

The results from this convolution are 3×3 matrices again which are summed up and combined to a new gray value representing the gradient of the respective pixel. The new image emerging from this is then treated as a height map to which a watershed transformation is applied [119]. This transformation finds segments in an image by filling in connected areas as if they were valleys in a landmass that is flooded with water. From the histogram of the original image, extreme points are taken to find positions in the gradient image which are usable as markers. Starting from these markers, the gradient image is then flooded, but areas originating from different markers are not merged. This way, a connected area is found that covers only the structure in the image. The center of this area, and thus of the detected structure, is then computed in the form of its center of mass. The current section of the overall image is then re-centered to this structure center. The central coordinates are also given to the next iteration of the algorithm, so the next image of the measurement is cropped to a 400×400 pixel area around this position, and the position of the structure in this new image is detected again. In this manner, the algorithm goes through the whole image stack, gaining a centered image of the structure from each step. The evaluation process is then performed on these centered images, eliminating the effect of thermal drifts down to pixel accuracy. I implemented the drift correction in Python, using methods from the SciPy and Scikit-Image packages [111, 120]. It was successfully applied on nanoform sample structures in row **A**. For rows **B** and **C**, structures were too small to be treated reliably with the watershed transformation, so a re-centering was impossible. Figure 3.29 shows a comparison of MUELLER matrix images without and with drift correction on structure **A10** as an example. Corrected images show a significant reduction in blur, which is most evident in the first matrix element m_{00} . Yet, edge and corner effects are still visible in off-diagonal matrix elements, indicating that they are not caused by the drift but valid responses from the structure [121]. In Section 5.2.1, we will compare these results to numerical simulations to further test this point. Drift corrected MUELLER matrix images of structures in row **A** are given in Appendix B.1.2.

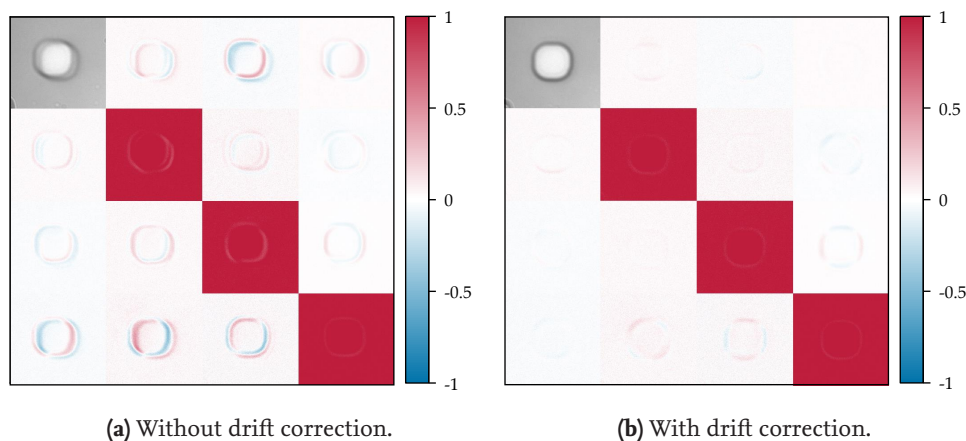


Figure 3.29 – MUELLER matrix images of structure **A10**, before (a) and after drift correction (b).

3.5.4 Intentionally Induced Drift

Using the sample stage of the EP4 ellipsometer, the sample can be moved intentionally during the measurement. This way, the effects of structure drift in different directions could be emulated and analyzed systematically. With sufficiently small movements, this might help to distinguish genuine effects in the measured MUELLER matrices from thermal drift effects. Figure 3.30 shows efforts in trying to measure MUELLER matrix images of structure A5 while the sample stage was moving as little as possible during the measurement. In Figures 3.30(b) and (c), the sample moved in x -direction around the middle with speeds of about 18 nm/s and 54 nm/s, respectively, while Figure 3.30(a) shows a comparison without any movement. However, even with the relatively slow velocities, the sample moved significantly more than when drifting due to thermal influences. Also, the sample moved uniformly in one direction instead of randomly around a center.

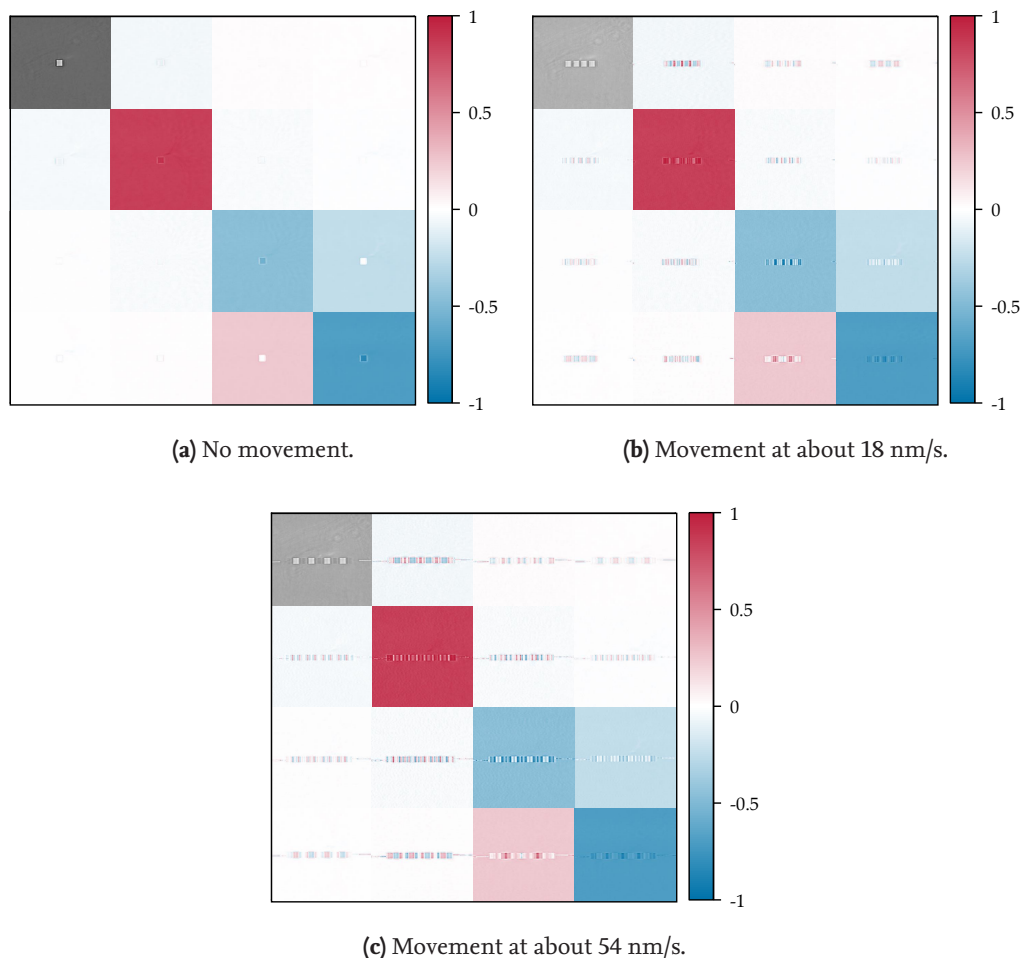


Figure 3.30 – Intentionally moving sample at different speeds (b, c) during MUELLER matrix image measurements, compared to measurement without movement (a).

Yet, this experiment delivered a valuable insight: Lateral movement of the sample during the measurement produces misleading effects in the MUELLER matrix images that might be mistaken as polarization effects. This can be observed in all matrix elements in Figure 3.30. If the sample moved less far, these effects would only appear at the edges of the structures perpendicular to the movement direction. The measurement process involves taking several images at different combinations of the polarizing optics. If the sample moves during the measurement, it appears in different positions for different states of polarization. In the evaluation process, this might be interpreted as, for example, multiple structures imposing different polarization effects, as seen in Figures 3.30(b) and (c), or as influences from the structures' edges, in accordance with the observations from Section 3.5.1.

The way the movement influences the interpretation of MUELLER matrix images depends strongly on both the movement speed and the measurement speed. If we assumed both to be discretized, we would only get an undisturbed measurement when it is completed faster than one step of sample movement. This naturally connects to larger influences from the surroundings the longer the measurement takes. Thus, when using slower measurement procedures, thermal drifts of the sample have to be taken into consideration as potential sources of error in MUELLER matrix imaging. Nevertheless, as we will see in Section 5.2.1, after tracking the sample position and correcting for potential drift, both measurement and simulation are in good agreement. Thus, we can suppress drift influences by algorithmic means, and the only challenge that remains is detecting the structures in the images. Further research of the interplay between sample movement and MUELLER matrix image alteration, possibly using techniques from pattern recognition, will help to characterize thermal influences in ellipsometric setups more fundamentally. Beyond that, a systematic use of deliberately moving samples might even help to emphasize structural features like edges in MUELLER matrix images, ultimately leading to new ways for an enhanced feature analysis.

4

Plasmonic Lens Devices

AS IMPLIED IN CHAPTER 2, THE INTERACTION OF LIGHT AND MATTER THAT LEADS to the excitation of evanescent fields includes promising prospects for modern nanometrology. Local plasmon resonances are inherently sensitive to even small changes of the structure geometry, from which optical methods like those presented in Chapter 3 can profit [122]. This chapter continues the view on plasmonics from Section 2.3 and introduces the application of plasmonic waveguides as a focusing metastructure, a so-called plasmonic lens. Based on this, we will discuss a novel design for plasmonic lenses which is oriented towards the limitations of fabrication. After optimizing the design parameters of these lenses for applications in the visible and near-infrared regime with focal lengths between 5 μm and 1 mm, we take a look at their performance, both in simulations as well as in measurements on fabricated lenses. In the end, I will discuss strategies to improve the design further towards multispectral applications in ellipsometric setups.

4.1 Plasmonic Waveguides

Although light is usually unable to pass through holes in a metal with a diameter smaller than half the wavelength, the excitation and coupling of SPPs can enable a form of extraordinary transmission. This allows light to propagate even through narrow metal holes, which in this case can be regarded as waveguides [44, 45, 50, 123, 124].

Understanding how SPPs pass through such waveguides requires a closer look on SPPs at metal-dielectric surfaces first. Consider the configuration illustrated in Figure 4.1(a): An interface between two media in the x - y -plane at $z = 0$ and a one-dimensional plane wave propagating along this interface in the x -direction while being polarized in the z -direction. We start from the Helmholtz equation for waves traveling along the interface:

$$\frac{\partial^2 \vec{E}(z)}{\partial z^2} + (k_0^2 \varepsilon - \beta^2) \vec{E} = 0, \quad (55)$$

where $k_0^2 \varepsilon - \beta^2 = k_z^2$ and $\beta = k_x$ is the so-called propagation constant. From this, equa-

tions for the relevant field components for TM and TE modes can be found [61, 83]:

$$\text{TM: } E_x = -i \frac{1}{\omega \varepsilon_0 \varepsilon} \frac{\partial H_y}{\partial z}, \quad (56a) \quad \text{TE: } H_x = i \frac{1}{\omega \mu_0} \frac{\partial E_y}{\partial z}, \quad (56c)$$

$$E_z = -\frac{\beta}{\omega \varepsilon_0 \varepsilon} H_y, \quad (56b) \quad H_z = \frac{\beta}{\omega \mu_0} E_y, \quad (56d)$$

as well as the wave equations for these modes:

$$\text{TM: } \frac{\partial^2 H_y}{\partial z^2} + (k_0^2 \varepsilon - \beta^2) H_y = 0, \quad (57a) \quad \text{TE: } \frac{\partial^2 E_y}{\partial z^2} + (k_0^2 \varepsilon - \beta^2) E_y = 0. \quad (57b)$$

We can use these equations to describe the fields depending on their z position. For $z > 0$, we get:

$$\text{TM: } E_x(z) = i A_2 \frac{1}{\omega \varepsilon_0 \varepsilon_2} k_2 e^{i\beta x} e^{-k_2 z}, \quad (58a) \quad \text{TE: } H_x(z) = -i A_2 \frac{1}{\omega \mu_0} k_2 e^{i\beta x} e^{-k_2 z}, \quad (58d)$$

$$H_y(z) = A_2 e^{i\beta x} e^{-k_2 z}, \quad (58b) \quad E_y(z) = A_2 e^{i\beta x} e^{-k_2 z}, \quad (58e)$$

$$E_z(z) = -A_2 \frac{\beta}{\omega \varepsilon_0 \varepsilon_2} e^{i\beta x} e^{-k_2 z}, \quad (58c) \quad H_z(z) = A_2 \frac{\beta}{\omega \mu_0} e^{i\beta x} e^{-k_2 z}, \quad (58f)$$

and for $z < 0$, we get:

$$\text{TM: } E_x(z) = -i A_1 \frac{1}{\omega \varepsilon_0 \varepsilon_1} k_1 e^{i\beta x} e^{k_1 z}, \quad (59a) \quad \text{TE: } H_x(z) = i A_1 \frac{1}{\omega \mu_0} k_1 e^{i\beta x} e^{k_1 z}, \quad (59d)$$

$$H_y(z) = A_1 e^{i\beta x} e^{k_1 z}, \quad (59b) \quad E_y(z) = A_1 e^{i\beta x} e^{k_1 z}, \quad (59e)$$

$$E_z(z) = -A_1 \frac{\beta}{\omega \varepsilon_0 \varepsilon_1} e^{i\beta x} e^{k_1 z}, \quad (59c) \quad H_z(z) = A_1 \frac{\beta}{\omega \mu_0} e^{i\beta x} e^{k_1 z}. \quad (59f)$$

At the interface, continuity conditions require E_x and H_y to be continuous in the TM case as well as H_x and E_y in the TE case. This leads to:

$$\text{TM: } A_1 = A_2, \quad (60a) \quad \text{TE: } A_1 = A_2, \quad (60d)$$

$$\frac{k_2}{k_1} = -\frac{\varepsilon_2}{\varepsilon_1}, \quad (60b) \quad -\frac{i A_2 k_2}{\omega \mu_0} = \frac{i A_1 k_1}{\omega \mu_0}, \quad (60e)$$

$$\beta = k_0 \sqrt{\frac{\varepsilon_1 \varepsilon_2}{\varepsilon_1 + \varepsilon_2}}, \quad (60c) \quad k_1 + k_2 = 0. \quad (60f)$$

In the TM case, this is the SPP dispersion relation we already know from Equation (34). In the TE case however, since the real parts of the wave numbers are required to be non-zero and positive, we don't get a solution. Hence, surface plasmon polaritons are inherently TM polarized [61, 83].

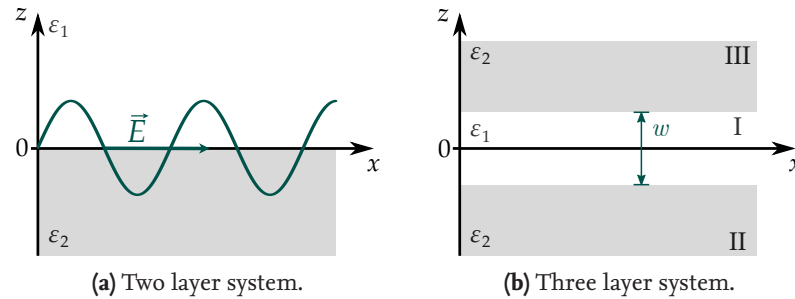


Figure 4.1 – Interfaces between two (a) and three media (b) with different permittivities.

Next, we consider two opposing interfaces as depicted in Figure 4.1(b). In this configuration, we distinguish three regions, two outer and one inner region. The derivation works similar to the case of only one interface and we will only regard cases where the outer regions are of the same material. Nevertheless, it is a significantly longer derivation, so the detailed version is given in Appendix A.5. Ultimately, it leads to the characteristic equation for the propagation of SPPs through a rectangular metal-dielectric-metal waveguide of width w [46, 48, 52, 61, 83, 125]:

$$\tanh\left(\frac{w}{2}\sqrt{\beta^2 - k_0^2\epsilon_d}\right) = -\frac{\epsilon_d}{\epsilon_m} \frac{\sqrt{\beta^2 - k_0^2\epsilon_m}}{\sqrt{\beta^2 - k_0^2\epsilon_d}}. \quad (61)$$

with the relative permittivities ϵ_d of the dielectric material (ϵ_1 in Figure 4.1) and ϵ_m of the metal (ϵ_2 in Figure 4.1). Apart from optical properties, the propagation β of SPPs through a metal-dielectric-metal waveguide, and thus the phase of the light propagating behind the waveguide, depends only on the waveguide width w .

4.2 Plasmonic Lenses

We rearrange Equation (61) to find the width w of a waveguide needed for a certain propagation:

$$w = \frac{2}{\sqrt{\beta^2 - k_0^2\epsilon_d}} \tanh^{-1}\left(-\frac{\epsilon_d \sqrt{\beta^2 - k_0^2\epsilon_m}}{\epsilon_m \sqrt{\beta^2 - k_0^2\epsilon_d}}\right). \quad (62)$$

By building an array of waveguides with different widths, a plane wavefront incoming on one side of the waveguide array could be altered in arbitrary ways. For example, the wavefront can be curved so that it forms a focal spot, which gives the waveguide array the functionality of a flat lens. To achieve this in a monochromatic case, the propagation constant β and therefore the phase shift ϕ introduced by the waveguides has to depend

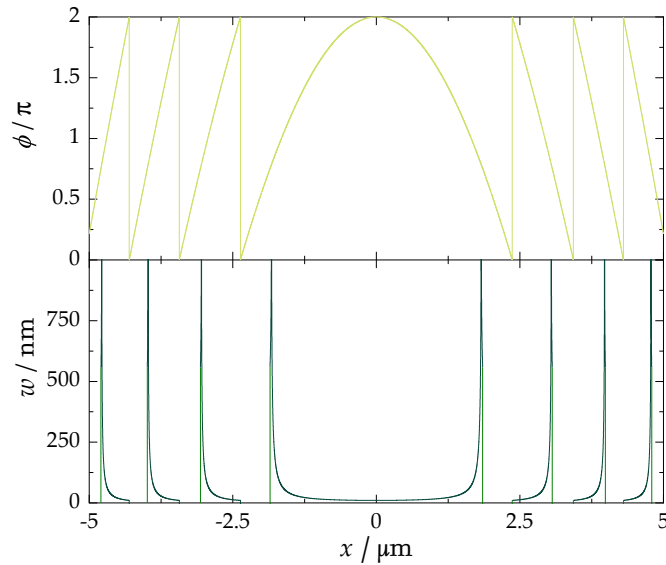


Figure 4.2 – Phase distribution (upper) and corresponding waveguide width (lower) for a plasmonic lens with $l = 200$ nm, $f = 5$ μm and $\lambda_0 = 532$ nm. Materials are iridium and air.

on the position x on the lens relative to its center [126]:

$$\phi(x) = \beta(x) \cdot l \quad (63a)$$

$$= 2\pi m + \frac{2\pi f}{\lambda_0} - \frac{2\pi\sqrt{f^2 + x^2}}{\lambda_0}, \quad (63b)$$

with $m \in \mathbb{N}$. To facilitate the simplest possible fabrication, each waveguide of a lens is considered to have the same length, denoted by l in Equation (63a). Therefore, this length will also be referred to as the thickness of the plasmonic lens. Considering an arrangement of slits in a metallic slab as plasmonic waveguides, each slit width w corresponds to a phase delay ϕ . In order to produce a focal spot at a distance f from the slab, the phase delay in the centre of the lens has to be the largest. With increasing distance from the centre, the phase delay has to decrease. The upper graph in Figure 4.2 shows an exemplary plot of the phase distribution resulting from Equation (63) for a lens with a thickness of $l = 200$ nm and a focal length of $f = 5$ μm at a wavelength of $\lambda_0 = 532$ nm. Complementary, the lower graph in Figure 4.2 plots the width w of the waveguides corresponding to this phase distribution of their position on the lens according to Equation (62). As we can see, with increasing distance from the center, the slit width increases, leading to a delayed phase. Close to the 2π phase shift, the width suddenly decreases. This is explained by numerical issues due to exponentially increasing values eventually exceeding the floating-point range [127]. The 2π periodicity of the phase is also the reason why the width does not get increasingly larger until the edge of the lens, but periodically jumps back to smaller widths in a Fresnel lens-like manner.

4.3 Inverted Plasmonic Lenses

The fabrication of conventional plasmonic lenses like described in Section 4.2 is challenging. They are usually realized by either cutting slits in metallic slabs or by stacking alternating metallic and dielectric layers. However, the latter would result in very large thicknesses l of the lenses so that SPPs couldn't propagate properly. Thus, further post-processing would be required to shorten the waveguides to the desired length and to mount the layerstack sideways on a substrate for easier lens handling, both of which could affect the lenses' functionality. Presumably, this is why top-down approaches are more frequently used in plasmonic lens production. In doing so, thin slits of around 100 nm width have to be cut into metallic slabs of up to 2 μm thickness. Usually, this is achieved by means of focused ion beam milling (FIB) [128, 129, 130, 131, 132, 133]. Though being a highly accurate method, FIB suffers from small preparation areas and low production speeds. This makes FIB appropriate for research purposes, but rather unsuited for larger quantities of structures with varying parameters, especially regarding future industrial uses [134, 135, 136]. With this in mind, the fabrication with etching techniques seems more promising. Yet, etching structures with such high aspect ratios in metal without high deviations remains challenging.

Therefore, I developed a new kind of plasmonic lens design which is compatible with the electron beam lithography fabrication process [137]. In the conventional plasmonic lens design shown in Figure 4.3(a), the SPPs travel along the metal-air-interfaces through the slits, where air takes the part of a dielectric medium as according to Section 2.3.2. In the new design, illustrated in Figure 4.3(b), they still travel along metal-dielectric-interfaces, but these are now realized as dielectric ridges covered with a metallic coating. In addition, the substrate is capped with a metallic layer to prevent unwanted light transmission. Because of the design inversion from slits to ridges, I call this design inverted plasmonic lens. Inspired by the production of wire grid polarizers [138], the dielectric ridges can be fabricated using electron beam lithography and afterwards, the coating is realized with atomic layer deposition (ALD). This mitigates the need to etch or mill high aspect ratio structures in metal while still retaining the functionality of the plasmonic structures. As an example, Figure 4.4 shows a comparison of the fields produced by both the conventional and the inverted design. Both designs used the same structural parameters that were optimized for the inverted design. In this example, the focal spot produced by the inverted design has an about 10 % higher intensity compared to the conventional design.

In the scope of this thesis, a set of inverted plasmonic lenses was designed, fabricated, and characterized. As mentioned in Section 2.3.2, different materials offer different responses to plasmonic excitations. The plasmonic lenses fabricated for this thesis are made of AZ1505 photoresist by MicroChemicals [139] as dielectric component as well as iridium as the metallic coating. The photoresist has a refractive index of about 1.65 in the visible and near-infrared regime and is easily processible in lithography. Iridium has a quality

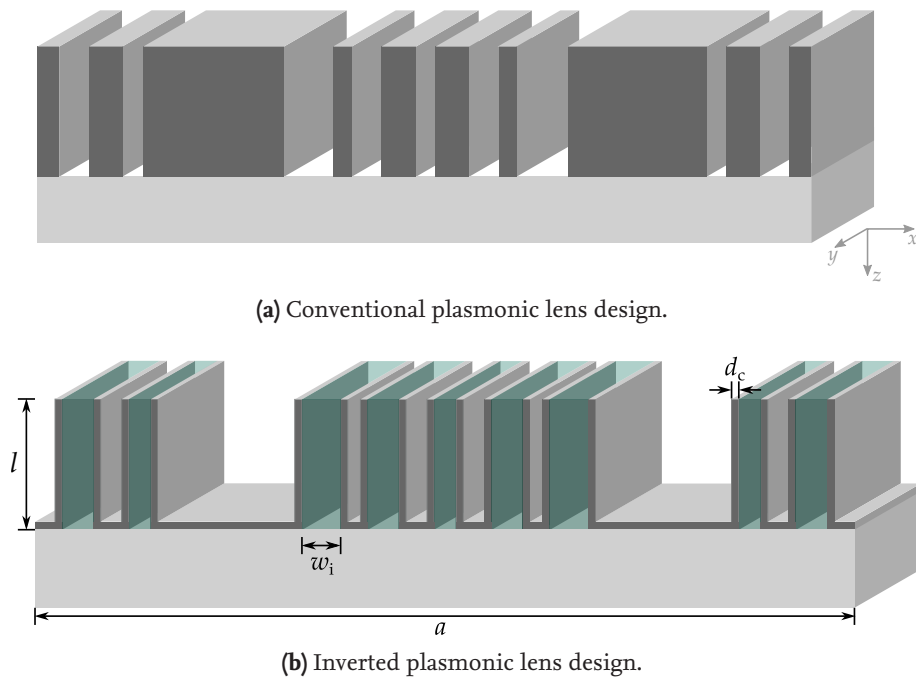


Figure 4.3 – Schematics of conventional (a) and inverted plasmonic lenses (b). Metallic structures (dark gray) on a dielectric substrate (light gray). In the inverted design, the ridges are filled with a dielectric material (green).

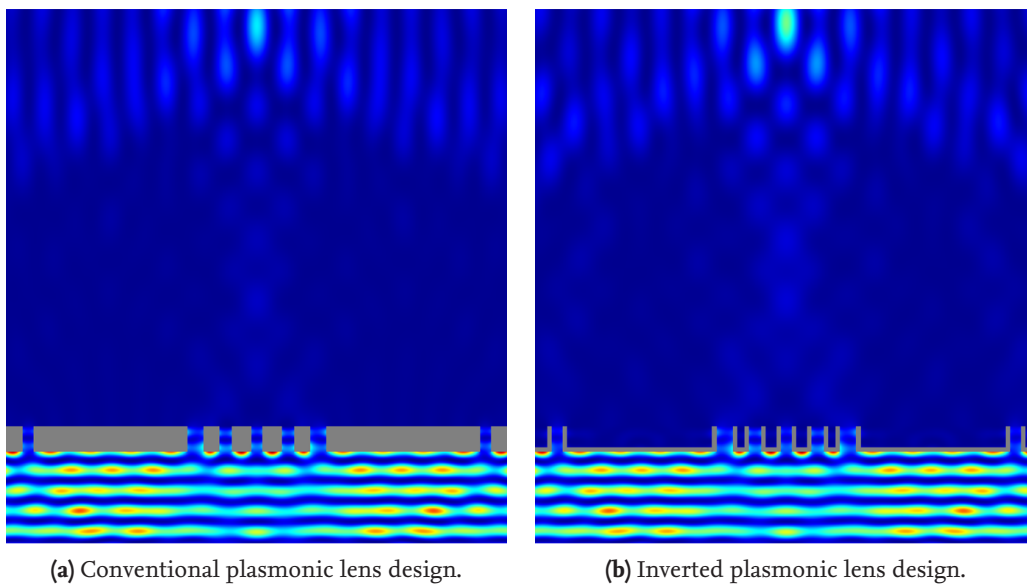


Figure 4.4 – Intensity distribution of conventional (a) and inverted plasmonic lenses (b) with the same structural parameters, cropped to area of interest.

factor of $Q_{\text{SPP}} \approx 9.67$ (data from [140]). This is much less than typical metals used in plasmonics, like silver, gold, copper, or aluminium. Nevertheless, iridium was chosen due to its comparably high oxidation resistance as well as its capability to be deposited by means of ALD. Apart from that, silicon dioxide (SiO_2) forms the substrate material of the fabricated lenses. The structural parameters of the lenses follow applications in the visible and near-infrared wavelength range at short focal lengths between $5 \mu\text{m}$ and 1mm . The wavelength range was chosen in accordance with the ranges available in common ellipsometric setups. The intention behind the short focal lengths was for future implementations of the lenses to be compact, while keeping the possibility to catch near-field effects from light-sample-interactions. Section 4.4 describes the parameter optimization process followed to obtain structural parameters for the different lens designs. Following this, an overview of the fabricated structures as well as an analysis of their performance is given in Section 4.5.

4.4 Lens Design and Parameter Optimization

The design of the inverted plasmonic lenses followed the methods described in Sections 4.2 and 4.3. After defining the parameters of the lens, their focal length, application wavelength, aperture, thickness, and coating thickness, I calculated the phase distribution for each position on the lens and the corresponding ridge widths in steps of 1nm from the lens center. At this stage, the lens computations and simulations are made in a two-dimensional cross-section of a lens due to high computational demands of three-dimensional numerical simulations. Next, spots on the lens where a ridge shall be placed are selected. They can't be placed arbitrarily close to each other because of their finite size. Two different ways to manage ridge arrangements are described in Section 4.4.3. In the end, if the lens dimensions are sufficiently small, a finite element simulation of the lens cross-section is performed to evaluate the spot generation and quality.

Structural parameters critically influence the performance of the lens. Therefore, I performed a series of numerical simulations using the finite element method (FEM) tool JCMSuite [141], supported by particle swarm optimization (PSO) to find optimal lens parameters for each set of focal lengths and application wavelengths.

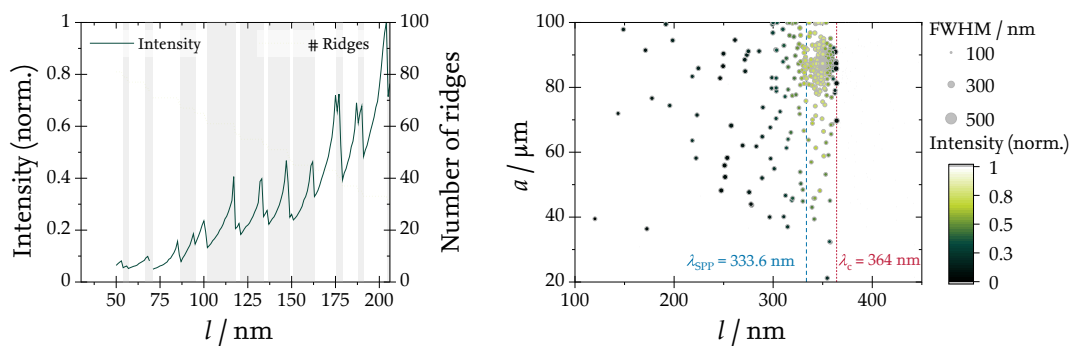
PSO is a global optimization algorithm that stochastically finds the solution to a multi-dimensional problem. Its idea originates from the swarm behaviour of certain animals, like birds or fish. The algorithm starts by statistically distributing starting points inside the given parameter space and assigning them to virtual particles. In each iteration, the objective function is evaluated at the particles positions in the parameter space. Then, the particles update their position based on their velocity vector. This vector contains three terms: the particle's inertia, the coordinates of their own best position so far, as well as the whole group's best position so far. The weighting of each of these hyperparameters determines whether a particle is more likely to explore the parameter space on its own

or if it flocks together with other particles. Eventually, the particle swarm will converge towards an optimum. Swarm dynamics are controlled by adjusting the hyperparameters and by implementing constriction coefficients to their movement [142, 143].

The following subsections first describe the optimization of the three lens parameters l , d_c , and a illustrated in Figure 4.3(b) using PSO. The algorithm's optimization objective was to minimize the ratio between full width at half maximum (FWHM) and intensity of the focal spot at focal distance from the lens surface. Larger intensities and slimmer focal spots led to smaller values of the objective function. Due to high computational costs, the optimizations were performed only for two wavelengths in the visible regime, 455 nm and 532 nm, as well as for the short focal lengths 5 and 10 μm to observe the general behaviour of the inverted plasmonic lens under parameter changes. The swarms, consisting of up to 30 particles, usually converged after up to 40 iterations. Apart from the lens dimensions, two different approaches to ridge arrangement will be discussed. The results of these investigations were then considered for the final lens designs that were ultimately fabricated.

4.4.1 Waveguide Length and Lens Aperture

As a first impression of the influence of the waveguide length l , I computed the parameters of plasmonic lenses with $f = 10 \mu\text{m}$ at $\lambda_0 = 532 \text{ nm}$ according to Equations (62) and (63) for different thicknesses l up to 200 nm. AZ1505 was used as dielectric material and iridium as metal. The aperture was fixed to 10 μm and the ridge widths and positions were recalculated for each thickness. Figure 4.5(a) shows the normalized intensity of the resulting focal spots depending on the thickness. Generally, the intensity increases with the thickness, but also falls back to lower values periodically. The reason for this behavior becomes clear when comparing this to the number of ridges generated within the fixed



(a) Intensity and number of ridges depending on ridge thickness. Gray bars highlight ridge number changes.

(b) Evaluation results from PSO performed over thickness and aperture.

Figure 4.5 – Influence of the waveguide length (a, b) and the aperture (b) on the focal spot.

aperture: From Equation (63a), we know that the propagation constant β is inversely proportional to the thickness l . Thus, with increasing thickness, the width of the ridges also has to increase. Generally wider ridges result in less ridges fitting inside the aperture. Also, in this case, the ridges were arranged as an array with a fixed pitch between ridge centers, and when ridges became too large and would overlap, they were removed from the design. Each time a ridge gets removed for one or the other reason, the intensity drops significantly as less light is able to propagate.

Figure 4.5(b) shows the results of each evaluation from a PSO performed over thickness and aperture with 35 particles in 35 iterations. The sizes of the points indicate the FWHM of the focal spot and their color denote the intensity. The swarm converged at a thickness of $l \approx 350$ nm and an aperture of $a \approx 87$ μm . On average, spots had a FWHM of about 190 nm and were overall smaller than the incident wavelength. The particles tended towards higher apertures and to thicknesses between the SPP wavelength $\lambda_{\text{SPP}} = 333.6$ nm and the wavelength inside the ridges $\lambda_c = \lambda_0/n_d = 364$ nm. Each evaluation attempt for thicknesses larger than λ_c failed to compute. We can comprehend this cut-off when we examine Equation (62). For non-magnetic materials, it is safe to assume that the refractive index relates to the permittivity by $n_d = \sqrt{\epsilon_d}$ [77]. In combination with Equation (63a), for the square root in Equation (62) follows:

$$\sqrt{\beta(x)^2 - k_0^2 \epsilon_d} = \sqrt{\beta(x)^2 - k_0^2 n_d^2} = \sqrt{\frac{\phi(x)^2}{l^2} - \frac{4\pi^2 n_d^2}{\lambda_0^2}}. \quad (64)$$

If the thickness l becomes equal or greater than λ_0/n_d , the radicand is always negative and therefore, the result of the square root is always complex-valued, which leads to the ridge width w also being complex-valued and thus not realizable. This indicates that it is advisable to choose thicknesses for the plasmonic lenses between λ_c and λ_{SPP} for optimal performance. Please note that the limitation due to λ_c solely comes from the mathematical model used to describe the phase shift provided by a certain waveguide width. A waveguide longer than λ_c will physically still be able to support SPP propagation and yield in a phase delay depending on its width and length.

Recalculating the ridge widths and positions for each thickness leads to a decreasing number of ridges per lens. Another approach to this is calculating the ridge parameters beforehand and then changing the lens' thickness while keeping a fixed set of ridge widths. This is especially reasonable when considering fabrication limits of the lens' thickness, because eventually, each lens on a wafer will have to have the same thickness. Figure 4.6 shows the first and last iterations of a PSO with fixed ridge parameters computed for $l = 200$ nm and $f = 5$ μm at $\lambda_0 = 455$ nm. The swarm consisted of 20 particles and optimized for 35 iterations. The arrows in the first iteration indicate the velocity of the particles. Some arrows are missing due to overshooting the limits of the parameter space. As highlighted by the red circle in the last iteration, the particles that were randomly distributed in the beginning collected at $l = 172$ nm and $a = 100$ μm . The optimized thickness lies well

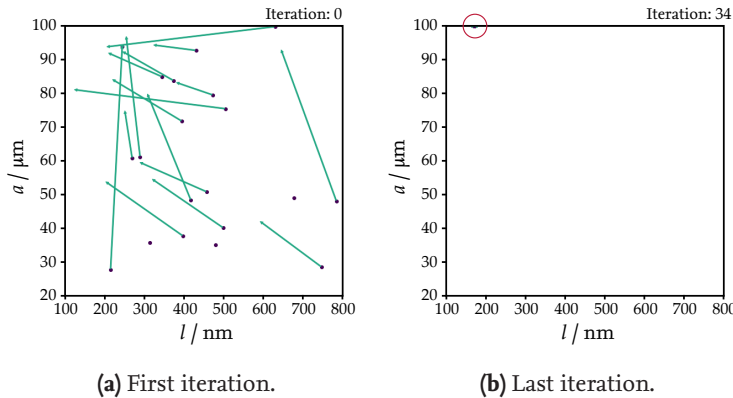


Figure 4.6 – First (a) and last iteration (b) of a PSO for fixed ridge parameters.

below the one this set of ridge parameters was designed for. When keeping also the aperture fixed to in this case $50\ \mu\text{m}$, we obtain Figure 4.7, which depicts focal spot intensity and FWHM depending on the thickness of a lens simulated with fixed ridge parameters in the same parameter space as the PSO in Figure 4.6. For constant ridge widths, as the lengths of the waveguides increase, the intensity of the focal spot decreases, because SPPs decay from their point of excitation, as described by their propagation length in Equation (38). So in general, the thicker the lens, the less energy can propagate through it, leading to weaker focal spots. In addition, we observe a periodicity in the intensity that is linked to the phase shift induced by the changing waveguide lengths. This phase shift causes the focal spot to move in and out of the plane of observation at the expected focal distance when evaluating the simulations. The influence of this movement is especially clear in the FWHM of the focal spot, which increases with decreasing intensity, but also oscillates with a periodicity of about $148\ \text{nm}$.

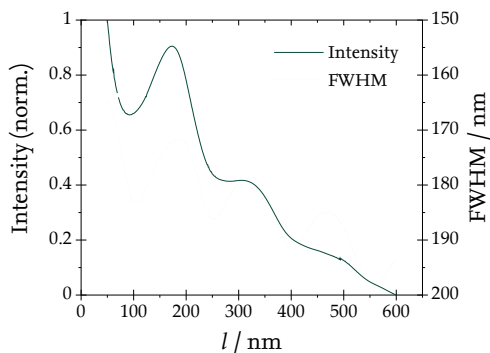


Figure 4.7 – Intensity and FWHM of focal spot for different lens thicknesses l .

To sum up the observations: For optimal lens performance, the ridge widths and positions should first be determined for a thickness between λ_{SPP} and λ_{c} , but the final thickness of the lens should then be optimized with the resulting fixed set of ridge parameters.

The particles of the optimization in Figure 4.6 collected at the upper bound of the aperture parameter space. In general, a larger aperture is preferable, as larger lenses obviously contain more ridges and therefore establish more throughput as well as a higher NA .

The NA is defined as [144]:

$$NA = n \sin(\theta_{\max}) = n \sin\left(\arctan\left(\frac{a}{2f}\right)\right). \quad (65)$$

For the parameter space in the PSO in Figure 4.6, the NA ranges between 0.894 and 0.995. Overall, this leads to a higher quality of the produced focal spot in terms of intensity and spot size. These observations are in agreement with early numerical investigations from the literature [145].

4.4.2 Coating Thickness

In the inverted plasmonic lens design, we encounter both types of three-layer-interfaces: metal-dielectric-metal and dielectric-metal-dielectric. The former are the plasmonic waveguides themselves; dielectric ridges coated with metal. The latter are the metallic coatings, facing the waveguide on one side and the surrounding dielectric material on the other. In both cases, the SPP penetration depths δ_d and δ_m play important roles. As introduced in Section 2.3.2, the evanescent fields corresponding to the SPPs decay with distance to the interface, and their penetration into both media depends on the respective permittivities. For a plasmonic waveguide, we want the SPPs on both sides of the waveguide to couple to create an efficient energy transport. Thus, the ridges should not be wider than δ_d . On the other hand, the fields also enter the metallic coating to a certain extent, and when the coating is thinner than δ_m , SPPs could form outside of the waveguides, too, leading to leakage [61]. For the material system in this thesis, δ_d and δ_m are depicted in Figures 4.8(a) and (b), respectively, for wavelengths in the visible and near-infrared regime. The penetration depths were calculated for both air and AZ1505 as dielectric materials. Above 480 nm, the penetration depth into AZ1505 is always higher than the minimum width required for a 2π phase shift, so SPP coupling can occur without problems.

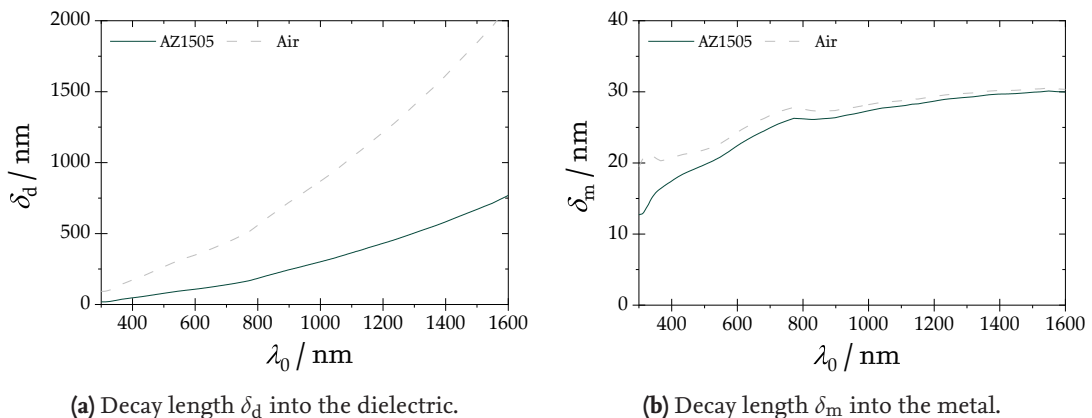


Figure 4.8 – SPP decay lengths into the dielectric (a) and the metal (b) perpendicular to an interface between iridium as a metal and either air or AZ1505 as a dielectric layer.

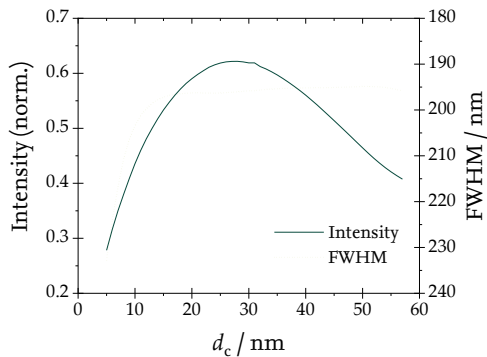


Figure 4.9 – Focal spot intensity and FWHM depending on coating thickness.

at 532 nm. At this wavelength, the metallic penetration depth is around $\delta_m \approx 21$ nm for air filled ridges. Figure 4.9 shows the normalized intensity and the FWHM of the focal spot over the coating thickness. As expected, for coatings thinner than δ_m , intensity vanishes and FWHM rises as the resulting leakage prevents proper plasmonic propagation and thus a distinguished focal spot to be formed. The intensity reaches its maximum at about 28 nm, but after that decreases again for larger thicknesses. This is most likely also a leakage effect: SPPs penetrating the metallic coating might transform to propagating waves, contributing to the overall intensity of the electromagnetic field behind the lens. So, while the intensity of the focal spot might have its maximum at about 28 nm, the intensity of the field around the spot, which was not observed, might also still be relatively strong. Thus, with thicker coatings, the probability for leakage decreases, together with the absolute intensity of the focal spot, while the relative intensity might stay the same. Eventually, increasing d_c would lead us back to the conventional design, where the intensity presumably converges to. Regarding the FWHM, the focal spot size stayed rather constant for coating thicknesses larger than the penetration depth and reached a minimum of about 194 nm at $d_c = 51$ nm.

Regarding the penetration into the metallic coating, the maximum lies at about 30.1 nm and for the visible regime, it lies significantly below that. Thus, a coating of around 35 nm thickness should already prevent leakage sufficiently. As the penetration depths are always smaller in the case using AZ1505, we will focus on air filled ridges for now.

For further examinations of the influence of the coating thickness, I simulated plasmonic lenses with fixed ridge positions and widths but different coating thicknesses for $f = 5 \mu\text{m}$

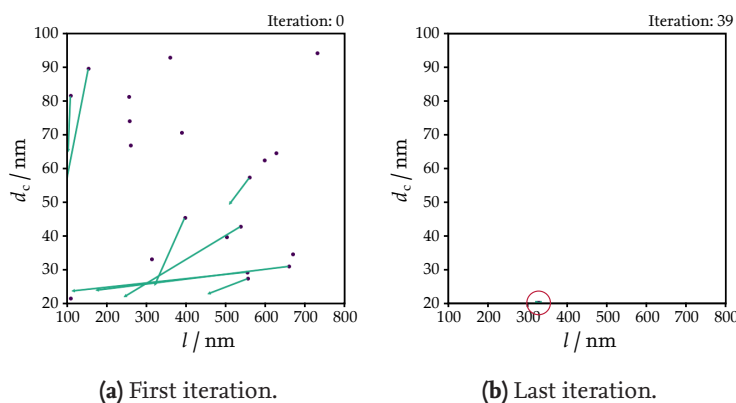


Figure 4.10 – First (a) and last iteration (b) of a PSO for the coating thickness d_c .

The optimization of the coating thickness in dependence of the thickness l using PSO was conducted for a lens with $f = 5 \mu\text{m}$ at a $\lambda_0 = 532 \text{ nm}$. The initial state of the particle swarm is shown in Figure 4.10(a) and the final state after 40 iterations in Figure 4.10(b). The swarm converged at a thickness of about 327 nm. Regarding the coating thickness, the swarm tended towards the lower bound of 20 nm, as highlighted in Figure 4.10(b). The reason lies in what we have already seen in Figure 4.9: The objective function of the swarm is to maximize the intensity of the focal spot in relation to its size. So in general, a higher intensity is preferred, which at lower coating thicknesses is achieved due to leakage and thus overall higher absolute field intensity.

4.4.3 Ridge Arrangement

Plasmonic lenses in the literature usually arrange the plasmonic waveguides in periodic arrays. They get their functionality from periodically differing either the width, the depth or the refractive index of the dielectric slits [129, 146, 147]. For the lenses in this thesis, this means choosing a certain period Λ and computing the width w of the ridge at each position on that array as illustrated in Figure 4.11(a). However, due to the interplay between waveguide width and phase delay, placing each ridge in a fixed distance to the next one is not always possible, as the width required at a certain position might lead to neighboring ridges overlapping each other. When a ridge is too wide for its designated position, it is skipped and no ridge is placed at that position. This leads to large areas on the lens with no waveguides at all, which significantly decreases the throughput and therefore the intensity of the focal spot.

For this reason, I implemented a second ridge arrangement style next to the conventional periodic one. In this second style, which is schematically shown in Figure 4.11(b), ridges are not placed on an array with a fixed pitch, but successively next to each other as soon as they fit. The design algorithm considers the width of the current ridge, accounts for

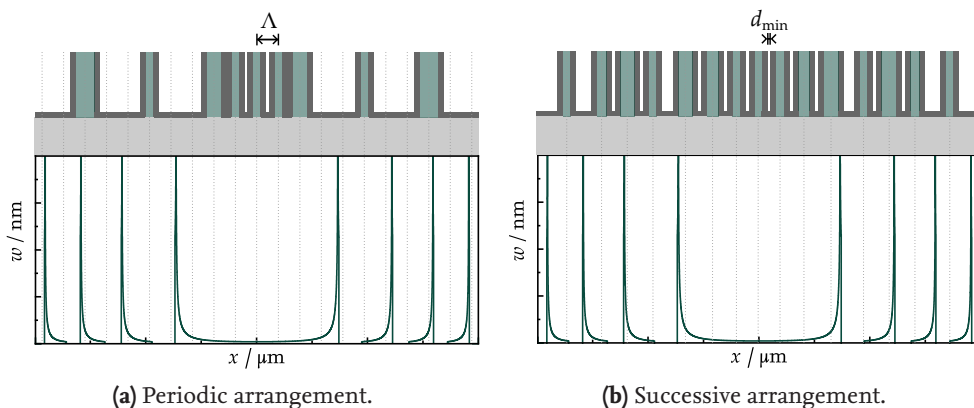


Figure 4.11 – Periodic (a) and successive ridge arrangement (b), illustrated over the ridge widths from Figure 4.2.

coating thickness d_c and a minimum gap thickness d_{\min} , and then looks ahead to find the next position a ridge could be placed without overlapping the current one. In this manner, no unnecessary large gaps form on the lens and the throughput is maximized. When compared to the periodic arrangement, the successive arrangement showed about twice as intense focal spots in numerical simulations, which is also why I will mostly focus on these types of lenses in the remainder of this thesis. Further differences between the two arrangement types will be discussed on the final designs in Section 4.4.4.

4.4.4 Final Designs

For the fabrication of inverted plasmonic lenses, I chose a set of application wavelengths and focal lengths based on practicability. Wavelengths for the lenses should range in the visible regime to be easily accessed by experimental means, but also go towards the infrared to address common use cases (e.g., telecommunications or lab-on-a-chip devices). Simulations to test the functionality of the lenses before their fabrication could only be performed for short focal lengths due to high computational costs. Therefore, two focal lengths in the micrometer regime were chosen which could be verified with simulations. Two longer focal lengths were added due to the difficulty of measuring at such short distances but not verified by simulations before fabrication.

Simulations so far have been performed with two-dimensional model geometries to save computational costs. In these simulations, an infinite extension of the waveguides into one dimension is assumed. This is approximated in fabrication by ridges of sufficient length. However, constructing the lenses this way leads to the formation of a focal line like from a cylindrical lens, rather than a spot. For circular spot formation, lenses are also realized as concentric rings with the same cross section as the cylindrical lens, with the middle ridge being at the center of the lens.

Each designed lens got a label according to its most important parameters for easier description. The labels consist of two uppercase letters and two digits, divided by a hyphen. The letters indicate whether the lens is fabricated as a spherical (O) or a cylindrical lens (C) and if the ridge arrangement is periodic (P) or successive (S) (see Section 4.4.3). The digits decode their intended focal length (first digit) and wavelength (second digit) according to Table 4.1.

Table 4.1 – Plasmonic lens labels.

$f \backslash \lambda_0$	455 nm	532 nm	632 nm	1064 nm	1550 nm
5 μm	X-00	X-01	X-02	X-03	X-04
10 μm	X-10	X-11	X-12	X-13	X-14
100 μm	S-20	S-21	S-22	S-23	S-24
1000 μm	S-30	S-31	S-32	S-33	S-34

The optimization process described in the previous sections was carried out for different combinations of application wavelengths and desired focal lengths. Due to the already indicated fabrication limits, lenses that are produced on the same wafer should have the same thickness. Therefore, I intended to find one thickness which is compatible with as many lenses as possible. Thus, the parameter space was confined to the range of 200 nm to 600 nm in steps of 100 nm. Table 4.2 lists the optimal thicknesses found for each lens configuration. As most of these lenses work best at 200 nm, this thickness was chosen for the fabricated set of plasmonic lenses.

As a result from Section 4.4.2, a coating thickness of $d_c = 35$ nm was chosen for the final design. It exceeds the required minimum thickness of the metallic coating to prevent SPP coupling to the outside and it leaves some space for fabrication deviations. While thin coatings are both time and cost efficient in fabrication, it is preferable for the coating to be too thick rather than too thin. The reason for this is that thicker coatings only converge towards the conventional design in functionality and thus reduce leakage further, while thinner ones impair the functionality of the lens.

While larger apertures enhance the intensity and quality of the focal spot, they also drastically enhance the computational costs tied to performing the numerical simulations required for the optimization process. Thus, a fixed aperture of 100 μm was chosen for nearly every lens. At lower wavelengths and focal lengths, even with an aperture of only 50 μm , sufficiently high beam qualities could be ensured, so the aperture was reduced for the sake of simulation time. A complete table of all parameters of the fabricated lenses is given in Appendix A.6.

Figure 4.12 shows a box plot statistic about the widths of the ridges and the distances between their centers. As the periodically arranged ridges are all placed in multiples of 200 nm, their mean distances between each other are comparatively low with only a few outliers, but show larger scattering around their average. Concurrently, their widths show a similar behavior and in general, the periodically arranged ridges are mostly thinner than in the successive design. Compared to that, most of the successively arranged ridges share the same width, though outliers are more likely here. We also observe that the scattering around the mean as well as the mean itself increase with increasing application wavelength and focal length. While ridge distances in the successive design are also comparably

Table 4.2 – Optimal plasmonic lens thicknesses.

$f \backslash \lambda_0$	455 nm	532 nm	632 nm	1064 nm	1550 nm
5 μm	200 nm	200 nm	300 nm	400 nm	600 nm
10 μm	200 nm	200 nm	200 nm	200 nm	600 nm
100 μm	200 nm	200 nm	200 nm	300 nm	500 nm
1000 μm	200 nm	200 nm	200 nm	300 nm	500 nm

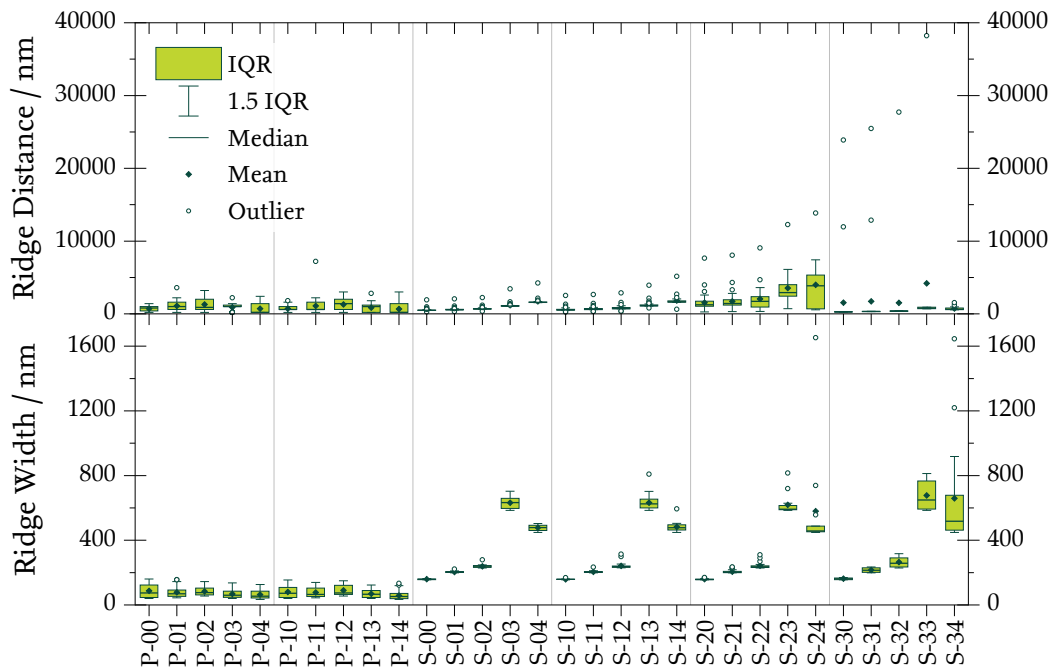


Figure 4.12 – Box plots of the ridge distances (upper) and widths (lower). The boxes illustrate the interquartile range (IQR) between the 25th and the 75th percentile of the data sets. The whiskers are determined from 1.5 times the IQR. Data points not covered by this are considered to be outliers [148].

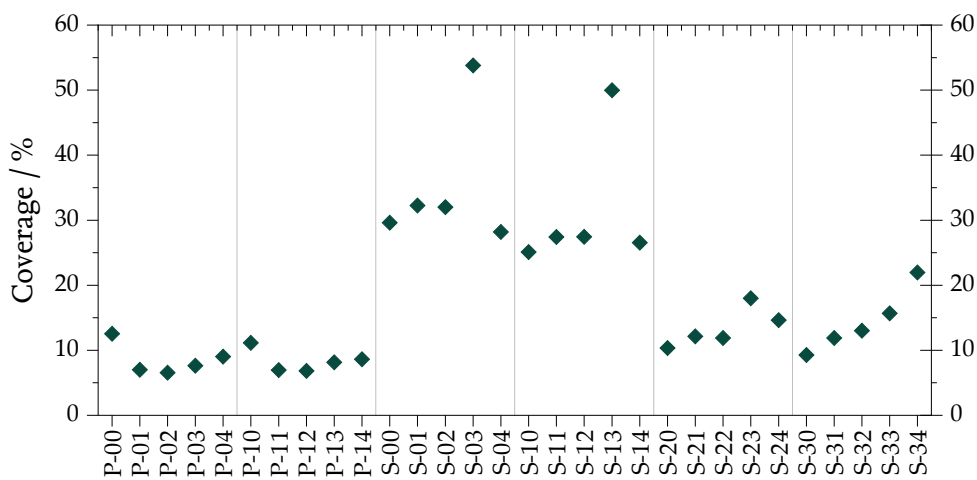


Figure 4.13 – Ridge coverage of the area of the final plasmonic lens designs.

less scattered than in the periodic one, lenses with focal lengths of $100\ \mu\text{m}$ seem more scattered. The larger deviations for lenses with longer focal lengths and application wavelengths are most likely the cause of the ridge widths increasing to ensure the functionality of the lens while still being limited to a fixed aperture. This leads to a smaller number of ridges fitting in the aperture, generally larger ridge distances and more variation.

The mean number of ridges for the periodic design is 98.6; in the successive design, it is only 58.2. However, due to their free placement, successively arranged ridges are generally wider. This leads to periodically arranged ridges only covering 8.45% of the lens on average, while the successive design has a mean coverage of 23.56%, so nearly 3 times higher. A higher coverage means that less lens area is obscured and in general, more light can be used for focal spot creation. Figure 4.13 demonstrates this further. There, we also observe a reduced coverage for the lenses with higher focal lengths. These lenses also showed outliers with large ridges far away from the others. Most likely, the aperture was too small for lenses with these focal lengths to give the space needed for enough ridges to be created. These lenses would have benefited from larger apertures which were not taken into account due to being too large for numerical simulations.

4.5 Lens Performance Evaluation

Inverted plasmonic lenses were fabricated using the designs from Section 4.4.4. Now we want to take a look on the performance of the lenses, both experimentally on the fabricated ones as well as from the design perspective in numerical simulations.

4.5.1 Tolerances to Deviations from Design

Fabrication processes often underlie deviations compared to the design. Therefore, I simulated a lens with $l = 300\ \text{nm}$ at a wavelength of $532\ \text{nm}$ and examined the intensity of the focal spot while assigning random changes to the ridge positions in order to estimate the influence of minor ridge misplacements. In Figure 4.14, we see the observed intensity depending on the scale γ of the Gaussian distribution used to randomly displace the ridges. Even with only one simulation per scale factor, the intensity significantly decreases with increasing randomness. For $\gamma = 100$, the intensity drops as low as half of the initial value. Nevertheless, for γ up to 10, the influence of the displacement is negligible, so deviations from the fabrication of up to $50\ \text{nm}$ are not crucial for lens performance.

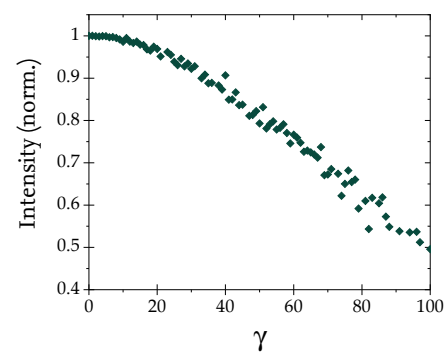


Figure 4.14 – Focal spot intensity under Gaussian distribution of ridges.

4.5.2 Wavelength Dependency

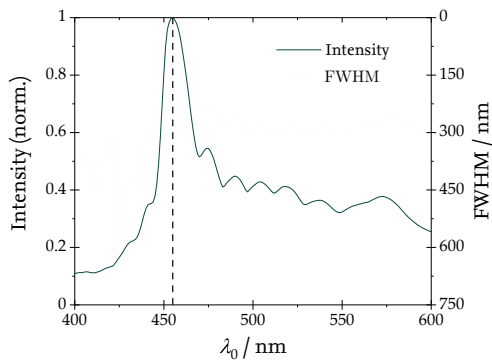


Figure 4.15 – Simulated intensity and FWHM of an inverted plasmonic lens' focal spot at focal length for different wavelengths.

Before fabricating the lenses, simulations already suggested a strong dependency of the focal spot on the incident wavelength. Figure 4.15 shows the normalized intensity and FWHM of the focal spot of a simulated lens designed for 455 nm at wavelengths between 400 and 600 nm. Spot size and intensity were evaluated at the intended focal distance only. The plot shows clearly that the focal spot gets less intense and at the same time broadens when leaving the design wavelength. This indicates a shift of the spot away from the design focal distance.

Figure 4.16 depicts a sketch of how the different lenses are arranged on the sample. As an example, Figure 4.17 shows two SEM images of fabricated plasmonic lenses. Using two different setups, the focal lengths of the produced plasmonic lenses were measured by means of through-focus scanning optical microscopy (TSOM) [149]. The first setup was a microscope, the second one was the EP4 MUELLER matrix ellipsometer introduced in Section 3.2.2. The reason for two different setups is that the focal length range of the lenses was too large to be covered with only one setup. At the microscope, focal scans of the lenses with focal lengths of 5 and 10 μm could be measured in steps of 100 nm, but the total range in focal direction was limited to 100 μm , so larger focal lengths could not be measured. On the other hand, at the EP4, the movement range goes up to several centimeters, which allowed for focal scans of the lenses with 100 and 1000 μm focal length, but with a minimum step size of 1 μm , so the lenses with shorter focal lengths could not be measured.

In the TSOM measurements, images of the lens were taken for different focal positions around the focused image of the lens itself. The focal range was chosen to cover up to at least twice the intended focal length of the lens in both directions from the focused image. For the evaluation of the images, the standard deviation of all pixels in the images was observed. In this context, higher standard deviation is correlated with a higher contrast in the image and thus a more focused image. In microscopy, this is one measure used to evaluate if the image under investigation is focused [150]. The assumption was that if a lens was imaged at different focal planes, it should produce at least two peaks in the standard deviation curve: One at the focused image of the structure itself, and one in a focal length distance from the focused image. As the lens is illuminated with collimated light which it focuses into the microscope's objective, this second peak should correspond to an image of the light source and thus, the image at this focal plane should resemble a small spot with high brightness.

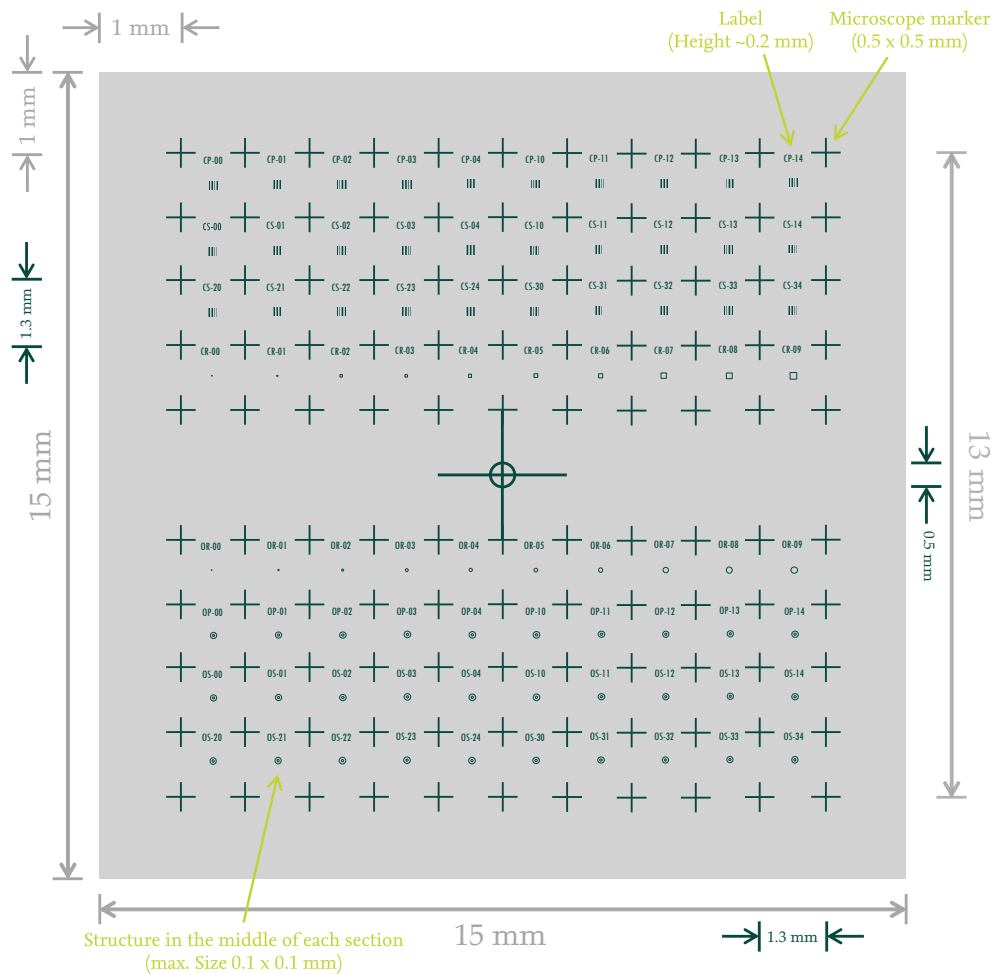


Figure 4.16 – Inverted plasmonic lens chip design.

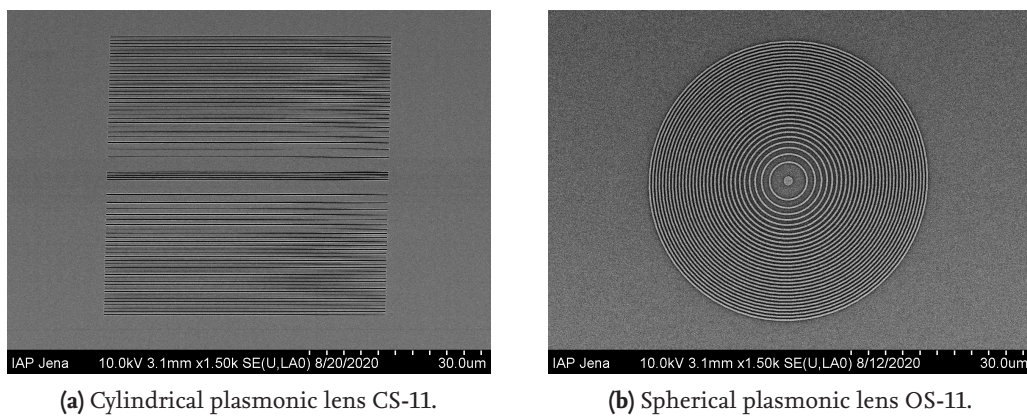


Figure 4.17 – SEM image examples of a fabricated cylindrical (a) and spherical (b) plasmonic lens with $f = 10 \mu\text{m}$ at a wavelength of 532 nm.

As an example, Figure 4.18(a) shows the standard deviation for the TSOM measurement of plasmonic lens OS-11 at a wavelength of 532 nm, measured with the microscope. We see that the assumption was met that peaks at the focused image as well as at the focal spot would be produced. The position of the focused image is marked by a dot in the middle of the scan. Next to this, the plot shows several oscillations which are most likely caused by moiré effects. The second peak is around 10 μm to the right of the focused image, which is at the expected distance for this lens. However, a third unexpected peak occurs, which is also located at focal length distance from the focused image, but in the opposite direction. It is assumed that this peak is a product of reflections inside the lens. These peaks are also visible in Figure 4.18(b), which shows an example for a TSOM scan of lens OS-11, where the images of each focal plane along the z -direction were stitched together to create a y - z -cross section. In the middle, the ridges of the plasmonic lens can be seen in the focused image, which blurs with growing distance from it. About 10 μm away to both directions, the two focal spots are located.

For each of the lenses, the distances of the two side peaks from the peak of the focused image were evaluated. The results are collected in Figure 4.19. When measuring the lenses with short focal lengths, both types of ridge arrangements discussed in Section 4.4.3, periodic and successive, were considered. Figure 4.19(a) shows the distances of only the expected peak from the focused image, divided by the intended focal length, over the difference between the measurement wavelength and the one the lens was designed for. As we can see, at their design wavelength, most lenses are also close to the design focal length. Lenses with a periodic ridge arrangement tend to longer distances, with up to twice the intended focal length at the design wavelength. Also, for other wavelengths, these lenses nearly always show a longer focal length than intended, with no clear correlation to the wavelength.

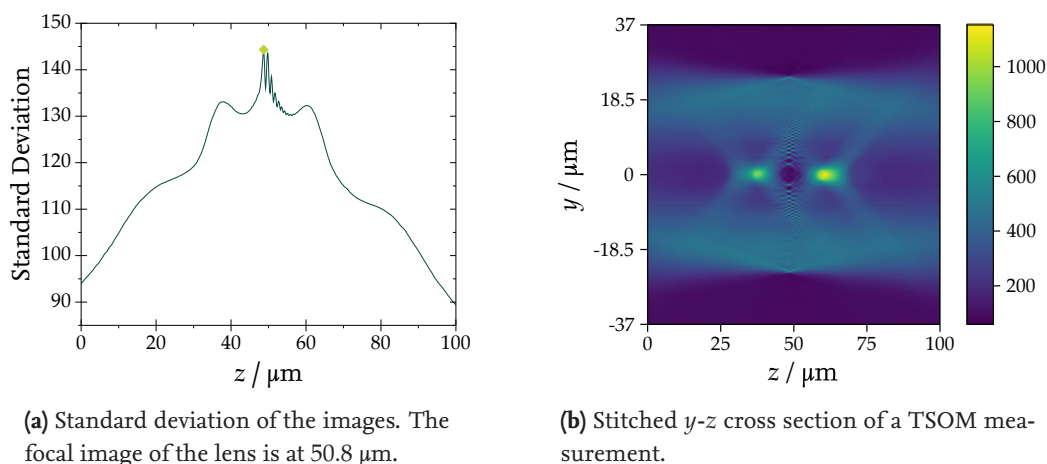
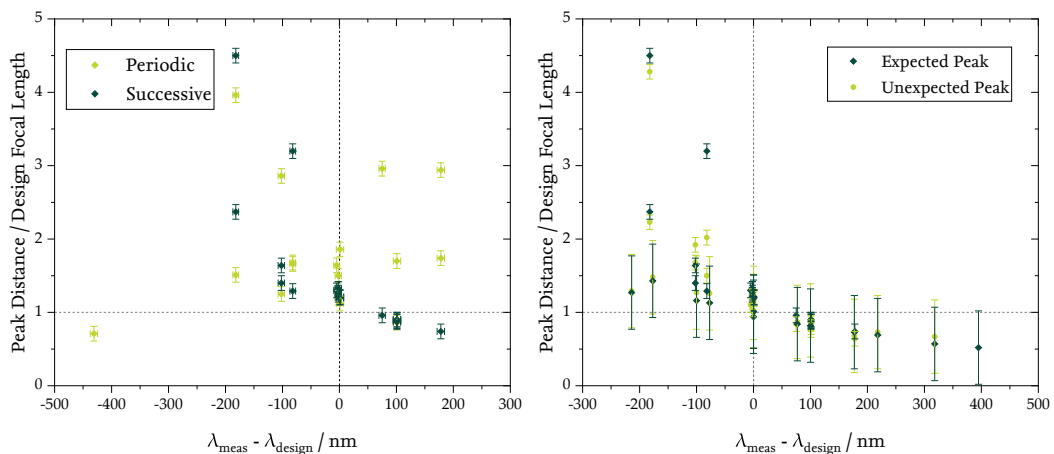


Figure 4.18 – Standard deviation (a) and image cross section (b) of an example TSOM measurement of plasmonic lens OS-11 at a wavelength of 530 nm.

In contrast, the lenses with successive ridge arrangements follow a clear trend: Their focal spot moves closer to the lens for larger wavelengths and vice versa. This resembles chromatic aberration which can also be observed in conventional lenses and is most likely caused by dispersive effects of the dielectric material inside the ridges of the lenses. We also see this effect in Figure 4.19(b), which shows the peak distances for both the expected and the unexpected peak, for all lenses measured at both setups. However, this time, only lenses with successive ridge arrangements were considered, as the focal distances of the lenses with periodically placed ridges showed a worse performance. We observe the same wavelength dependence for each lens, even for the unexpected peaks, reinforcing the impression that it is mainly influenced by material properties. Unfortunately, lenses designed with larger focal lengths of 1 mm didn't show any peaks in the standard deviation besides the focal image and thus didn't produce a focal spot. Reason for this is most likely the design of these lenses itself as it consisted of only a small number of ridges due to the large focal length, while it was still limited to the same aperture of 100 μm as the other lenses to keep fabrication reasonable. Apparently, the small number of ridges is not sufficient for the functionality of the structures as a lens.



(a) Distances of the expected peaks for plasmonic lenses with different ridge arrangements.

(b) Distances of observed peaks for all plasmonic lenses.

Figure 4.19 – Wavelength dependent distances of observed peaks in the standard deviation for fabricated plasmonic lenses with focal lengths of 5 and 10 μm , measured at a microscope setup (a) and results for all plasmonic lenses measured at both setups (b).

4.6 Concepts for Achromatic Plasmonic Lenses

As shown in Section 4.5.2, the focal length of the inverted plasmonic lenses is inherently wavelength dependent. Now, we take a look at theoretical concepts how to remove or at least reduce this wavelength dependency to expand the design of inverted plasmonic lenses to an achromatic functionality. So far, the realization of multispectral plasmonic lenses has been achieved with design approaches using meta-atoms two-dimensionally distributed on a surface [151, 152, 153, 154] or by realizing complex material gradients [155, 156]. Generally, over the last years, the focus in research shifted from plasmonic to dielectric metastructures, as they are capable to provide more efficient effects [157]. For this reason, current literature offers little consideration of achromatic plasmonic lenses. This section starts with the most formal way to realize dispersion-free lenses from current literature oriented at dielectric metasurfaces and discusses limitations for the applicability to the inverted plasmonic lens design as well as possible alternatives.

4.6.1 Dispersion-Free Meta-Lenses

For any metastructure to produce a focal spot, the meta-atoms have to induce a relative phase to an incoming plane wavefront which depends on the position r of the meta-atom in relation to the center of the lens [126]:

$$\phi(r, \omega) = -\frac{\omega}{c} \left(\sqrt{r^2 + f^2} - f \right), \quad (66)$$

where f is the intended focal length of the lens. In Section 4.2, we only regarded the distribution of the phase over the position. If the lens is also supposed to be achromatic, however, the phase also has to depend on the angular frequency ω or the wavelength λ . An achromatic lens focuses different wavelengths to the same focal length. Therefore, the meta-atoms not only have to deliver a certain phase change, but also higher-order dependencies of the phase on the wavelength need to be matched [158]. We can expand the phase into a TAYLOR series to access these higher orders:

$$\phi(r, \omega) = \phi(r, \omega_v) + \left. \frac{\partial \phi(r, \omega)}{\partial \omega} \right|_{\omega=\omega_v} (\omega - \omega_v) + \left. \frac{\partial^2 \phi(r, \omega)}{\partial \omega^2} \right|_{\omega=\omega_v} (\omega - \omega_v)^2 + \dots \quad (67)$$

The first derivative of the phase in the TAYLOR series is called the relative group delay, the second derivative is the group delay dispersion. When designing a meta-lens, we not only have to match the phase of the meta-atoms, but also these two quantities, thus gaining dispersion control via higher orders. We want the focal length not to depend on the frequency, so we can simply determine the first and second order derivatives of the phase from Equation (66):

$$\frac{\partial \phi(r, \omega)}{\partial \omega} = -\frac{1}{c} \left(\sqrt{r^2 + f^2} - f \right), \quad (68a)$$

$$\frac{\partial^2 \phi(r, \omega)}{\partial \omega^2} = 0. \quad (68b)$$

As we can see, the dispersion vanishes, so this case already describes an achromatic lens. For the description of diffractive lenses, please refer to [158].

The next step would involve the design of plasmonic waveguides, this time considering not only the phase, but also its first and second order derivatives, with high emphasize on the dispersion being as close to zero as possible. The control over all three factors requires at least three degrees of freedom in the design of the plasmonic waveguides. Apart from the waveguide widths w , other possible degrees of freedom, that would also influence the phase, are the waveguide lengths, the material composition, or the sidewall angles. These are rather hard to control or realize during the fabrication process, and in the first place, the argumentation behind the inverted lens design was to comply with limitations from fabrication. Therefore, we only considered one degree of freedom, the width w of the waveguides. Using any of the other parameters would make the production of the lenses considerably more challenging.

Apart from missing the relevant degrees of freedom, the current design of the plasmonic lenses relies on the characteristic Equation (61) that links the waveguide width to its propagation constant. For different geometries, a similar analytical equation would be necessary to enable a quick design process. Otherwise, the design would have to rely on simulating phases for different geometries, which might be manageable in a machine learning context, but would significantly slow down the design process nevertheless.

4.6.2 Cylindrical Plasmonic Meta-Atoms

So far, we only considered rectangular waveguides for SPPs, like depicted in Figure 4.20(a). They are historically the common way to realize plasmonic nanoslit lenses, as we have seen in Section 4.2, but they are also inherently selective to states of polarization due to their geometry. Therefore, it is appealing to also consider circular waveguides, where the excitation of plasmonic modes under normal incidence does not depend on the polar-

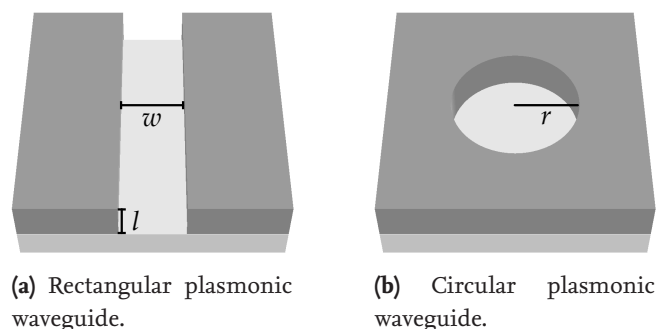


Figure 4.20 – Example for a rectangular (a) waveguide of width w and thickness l and a circular plasmonic waveguide as a hole with radius r in a metallic layer on a substrate.

ization. A visualization for such a waveguide is given in Figure 4.20(b). In a way similar to meta-atoms, these waveguides can locally influence the phase of the transmitted light based on SPP propagation. Thus, we could use them as building blocks for achromatic plasmonic lenses, for example in windmill-like arrangements similar to those we will discuss in Section 4.6.3. Although plasmonic lenses based on circular nanoholes have already been investigated [159, 160, 161, 162, 163, 164], their use for achromatic focusing purposes is yet to be fully explored. For this concept to work, we have to take a look on the phase retardation from circular plasmonic waveguides. Their dispersion equation is different from the characteristic Equation (61) discussed in Section 4.1 [165, 166]:

$$\left(\frac{1}{\xi_d} \frac{I'_v(\xi_d)}{I_v(\xi_d)} - \frac{1}{\xi_m} \frac{K'_v(\xi_m)}{K_v(\xi_m)} \right) \left(\frac{\varepsilon_d}{\xi_d} \frac{I'_v(\xi_d)}{I_v(\xi_d)} - \frac{\varepsilon_m}{\xi_m} \frac{K'_v(\xi_m)}{K_v(\xi_m)} \right) = v^2 \left(\frac{\beta}{k_0} \right)^2 \left(\frac{1}{\xi_d^2} - \frac{1}{\xi_m^2} \right)^2, \quad (69)$$

for the v -th order hybrid mode and with:

$$\xi_{m,d} = r \cdot \sqrt{\beta^2 - \varepsilon_{m,d} k_0^2}, \quad (70)$$

where r is the waveguide radius. Furthermore, I_v and K_v are the modified BESSEL functions of order v , and I'_v and K'_v are their derivatives [59, 165]:

$$I_v(x) = \sum_{m=0}^{\infty} \frac{1}{m! \Gamma(m+v+1)} \left(\frac{x}{2} \right)^{2m+v}, \quad (71a)$$

$$K_v(x) = \frac{\pi}{2} \frac{I_{-v}(x) - I_v(x)}{\sin(v\pi)}, \quad (71b)$$

with the Gamma function

$$\Gamma(z) = \int_0^{\infty} x^{z-1} e^{-x} dx. \quad (72)$$

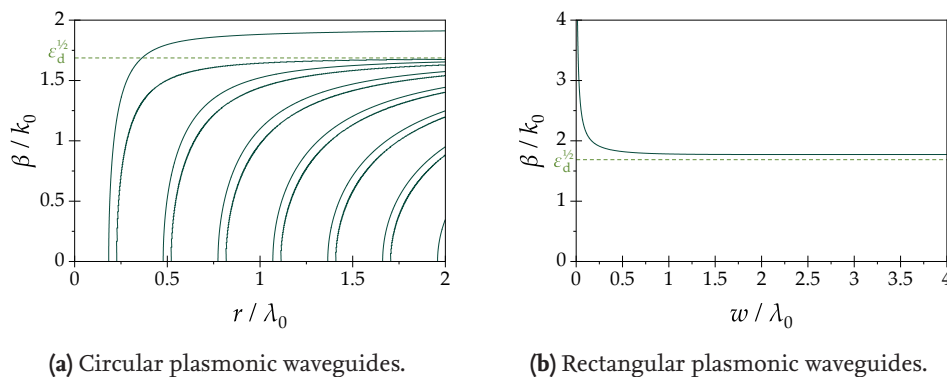


Figure 4.21 – Numerical solutions of the characteristic equations for circular (a) and rectangular geometries (b) of resist waveguides in iridium.

From Equation (69), we can get the characteristic equation for the 0th order TM mode with $v = 0$ by using $I'_0(x) = I_1(x)$ and $K'_0(x) = -K_1(x)$:

$$\frac{\epsilon_1 I_1(\xi_1)}{\xi_1 I_0(\xi_1)} + \frac{\epsilon_2 K_1(\xi_2)}{\xi_2 K_0(\xi_2)} = 0. \tag{73}$$

As the modified BESSEL functions depend on the waveguide radius r , Equation (73) has no analytical solution for r . Thus, we have to determine r numerically for different values of the propagation constant β [166]. Figure 4.21(a) depicts this numerical solution for an example where a circular waveguide made of AZ1505 resist in iridium is illuminated with a wavelength of 532 nm. The plot shows all possible solutions to Equation (73) for waveguide radii r between 0 and 2 times the incident wavelength and for propagation constants β from 0 to 2 times the wavenumber. In this case, only one solution exceeds $\epsilon_d^{1/2}$ and is therefore associated with the propagation of SPPs [166]. In addition, we observe no possible solution for radii below about 97 nm. In comparison, Figure 4.21(b) shows the solution for a rectangular waveguide under the same conditions with different waveguide widths w according to Equation (61). Here, we observe only one solution, which is the excited SPP mode that shows a propagation constant that changes only for small widths.

Another approach to this is the use of FEM simulations to examine the phase delay of circular waveguides with different widths. Figure 4.22 shows the total transmission and the relative phase of the electric field through a circular waveguide depending on its radius. The transmission steadily increases with larger waveguides, but subwavelength structures even down to 100 nm radius still show some transmission. However, plasmonic excitation could not be observed for such small waveguides as in the rectangular case, and the transmission vanishes rapidly below about 60 nm radius. Considering this, we only take radii above 60 nm into account. The relative phase is similar to the numerical solution of Equation (73) shown in Figure 4.21(a), which is plausible when considering the relationship between phase and propagation constant from Equation (63a). Both phase and

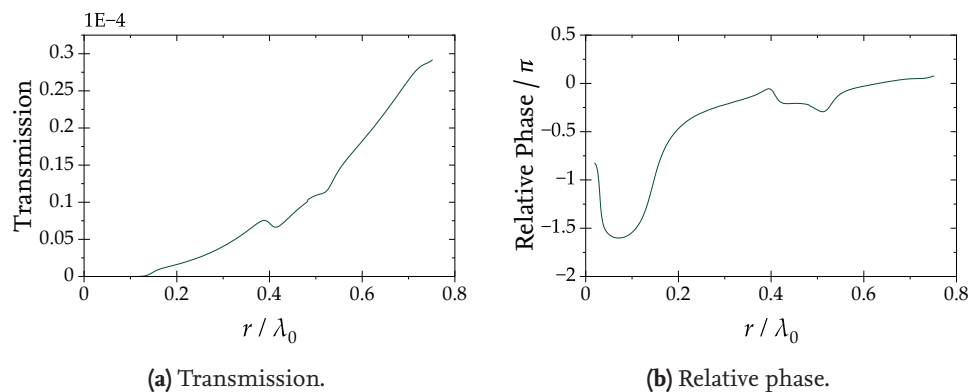


Figure 4.22 – Simulated transmission (a) and relative phase (b) for different geometries of resist waveguides in iridium.

transmission also show some kind of resonance at a radius of around half the incident wavelength which is most likely not caused by plasmonic effects.

The phase delays generated by circular plasmonic waveguides of different radii would be suited for the construction of plasmonic lenses. However, the waveguide dimensions would be significantly larger compared to the rectangular waveguide design. This results in less waveguides per lens area and therefore in a worse control of the local phase, which is adverse for the functionality of the lens.

4.6.3 Merged Plasmonic Lens Design

As explained in Section 4.6.1, the current inverted plasmonic lens design has not enough addressable degrees of freedom to support a dispersion-free design. A quick solution for this using rectangular waveguides of varying widths is proposed in Figure 4.23. By simply merging lenses designed for different wavelengths, the resulting structure would be able to focus these wavelengths to the same focal spot, albeit with some chromatic aberration when leaving the focal plane. Dividing the circular lens area in sections undermines its polarization insensitivity, but a certain symmetry in the division is required to ensure the formation of a symmetric focal spot. The division in four sections per wavelength thus constitutes a compromise between symmetry and polarization insensitivity. Another option is the division into even smaller sections. This would lead to a better performance under arbitrary states of polarization, but it would also significantly shorten the plasmonic ridges, which might adversely affect the phase delay produced by this ridge. As illustrated in Figure 4.23, the sectioning concept could even be transferred to more than two wavelengths per lens, again while losing polarization insensitivity.

As a first step to see if truncating the waveguides impedes the formation of SPPs, I simulated air-filled waveguides in a 200 nm thick silver layer with different lengths and widths,

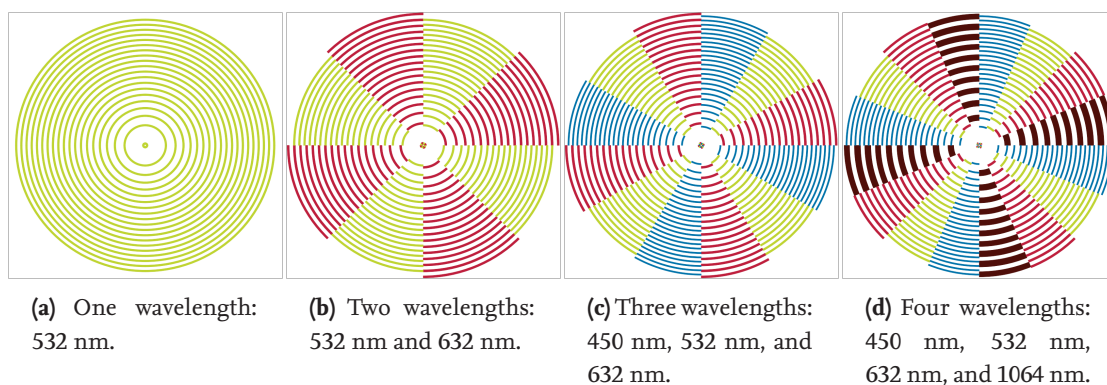


Figure 4.23 – Merged plasmonic lens concepts for one (a), two (b), three (c), and four wavelengths (d).

illuminated at a wavelength of 532 nm. Figure 4.24 shows the intensity and phase of light that propagated through these waveguides, normalized to unobstructed propagation. Following the discussions in Section 4.1, the width of the waveguide is directly connected to the phase of the transmitted light, but these considerations always assume an infinite length. In Figure 4.24(b), we see that only under about 300 nm, the length significantly influences the phase. In addition, the intensity of the transmitted light significantly drops towards shorter waveguides, which is most likely caused by a smaller ratio between waveguide and computational domain area. It should be noted that these simulations were performed for s-polarized light only, preventing SPP excitation along the length of the waveguide, which under illumination with mixed polarization might also happen. Neglecting curvature for now, a ring-shaped waveguide with a circumference of 300 nm would have a radius of about 47.75 nm. For the monochromatic lens designs, most rings apart from the central ridge are longer than this, so waveguide length should be no limiting factor. However, the merged design as proposed in Figure 4.23 cuts the rings to at least $1/8$ of their initial size. For the smaller, inner rings, this might already lead to a diminished functionality.

Examining the influence of ridge curvature, I also simulated 18 nm wide waveguides with a fixed arc length of 900 nm, which should be long enough to not impede its functionality following the results from Figure 4.24, while bending the waveguide to different radii. Curvature is defined as the reciprocal radius of the curve [167]. A curvature of 0 denotes a perfectly straight line (infinite radius), and for an arc length of 900 nm, the largest possible curvature is $6.98 \mu\text{m}^{-1}$, which corresponds to a perfect circle with a radius of about 143.24 nm. Figure 4.25 illustrates different curvatures. Larger curvatures are only

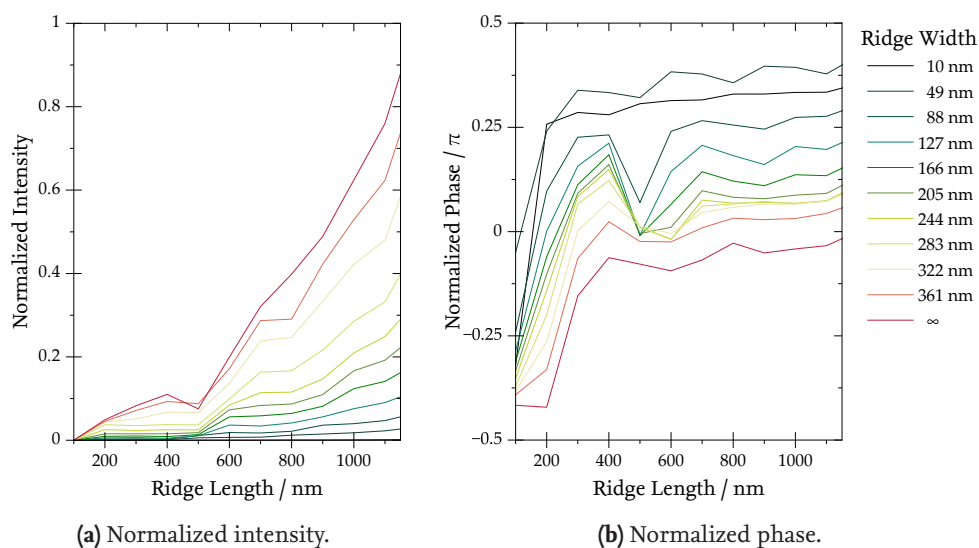


Figure 4.24 – Simulated intensity (a) and phase (b) of light transmitted through 200 nm thick plasmonic waveguides of different lengths and widths.

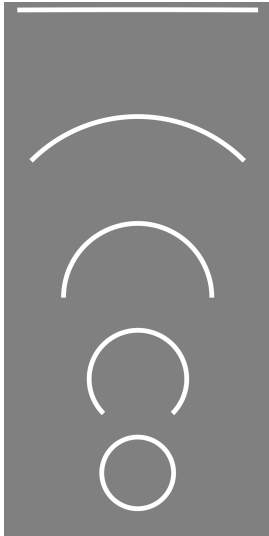


Figure 4.25 – Curved waveguides.

theoretically possible when considering elliptical shapes which are not of interest here. Figure 4.26 shows the transmission and phase of s- and p-polarized light propagating through waveguides of different curvature. The transmission is normalized to the maximum value. As we can see, for a straight line, no s-polarized light is transmitted because only p-polarized light excites SPPs as discussed in Section 4.1. When the waveguide starts to curve, more and more parts of it shift their orientation so that s-polarized light also excites SPPs. For curvatures larger than $3.5 \mu\text{m}^{-1}$, where the waveguide is bent to a semicircle, the decline of p-polarized transmission reaches an inflection point. Further bending of the waveguide also shifts the orientation of parts of it back so that eventually, the amount of p-polarized transmission increases again. In the end, for the full circle, both s- and p-polarized light show the same transmission for reasons of symmetry. The discontinuity right before this

case most likely comes from the small gap between the waveguide ends closing. Similarly, the phases for s- and p-polarized light are the same for the full circle case. In general, phases for both polarization cases don't differ much from each other, but change by up to 0.75π with curvature.

To test these influences in the context of a real lens, a proof-of-concept simulation was necessary to show if a merged plasmonic lens would really diminish the dispersive be-

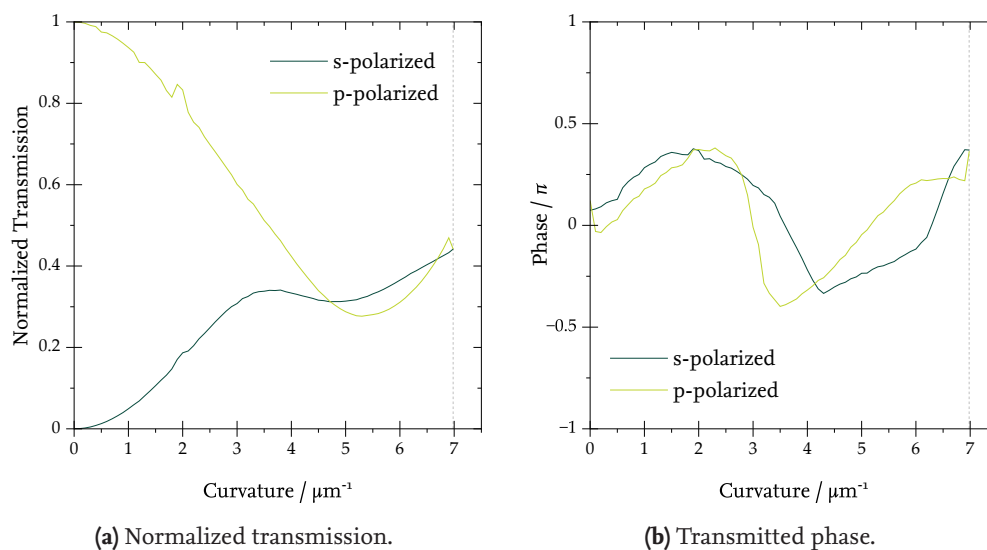


Figure 4.26 – Simulated transmission (a) and phase (b) of light through curved plasmonic waveguides. The dashed line at $6.98 \mu\text{m}^{-1}$ indicates a closed circle.

behaviour. Due to the nature of finite element simulations, performing one such simulation in three dimensions for one of the cases described in Section 4.4.4 takes a high amount of computational resources. Time and memory requirements of these simulations heavily depend on the extents of the computational domain as well as the sizes of the smallest parts of the mesh. Thus, in what follows, we want to observe a minimal proof-of-principle design which allows us to examine how the lens concept described here would perform under different incident wavelengths. As the lens layouts used here are optimized for taking less computational resources, they lack in functionality and generally underperform in terms of focal spot intensity and size. However, their simulations could be carried out in reasonable time and deliver information about the dispersive behaviour of the different lens designs. Figure 4.27 shows the proof-of-concept FEM simulation model of a merged plasmonic lens for two wavelengths, 532 nm and 632 nm, realized using JCMsuite [141]. An in-detail list of the lens parameters is given in Appendix A.6. To minimize the computational requirements of this model, instead of the inverted lens design, the model has dielectric AZ1505 ridges completely embedded in a sheet of iridium. As discussed in Section 4.4.2, this does not impair the functionality of the lens. A focal length of $0.75\ \mu\text{m}$ and an aperture of $5\ \mu\text{m}$ were chosen, as these sizes are still manageable in FEM at acceptable timescales.

Simulations were carried out for incident wavelengths between 507 and 907 nm in steps of 25 nm. As a direct comparison, a lens with the same dimensions but only for a wavelength of 532 nm was also simulated. The circular shape of the lenses guarantees a symmetric behavior of s- and p-polarized light. Thus, we will only compare simulations for p-polarized light in what follows. Figure 4.28 illustrates the results from this simulation, which were gathered by measuring the intensity and position of the produced focal spot from the simulated electric field. In Figure 4.28(a), we observe a reduction of the overall intensity to around 2 % of the incident intensity for the merged lens, compared to the about 5 % of the monochromatic lens. The small values of these intensities are mostly

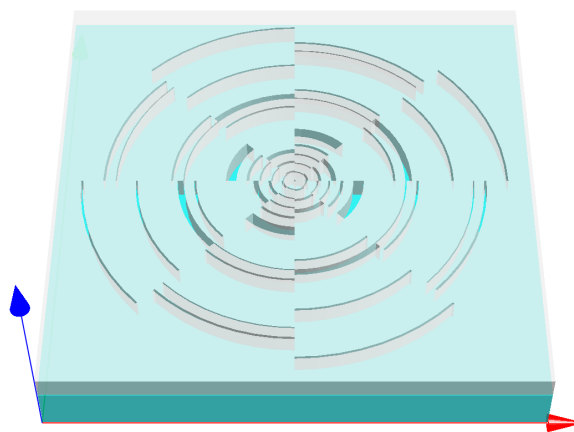


Figure 4.27 – Numerical model of the merged plasmonic lens proof-of-concept.

due to the small aperture of the proof-of-principle geometries, which were only $5\ \mu\text{m}$. The difference between the intensities of the two lenses is assumed to be the result of the previous observations from single waveguides. This effect is also enhanced by the small proof-of-principle geometries. Nevertheless, compared to the monochromatic lens, the merged lens shows a clearly reduced dependence of the intensity on the wavelength. Interestingly, the monochromatic lens has nearly the same intensity for both design wavelengths, but this is only an artifact from the lens having an intensity peak at about $580\ \text{nm}$, which stems from the non-optimized design. The merged two-wavelength lens, however, does not show this peak and therefore has a more uniform response to the wavelength, speaking for this approach at least from the perspective of intensity uniformity. The spot position illustrated in Figure 4.28(b) is more crucial as it represents the lenses' chromatic aberration. As observed in Section 4.5.2, the focal spot shifts closer to the lenses with increasing wavelength. However, this shift is less pronounced for the merged lens compared to the monochromatic lens. Parameters for the parabolic fit are collected in Table A.7 in Appendix A.4. Thus, the merged lens' dispersion is visibly reduced compared to the monochromatic lens, indicating that this approach indeed helps to create achromatic plasmonic lenses, albeit at the expense of spot intensity. Further investigations into the development of working designs are needed, though, as the choice of design wavelengths for optimal dispersion reduction is likely very crucial. Probably, designs with more sections of different wavelengths might also help to further reduce dispersion, again at the expense of intensity. An increasing number of sections might even converge towards a spiral-like design, although this would be highly challenging to fabricate.

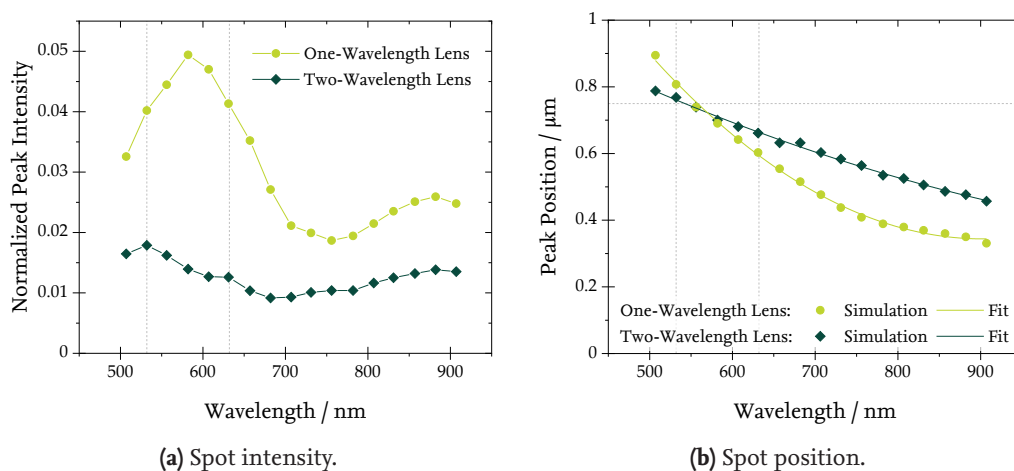


Figure 4.28 – Spot intensity (a) and position (b) of merged plasmonic lens and comparison lens depending on the wavelength of the incident light. Dotted lines indicate design values.

5

Advanced Methods for Imaging Ellipsometry

THE PLASMONIC LENSES FROM CHAPTER 4 HAVE THE PURPOSE TO SERVE OPTICAL NANOMETROLOGY by being designed around their compatibility with both fabrication and integration in ellipsometric setups. For the latter, it is necessary to characterize their polarization properties, a task which naturally links to the measurement methods explored in this thesis. Apart from that, this chapter covers the conceptual integration of plasmonic lenses into ellipsometric setups as well as the numerical evaluation of MUELLER matrix images. Solving the inverse problem is the common way to retrieve geometrical parameters from ellipsometric measurements, but with imaging ellipsometry, simulating the necessarily three-dimensional models is still connected to high computational costs. For this reason, we also look out towards machine learning for inspiration concerning other evaluation approaches. This chapter starts out with MUELLER matrix measurements performed with the methods described in Chapter 3 on the plasmonic lenses introduced in Chapter 4. This is followed by simulations of MUELLER matrix images using FEM as well as a numerical experiment on the applicability of inverted plasmonic lenses in ellipsometric measurements. In the end, we take a look on HAAR-like features of MUELLER matrix images to estimate the benefit of ellipsometric evaluations in the context of machine learning and vice versa.

5.1 MUELLER Matrix Images of Fabricated Plasmonic Lenses

As described in Section 4.1, only TM polarized light can excite SPPs, and light propagating from a plasmonic lens will inevitably be polarized. The lenses introduced in Section 4.4 have a circular design that is supposed to not only create the functionality of a spherical lens, but also make up for the polarization selectivity of the plasmonic waveguides.

The ring-shaped ridges allow for polarized light from arbitrary orientations to generate SPPs and thus to be focused. It is questionable if the central ridge, which in this case is a circular waveguide rather than a curved rectangular one, correctly contributes to the functionality, because circular structures present different SPP propagation behaviour, as seen in Section 4.6.2. Nevertheless, the presence of focal spots in the measurements from Section 4.5.2 is evidence for the functionality of the lenses, as long as they have enough ridges inside their aperture. Now, we want to take a look into their polarization selectivity by taking MUELLER matrix images of the plasmonic lenses. Additionally, we look at a MUELLER matrix focus scan measurement of one lens, with a set of MUELLER matrix images for each focal plane in the measurement series. This way, we can analyze the polarization properties of the lens and its focal spot, which is necessary if the lens should be considered as an optical component used in ellipsometry.

5.1.1 MUELLER Matrix Images at Different Wavelengths

Figure 5.1 shows the MUELLER matrix images of plasmonic lens OS-00 measured at the MUELLER matrix microscope in transmission mode at 455 nm wavelength. Drift correction as described in Section 3.5.3 was not applied yet due to the high structure complexity of the lenses. Effects from thermal drifts appear in this measurement, however, most noticeably in the m_{14} and m_{41} elements, which are more likely to be closer to zero without the drift. As expected, different regions on the lens show different polarizing behavior, depending on their rotation relative to the global orientation of the polarizing system. Averaging the pixels over the lens area only, the mean MUELLER matrix of the lens reads:

$$\underline{M}_{OS-00}(455 \text{ nm}) = \begin{pmatrix} 1.000 & 0.027 & -0.017 & -0.009 \\ 0.074 & 0.399 & -0.007 & 0.006 \\ -0.013 & 0.036 & 0.407 & 0.008 \\ 0.055 & -0.086 & 0.004 & 0.236 \end{pmatrix}. \quad (74)$$

Apart from the main diagonal, the local polarization introduced by the lens vanishes for the most part when averaging over the lens area. Based on this example, Figure 5.1 and its mean values indicate a sufficient polarization neutrality of the inverted plasmonic lenses, despite some depolarization, showing in the main diagonal that differs from 1. Therefore, their potential use in ellipsometric setups is not impaired by the polarization selectivity of SPPs, as intended by constructing the lenses as concentric rings.

Measurements at the EP4 setup were performed to examine the spectral behavior of the lenses' MUELLER matrix for wavelengths from 407 to 807 nm for the same lens OS-00. As an example, Figure 5.2 shows the matrix images of this lens measured at 457 nm wavelength for both measurement methods at this setup according to Section 3.2.2. Overall, these measurements show good agreement between each other and with the results from the MUELLER matrix microscope setup. Figures 5.3 and 5.4 collect the MUELLER matrix images at the different wavelengths averaged over the lens areas for the measurements

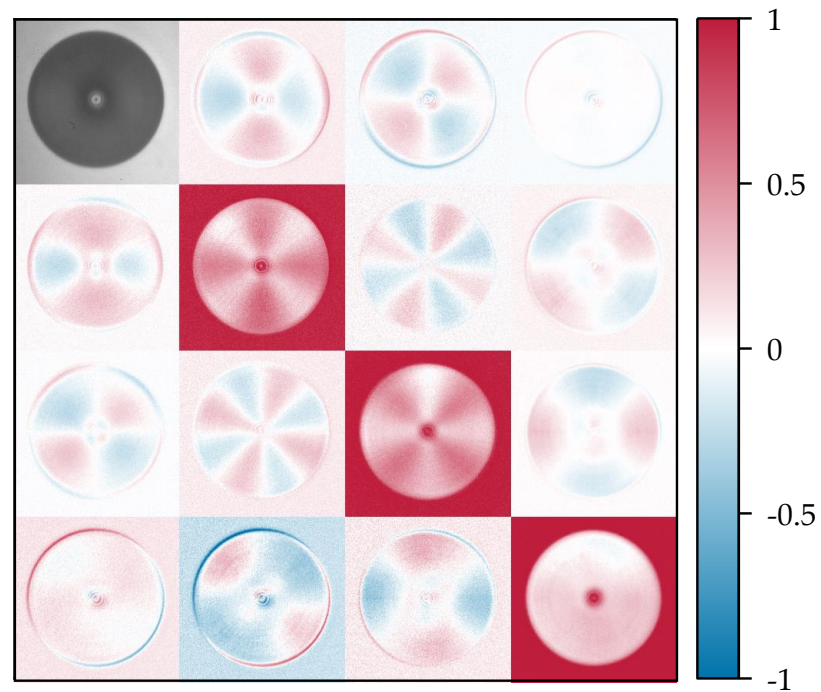
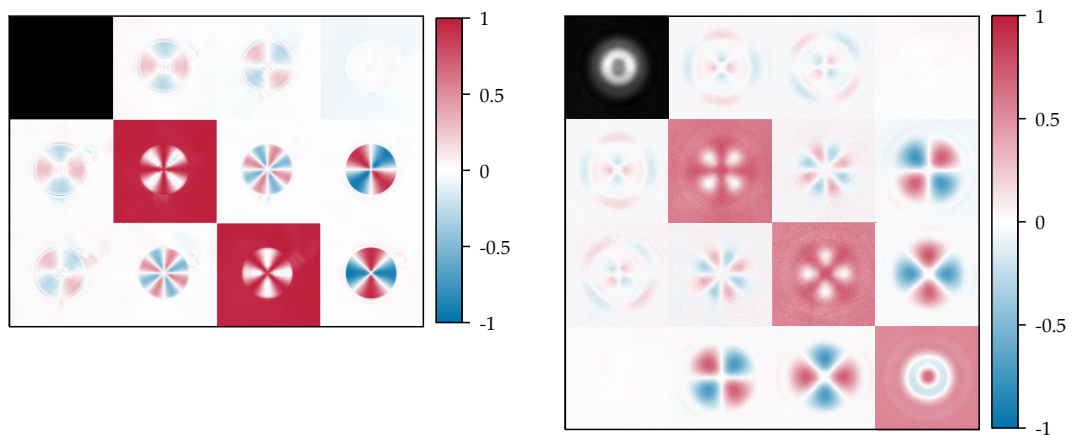


Figure 5.1 – MUELLER matrix image of plasmonic lens OS-00, measured at the MUELLER matrix microscope, without drift correction.



(a) Measurement without second compensator.

(b) Measurement with second compensator.

Figure 5.2 – MUELLER matrix image of plasmonic lens OS-00, measured at the EP4 setup at 457 nm wavelength in PCSA (a) and PCSCA configuration (b).

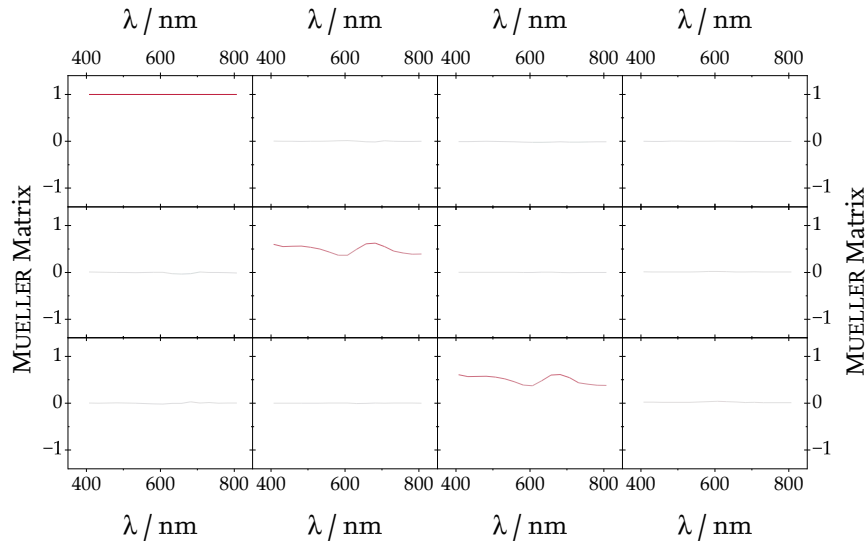


Figure 5.3 – Mean MUELLER matrix images of plasmonic lens OS-00, measured at the EP4 imaging ellipsometer without second compensator (PCSA), averaged over the lens area.

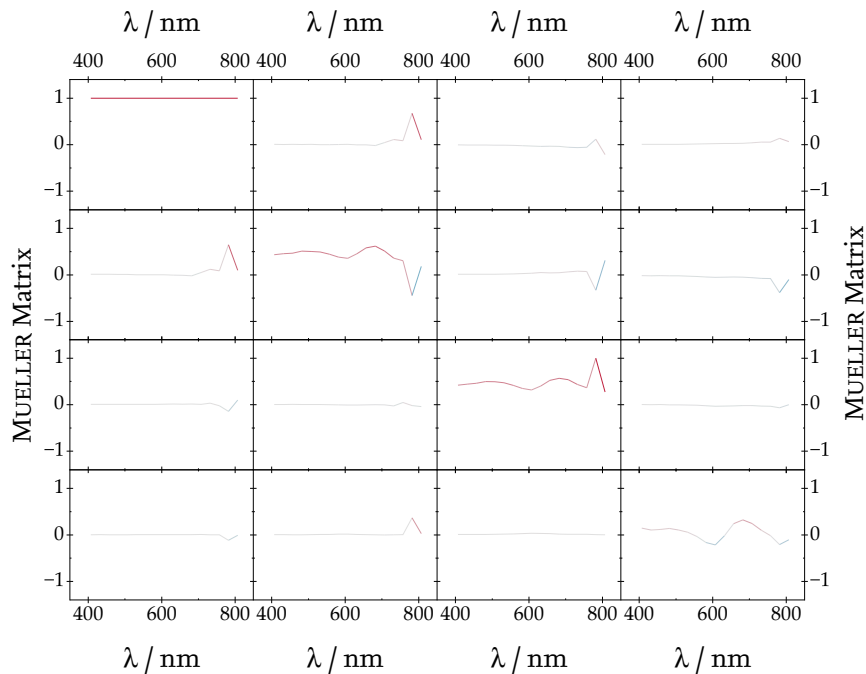


Figure 5.4 – Mean MUELLER matrix images of plasmonic lens OS-00, measured at the EP4 imaging ellipsometer with second compensator (PCSA), averaged over the lens area. The outlier at 782 nm stems from high noise in the images due to low transmittance at this wavelength.

without and with second compensator, respectively. Comparable to the measurement from the MUELLER matrix microscope at 455 nm wavelength, we see that the mean values show no major influence of the whole lens on the polarization, apart from some depolarization. Slight changes with the wavelength are observable, but as the lens was optimized to work at only one wavelength, a wavelength dependency was expected. It is most prominent on the main diagonal in Figure 5.4 and follows the observations made in Section 4.5.2 about the dispersion of the lenses. Additionally, Figure 5.2(b) suggests that the lens was out of focus during the measurements. Figure 5.5 further illustrates this by showing the standard deviation of the first matrix element over the wavelength. Just as with the TSOM measurements in Section 4.5.2, we see a peak in the standard deviation, indicating a shift of the focal plane. The reason for this is the long term measurement series during which these images were taken, revealing a drift of the structure out of focus during longer time periods, even at the more stable EP4 setup. The impact of focal shifts is further discussed in Section 5.1.2. MUELLER matrix images for the other wavelengths are collected in Appendix B.2.

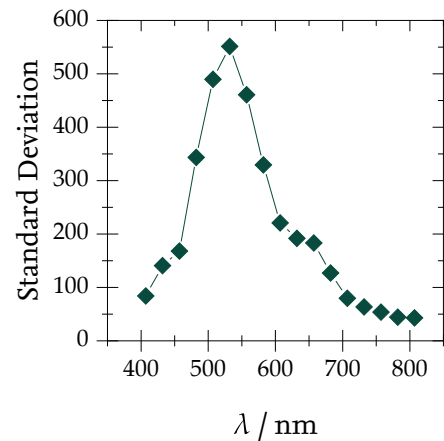


Figure 5.5 – Standard deviation of the first matrix element measured in PC-SCA configuration.

5.1.2 MUELLER Matrix Images at Different Focus Positions

In Section 5.1.1, we saw that for long term measurements, samples examined at the EP4 setup might drift out of focus of the imaging system. Thus, it is reasonable to investigate how much the focus of the recorded images affects the measured MUELLER matrix images. Additionally, to assess the usability of the lenses in ellipsometric setups, we need to evaluate the polarization of the resulting focal spot. As described in Section 4.5.2, the focal distance of the fabricated plasmonic lenses was verified via TSOM. In a similar way, the polarization of the focal spot was evaluated by performing MUELLER matrix through-focus scan measurements on lens OS-21 at its intended wavelength of 532 nm. For each focal plane in a range of $\pm 200 \mu\text{m}$ around the focused image of the lens, MUELLER matrix images were recorded, leading to 16 individual image stacks, each representing a focus scan series of one specific MUELLER matrix element.

Figure 5.6 shows the mean MUELLER matrix images per focal plane and the respective standard deviations. Like in Section 5.1.1, we can see from Figure 5.6(a) no major influence of the focal plane on the mean MUELLER matrix elements. The standard deviations in Figure 5.6(b), however, were affected by the focus scan. The first matrix element doesn't show up because of normalization. In all the other matrix elements, the central peak of the focused image of the lens is clearly visible, but the other two side peaks observed in

Section 4.5.2 are mostly missing. In some elements, especially m_{10} and m_{11} , there is a shoulder to the left of the central peak, but it is too close to be from the focal spot. In other elements, most noticeably those in the last row or column, small dips very close to the design focal length are observable. Thus, focused images are very clearly recognizable from MUELLER matrix images, but while the focal spots are slightly visible in the standard deviation, their polarization should be sufficiently uniform for polarimetric means.

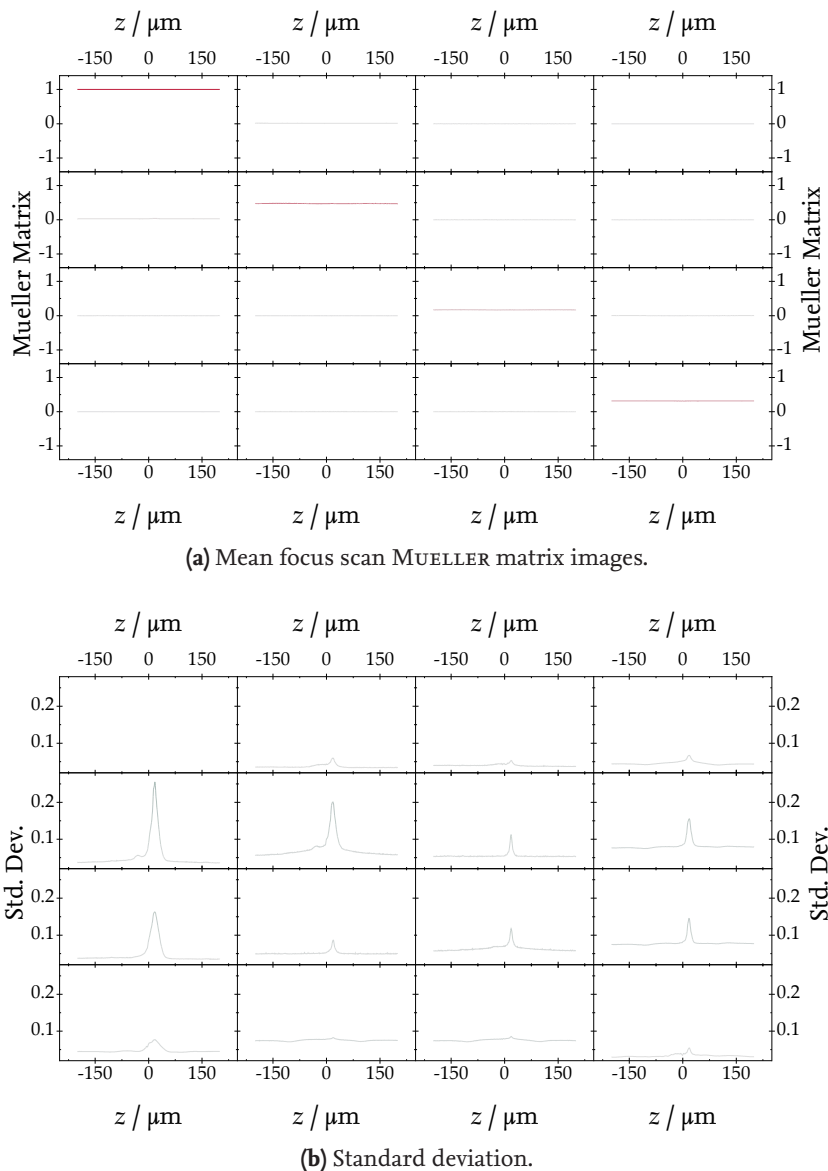


Figure 5.6 – Mean MUELLER matrix images per focal plane (a) and respective standard deviations (b).

5.2 Numerical Simulations of MUELLER Matrix Images

Ellipsometry relies on the solution of the inverse problem: By performing numerical simulations with varying parameters and comparing them with measurement results, the geometrical properties of the structure under investigation are successively determined. While this process is widely used and its implementations are generally fast, numerical models are usually defined in two dimensions only. Two-dimensional models are evaluated quickly, with single simulations taking rarely more than a second. The computational costs of such simulations, their duration and memory usage, strongly depend on the sizes of the computational domain, the mesh, and the layers present in the model, as well as on the wavelength. More complex structures necessitate higher computational costs.

For imaging ellipsometry, the logical step would be to use three-dimensional models for the inverse problem, as in the example in Figure 5.7. Structures like those from the nanoform sample (Section 3.3) are simply impossible to model in two dimensions only. Nevertheless, even for commercial imaging ellipsometry setups, measurement evaluation is usually realized by averaging over regions of interest (ROIs) in the image and then evaluating the mean matrix values like in conventional ellipsometry. This is easily done and compatible with existing tools, but it also neglects most advantages of imaging ellipsometry, apart from choosing more refined ROIs than would be possible without imaging. In the example of singular structures as on the nanoform sample, we could just use average values of ROIs inside and outside the structure to determine, e.g., the depth of the structure or the material composition of its surrounding. However, edge and corner effects as observed in Section 3.4 and the structural information coming with them would be completely unused. Only when solving the inverse problem with three-dimensional models, these effects are correctly accounted for and contribute to the parameter reconstruction of the sample. On the downside, three-dimensional simulations require high computational costs, making them unattractive for larger geometries or parameter spaces.

The simulation of MUELLER matrix images forms a necessary step towards the solution of the inverse problem in imaging ellipsometry. This section discusses the numerical simulation of MUELLER matrix images of the samples introduced in this thesis and the challenges related to them. In addition, we will look on simulated MUELLER matrix images in combination with plasmonic lenses to estimate the lenses' influence on an ellipsometric measurement.

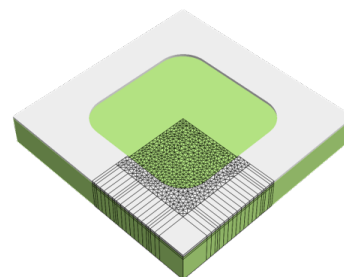


Figure 5.7 – Example for an FEM model of a structure from the nanoform sample.

5.2.1 Simulated MUELLER Matrix Images of the Nanoform Sample

For a direct comparison, simulations of the structures from the nanoform sample were performed with JCMSuite [141]. Figure 5.7 illustrates an example for a model used in the FEM simulations. It has the same dimensions as specified in the design in Section 3.3. The source was defined as a plane wave with 0° incidence from above at a wavelength of $\lambda_0 = 455$ nm. The use of multiple pupil points per illumination source was considered but rejected. As the measurement system works with nearly collimated light, going from a plane wave illumination to multiple pupil points would only lead to disproportionately longer simulation times. The MUELLER matrix images were simulated by computing several microscope images of the sample at different STOKES vectors for the illumination and then using these to derive the MUELLER matrix elements pixelwise [105]. Figure 5.8 shows examples of the simulated MUELLER matrix images for the same structures as in

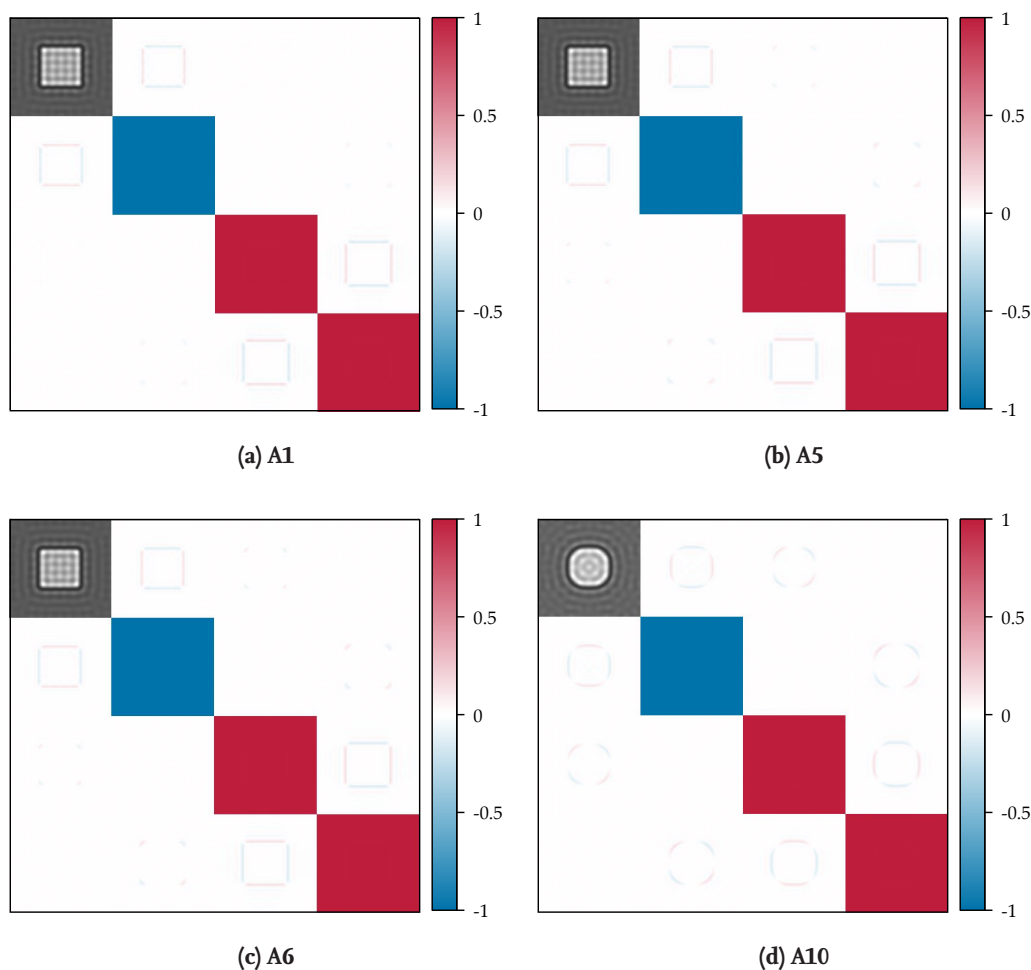


Figure 5.8 – Simulated MUELLER matrix images of structures A1 (a), A5 (b), A6 (c), and A10 (d) from the nanoform sample. Further images are given in Appendix B.1.3

Figure 3.17 in Section 3.4.1. Although the measurements were performed in the perpendicular incidence reflection mode, the measured images resemble those of transmission measurements, because the light passed a couple of mirrors on its way to the camera, switching the sign of corresponding matrix elements each time. The simulation does not take these mirrors into account. Therefore, some simulated MUELLER matrix elements show the opposite sign compared to the measurements, which is most prominent in the m_{22} element. Figure 5.9 collects selected measured and simulated MUELLER matrix images for an easier comparison. Measurements from the EP4 setup are not considered here as the simulations used the same perpendicular incidence illumination as the MUELLER matrix microscope setup. Thus, the oblique angle of incidence from the EP4 setup hinders a direct comparison to the simulation results. Again, we see distinct polarization effects at the edges and in the corners of the structures in the drift corrected images. These effects are confirmed by the simulated images, which show the same kinds of effects in the same matrix elements as the drift corrected measurement, besides the mentioned sign difference. Therefore, it is legitimate to assume that these effects do not stem from sample movements from, e.g., thermal drifts alone and are indeed inherent responses from the structures themselves. Furthermore, both measurement and simulation are in good agreement after drift correction, which means that the suppression of drift influences by algorithmic means is a viable strategy. The only challenge that remains here is that the drift correction algorithm has to detect structures in the images to work, which has to be done on a case-by-case basis.

Concerning their metrological use, we want to take a closer look on the additional information delivered by off-diagonal matrix images. With the examples of elements m_{00} and m_{13} in Figure 5.9, we see that the microscope images of structures **A1** and **A5** are barely distinguishable. Their only difference is a change of their corner radius from 100 nm to 400 nm, which is a feature difference smaller than the resolution of the imaging system of about 800 nm [102]. However, in element m_{13} , this change is evident from the absolute value of the matrix element in the corners. We see that corners have different signs depending on their orientation. By computing the mean matrix element values in each quadrant of the image and then further averaging the values of the quadrants with the same sign, we can obtain the mean difference between the absolute values in the different corners. Figure 5.10 collects these quadrant mean value differences for element m_{13} for both measured and simulated matrix images. The results are plotted over the ratio between the corner radius and the structure width, which is 5 μm . Thus, a corner ratio of 0 represents a perfect square while a ratio of 0.5 would be a perfect circle. We see a clear correlation between the corner radius and the absolute values of the matrix element in the corners. In the measurements, it is highly influenced by noise, but it follows the same trend as the simulations. Going from **A1** to **A5**, the absolute value of the matrix element in the corners changes by 15 % in the measurements and by 85 % in the simulations. The change from **A5** to **A10** is with about 160 % in both measurements and simulations even more pronounced. Other off-diagonal matrix elements also show a sensitivity of the ab-

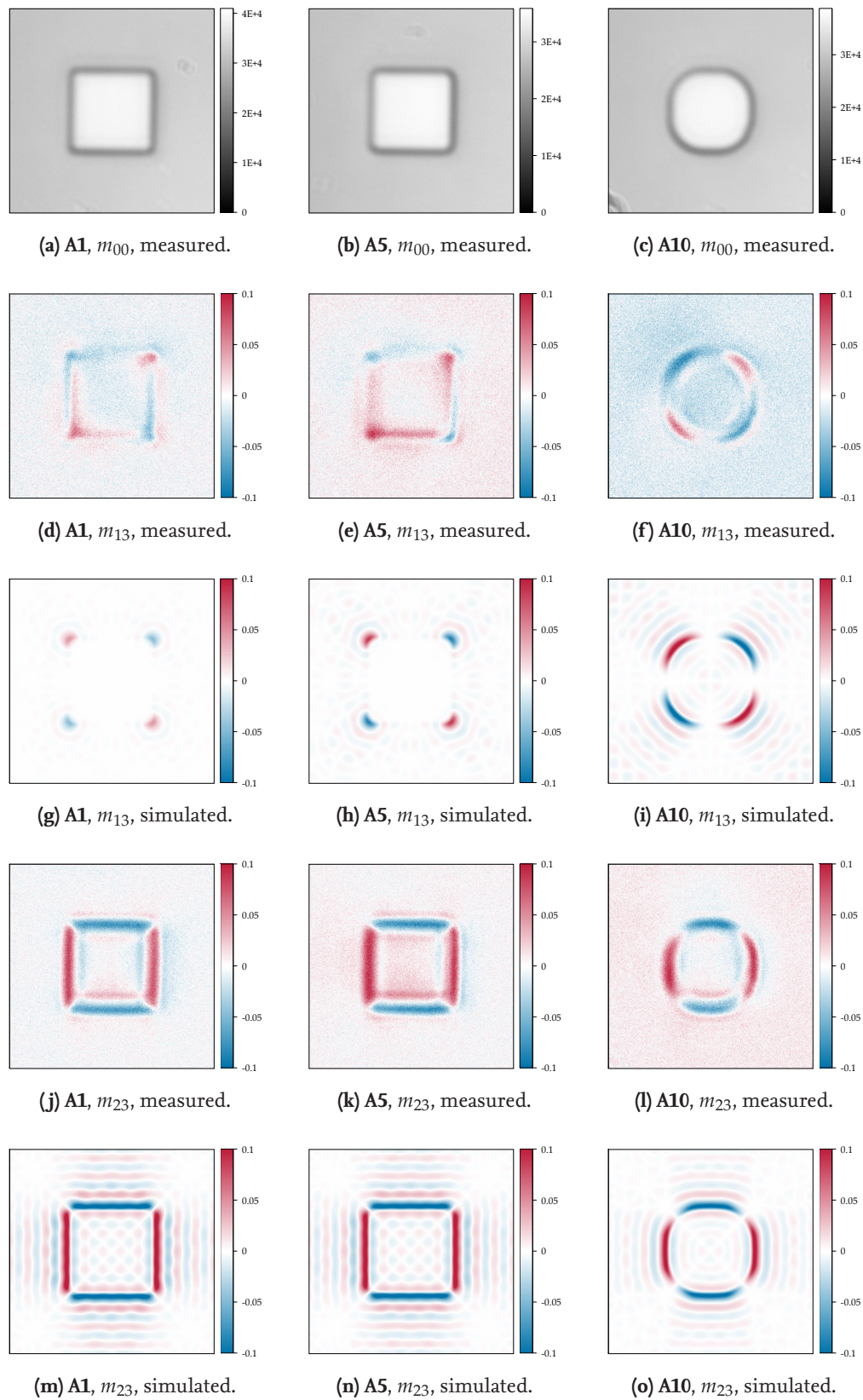


Figure 5.9 – Selected measured and simulated MUELLER matrix images m_{00} (a - c), m_{13} (d - i), and m_{23} (j - o).

solute values in the corners or on the edges of the structures on the corner radius. Thus, local geometry features like the orientation of an edge or the curvature of a corner do have significant connections to the local MUELLER matrix, even for sub-wavelength sized feature changes. These offer information channels exceeding those of microscopy or ellipsometry alone, making the model-based evaluation of the measurements promising for structural parameter retrieval [115, 121].

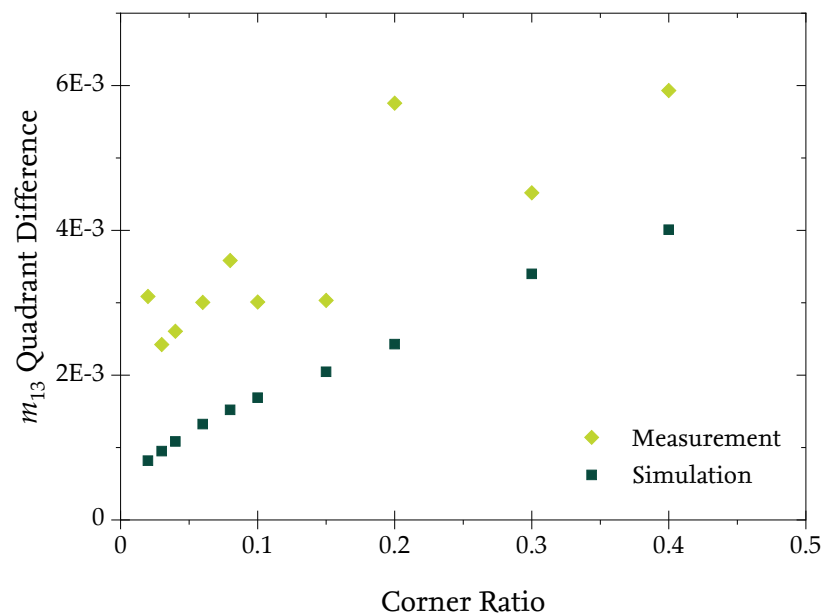


Figure 5.10 – Quadrant mean value differences for element m_{24} for both measured and simulated matrix images.

5.2.2 Plasmonic Lens Supported Ellipsometry Simulations

Imaging ellipsometry, as a tool for the local examination of polarizing properties, is suitable even for non-periodic samples. As such, advancing the system not only from the evaluation point of view, but also its hardware, would bring benefits to optical nanometrology. Research on making ellipsometric systems more compact is currently on-going and focuses mostly on using metastructures to replace bulky optical components [168, 169]. After examining design strategies for plasmonic lenses that facilitate the fabrication process in Chapter 4, we now want to take a look on the integrability of plasmonic lenses in ellipsometric setups. The idea is to implement lenses with short focal lengths and small spots by, e.g., replacing the focusing optics on the illumination side of the ellipsometer. From the results in Section 5.1, we know that the lenses provide sufficient polarization neutrality to allow for this kind of illumination. The shorter focal lengths would help to make the setup more compact, while the closer placement to the sample might lead to a higher sensitivity to topological information, maybe in extreme cases even from near-field interactions. The much smaller focal spots produced by plasmonic lenses could also be scanned over the sample, so that even in non-imaging use cases, a SNOM kind of scanning ellipsometry with possibly sub-wavelength resolution could be realized.

As a proof-of-concept, I performed two-dimensional numerical simulations of a single gap of varying width in a 500 nm thick layer of silicon. The gap was illuminated by a plane wave with a wavelength of 532 nm. Figure 5.11(a) shows a sketch of the simulation layout for this. Similar to the simulations in Section 5.2.1, one-dimensional MUELLER matrix images were computed for this structure for different widths of the gap in the silicon layer in transmission. The results for this are collected in Figure 5.11(b). In the m_{00} element, we see that light can only really pass through the gap when its width comes close to the wavelength of the incident light. However, we already see strong effects in the MUELLER matrix images, even for widths below the wavelength. Towards the sides, stripes show up, which are most likely caused by the numerical floating point accuracy.

Next, a plasmonic lens is inserted at focal distance to the gap in the illumination side, as shown in Figure 5.11(c), so the light is focused on the gap. The lens has the S-01 design as specified in Section 4.4.4, so it has a focal length of 5 μm with an aperture of 50 μm and is optimized to work at 532 nm wavelength. After inserting, the gap is now visible in the m_{00} element even well below the wavelength and the effects in the other matrix elements are much more pronounced and stretched over the whole image, as depicted in Figure 5.11(d). Except for the mentioned stripes, the MUELLER matrix images in the upper left and lower right quadrant now show a clear dependency on the gap width. Further analysis towards this, especially how a lateral scan of the focal spot might enhance correlations between structure size and the MUELLER matrix, are requisite.

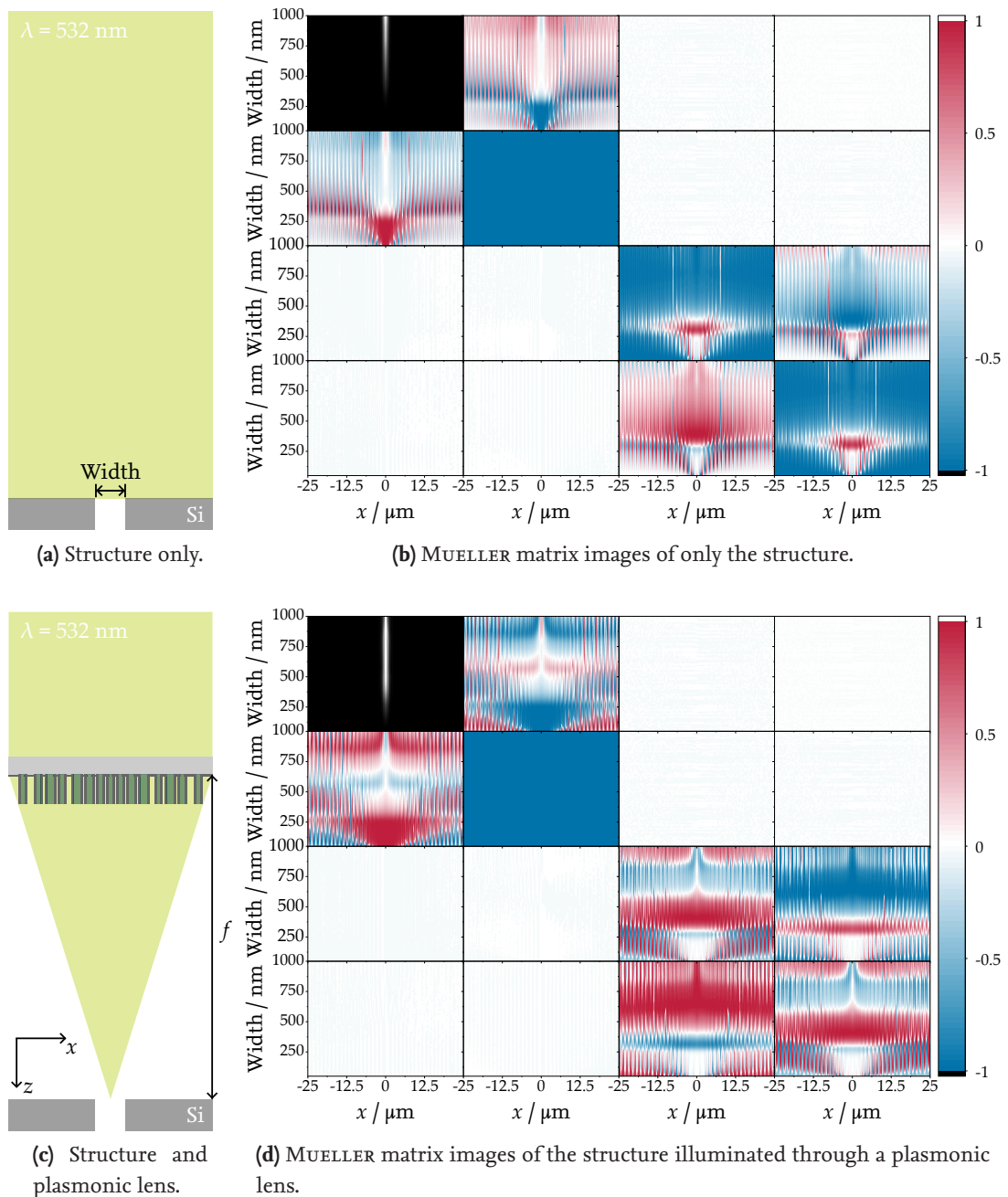


Figure 5.11 – Simulation layout and results for the plasmonic lens supported ellipsometry concept, without (a, b) and with a plasmonic lens (c, d).

5.3 Machine Learning Concepts for MUELLER Matrix Images

Over the last years, the importance of machine learning in research and development drastically increased. Some attempts have also been made to use artificial intelligence in the fields of ellipsometry and scatterometry, which is a natural development considering the large number of simulations that usually have to be performed to solve the inverse problem [170, 171, 172, 173, 174]. These applications however usually focus on the evaluation of conventional ellipsometric measurements. But typically only certain areas of the sample are of interest, and especially when dealing with nanostructures, the distinction between individual structures and whole sample areas becomes crucial. In some cases, it might not be evident from a microscope image alone which areas are relevant for further inspections. This is where imaging ellipsometry is helpful. MUELLER matrix images have proven to be useful to distinguish structures which look similar in pure microscope images. A potential field of application for this is defect inspection, e.g. when trying to classify pyramidal defects on GaN surfaces for modern compound semiconductor devices used in power electronics [175]. Thus, it is reasonable to use MUELLER matrix images in object detection frameworks where the algorithm fails to detect structures based on the microscope image alone due to the high similarity between different structures. In this section, we want to approach this topic not from the view of the inverse problem in ellipsometry, but starting with how images are usually treated in machine learning, and try to apply general object detection algorithms to MUELLER matrix images.

5.3.1 Wavelets and Features

Digital images are made of pixels with different values. Looking at smaller subsets of images, their pixel values can show recurring patterns, which are referred to as features. In face recognition, images are usually analyzed for certain features, the most common ones being so-called HAAR-like features. They derive from HAAR wavelets, which are the simplest possible wavelets. Mathematically, they are constructed from a fundamental wavelet function [176]:

$$\psi(x) = \begin{cases} 1 & 0 \leq x < \frac{1}{2}, \\ -1 & \frac{1}{2} \leq x < 1, \\ 0 & \text{else.} \end{cases} \quad (75)$$

From this, the HAAR function is constructed:

$$\psi_{u,v}(x) = 2^{\frac{u}{2}} \psi(2^u x - v), \quad u, v \in \mathbb{Z}, \quad x \in \mathbb{R}. \quad (76)$$

Figure 5.12 shows examples for different HAAR wavelets. Similar to these wavelets, HAAR-like features are defined as certain patterns of lighter and darker valued pixel areas. Most commonly, a set of five different HAAR-like features, presented in Figure 5.13, is used.

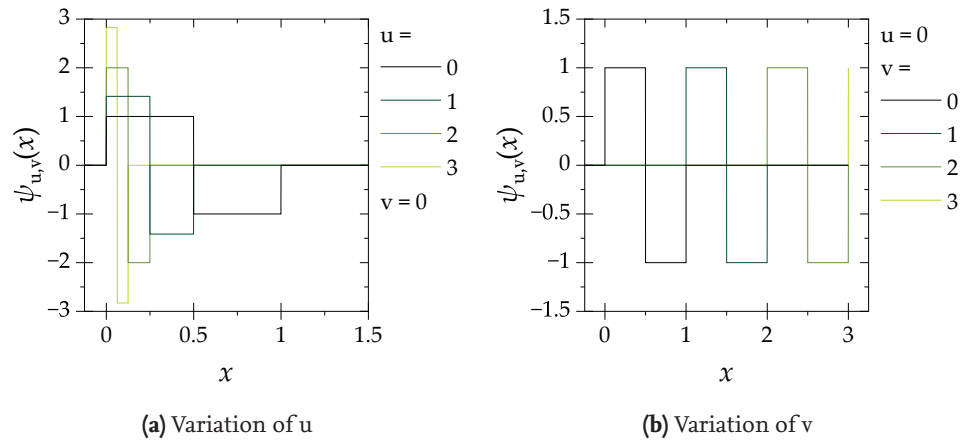


Figure 5.12 – Examples for HAAR functions with different parameters u (a) and v (b).

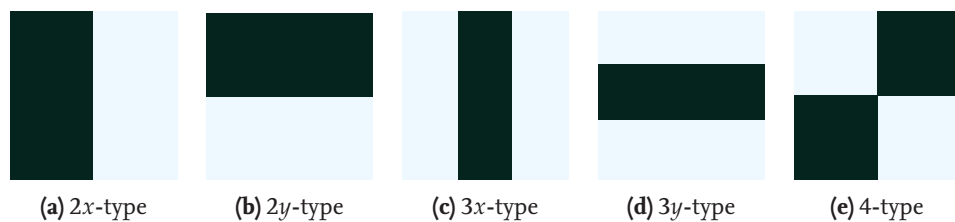


Figure 5.13 – HAAR-like features with two- (a, b), three- (c, d), and four-fold division (e).

These features are characterized by their symmetry type. For example, the 2x- and 2y-type features in Figures 5.13(a) and (b) describe a light area next to a dark area, with an either vertical or horizontal interface, respectively. A feature's numerical value is given by the difference between the sums of all pixel values in the lighter and darker areas. The most prominent use of HAAR-like features is the VIOLA-JONES algorithm. It detects objects in grayscale images after being trained on labeled images as a training set [177, 178].

5.3.2 Application to MUELLER Matrix Images

HAAR-like features are widely in use to detect objects or faces in images. They reduce complex images to a set of recurring patterns that especially highlight local contrast changes, which is useful in image classification. In Section 5.2.1, we observed measured and simulated MUELLER matrix images of the nanostructures described in Section 3.3. These images presented symmetries that resemble those of HAAR-like features. Thus, examining these features of MUELLER matrix images might help in the detection and localization of edges or corners of non-periodic nanostructures.

As a test for the sensitivity of HAAR-like features on subwavelength sized changes of the structure, I computed the features from Figure 5.13 for each subset of pixels in each simulated MUELLER matrix image of nanoform structures with corner radii up to 400 nm. Although the simulated images used in this analysis had a size of only 21 by 21 pixels, the number of possible subsets is quite large¹. Algorithms like VIOLA-JONES deal with this issue by using integral images and further machine learning techniques [178]. For now, we want to focus only on the values of the most prominent features of each type. Figure 5.14 shows these values for each MUELLER matrix element depending on the corner radius of the structure. Due to structure symmetry, values for x - and y -type features are mostly identical, except for the $3x$ - and $3y$ -type features in the matrix elements m_{01} and m_{10} as well as m_{23} and m_{32} , where they change places respectively. The m_{00} element, which mostly represents the overall image intensity, shows comparably low feature values, connected to the contrast of the structures. Furthermore, with a mean of 0.005 to 0.007 per nanometer, the feature values only change marginally with the corner radius. In the other matrix elements however, a higher sensitivity to the corner radius can be observed. The most prominent influence shows up in the m_{13} and m_{31} elements, where the 4-type feature nearly doubles over the corner radius range with an about four times enhanced mean change per nanometer of 0.028. Other elements also show an enhanced sensitivity, illustrated by

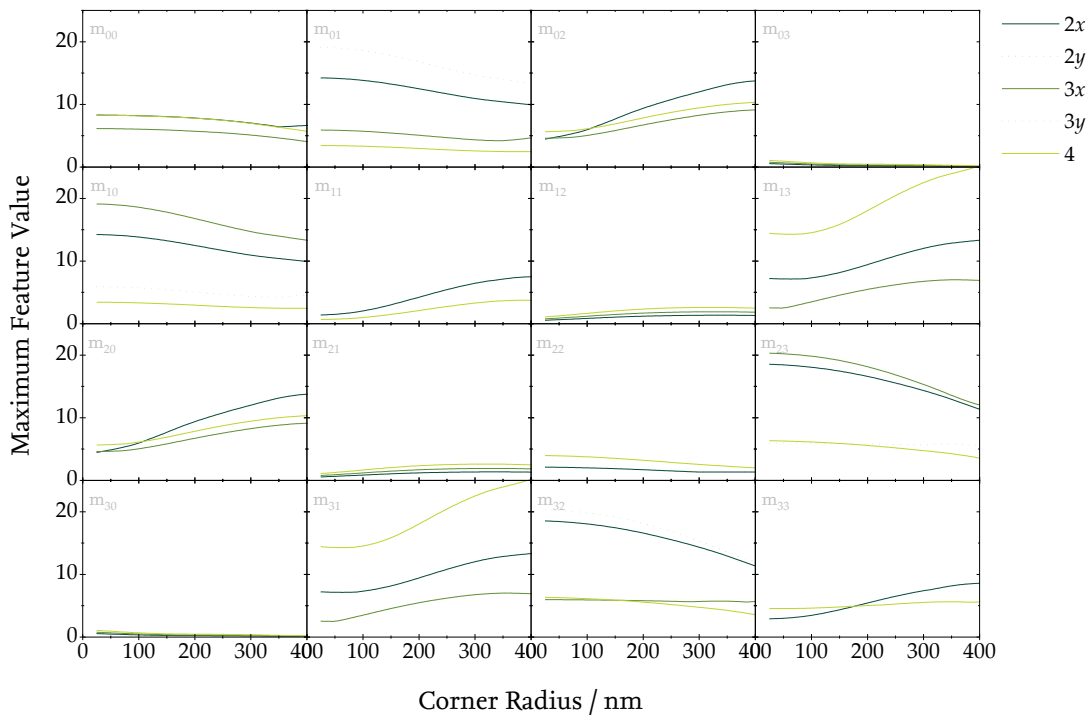


Figure 5.14 – Most prominent feature values depending on the corner radius.

¹The number of all possible image subsets of a $u \times v$ pixel sized image can be calculated by $\sum_{y=1}^v \sum_{x=1}^u (x \cdot y)$, which is 53361 for a 21 by 21 pixel sized image.

Table 5.1, which collects the mean changes per nanometer for each matrix element and all five feature types. The results indicate that MUELLER matrix images enable a higher receptivity for local feature changes compared to microscope images alone and that a more complete analysis of HAAR-like features in MUELLER matrix images is a promising approach for the application of machine learning techniques in ellipsometry [179].

Table 5.1 – Mean change of maximum HAAR-like feature values per nanometer.

type	m_{00}	m_{01}	m_{02}	m_{03}	m_{10}	m_{11}	m_{12}	m_{13}
$2x$	0.005	0.011	0.022	0.001	0.011	0.015	0.002	0.015
$2y$	0.005	0.011	0.022	0.001	0.011	0.015	0.002	0.015
$3x$	0.006	0.007	0.011	0.002	0.015	0.016	0.003	0.011
$3y$	0.006	0.015	0.011	0.002	0.007	0.016	0.003	0.011
4	0.008	0.003	0.011	0.002	0.003	0.008	0.004	0.028
type	m_{20}	m_{21}	m_{22}	m_{23}	m_{30}	m_{31}	m_{32}	m_{33}
$2x$	0.022	0.002	0.002	0.020	0.001	0.015	0.020	0.014
$2y$	0.022	0.002	0.002	0.020	0.001	0.015	0.020	0.014
$3x$	0.011	0.003	0.000	0.021	0.002	0.011	0.002	0.001
$3y$	0.011	0.003	0.000	0.002	0.002	0.011	0.021	0.001
4	0.011	0.004	0.005	0.009	0.002	0.028	0.009	0.003

Conclusion

IN THIS WORK, I DISCUSSED WAYS TO IMPROVE ON IMAGING MUELLER MATRIX ELLIPSOmetry measurements and showed that they are able to reveal topological information about nanostructures, even below the diffraction limit, that would be lost in conventional ellipsometry or light microscopy alone. In doing so, I proved that for the optical examination of individual nanostructures or structured fields smaller than the illumination area, imaging ellipsometry is indispensable for modern nanometrology.

The observed effects in MUELLER matrix images are largely dependent on the shape and size of the structures, which I systematically observed on a set of specifically designed nanostructures. These structures consist of basic geometrical shapes with feature parameters varying in ranges from 50 nm to 5 μ m. Local polarization effects were apparent in MUELLER matrix images taken at both imaging ellipsometry setups used for the measurements. Therefore, these effects, which bear information from the subwavelength regime, are accessible in measurements, but at the same time, they are usually disregarded in favor of evaluation simplicity. Using simulated MUELLER matrix images, I showed that, when used in a machine learning context, images of off-diagonal matrix elements provide information exceeding those of microscopy images alone, which strengthens the potential combination of MUELLER matrix ellipsometry with machine learning techniques. This might be achieved either by using neural networks instead of inverse problem solving for faster evaluations of the measurements or by using the additional information from MUELLER matrix images for a better object recognition. Similar approaches are currently emerging in biological areas of application like cancer detection (e.g., [180, 181]), and the results from this thesis are most likely to help establishing this kind of evaluation also in metrology. Either way, the results show that three-dimensional numerical simulations are not inevitable and that methods which are already used in other fields can help to evaluate local polarization effects. A more complete examination of MUELLER matrix images, especially in combination with faster ways to access the structural information they contain, will unlock the potential of imaging ellipsometry not only for metrological applications, but also in industrial areas. Possibly, methods like these can be applied in fields like defect inspection, where a fast evaluation of imaging ellipsometry measure-

ments will help to both find and characterize defects on samples and wafers. Apart from the evaluation, a stable image acquisition is key for the success of imaging ellipsometry. A thermally induced drift of the samples was observed during the measurements in this thesis. While these drifts are usually not an issue in conventional ellipsometry due to homogeneous areas under investigation, I demonstrated that sample movement during the measurement, e.g. due to thermal drifts, might induce effects in MUELLER matrix images that can be misinterpreted for sample influences and therefore pose a potential source of uncertainty. This has repercussions for applications of imaging ellipsometry, for example in biological fields where the samples under investigation are more prone to deliberate movements. Thermal drifts are usually suppressed by stabilizing the laboratory environment or by speeding up the measurement process. As an alternative, I proposed the application of algorithmic image stabilization techniques based on edge detection methods. This algorithmic approach has the advantage of being universally implementable even in already existing setups that weren't optimized in regards of high stability or speed without requiring costly modifications. Using this, the measurements in this thesis could successfully be corrected for the sample drift so far that the measured images are in good agreement with numerical simulations of the structures. This verified both, the algorithm being capable of eliminating thermal drifts from the measurements as well as the remaining polarization effects indeed stemming from the structure under investigation and not being remnant of the drift.

As another approach to advance modern ellipsometry, I investigated the use of plasmonic lenses as focusing metastructures. For this purpose, I developed a workflow for the design and optimization of plasmonic lenses using numerical simulations based on FEM in combination with optimization algorithms. This enabled the design of plasmonic lenses with nearly arbitrary focal lengths. The optimization process involved in this was based on particle swarm optimization, which was chosen due to its typically fast convergence. Later, Bayesian optimization turned out to be better suited for multi-dimensional parameter optimization problems [182]. It proved to be advisable to refer to these kinds of optimization techniques, although for the rather low-dimensional problems shown in this thesis, PSO was more than sufficient. In addition to the design workflow, I invented the inverted plasmonic lens, a new concept for plasmonic lenses where, instead of milling slits into a slab of metal, dielectric ridges are coated with a thin layer of metal. This way, these lenses can be fabricated by means of electron beam lithography and atomic layer deposition, making them available for fabrication without the need for focused ion beam milling and thus enabling higher fabrication rates for possible future industrial productions. This also weakens one of the advantages of dielectric meta-lenses over plasmonic ones, namely the lower fabrication complexity. Furthermore, I could show that, for the lenses to work, they do not require a periodic placement of the ridges as is common in current literature. Instead, I proved that by placing the ridges in a successive manner, not only the same focal spots were produced, but the throughput of the lenses could be maximized. This, too, helps plasmonic lenses staying competitive compared to dielectric

meta-lenses. The intensity of the focal spot produced by plasmonic lenses still forms a major challenge, which however might be addressed already by larger sized lens apertures. Several different lenses with focal lengths from only 5 μm up to 1 mm at wavelengths between 455 and 1550 nm were fabricated and examined for their polarization using imaging MUELLER matrix ellipsometry, which was the ideal tool for this as the lenses were too small to be analyzed in conventional ellipsometry. Yet, it was important to characterize their polarization properties to test their suitability for applications in ellipsometric setups. I showed that the concentric rings of the plasmonic lenses indeed produced focal spots at the expected distances without changing the polarization of the source except for a small amount of depolarization. Concerning the application of plasmonic lenses in ellipsometric setups, I showed that when used to focus an illuminating plane wave on a sample, the sensitivity to even subwavelength sized gaps could be enhanced significantly. Together with the observed small focal spot sizes, the lenses could potentially be used in stitching or scanning type measurement methods for specialized forms of structured illumination to achieve superresolution via higher spatial frequencies. The combination of subwavelength sized spots and macroscopic working distances, that plasmonic lenses enable, is a significant advantage over near-field methods that receive similar sized spots only for distances in close proximity to the sample. As an extension of the inverted plasmonic lens design, I compared different concepts for a multispectral realization which would enable the application of these types of lenses at many different wavelengths. I proved that the merged lens approach would significantly reduce the dispersion, even for just two different types of sections. Further investigations about the trade-off between the dispersion reduction of even more sections and the polarization issues involved are needed, but literature suggests a trend in research moving away from plasmonic lenses towards dielectric meta-lenses, due to their flexibility and efficiency [157]. Nevertheless, the results from this thesis are likely to help strengthen the relevance of plasmonic lenses both in current metastructure research as well as in ellipsometric applications.

All in all, these contributions create a foundation to help advance modern ellipsometry, to establish imaging ellipsometry as a tool in nanometrology, and to push optical metrology further beyond its classical limits to keep up with developments from industrial areas. It is hard to imagine where semiconductor technology will lead us in the future. But it is safe to say that metrology has to keep pace, one way or another. Prospectively, the results from this work are going to play a role in the development of imaging ellipsometry towards metrological applications, making it a viable tool for the characterization of nanoscale structures like computer chips with inconceivably high processing power. Back when I had my Tamagotchi, it was hard to imagine having something like a tiny but powerful computer in my pocket, capable of almost everything, from taking pictures and running games to just talking to my friends. Teachers used to say we would never have a calculator with us everywhere we go. How wrong they were. Who knows what we are wrong about now?

Bibliography

- [1] Electronic Devices Marketing Division. *E0C6S46. 4-bit Single Chip Microcomputer*. Tech. rep. Seiko Epson Corporation, 1999. URL: https://download.epson-europe.com/pub/electronics-de/asmic/4bit/62family/datasheet/ds_6s46.pdf.
- [2] Electronic Devices Marketing Division. *E0C6S46 Technical Manual*. Tech. rep. Seiko Epson Corporation, 1999. URL: https://download.epson-europe.com/pub/electronics-de/asmic/4bit/62family/technicalmanual/tm_6s46.pdf.
- [3] L. Rubio. *Tamagotchi Tech Specs. GitHub repository*. 2019. URL: <https://github.com/loociano/tamagotchi-tech-specs> (visited on 06/15/2023).
- [4] HUAWEI. *HUAWEI stellt Kirin 980 vor*. 2018. URL: <https://consumer.huawei.com/de/press/news/2018/huawei-stellt-kirin-980-vor/> (visited on 06/15/2023).
- [5] A. Fagot. *Viele Unterschiede im Detail: Huawei P30 und P30 Pro mit allen Specs*. 2019. URL: <https://www.notebookcheck.com/Viele-Unterschiede-im-Detail-Huawei-P30-und-P30-Pro-mit-alLEN-Specs.414521.0.html> (visited on 06/15/2023).
- [6] S. Purab, M. Nishil, and T. Gopalakrishnan. "A Comparative Study on the Recent Smart Mobile Phone Processors". In: *IEEE 7th International Conference on Smart Structures and Systems (2020)*. DOI: 10.1109/ICSSS49621.2020.9202174. URL: <https://nanoreview.net/en/soc/hisilicon-kirin-980>.
- [7] TSMC. *7nm Technology*. 2023. URL: https://www.tsmc.com/english/dedicatedFoundry/technology/logic/1_7nm (visited on 06/15/2023).
- [8] WikiChip. *7 nm lithography process*. 2023. URL: https://en.wikichip.org/wiki/7_nm_lithography_process (visited on 06/15/2023).
- [9] I. Cutress. *Samsung Foundry: 2nm Silicon in 2025*. 2021. URL: <https://www.anandtech.com/show/16995/samsung-foundry-2nm-silicon-in-2025> (visited on 06/14/2023).
- [10] R. Zafar. *TSMC Exceeds 3nm Yield Expectations and Production Can Start Sooner Than Planned*. 2022. URL: <https://wccftech.com/tsmc-exceeds-3nm-yield-expectations-production-can-start-sooner-than-planned/> (visited on 06/14/2023).

- [11] G. Ragonnaud. *The EU chips act. Securing Europe's supply of semiconductors*. European Parliamentary Research Service. 2022. URL: <https://www.europarl.europa.eu/RegData/etudes/BRIE/2022/733596/EPRS-Briefing-733596-EU-chips-act-V2-FINAL.pdf> (visited on 06/14/2023).
- [12] European Union. *European Chips Act*. European Commission. 2022. DOI: 10.2759/197183. URL: https://apre.it/wp-content/uploads/2022/02/Chips_Act_Factsheet_20220208_FINAL_XsC5TsNXlyer6N2NSftbi86EQ_83080.pdf (visited on 06/14/2023).
- [13] Museum Rotterdam. *Gele tamagotchi*. Wikimedia. 1997. URL: https://commons.wikimedia.org/wiki/File:Gele_tamagotchi,_objectnr_78041.JPG?uselang=en (visited on 09/06/2023).
- [14] K. C. A. Smith and C. W. Oatley. "The scanning electron microscope and its fields of application". In: *British Journal of Applied Physics* 6.11 (1955). DOI: 10.1088/0508-3443/6/11/304.
- [15] G. Binnig, C. F. Quate, and C. Gerber. "Atomic Force Microscope". In: *Physical Review Letters* 56.930 (1986). DOI: 10.1103/PhysRevLett.56.930.
- [16] P.-E. Hansen and G. Roebben, eds. *Introductory Guide to Nanometrology*. European Commission, 2010. ISBN: 9780956680914.
- [17] W. Demtröder. *Experimentalphysik 2*. Vol. 6. Springer Berlin Heidelberg, 2013. 482 pp. ISBN: 978-3-642-29944-5. DOI: 10.1007/978-3-642-29944-5. URL: https://www.ebook.de/de/product/22876029/wolfgang_demtroeder_experimentalphysik_2.html.
- [18] Nobel Prize Outreach. *The Nobel Prize in Chemistry 2014. Press release*. Nobel Prize Outreach AB. 2014. URL: <https://www.nobelprize.org/prizes/chemistry/2014/press-release/> (visited on 06/14/2023).
- [19] S. W. Hell and J. Wichmann. "Breaking the diffraction resolution limit and by stimulated emission: stimulated-emission-depletion fluorescence microscopy". In: *Optics Letters* 19.11 (1994), p. 780. DOI: 10.1364/ol.19.000780.
- [20] E. Betzig et al. "Imaging Intracellular Fluorescent Proteins at Nanometer Resolution". In: *Science* 313 (5793 2006), pp. 1642–1645. DOI: 10.1126/science.1127344.
- [21] M. J. Rust, M. Bates, and X. Zhuang. "Sub-diffraction-limit imaging by stochastic optical reconstruction microscopy (STORM)". In: *Nature Methods* 3.10 (2006), pp. 793–796. DOI: 10.1038/NMETH929.
- [22] B. K. Minhas et al. "Ellipsometric scatterometry for the metrology of sub-0.1- μm -linewidth structures". In: *Applied Optics* 37 (22 1998), pp. 5112–5115. DOI: 10.1364/AO.37.005112.
- [23] H. G. Tompkins and E. A. Irene, eds. *Handbook of Ellipsometry*. William Andrew Publishing, 2005. ISBN: 0-8155-1499-9.

- [24] A. De Martino et al. “Comparison of spectroscopic Mueller polarimetry, standard scatterometry, and real space imaging techniques (SEM and 3D-AFM) for dimensional characterization of periodic structures”. In: *Proceedings of SPIE 6922, Metrology, Inspection, and Process Control for Microlithography XXII 6922* (2008). DOI: 10.1117/12.772721.
- [25] M. Losurdo and K. Hingerl, eds. *Ellipsometry at the Nanoscale*. Springer Berlin Heidelberg, 2013. ISBN: 978-3-642-33955-4. DOI: 10.1007/978-3-642-33956-1.
- [26] Merriam-Webster Dictionary. *Meter*. June 14, 2023. URL: <https://www.merriam-webster.com/dictionary/meter> (visited on 06/14/2023).
- [27] A. Rothen. “The Ellipsometer, an Apparatus to Measure Thicknesses of Thin Surface Films”. In: *Review of Scientific Instruments* 16 (2 1945), pp. 26–30. DOI: 10.1063/1.1770315.
- [28] R. M. A. Azzam. “The intertwined history of polarimetry and ellipsometry”. In: *Thin Solid Films* 519.9 (2011), pp. 2584–2588. DOI: 10.1016/j.tsf.2010.12.072.
- [29] U. Rossow. “A Brief History of Ellipsometry”. In: *Physica Status Solidi B* 256.2 (2019), p. 1800307. DOI: 10.1002/pssb.201800307.
- [30] S. Liu et al. “Mueller matrix imaging ellipsometry for nanostructure metrology”. In: *Optics Express* 23.13 (2015), p. 17316. DOI: 10.1364/OE.23.017316.
- [31] H. Jiang et al. “Nondestructive investigation on the nanocomposite ordering upon holography using Mueller matrix ellipsometry”. In: *European Polymer Journal* 110 (2019), pp. 123–129. DOI: 10.1016/j.eurpolymj.2018.11.023.
- [32] P.-E. Hansen et al. “Enhanced Measurement Accuracy for Nanostructures Using Hybrid Metrology”. In: *Frontiers in Physics* 9 (2022). DOI: 10.3389/fphy.2021.791459.
- [33] J. Oh et al. “Wide-field massive CD metrology based on the imaging Mueller-matrix ellipsometry for semiconductor devices”. In: *Proceedings of SPIE 12496, Metrology, Inspection, and Process Control XXXVII* (2023). DOI: 10.1117/12.2658131.
- [34] L. Martínez Herraiz, J. L. Plaza Canga-argüelles, and A. F. Braña de Cal. “Ellipsometry Characterisation for the Cd_{1-x}Zn_xTe_{1-y}Se_y Semiconductor Used in X-ray and Gamma Radiation Detectors”. In: *Crystals* 13 (4 2023), p. 693. DOI: 10.3390/cryst13040693.
- [35] S. Funke et al. “Determining the Dielectric Tensor of Microtextured Organic Thin Films by Imaging Mueller Matrix Ellipsometry”. In: *Journal of Physical Chemistry Letters* 12 (2021), pp. 3053–3058. DOI: 10.1021/acs.jpcllett.1c00317.
- [36] X. Chen et al. “Advanced Mueller matrix ellipsometry: Instrumentation and emerging applications”. In: *Science China Technological Sciences* (2022). DOI: 10.1007/s11431-022-2090-4.

- [37] D. N. Ignatenko et al. “Applications of Mueller Matrix Polarimetry to Biological and Agricultural Diagnostics: A Review”. In: *Applied Sciences* 12.5258 (2022). DOI: 10.3390/app12105258.
- [38] H. Bettin, K. Fujii, and A. Nicolaus. “Silicon spheres for the future realization of the kilogram and the mole”. In: *Comptes Rendus Physique* 20 (1-2 2019), pp. 64–76. DOI: 10.1016/j.crhy.2018.12.005.
- [39] J. L. Pezzaniti and R. A. Chipman. “Imaging polarimeters for optical metrology”. In: *Proceedings of SPIE 1317, Polarimetry: Radar, Infrared, Visible, Ultraviolet, and X-Ray*. Ed. by Russell A. Chipman and John W. Morris. SPIE, 1990. DOI: 10.1117/12.22065.
- [40] J. L. Pezzaniti and R. A. Chipman. “Mueller matrix imaging polarimetry”. In: *Optical Engineering* 34.6 (1995), pp. 1558–1568. DOI: 10.1117/12.206161.
- [41] G. Jin, R. Jansson, and H. Arwin. “Imaging ellipsometry revisited: Developments for visualization of thin transparent layers on silicon substrates”. In: *Review of Scientific Instruments* 67.2930 (1996). DOI: 10.1063/1.1147074.
- [42] Accurion GmbH. *Accurion. Solutions for Science*. Oct. 7, 2022. URL: <https://accurion.com/>.
- [43] K. Hingerl. “Imaging ellipsometry for structured and plasmonic materials”. In: *Journal of Applied Physics* 129.113101 (11 2021). DOI: 10.1063/5.0039150.
- [44] H. A. Bethe. “Theory of Diffraction by Small Holes”. In: *Physical Review* 66.7-8 (1944), pp. 163–182. DOI: 10.1103/physrev.66.163.
- [45] C. Genet and T. W. Ebbesen. “Light in tiny holes”. In: *Nature* 445.7123 (2007), pp. 39–46. DOI: 10.1038/nature05350.
- [46] J. Jahns and S. Helfert. *Introduction to Micro- and Nanooptics*. WILEY-VCH, 2012. ISBN: 978-3-527-40891-7.
- [47] S. G. Rodrigo, F. de Leon-Perez, and L. Martin-Moreno. “Extraordinary Optical Transmission: Fundamentals and Applications”. In: *Proceedings of the IEEE* 104.12 (2016), pp. 2288–2306. DOI: 10.1109/jproc.2016.2580664.
- [48] E. N. Economou. “Surface plasmons in thin films”. In: *Physical Review* 182.2 (1969), pp. 539–554. DOI: 10.1103/PhysRev.182.539.
- [49] K. J. Klein Koerkamp et al. “Strong Influence of Hole Shape on Extraordinary Transmission through Periodic Arrays of Subwavelength Holes”. In: *Physical Review Letters* 92.18 (2004), p. 183901. DOI: 10.1103/physrevlett.92.183901.
- [50] R. Gordon and A. G. Brolo. “Increased cut-off wavelength for a subwavelength hole in a real metal”. In: *Optics Express* 13.6 (2005), p. 1933. DOI: 10.1364/OPEX.13.001933.
- [51] P. B. Catrysse, H. Shin, and S. Fan. “Propagating modes in subwavelength cylindrical holes”. In: *Journal of Vacuum Science and Technology B: Microelectronics and Nanometer Structures* 23.6 (2005), p. 2675. DOI: 10.1116/1.2130344.

- [52] H. Shi et al. “Beam manipulating by metallic nano-slits with variant widths”. In: *Optics Express* 13.18 (2005), p. 6815. DOI: 10.1364/opex.13.006815.
- [53] T. Xu et al. “Subwavelength imaging by metallic slab lens with nanoslits”. In: *Applied Physics Letters* 91.20 (2007), p. 201501. DOI: 10.1063/1.2811711.
- [54] A. Grbic, L. Jiang, and R. Merlin. “Near-Field Plates: Subdiffraction Focusing with Patterned Surfaces”. In: *Science* 320.5875 (2008), pp. 511–513. DOI: 10.1126/science.1154753.
- [55] P. B. Catrysse et al. “Nanoscale slit arrays as planar far-field lenses”. In: *Proceedings of SPIE 7394, Plasmonics: Metallic Nanostructures and Their Optical Properties VII*. Ed. by Mark I. Stockman. 73940B. SPIE, Aug. 2009. DOI: 10.1117/12.826662.
- [56] L. Verslegers et al. “Planar Lenses Based on Nanoscale Slit Arrays in a Metallic Film”. In: *Nano Letters* 9.1 (2009), pp. 235–238. DOI: 10.1021/nl802830y.
- [57] S. Saxena et al. “Plasmonic Micro Lens for Extraordinary Transmission of Broadband Light”. In: *Scientific Reports* 4.1 (2014). DOI: 10.1038/srep05586.
- [58] E. Hecht. *Optik*. 3rd ed. Oldenbourg Verlag München Wien, 2001. ISBN: 3-486-24917-7.
- [59] H. Stöcker. *Taschenbuch der Physik: Formeln, Tabellen, Übersichten*. 6th ed. Frankfurt am Main: Deutsch, 2010. ISBN: 978-3-8171-1860-1.
- [60] W. Demtröder. *Experimentalphysik 2*. Springer-Lehrbuch. Springer Berlin Heidelberg, 2013. ISBN: 978-3-642-29943-8.
- [61] S. A. Maier. *Plasmonics: Fundamentals and Applications*. Vol. 1. Springer, New York, 2007. ISBN: 978-0-387-33150-8. DOI: 10.1007/0-387-37825-1.
- [62] D. Meschede. *Optik, Licht und Laser*. 3rd ed. Wiesbaden: Vieweg+Teubner, 2008. ISBN: 9783835101432.
- [63] M. Born and E. Wolf. *Principles of Optics. Electromagnetic Theory of Propagation, Interference and Diffraction of Light*. 4th ed. Pergamon Press, 1970.
- [64] L. Novotny and B. Hecht. *Principles of Nano-Optics*. CAMBRIDGE, 2006. 539 pp. ISBN: 978-0-521-83224-3. URL: https://www.ebook.de/de/product/5132648/lukas_novotny_bert_hecht_principles_of_nano_optics.html.
- [65] M. Milosevic. “On the Nature of the Evanescent Wave”. In: *Applied Spectroscopy* 67.2 (2013), pp. 126–131. DOI: 10.1366/12-06707.
- [66] P. P. Ewald. “Zur Theorie der Interferenzen der Röntgenstrahlen in Kristallen”. In: *Physikalische Zeitschrift* 14.11 (1913), p. 465.
- [67] T. Habashy and E. Wolf. “Reconstruction of Scattering Potentials from Incomplete Data”. In: *Journal of Modern Optics* 41.9 (1994), pp. 1679–1685. DOI: 10.1080/09500349414551651.

- [68] G. S. Agarwal. “Subwavelength resolution using evanescent waves”. In: *Pure and Applied Optics: Journal of the European Optical Society Part A* 7.5 (1998), pp. 1143–1149. DOI: 10.1088/0963-9659/7/5/021.
- [69] E. H. Synge. “A suggested method for extending microscopic resolution into the ultra-microscopic region”. In: *The London, Edinburgh, and Dublin Philosophical Magazine and Journal of Science* 6.35 (1928), pp. 356–362. DOI: 10.1080/14786440808564615.
- [70] D. Goldstein. *Polarized light*. 2nd ed. Marcel Dekker, Inc., 2003. ISBN: 0-8247-4053-X.
- [71] R. C. Jones. “A New Calculus for the Treatment of Optical Systems. I. Description and Discussion of the Calculus”. In: *Journal of the Optical Society of America* 31.7 (1941), p. 488. DOI: 10.1364/josa.31.000488.
- [72] G. G. Stokes. “On the Composition and Resolution of Streams of Polarized Light from different Sources”. In: *Transactions of the Cambridge Philosophical Society* 9 (1851), p. 399. URL: <https://ui.adsabs.harvard.edu/abs/1851TCaPS...9...399S>.
- [73] K. Järrendahl and B. Kahr. “Hans Mueller (1900-1965)”. In: *Woollam Annual Newsletter* 12 (2011), p. 8.
- [74] M. J. Walker. “Matrix Calculus and the Stokes Parameters of Polarized Radiation”. In: *American Journal of Physics* 22.4 (1954), pp. 170–174. DOI: 10.1119/1.1933670.
- [75] J. J. Gil Pérez and R. Ossikovski. *Polarized Light and the Mueller Matrix Approach*. CRC Press, 2016. ISBN: 9781315372525. DOI: 10.1201/b19711.
- [76] J. J. Gil and E. Bernabeu. “Depolarization and Polarization Indices of an Optical System”. In: *Optica Acta: International Journal of Optics* 33.2 (1986), pp. 185–189. DOI: 10.1080/713821924.
- [77] C. Kittel. *Einführung in die Festkörperphysik*. 15th ed. München: Oldenbourg Wissenschaftsverlag, 2013. ISBN: 9783486597554.
- [78] P. Gibbon. “Introduction to Plasma Physics”. In: *CERN Yellow Reports* (2016). DOI: 10.5170/CERN-2016-001.51.
- [79] C. Gerthsen. *Gerthsen Physik*. Ed. by Dieter Meschede. Vol. 24. Springer-Lehrbuch. Springer, Heidelberg, 2010. ISBN: 978-3-642-12894-3.
- [80] R. H. Ritchie. “Plasma losses by fast electrons in thin films”. In: *Physical Review* 106.5 (1957), p. 874. DOI: 10.1103/PhysRev.106.874.
- [81] A. Otto. “Excitation of nonradiative surface plasma waves in silver by the method of frustrated total reflection”. In: *Zeitschrift für Physik A Hadrons and nuclei* 216.4 (1968), pp. 398–410. DOI: 10.1007/BF01391532.
- [82] H. Raether. *Surface Plasmons on Smooth and Rough Surfaces and on Gratings*. Springer Berlin Heidelberg, 1988. ISBN: 978-3-662-15124-2. DOI: 10.1007/BFb0048317.

- [83] M. Bertolotti, C. Sibia, and Á. M. Guzmán. *Evanescence Waves in Optics: An Introduction to Plasmonics*. Springer Cham, 2017. ISBN: 978-3-319-61261-4. DOI: 10.1007/978-3-319-61261-4.
- [84] J. Zhang, L. Zhang, and W. Xu. “Surface plasmon polaritons: physics and applications”. In: *Journal of Physics D: Applied Physics* 45.11 (2012), p. 113001. DOI: 10.1088/0022-3727/45/11/113001.
- [85] M. G. Blaber, M. D. Arnold, and M. J. Ford. “A review of the optical properties of alloys and intermetallics for plasmonics”. In: *Journal of Physics: Condensed Matter* 22.14 (2010), p. 143201. DOI: 10.1088/0953-8984/22/14/143201.
- [86] P. R. West et al. “Searching for better plasmonic materials”. In: *Laser Photonics Reviews* 4.6 (2010), pp. 795–808. DOI: 10.1002/lpor.200900055.
- [87] P. B. Johnson and R. W. Christy. “Optical Constants of the Noble Metals”. In: *Physical Review B* 6.12 (1972), pp. 4370–4379. DOI: 10.1103/physrevb.6.4370.
- [88] W. L. Barnes. “Surface plasmon–polariton length scales: a route to sub-wavelength optics”. In: *Journal of Optics A: Pure and Applied Optics* 8.4 (2006), S87–S93. DOI: 10.1088/1464-4258/8/4/s06.
- [89] M. Bass et al., eds. *Handbook of Optics, Volume II - Devices, Measurements, and Properties*. 2nd ed. McGraw-Hill, 1995. ISBN: 0-07-047974-7.
- [90] R. M. A. Azzam. “A perspective on ellipsometry”. In: *Surface Science* 56 (1976), pp. 6–18. DOI: 10.1016/0039-6028(76)90430-1.
- [91] R. Schmidt-Grund, C. Sturm, and A. Hertwig. “Ellipsometry and polarimetry – classical measurement techniques with always new developments, concepts, and applications”. In: *Advanced Optical Technologies* 11.3-4 (2022), pp. 57–58. DOI: 10.1515/aot-2022-0025.
- [92] R. M. A. Azzam. “Photopolarimetric measurement of the Mueller matrix by Fourier analysis of a single detected signal”. In: *Optics Letters* 2.6 (1978), p. 148. DOI: 10.1364/OL.2.000148.
- [93] D. H. Goldstein. “Mueller matrix dual-rotating retarder polarimeter”. In: *Applied Optics* 31 (31 1992), pp. 6676–6683. DOI: 10.1364/AO.31.006676.
- [94] D. H. Goldstein and R. A. Chipman. “Error analysis of a Mueller matrix polarimeter”. In: *Journal of the Optical Society of America A* 7.4 (1990), p. 693. DOI: 10.1364/josaa.7.000693.
- [95] D. B. Chenault, J. L. Pezzaniti, and R. A. Chipman. “Mueller matrix algorithms”. In: *Proceedings of SPIE 1746, Polarization Analysis and Measurement*. San Diego '92. Ed. by Dennis H. Goldstein and Russell A. Chipman. SPIE, 1992. DOI: 10.1117/12.138793.
- [96] R. Rosa. “The inverse problem of ellipsometry: a bootstrap approach”. In: *Inverse Problems* 4 (1988), pp. 887–900. DOI: 10.1088/0266-5611/4/3/021.

- [97] X. Chen et al. “Measurement configuration optimization for accurate grating reconstruction by Mueller matrix polarimetry”. In: *Journal of Micro/Nanolithography, MEMS, and MOEMS* 12.033013 (3 2013). DOI: 10.1117/1.JMM.12.3.033013.
- [98] E. Garcia-Caurel et al. “Application of Spectroscopic Ellipsometry and Mueller Ellipsometry to Optical Characterization”. In: *Applied Spectroscopy* 67.1 (2013), pp. 1–21. DOI: 10.1366/12-06883.
- [99] G. R. Muthinti et al. “Characterization of e-beam patterned grating structures using Mueller matrix based scatterometry”. In: *Journal of Micro/Nanolithography, MEMS, and MOEMS* 12.013018 (1 2013). DOI: 10.1117/1.JMM.12.1.013018.
- [100] T. Grunewald et al. “Measurement of layer thicknesses with an improved optimization method for depolarizing Mueller matrices”. In: *Measurement Science and Technology* 31.11 (2020), p. 115010. DOI: 10.1088/1361-6501/ab95da.
- [101] SENTECH Instruments GmbH. *Spectroscopic ellipsometer SENresearch 4.0*. URL: https://www.sentech.com/en/SENresearch__219/ (visited on 11/17/2022).
- [102] J. Grundmann. “Konzeption und Realisierung eines experimentellen Müller-Matrix-Mikroskop-Aufbaus”. MA thesis. Technische Universität Braunschweig, 2020.
- [103] A. Köhler. “Ein neues Beleuchtungsverfahren für mikrophotographische Zwecke”. In: *Zeitschrift für wissenschaftliche Mikroskopie und für Mikroskopische Technik* 10.4 (1893), pp. 433–440.
- [104] T. Käseberg et al. “Mueller matrix ellipsometry for enhanced optical form metrology of sub-lambda structures”. In: *Proceedings of SPIE 11057, Modeling Aspects in Optical Metrology VII*. Ed. by Bernd Bodermann, Karsten Frenner, and Richard M. Silver. 110570R. SPIE, June 2019. DOI: 10.1117/12.2527419.
- [105] N. Kerwien. “Zum Einfluss von Polarisierungseffekten in der mikroskopischen Bildentstehung”. PhD thesis. Institut für Technische Optik Universität Stuttgart, 2007. ISBN: 978-3-923560-57-8.
- [106] J. Canny. “A Computational Approach to Edge Detection”. In: *IEEE Transactions on Pattern Analysis and Machine Intelligence* PAMI-8.6 (1986), pp. 679–698. DOI: 10.1109/tpami.1986.4767851.
- [107] P. V. C. Hough. “Machine Analysis of Bubble Chamber Pictures”. In: *Proceedings of the International Conference on High-Energy Accelerators and Instrumentation* 590914 (1959), pp. 554–558.
- [108] R. O. Duda and P. E. Hart. “Use of the Hough transformation to detect lines and curves in pictures”. In: *Communications of the ACM* 15.1 (1972), pp. 11–15. DOI: 10.1145/361237.361242.
- [109] C. Galamhos, J. Matas, and J. Kittler. “Progressive probabilistic Hough transform for line detection”. In: *Proceedings of the IEEE Computer Society Conference on Computer Vision and Pattern Recognition*. IEEE Comput. Soc, 1999. DOI: 10.1109/cvpr.1999.786993.

- [110] G. H. Golub and C. F. van Loan. *Matrix Computations*. 3rd ed. Baltimore, London: The John Hopkins University Press, 1996. ISBN: 0-8018-5414-8.
- [111] S. van der Walt et al. “scikit-image: image processing in Python”. In: *PeerJ* 2 (2014), e453. DOI: 10.7717/peerj.453.
- [112] C. G. Frase, E. Buhr, and K. Dirscherl. “CD characterization of nanostructures in SEM metrology”. In: *Measurement Science and Technology* 18.2 (2007), pp. 510–519. DOI: 10.1088/0957-0233/18/2/S26.
- [113] Z. J. Ding. “Sensitivity of scanning electron microscope width measurements to model assumptions”. In: *Journal of Micro/Nanolithography, MEMS, and MOEMS* 8.3 (2009), p. 033003. DOI: 10.1117/1.3190168.
- [114] J. Lazar et al. “Short-Range Six-Axis Interferometer Controlled Positioning for Scanning Probe Microscopy”. In: *Sensors* 14.1 (2014), pp. 877–886. DOI: 10.3390/s14010877.
- [115] T. Käseberg et al. “Mueller Matrix Ellipsometric Approach on the Imaging of Sub-Wavelength Nanostructures”. In: *Frontiers in Physics* 9 (2022). DOI: 10.3389/fphy.2021.814559.
- [116] O. D. Payton, L. Picco, and T. B. Scott. “High-speed atomic force microscopy for materials science”. In: *International Materials Reviews* 61.8 (2016), pp. 473–494. DOI: 10.1080/09506608.2016.1156301.
- [117] D. Nečas and P. Klapetek. “Gwyddion: an open-source software for SPM data analysis”. In: *Open Physics* 10.1 (2012). DOI: 10.2478/s11534-011-0096-2.
- [118] P.-E. Danielsson and O. Seger. “Generalized and Separable Sobel Operators”. In: *Machine Vision for Three-Dimensional Scenes*. Ed. by Herbert Freeman. Elsevier Science & Technology, 1990. Chap. 12. ISBN: 9780323150637. URL: https://www.ebook.de/de/product/21134811/machine_vision_for_three_dimensional_scenes.html.
- [119] S. Beucher and F. Meyer. “The Morphological Approach to Segmentation: The Watershed Transformation”. In: *Mathematical Morphology in Image Processing*. Ed. by Edward R. Dougherty. CRC Press, 1993. Chap. 12, pp. 433–481. ISBN: 9781315214610. DOI: 10.1201/9781482277234-12.
- [120] P. Virtanen et al. “SciPy 1.0: fundamental algorithms for scientific computing in Python”. In: *Nature Methods* 17.3 (2020), pp. 261–272. DOI: 10.1038/s41592-019-0686-2.
- [121] T. Käseberg et al. “Abbildende Müller-Matrix-Ellipsometrie für die Charakterisierung vereinzelter Nanostrukturen”. In: *tm - Technisches Messen* 89.6 (2022). DOI: 10.1515/teme-2021-0133.
- [122] M. Wurm et al. “Metrology of nanoscale grating structures by UV scatterometry”. In: *Optics Express* 25 (3 2017), pp. 2460–2468. DOI: 10.1364/OE.25.002460.

- [123] Lord Rayleigh. “XVIII. On the passage of electric waves through tubes, or the vibrations of dielectric cylinders”. In: *The London, Edinburgh, and Dublin Philosophical Magazine and Journal of Science* 43.261 (1897), pp. 125–132. DOI: 10.1080/14786449708620969.
- [124] T. W. Ebbesen et al. “Extraordinary optical transmission through sub-wavelength hole arrays”. In: *Nature* 391.6668 (1998), pp. 667–669. DOI: 10.1038/35570.
- [125] B. Prade, J. Y. Vinet, and A. Mysyrowicz. “Guided optical waves in planar heterostructures with negative dielectric constant”. In: *Physical Review B* 44.24 (1991), p. 13556. DOI: 10.1103/PhysRevB.44.13556.
- [126] F. Aieta et al. “Aberration-Free Ultrathin Flat Lenses and Axicons at Telecom Wavelengths Based on Plasmonic Metasurfaces”. In: *Nano Letters* 12.9 (2012), pp. 4932–4936. DOI: 10.1021/nl302516v.
- [127] Python Software Foundation. *Floating Point Arithmetic: Issues and Limitations*. 2022. URL: <https://docs.python.org/3/tutorial/float.html> (visited on 11/07/2022).
- [128] W. Srituravanich et al. “Flying plasmonic lens in the near field for high-speed nanolithography”. In: *Nature Nanotechnology* 3.12 (2008), pp. 733–737. DOI: 10.1038/nnano.2008.303.
- [129] Y. Fu and X. Zhou. “Plasmonic Lenses: A Review”. In: *Plasmonics* 5.3 (2010), pp. 287–310. DOI: 10.1007/s11468-010-9144-9.
- [130] Y. Fu et al. “Experimental investigation of superfocusing of plasmonic lens with chirped circular nanoslits”. In: *Optics Express* 18.4 (2010), p. 3438. DOI: 10.1364/oe.18.003438.
- [131] H. Li et al. “Cascaded plasmonic superlens for far-field imaging with magnification at visible wavelength”. In: *Optics Express* 26.8 (2018), p. 10888. DOI: 10.1364/oe.26.010888.
- [132] H. Li et al. “Cascaded DBR plasmonic cavity lens for far-field subwavelength imaging at a visible wavelength”. In: *Optics Express* 26.15 (2018), p. 19574. DOI: 10.1364/oe.26.019574.
- [133] D. B. Durham et al. “Plasmonic Lenses for Tunable Ultrafast Electron Emitters at the Nanoscale”. In: *Physical Review Applied* 12.5 (2019), p. 054057. DOI: 10.1103/physrevapplied.12.054057.
- [134] D. Petit et al. “Nanometer scale patterning using focused ion beam milling”. In: *Review of Scientific Instruments* 76.2 (2005), p. 026105. DOI: 10.1063/1.1844431.
- [135] T. Volkenandt, F. Pérez Willard, and B. Tordoff. “Save your FIB from the hard work – Large-scale sample prep using a LaserFIB”. In: *Microscopy and Microanalysis* 27.S1 (2021), pp. 18–19. DOI: 10.1017/s1431927621000659.

- [136] L. Palasse and P. Nowakowski. “Advances in EBSD sample preparation by broad ion beam milling”. In: *Microscopy and Microanalysis* 27.S1 (2021), pp. 1836–1839. DOI: 10.1017/s1431927621006711.
- [137] T. Käseberg et al. “Inverted plasmonic lens design for nanometrology applications”. In: *Measurement Science and Technology* 31.7 (2020), p. 074013. DOI: 10.1088/1361-6501/ab7e6b.
- [138] T. Siefke et al. “Fabrication influences on deep-ultraviolet tungsten wire grid polarizers manufactured by double patterning”. In: *Optics Letters* 39.22 (2014), p. 6434. DOI: 10.1364/OL.39.006434.
- [139] MicroChemicals GmbH. AZ® 1500-Series. *Positive Thin Resists for Wet Etching*. URL: https://www.microchemicals.com/products/photoresists/az_1505.html (visited on 11/03/2022).
- [140] A. Lehmuskero, M. Kuittinen, and P. Vahimaa. “Refractive index and extinction coefficient dependence of thin Al and Ir films on deposition technique and thickness”. In: *Optics Express* 15.17 (2007), p. 10744. DOI: 10.1364/oe.15.010744.
- [141] JCMwave GmbH. *JCMsuite. The Simulation Suite for Nano-Optics*. Berlin, 2001. URL: <https://jcmwave.com/> (visited on 09/23/2022).
- [142] J. Kennedy and R. Eberhart. “Particle swarm optimization”. In: *Proceedings of ICNN'95 - International Conference on Neural Networks*. Perth, WA, Australia: IEEE, 1995. ISBN: 0-7803-2768-3. DOI: 10.1109/icnn.1995.488968.
- [143] M. Clerc and J. Kennedy. “The particle swarm - explosion, stability, and convergence in a multidimensional complex space”. In: *IEEE Transactions on Evolutionary Computation* 6.1 (2002), pp. 58–73. DOI: 10.1109/4235.985692.
- [144] G. Brooker. *Modern Classical Optics*. Oxford Univ. Pr., 2003. 326 pp. ISBN: 019859965X. URL: https://www.ebook.de/de/product/2769230/geoffrey_brooker_modern_classical_optics.html.
- [145] Y. Yu and H. Zappe. “Effect of lens size on the focusing performance of plasmonic lenses and suggestions for the design”. In: *Optics Express* 19.10 (2011), p. 9434. DOI: 10.1364/oe.19.009434.
- [146] H. Shi and L. J. Guo. “Design of plasmonic near field plate at optical frequency”. In: *Applied Physics Letters* 96.14 (2010), p. 141107. DOI: 10.1063/1.3378997.
- [147] Q. Chen. “Effect of the Number of Zones in a One-Dimensional Plasmonic Zone Plate Lens: Simulation and Experiment”. In: *Plasmonics* 6.1 (2010), pp. 75–82. DOI: 10.1007/s11468-010-9171-6.
- [148] F. M. Dekking et al. *A Modern Introduction to Probability and Statistics: Understanding Why and How*. Springer Nature, 2007. 488 pp. ISBN: 1852338962. URL: https://www.ebook.de/de/product/3054516/f_m_dekking_c_kraaikamp_h_p_lopuhaae_l_e_meester_a_modern_introduction_to_probability_and_statistics_understanding_why_and_how.html.

- [149] R. Attota, R. G. Dixon, and A. E. Vladár. “Through-focus Scanning Optical Microscopy”. In: *Proceedings of SPIE 8036, Scanning Microscopies 2011* 803610 (2011). DOI: 10.1117/12.884706.
- [150] Y. Sun, S. Duthaler, and B. J. Nelson. “Autofocusing in Computer Microscopy: Selecting the Optical Focus Algorithm”. In: *Microscopy Research and Technique* 65 (3 2004), pp. 139–149. DOI: 10.1002/jemt.20118.
- [151] Z. Zhao et al. “Multispectral optical metasurfaces enabled by achromatic phase transition”. In: *Scientific Reports* 5.15781 (2015). DOI: 10.1038/srep15781.
- [152] J. Hu et al. “Plasmonic Lattice Lenses for Multiwavelength Achromatic Focusing”. In: *ACS Nano* 10.11 (2016), pp. 10275–10282. DOI: 10.1021/acsnano.6b05855.
- [153] O. Avayu et al. “Composite functional metasurfaces for multispectral achromatic optics”. In: *Nature Communications* 8.14992 (2017). DOI: 10.1038/ncomms14992.
- [154] W. Wang et al. “Spin-Selected Dual-Wavelength Plasmonic Metalenses”. In: *Nanomaterials* 9.5 (2019), p. 761. DOI: 10.3390/nano9050761.
- [155] Y. Li et al. “Achromatic flat optical components via compensation between structure and material dispersions”. In: *Scientific Reports* 6.19885 (2016). DOI: 10.1038/srep19885.
- [156] J. Yang et al. “Achromatic flat focusing lens based on dispersion engineering of spoof surface plasmon polaritons”. In: *Applied Physics Letters* 110.203507 (2017). DOI: 10.1063/1.4983831.
- [157] P. Genevet et al. “Recent advances in planar optics: from plasmonic to dielectric metasurfaces”. In: *Optica* 4 (1 2017), pp. 139–152. DOI: 10.1364/OPTICA.4.000139.
- [158] W.-T. Chen et al. “A broadband achromatic metalens for focusing and imaging in the visible”. In: *Nature Nanotechnology* 13.3 (2018), pp. 220–226. DOI: 10.1038/s41565-017-0034-6.
- [159] F. M. Huang et al. “Focusing of light by a nanohole array”. In: *Applied Physics Letters* 90.091119 (2007). DOI: 10.1063/1.2710775.
- [160] Y. Fu et al. “Nanopinholes-Based Optical Superlens”. In: *Research Letters in Physics* 2008, 148505 (2008). DOI: 10.1155/2008/148505.
- [161] Z. Shi et al. “Polarization Effect on Superfocusing of a Plasmonic Lens Structured with Radialized and Chirped Elliptical Nanopinholes”. In: *Plasmonics* 5 (2010), pp. 175–182. DOI: 10.1007/s11468-010-9131-1.
- [162] Y. Zhang, Y. Fu, and X. Zhou. “Investigation of Metallic Elliptical Nano-Pinholes Structure-Based Plasmonic Lenses: From Design to Testing”. In: *Insciences Journal* 1.1 (2011), pp. 18–29. DOI: 10.5640/insc.010118.
- [163] E. Seo et al. “Far-field control of focusing plasmonic waves through disordered nanoholes”. In: *Optics Letters* 39.20 (2014). DOI: 10.1364/OL.39.005838.

- [164] J. Zhang et al. “Plasmonic focusing lens based on single-turn nano-pinholes array”. In: *Optics Express* 23 (14 2015), pp. 17883–17891. DOI: 10.1364/OE.23.017883.
- [165] B. Sturman, E. Podivilov, and M. Gorkunov. “Eigenmodes for metal-dielectric light-transmitting nanostructures”. In: *Physical Review B* 76.12 (2007), p. 125104. DOI: 10.1103/physrevb.76.125104.
- [166] S. I. Bozhevolnyi. *Plasmonic Nanoguides and Circuits*. Pan Stanford Publishing, 2008. ISBN: 978-981-4241-32-8. DOI: 10.1364/meta_plas.2008.mwd3.
- [167] I. N. Bronstein et al. *Taschenbuch der Mathematik*. 8th ed. Wissenschaftlicher Verlag Harri Deutsch GmbH, Frankfurt am Main, 2012. ISBN: 978-3-8171-2008-6.
- [168] C. Stock et al. “Fully integrated stokes snapshot imaging polarimeter”. In: *EPJ Web of Conferences* 238 (2020), p. 06018. DOI: 10.1051/epjconf/202023806018.
- [169] A. Zaidi et al. *Metasurface-enabled compact, single-shot and complete Mueller matrix imaging*. 2023. DOI: 10.48550/arXiv.2305.08704. arXiv: 2305.08704 [physics.optics]. URL: <https://arxiv.org/abs/2305.08704>.
- [170] I. Gereige et al. “Recognition of diffraction-grating profile using a neural network classifier in optical scatterometry”. In: *Journal of the Optical Society of America A* 25.7 (2008), p. 1661. DOI: 10.1364/josaa.25.001661.
- [171] Y. Quéau et al. “Learning to classify materials using Mueller imaging polarimetry”. In: *Fourteenth International Conference on Quality Control by Artificial Vision*. Ed. by Christophe Cudel, Stéphane Bazeille, and Nicolas Verrier. SPIE, July 2019. DOI: 10.1117/12.2516351.
- [172] J. Liu et al. “Machine learning powered ellipsometry”. In: *Light: Science and Applications* 10.1 (2021). DOI: 10.1038/s41377-021-00482-0.
- [173] A. Arunachalam et al. “Machine learning approach to thickness prediction from in situ spectroscopic ellipsometry data for atomic layer deposition processes”. In: *Journal of Vacuum Science and Technology A* 40.012405 (2022). DOI: 10.1116/6.0001482.
- [174] S. Liu et al. “Machine learning aided solution to the inverse problem in optical scatterometry”. In: *Measurement* 191.110811 (2022). DOI: 10.1016/j.measurement.2022.110811.
- [175] Y. Zhong et al. “A review on the GaN-on-Si power electronic devices”. In: *Fundamental Research* 2 (3 2022), pp. 462–475. DOI: 10.1016/j.fmre.2021.11.028.
- [176] A. Haar. “Zur Theorie der orthogonalen Funktionensysteme”. In: *Mathematische Annalen* 71 (1911), pp. 38–53. DOI: 10.1007/BF01456927.
- [177] C. P. Papageorgiou, M. Oren, and T. Poggio. “A general framework for object detection”. In: *Sixth International Conference on Computer Vision (IEEE Cat. No. 98CH36271)* (1998), pp. 555–562. DOI: 10.1109/ICCV.1998.710772.

- [178] P. Viola and M. Jones. “Rapid Object Detection Using a Boosted Cascade of Simple Features”. In: *Proceedings of the 2001 IEEE Computer Society Conference on Computer Vision and Pattern Recognition* (2001).
- [179] T. Käseberg et al. “Nanoform evaluation approach using Mueller matrix microscopy and machine learning concepts”. In: *EPJ Web of Conferences* 266 (2022). Ed. by M. F. Costa et al., p. 10007. DOI: 10.1051/epjconf/202226610007.
- [180] T.-T.-H. Pham et al. “Combined Mueller matrix imaging and artificial intelligence classification framework for Hepatitis B detection”. In: *Journal of Biomedical Optics* 27.7 (2022). DOI: 10.1117/1.JBO.27.7.075002.
- [181] C. Rodríguez et al. “Optimizing the classification of biological tissues using machine learning models based on polarized data”. In: *Journal of Biophotonics* 16 (4 2023). DOI: 10.1002/jbio.202200308.
- [182] P.-I. Schneider et al. “Benchmarking five global optimization approaches for nano-optical shape optimization”. In: *ACS Photonics* 6.11 (2019), pp. 2726–2733. DOI: 10.1021/acsp Photonics.9b00706.
- [183] W. A. Shurcliff and S. S. Ballard. *Polarized Light*. Princeton, New Jersey: D. van Nostrand Company, 1964.

List of Figures

1.1	Tamagotchi and smartphone.	3
2.1	Polarization ellipse	12
2.2	States of polarization	13
2.3	TM and TE polarized light	13
2.4	SPPs at the interface between two materials.	17
2.5	SPP dispersion	19
3.1	Examples for polarization state analyzers.	23
3.2	Intensity modulation due to rotating optical elements.	23
3.3	MUELLER matrix ellipsometry configurations	25
3.4	Error compensation parameters.	27
3.5	Conventional spectroscopic ellipsometry measurement example.	29
3.6	Imaging ellipsometry in PCSCA configuration.	30
3.7	MUELLER matrix microscope	31
3.8	Custom Accurion EP4 imaging ellipsometer.	33
3.9	Nanoform structures for investigations on imaging ellipsometry.	34
3.10	Nanoform test wafer	35
3.11	SEM images of nanoform structures	35
3.12	SEM evaluation example	36
3.13	SEM corner evaluation example	36
3.14	SEM image evaluation results.	37
3.15	Nanoform wafer	38
3.16	AFM images of selected structures from the nanoform sample.	40
3.17	Row A measured at MUELLER matrix microscope setup, corrected for drift.	42
3.18	Detailed view of drift corrected MUELLER matrix element images.	43
3.19	Structures of row C measured at the MUELLER matrix microscope setup.	44
3.20	Row A measured at the EP4 setup in PCSCA configuration.	45
3.21	Nanoform sample measurements at EP4 setup in PCSCA configuration.	46
3.22	Averaged MUELLER matrices over wavelength and corner radius.	47
3.23	Blur during measurement at MUELLER matrix microscope.	48
3.24	Thermal influences at MUELLER matrix microscope, correlation matrix.	49
3.25	Thermal drift at MUELLER matrix microscope setup.	49

3.26	Thermal influences at EP4, correlation matrix.	50
3.27	Thermal drift at EP4 setup.	50
3.28	Drift correction algorithm, flow chart.	51
3.29	MUELLER matrix images of A10 , before and after drift correction.	52
3.30	Intentionally moving sample during MUELLER matrix imaging.	53
4.1	Interfaces between media with different permittivities.	57
4.2	Phase distribution and waveguide width.	58
4.3	Schematics of conventional and inverted plasmonic lenses.	60
4.4	Intensity of conventional and inverted plasmonic lenses.	60
4.5	Influence of waveguide length and aperture on the focal spot.	62
4.6	Particle swarm optimization for fixed ridge parameters.	64
4.7	Intensity and FWHM of focal spot for different lens thicknesses l	64
4.8	SPP decay lengths.	65
4.9	Focal spot intensity and FWHM depending on coating thickness.	66
4.10	Particle swarm optimization for the coating thickness d_c	66
4.11	Two types of ridge arrangement	67
4.12	Box plots of the ridge distances (upper) and widths (lower).	70
4.13	Ridge coverage of the area of the final plasmonic lens designs.	70
4.14	Focal spot intensity under Gaussian distribution of ridges.	71
4.15	Simulated intensity and FWHM of the focal spot of a plasmonic lens.	72
4.16	Inverted plasmonic lens chip design.	73
4.17	Plasmonic lens SEM images.	73
4.18	Example TSOM measurement of plasmonic lens OS-11.	74
4.19	Wavelength dependent distances of peaks in the standard deviation.	75
4.20	Circular plasmonic waveguide comparison.	77
4.21	Numerical solutions of the characteristic equations for waveguides.	78
4.22	Simulated transmission and phase for resist waveguides in iridium.	79
4.23	Merged plasmonic lens concepts for up to four wavelengths.	80
4.24	Simulated intensity and phase for different lengths and widths.	81
4.25	Curved waveguides	82
4.26	Simulated transmission and phase of light through curved waveguides.	82
4.27	Numerical model of the merged plasmonic lens proof-of-concept.	83
4.28	Spot intensity and position of merged plasmonic lens.	84
5.1	Image of a plasmonic lens at MUELLER matrix microscope.	87
5.2	MUELLER matrix image of plasmonic lens OS-00 at EP4.	87
5.3	Mean MUELLER matrix images of plasmonic lens OS-00, PCSA	88
5.4	Mean MUELLER matrix images of plasmonic lens OS-00, PCSCA	88
5.5	Standard deviation of the first matrix element in PCSCA configuration	89
5.6	Mean MUELLER matrix images and standard deviations per focal plane.	90
5.7	FEM model nanoform sample.	91

5.8	Simulated MUELLER matrix images of row A structures.	92
5.9	Selected measured and simulated MUELLER matrix images.	94
5.10	Quadrant mean value differences.	95
5.11	Simulation of plasmonic lens supported ellipsometry concept.	97
5.12	Examples for HAAR functions with different parameters u (a) and v (b). . .	99
5.13	Haar-like features.	99
5.14	Most prominent feature values depending on the corner radius.	100
B.1	Measured MUELLER matrix images of row A without drift correction, 1. . .	156
B.2	Measured MUELLER matrix images of row A without drift correction, 2. . .	157
B.3	Measured MUELLER matrix images of row A with drift correction, 1.	158
B.4	Measured MUELLER matrix images of row A with drift correction, 2.	159
B.5	Simulated MUELLER matrix images of row A, part 1.	160
B.6	Simulated MUELLER matrix images of row A, part 2.	161
B.7	Measured MUELLER matrix images of row C without drift correction, part 1.	162
B.8	Measured MUELLER matrix images of row C without drift correction, part 2.	163
B.9	Measured MUELLER matrix images at different wavelengths, part 1.	164
B.10	Measured MUELLER matrix images at different wavelengths, part 2.	165
B.11	Measured MUELLER matrix images at different wavelengths, part 1.	166
B.12	Measured MUELLER matrix images at different wavelengths, part 2.	167

List of Tables

3.1	Structure specifications of the designed nanoform structures.	34
3.2	Selected structures and AFM measurement results.	39
4.1	Plasmonic lens labels.	68
4.2	Optimal plasmonic lens thicknesses.	69
5.1	Mean change of maximum HAAR-like feature values per nanometer.	101
A.1	Overview of relevant JONES and MUELLER matrices [58, 70, 183].	129
A.2	Fit parameters of Figure 3.14(a).	141
A.3	Fit parameters of Figure 3.14(c).	141
A.4	Fit parameters of Figure 3.14(b).	141
A.5	Fit parameters of Figure 3.14(d).	141
A.6	Fit parameters of Figure 3.25(a).	141
A.7	Fit parameters of Figure 4.28(b).	141
A.8	Design parameters of inverted plasmonic lenses	146
A.9	Periodic ridge arrangement, 5 μm focal length, part 1.	147
A.10	Periodic ridge arrangement, 5 μm focal length, part 2.	148
A.11	Periodic ridge arrangement, 10 μm focal length, part 1.	149
A.12	Periodic ridge arrangement, 10 μm focal length, part 2.	150
A.13	Successive ridge arrangement, 5 μm focal length.	151
A.14	Successive ridge arrangement, 10 μm focal length.	152
A.15	Successive ridge arrangement, 100 μm focal length.	153
A.16	Successive ridge arrangement, 1000 μm focal length.	154
A.17	Proof-of-concept merged plasmonic lens parameters.	154



Mathematical Details and Derivations

A.1 Derivation of the Wave Equation and the HELMHOLTZ Equation

We start from MAXWELL's equations (1), from the law of induction (1c) to be specific, which we apply the curl operator to:

$$\nabla \times \nabla \times \vec{E} = \nabla \times \left(-\frac{\partial \vec{B}}{\partial t} \right) \quad (77a)$$

$$= -\frac{\partial}{\partial t} (\nabla \times \vec{B}). \quad (77b)$$

Then we insert Equation (1d):

$$= -\frac{\partial}{\partial t} \left(\mu \vec{j} + \epsilon \mu \frac{\partial \vec{E}}{\partial t} \right) \quad (78a)$$

$$= -\mu \frac{\partial \vec{j}}{\partial t} - \epsilon \mu \frac{\partial^2 \vec{E}}{\partial t^2}. \quad (78b)$$

We use the proportionality between current density and electric field from Equation (3):

$$= -\mu \sigma \frac{\partial \vec{E}}{\partial t} - \epsilon \mu \frac{\partial^2 \vec{E}}{\partial t^2}. \quad (79)$$

For the left side, we use the following vector identity [167]:

$$\nabla \times \nabla \times \vec{E} = \nabla(\nabla \cdot \vec{E}) - \nabla^2 \vec{E}. \quad (80)$$

According to Equation (1a), the divergence of the electric field is a constant and the gradient of a constant vanishes [167], thus:

$$-\nabla^2 \vec{E} = -\mu\sigma \frac{\partial \vec{E}}{\partial t} - \epsilon\mu \frac{\partial^2 \vec{E}}{\partial t^2} \quad (81a)$$

$$\frac{1}{\epsilon\mu} \nabla^2 \vec{E} = \frac{\sigma}{\epsilon} \frac{\partial \vec{E}}{\partial t} + \frac{\partial^2 \vec{E}}{\partial t^2} \quad (81b)$$

$$c^2 \nabla^2 \vec{E} = \frac{\sigma}{\epsilon} \frac{\partial \vec{E}}{\partial t} + \frac{\partial^2 \vec{E}}{\partial t^2}, \quad (81c)$$

which is the wave equation in a conducting medium as stated in Equation (2).

In the charge- and current-free case ($\sigma = 0$ and $\vec{j} = \vec{0}$), the wave equation simplifies to:

$$\nabla^2 \vec{E} - \frac{1}{c^2} \frac{\partial^2 \vec{E}}{\partial t^2} = 0. \quad (82)$$

We can assume that the fields are time harmonic, so $\vec{E}(\vec{r}, t) = \vec{E}(\vec{r})e^{-i\omega t}$. Using this ansatz, we get the HELMHOLTZ equation [46, 61]:

$$\nabla^2 \vec{E}(\vec{r}) + k_0^2 \vec{E}(\vec{r}) = 0. \quad (83)$$

A.2 MUELLER Matrices

Table A.1: Overview of relevant JONES and MUELLER matrices [58, 70, 183].

Element	JONES matrix	MUELLER matrix
Free space	$\begin{pmatrix} 1 & 0 \\ 0 & 1 \end{pmatrix}$	$\begin{pmatrix} 1 & 0 & 0 & 0 \\ 0 & 1 & 0 & 0 \\ 0 & 0 & 1 & 0 \\ 0 & 0 & 0 & 1 \end{pmatrix}$
Filter, degree of transmission κ	$\begin{pmatrix} \sqrt{\kappa} & 0 \\ 0 & \sqrt{\kappa} \end{pmatrix}$	$\begin{pmatrix} \kappa & 0 & 0 & 0 \\ 0 & \kappa & 0 & 0 \\ 0 & 0 & \kappa & 0 \\ 0 & 0 & 0 & \kappa \end{pmatrix}$
Polarizer, linear horizontal	$\begin{pmatrix} 1 & 0 \\ 0 & 0 \end{pmatrix}$	$\frac{1}{2} \begin{pmatrix} 1 & 1 & 0 & 0 \\ 1 & 1 & 0 & 0 \\ 0 & 0 & 0 & 0 \\ 0 & 0 & 0 & 0 \end{pmatrix}$
Polarizer, linear vertical	$\begin{pmatrix} 0 & 0 \\ 0 & 1 \end{pmatrix}$	$\frac{1}{2} \begin{pmatrix} 1 & -1 & 0 & 0 \\ -1 & 1 & 0 & 0 \\ 0 & 0 & 0 & 0 \\ 0 & 0 & 0 & 0 \end{pmatrix}$
Polarizer, linear $\pm 45^\circ$	$\frac{1}{2} \begin{pmatrix} 1 & \pm 1 \\ \pm 1 & 1 \end{pmatrix}$	$\frac{1}{2} \begin{pmatrix} 1 & 0 & \pm 1 & 0 \\ 0 & 0 & 0 & 0 \\ \pm 1 & 0 & 1 & 0 \\ 0 & 0 & 0 & 0 \end{pmatrix}$
Polarizer, right- (+) and left-circular (-)	$\frac{1}{2} \begin{pmatrix} 1 & \pm i \\ \mp i & 1 \end{pmatrix}$	$\frac{1}{2} \begin{pmatrix} 1 & 0 & 0 & \pm 1 \\ 0 & 0 & 0 & 0 \\ 0 & 0 & 0 & 0 \\ \pm 1 & 0 & 0 & 1 \end{pmatrix}$
Half-wave plate, fast axis at $\pm 45^\circ$	$\begin{pmatrix} 0 & 1 \\ 1 & 0 \end{pmatrix}$	$\begin{pmatrix} 1 & 0 & 0 & 0 \\ 0 & -1 & 0 & 0 \\ 0 & 0 & 1 & 0 \\ 0 & 0 & 0 & -1 \end{pmatrix}$
Quarter-wave plate, fast axis vertical (+) and horizontal (-)	$\begin{pmatrix} e^{\mp i \frac{\pi}{4}} & 0 \\ 0 & e^{\pm i \frac{\pi}{4}} \end{pmatrix}$	$\begin{pmatrix} 1 & 0 & 0 & 0 \\ 0 & 1 & 0 & 0 \\ 0 & 0 & 0 & \mp 1 \\ 0 & 0 & \pm 1 & 0 \end{pmatrix}$

A.3 Rotating Retarder MUELLER Matrix Ellipsometry

A.3.1 Transition from FOURIER Coefficients to MUELLER Matrix Elements

Section 3.1.3 focuses on the dual-rotating retarder configuration, or PCSCA. For this thesis, it is the more interesting case as it enables us to measure the full MUELLER matrix. However, the EP4 setup described in Section 3.2.2 also uses the PCSA configuration with only one compensator. Hence, for the sake of completion, this configuration will be discussed here, too.

PCSCA Configuration

In general, for any ellipsometric system, the modulated intensity measured at the detector comes from the MUELLER matrix \underline{M} of the sample, the MUELLER matrix of the PSA, and the STOKES vector coming from the PSG. As we are only interested in the intensity, we can omit the other rows [70]:

$$\vec{S}' = \underline{M}_{\text{PSA}} \cdot \underline{M} \cdot \vec{S}_{\text{PSG}}, \quad (84a)$$

$$\begin{pmatrix} I \\ \cdot \\ \cdot \\ \cdot \end{pmatrix} = \begin{pmatrix} m_{a,0} & m_{a,1} & m_{a,2} & m_{a,3} \\ \cdot & \cdot & \cdot & \cdot \\ \cdot & \cdot & \cdot & \cdot \\ \cdot & \cdot & \cdot & \cdot \end{pmatrix} \cdot \begin{pmatrix} m_{00} & m_{01} & m_{02} & m_{03} \\ m_{10} & m_{11} & m_{12} & m_{13} \\ m_{20} & m_{21} & m_{22} & m_{23} \\ m_{30} & m_{31} & m_{32} & m_{33} \end{pmatrix} \cdot \begin{pmatrix} S_{g,0} \\ S_{g,1} \\ S_{g,2} \\ S_{g,3} \end{pmatrix}, \quad (84b)$$

$$\Rightarrow I = \sum_{u,v=0}^3 m_{a,u} m_{uv} S_{g,v} = \sum_{u,v=0}^3 \mu_{uv} m_{uv}, \quad (84c)$$

with $\mu_{uv} = m_{a,u} S_{g,v}$. We can specify this further, for the PCSCA configuration:

$$\vec{S}' = \underline{M}_{\text{PSA}} \cdot \underline{M} \cdot \vec{S}_{\text{PSG}} \quad (85a)$$

$$= \underline{M}_{\text{pol}} \cdot \underline{R}(-\theta_A) \cdot \underline{M}_{\lambda/4} \cdot \underline{R}(\theta_A) \cdot \underline{M} \cdot \underline{R}(-\theta_G) \cdot \underline{M}_{\lambda/4} \cdot \underline{R}(\theta_G) \cdot \underline{M}_{\text{pol}} \cdot \vec{S}. \quad (85b)$$

The retarders of the PSA and PSG need to rotate with different speeds to obtain enough modulation for the FOURIER analysis. Though many different ratios for their speeds are possible, we want to consider only the lowest possible one, which is 5:1 [70], so $\theta_G = \theta$ and $\theta_A = 5\theta$. Given that the source light is generally unpolarized and using trigonometric identities, we get:

$$\vec{S}_{\text{PSG}} = \underline{R}(-\theta) \cdot \underline{M}_{\lambda/4} \cdot \underline{R}(\theta) \cdot \underline{M}_{\text{pol}} \cdot \vec{S} \tag{86a}$$

$$= \underline{R}(-\theta) \cdot \underline{M}_{\lambda/4} \cdot \underline{R}(\theta) \cdot \frac{1}{2} \begin{pmatrix} 1 & 1 & 0 & 0 \\ 1 & 1 & 0 & 0 \\ 0 & 0 & 0 & 0 \\ 0 & 0 & 0 & 0 \end{pmatrix} \cdot \begin{pmatrix} 1 \\ 0 \\ 0 \\ 0 \end{pmatrix} \tag{86b}$$

$$= \underline{R}(-\theta) \cdot \underline{M}_{\lambda/4} \cdot \begin{pmatrix} 1 & 0 & 0 & 0 \\ 0 & \cos(2\theta) & \sin(2\theta) & 0 \\ 0 & -\sin(2\theta) & \cos(2\theta) & 0 \\ 0 & 0 & 0 & 1 \end{pmatrix} \cdot \frac{1}{2} \begin{pmatrix} 1 \\ 1 \\ 0 \\ 0 \end{pmatrix} \tag{86c}$$

$$= \underline{R}(-\theta) \cdot \begin{pmatrix} 1 & 0 & 0 & 0 \\ 0 & 1 & 0 & 0 \\ 0 & 0 & 0 & 1 \\ 0 & 0 & -1 & 0 \end{pmatrix} \cdot \frac{1}{2} \begin{pmatrix} 1 \\ \cos(2\theta) \\ -\sin(2\theta) \\ 0 \end{pmatrix} \tag{86d}$$

$$= \begin{pmatrix} 1 & 0 & 0 & 0 \\ 0 & \cos(-2\theta) & \sin(-2\theta) & 0 \\ 0 & -\sin(-2\theta) & \cos(-2\theta) & 0 \\ 0 & 0 & 0 & 1 \end{pmatrix} \cdot \frac{1}{2} \begin{pmatrix} 1 \\ \cos(2\theta) \\ 0 \\ \sin(2\theta) \end{pmatrix} \tag{86e}$$

$$= \frac{1}{2} \begin{pmatrix} 1 \\ \cos^2(2\theta) \\ \sin(2\theta) \cos(2\theta) \\ \sin(2\theta) \end{pmatrix}, \tag{86f}$$

and:

$$\underline{M}_{\text{PSA}} = \underline{M}_{\text{pol}} \cdot \underline{R}(-5\theta) \cdot \underline{M}_{\lambda/4} \cdot \underline{R}(5\theta) \tag{87a}$$

$$= \underline{M}_{\text{pol}} \cdot \underline{R}(-5\theta) \cdot \begin{pmatrix} 1 & 0 & 0 & 0 \\ 0 & 1 & 0 & 0 \\ 0 & 0 & 0 & 1 \\ 0 & 0 & -1 & 0 \end{pmatrix} \cdot \begin{pmatrix} 1 & 0 & 0 & 0 \\ 0 & \cos(10\theta) & \sin(10\theta) & 0 \\ 0 & -\sin(10\theta) & \cos(10\theta) & 0 \\ 0 & 0 & 0 & 1 \end{pmatrix} \tag{87b}$$

$$= \underline{M}_{\text{pol}} \cdot \begin{pmatrix} 1 & 0 & 0 & 0 \\ 0 & \cos(-10\theta) & \sin(-10\theta) & 0 \\ 0 & -\sin(-10\theta) & \cos(-10\theta) & 0 \\ 0 & 0 & 0 & 1 \end{pmatrix} \cdot \begin{pmatrix} 1 & 0 & 0 & 0 \\ 0 & \cos(10\theta) & \sin(10\theta) & 0 \\ 0 & 0 & 0 & 1 \\ 0 & \sin(10\theta) & -\cos(10\theta) & 0 \end{pmatrix} \tag{87c}$$

$$= \frac{1}{2} \begin{pmatrix} 1 & 1 & 0 & 0 \\ 1 & 1 & 0 & 0 \\ 0 & 0 & 0 & 0 \\ 0 & 0 & 0 & 0 \end{pmatrix} \cdot \begin{pmatrix} 1 & 0 & 0 & 0 \\ 0 & \cos^2(10\theta) & \sin(10\theta) \cos(10\theta) & -\sin(10\theta) \\ 0 & \sin(10\theta) \cos(10\theta) & \sin^2(10\theta) & \cos(10\theta) \\ 0 & \sin(10\theta) & -\cos(10\theta) & 0 \end{pmatrix} \tag{87d}$$

$$= \frac{1}{2} \begin{pmatrix} 1 & \cos^2(10\theta) & \sin(10\theta) \cos(10\theta) & -\sin(10\theta) \\ 1 & \cos^2(10\theta) & \sin(10\theta) \cos(10\theta) & -\sin(10\theta) \\ 0 & 0 & 0 & 0 \\ 0 & 0 & 0 & 0 \end{pmatrix}. \tag{87e}$$

When we neglect the factors of 1/2 because they are just intensity scaling factors, we get for the respective vectors of PSA and PSG:

$$\begin{pmatrix} m_{a,0} & m_{a,1} & m_{a,2} & m_{a,3} \end{pmatrix} = \begin{pmatrix} 1 & \cos^2(10\theta) & \sin(10\theta) \cos(10\theta) & -\sin(10\theta) \end{pmatrix}, \tag{88}$$

$$\begin{pmatrix} S_{g,0} \\ S_{g,1} \\ S_{g,2} \\ S_{g,3} \end{pmatrix} = \begin{pmatrix} 1 \\ \cos^2(2\theta) \\ \sin(2\theta) \cos(2\theta) \\ \sin(2\theta) \end{pmatrix}. \tag{89}$$

Thus, with $\mu_{uv} = m_{a,u} S_{g,v}$, the 16 elements of μ_{uv} are:

$$\begin{aligned} \mu_{00} &= 1, \\ \mu_{01} &= \cos^2(2\theta) &= \frac{1}{2} + \frac{1}{2} \cos(4\theta), \\ \mu_{02} &= \sin(2\theta) \cos(2\theta) &= \frac{1}{2} \sin(4\theta), \\ \mu_{03} &= \sin(2\theta), \\ \mu_{10} &= \cos^2(10\theta) &= \frac{1}{2} + \frac{1}{2} \cos(20\theta), \\ \mu_{11} &= \cos^2(2\theta) \cos^2(10\theta) &= \frac{1}{4} + \frac{1}{4} \cos(4\theta) + \frac{1}{4} \cos(20\theta) \\ & & \quad + \frac{1}{8} \cos(16\theta) + \frac{1}{8} \cos(24\theta), \\ \mu_{12} &= \sin(2\theta) \cos(2\theta) \cos^2(10\theta) &= \frac{1}{4} \sin(4\theta) - \frac{1}{8} \sin(16\theta) + \frac{1}{8} \sin(24\theta), \\ \mu_{13} &= \sin(2\theta) \cos^2(10\theta) &= \frac{1}{2} \sin(2\theta) - \frac{1}{4} \sin(18\theta) + \frac{1}{4} \sin(22\theta), \\ \mu_{20} &= \sin(10\theta) \cos(10\theta) &= \frac{1}{2} \sin(20\theta), \\ \mu_{21} &= \cos^2(2\theta) \sin(10\theta) \cos(10\theta) &= -\frac{1}{8} \sin(16\theta) + \frac{1}{4} \sin(20\theta) + \frac{1}{8} \sin(24\theta), \\ \mu_{22} &= \sin(2\theta) \cos(2\theta) \sin(10\theta) \cos(10\theta) &= \frac{1}{8} \cos(16\theta) - \frac{1}{8} \cos(24\theta), \\ \mu_{23} &= \sin(2\theta) \sin(10\theta) \cos(10\theta) &= \frac{1}{4} \cos(18\theta) - \frac{1}{4} \cos(22\theta), \\ \mu_{30} &= -\sin(10\theta), \\ \mu_{31} &= -\cos^2(2\theta) \sin(10\theta) &= -\frac{1}{4} \sin(6\theta) - \frac{1}{2} \sin(10\theta) - \frac{1}{4} \sin(14\theta), \\ \mu_{32} &= -\sin(2\theta) \cos(2\theta) \sin(10\theta) &= -\frac{1}{4} \cos(6\theta) + \frac{1}{4} \cos(14\theta), \\ \mu_{33} &= -\sin(2\theta) \sin(10\theta) &= -\frac{1}{2} \cos(8\theta) + \frac{1}{2} \cos(12\theta). \end{aligned}$$

Next, we write out the intensity and rearrange it for the different harmonics:

$$\begin{aligned}
 I &= \sum_{u,v=0}^3 \mu_{uv} m_{uv} \\
 &= \mu_{00} m_{00} + \mu_{01} m_{01} + \mu_{02} m_{02} + \mu_{03} m_{03} + \mu_{10} m_{10} + \mu_{11} m_{11} + \mu_{12} m_{12} + \mu_{13} m_{13} \\
 &\quad + \mu_{20} m_{20} + \mu_{21} m_{21} + \mu_{22} m_{22} + \mu_{23} m_{23} + \mu_{30} m_{30} + \mu_{31} m_{31} + \mu_{32} m_{32} + \mu_{33} m_{33} \\
 &= m_{00} + \frac{1}{2} m_{01} + \frac{1}{2} m_{01} \cos(4\theta) + \frac{1}{2} m_{02} \sin(4\theta) + m_{03} \sin(2\theta) + \frac{1}{2} m_{10} + \frac{1}{2} m_{10} \cos(20\theta) \\
 &\quad + \frac{1}{4} m_{11} + \frac{1}{4} m_{11} \cos(4\theta) + \frac{1}{4} m_{11} \cos(20\theta) + \frac{1}{8} m_{11} \cos(16\theta) + \frac{1}{8} m_{11} \cos(24\theta) \\
 &\quad + \frac{1}{4} m_{12} \sin(4\theta) - \frac{1}{8} m_{12} \sin(16\theta) + \frac{1}{8} m_{12} \sin(24\theta) + \frac{1}{2} m_{13} \sin(2\theta) - \frac{1}{4} m_{13} \sin(18\theta) \\
 &\quad + \frac{1}{4} m_{13} \sin(22\theta) + \frac{1}{2} m_{20} \sin(20\theta) - \frac{1}{8} m_{21} \sin(16\theta) + \frac{1}{4} m_{21} \sin(20\theta) + \frac{1}{8} m_{21} \sin(24\theta) \\
 &\quad + \frac{1}{8} m_{22} \cos(16\theta) - \frac{1}{8} m_{22} \cos(24\theta) + \frac{1}{4} m_{23} \cos(18\theta) - \frac{1}{4} m_{23} \cos(22\theta) - m_{30} \sin(10\theta) \\
 &\quad - \frac{1}{4} m_{31} \sin(6\theta) - \frac{1}{2} m_{31} \sin(10\theta) - \frac{1}{4} m_{31} \sin(14\theta) - \frac{1}{4} m_{32} \cos(6\theta) + \frac{1}{4} m_{32} \cos(14\theta) \\
 &\quad - \frac{1}{2} m_{33} \cos(8\theta) + \frac{1}{2} m_{33} \cos(12\theta) \\
 &= (m_{00} + \frac{1}{2} m_{01} + \frac{1}{2} m_{10} + \frac{1}{4} m_{11}) + (m_{03} + \frac{1}{2} m_{13}) \sin(2\theta) \\
 &\quad + (\frac{1}{2} m_{01} + \frac{1}{4} m_{11}) \cos(4\theta) + (\frac{1}{2} m_{02} + \frac{1}{4} m_{12}) \sin(4\theta) \\
 &\quad + (-\frac{1}{4} m_{32}) \cos(6\theta) + (-\frac{1}{4} m_{31}) \sin(6\theta) + (-\frac{1}{2} m_{33}) \cos(8\theta) \\
 &\quad + (-m_{30} - \frac{1}{2} m_{31}) \sin(10\theta) + (\frac{1}{2} m_{33}) \cos(12\theta) \\
 &\quad + (\frac{1}{4} m_{32}) \cos(14\theta) + (-\frac{1}{4} m_{31}) \sin(14\theta) \\
 &\quad + (\frac{1}{8} m_{11} + \frac{1}{8} m_{22}) \cos(16\theta) + (-\frac{1}{8} m_{12} - \frac{1}{8} m_{21}) \sin(16\theta) \\
 &\quad + (\frac{1}{4} m_{23}) \cos(18\theta) + (-\frac{1}{4} m_{13}) \sin(18\theta) \\
 &\quad + (\frac{1}{2} m_{10} + \frac{1}{4} m_{11}) \cos(20\theta) + (\frac{1}{2} m_{20} + \frac{1}{4} m_{21}) \sin(20\theta) \\
 &\quad + (-\frac{1}{4} m_{23}) \cos(22\theta) + (\frac{1}{4} m_{13}) \sin(22\theta) \\
 &\quad + (\frac{1}{8} m_{11} - \frac{1}{8} m_{22}) \cos(24\theta) + (\frac{1}{8} m_{12} + \frac{1}{8} m_{21}) \sin(24\theta) \\
 &= a_0 + b_1 \sin(2\theta) + a_2 \cos(4\theta) + b_2 \sin(4\theta) + a_3 \cos(6\theta) + b_3 \sin(6\theta) + a_4 \cos(8\theta) \\
 &\quad + b_5 \sin(10\theta) + a_6 \cos(12\theta) + a_7 \cos(14\theta) + b_7 \sin(14\theta) + a_8 \cos(16\theta) + b_8 \sin(16\theta) \\
 &\quad + a_9 \cos(18\theta) + b_9 \sin(18\theta) + a_{10} \cos(20\theta) + b_{10} \sin(20\theta) + a_{11} \cos(22\theta) + b_{11} \sin(22\theta) \\
 &\quad + a_{12} \cos(24\theta) + b_{12} \sin(24\theta) \\
 &= a_0 + \sum_{j=1}^{12} (a_j \cos(2j\theta) + b_j \sin(2j\theta)) = I(\theta).
 \end{aligned}$$

Thus, we obtained expressions that connect MUELLER matrix elements and FOURIER coefficients of the measured intensity signal:

$$a_0 = m_{00} + \frac{1}{2}(m_{01} + m_{10}) + \frac{1}{4}m_{11} \quad (91)$$

$$\begin{array}{llll} a_1 = 0 & a_7 = \frac{1}{4}m_{32} & b_1 = m_{03} + \frac{1}{2}m_{13} & b_7 = -\frac{1}{4}m_{31} \\ a_2 = \frac{1}{2}m_{01} + \frac{1}{4}m_{11} & a_8 = \frac{1}{8}m_{11} + \frac{1}{8}m_{22} & b_2 = \frac{1}{2}m_{02} + \frac{1}{4}m_{12} & b_8 = -\frac{1}{8}m_{12} - \frac{1}{8}m_{21} \\ a_3 = -\frac{1}{4}m_{32} & a_9 = \frac{1}{4}m_{23} & b_3 = -\frac{1}{4}m_{31} & b_9 = -\frac{1}{4}m_{13} \\ a_4 = -\frac{1}{2}m_{33} & a_{10} = \frac{1}{2}m_{10} + \frac{1}{4}m_{11} & b_4 = 0 & b_{10} = \frac{1}{2}m_{20} + \frac{1}{4}m_{21} \\ a_5 = 0 & a_{11} = -\frac{1}{4}m_{23} & b_5 = -m_{30} - \frac{1}{2}m_{31} & b_{11} = \frac{1}{4}m_{13} \\ a_6 = \frac{1}{2}m_{33} & a_{12} = \frac{1}{8}m_{11} - \frac{1}{8}m_{22} & b_6 = 0 & b_{12} = \frac{1}{8}m_{12} + \frac{1}{8}m_{21} \end{array}$$

\Leftrightarrow

$$\begin{array}{ll} m_{00} = a_0 - a_2 + a_8 - a_{10} + a_{12} & m_{20} = -2b_8 + 2b_{10} - 2b_{12} \\ m_{01} = 2a_2 - 2a_8 - 2a_{12} & m_{21} = 4b_8 + 4b_{12} \\ m_{02} = 2b_2 + 2b_8 - 2b_{12} & m_{22} = 4a_8 - 4a_{12} \\ m_{03} = b_1 + b_9 - b_{11} & m_{23} = 2(a_9 - a_{11}) \\ m_{10} = -2a_8 + 2a_{10} - 2a_{12} & m_{30} = b_3 - b_5 + b_7 \\ m_{11} = 4a_8 + 4a_{12} & m_{31} = -2(b_3 + b_7) \\ m_{12} = -4b_8 + 4b_{12} & m_{32} = 2(-a_3 + a_7) \\ m_{13} = 2(-b_9 + b_{11}) & m_{33} = -a_4 + a_6 \end{array}$$

PCSA Configuration

Similar to the PCSCA case, we start with the modulated intensity:

$$\vec{S}' = \underline{M}_{\text{PSA}} \cdot \underline{M} \cdot \vec{S}_{\text{PSG}}. \tag{92a}$$

This time, we describe the PSG and PSA more generally:

$$\vec{S}_{\text{PSG}} = \underline{R}(-\theta_G) \cdot \underline{M}_{\lambda/4} \cdot \underline{R}(\theta_G) \cdot \underline{R}(-\theta_P) \cdot \underline{M}_{\text{pol}} \cdot \underline{R}(\theta_P) \cdot \vec{S} \tag{93a}$$

$$= \underline{R}(-\theta_G) \cdot \underline{M}_{\lambda/4} \cdot \underline{R}(\theta_G) \cdot \underline{R}(-\theta_P) \cdot \underline{M}_{\text{pol}} \cdot \begin{pmatrix} 1 & 0 & 0 & 0 \\ 0 & \cos(2\theta_P) & \sin(2\theta_P) & 0 \\ 0 & -\sin(2\theta_P) & \cos(2\theta_P) & 0 \\ 0 & 0 & 0 & 1 \end{pmatrix} \cdot \begin{pmatrix} 1 \\ 0 \\ 0 \\ 0 \end{pmatrix} \tag{93b}$$

$$= \underline{R}(-\theta_G) \cdot \underline{M}_{\lambda/4} \cdot \underline{R}(\theta_G) \cdot \underline{R}(-\theta_P) \cdot \frac{1}{2} \begin{pmatrix} 1 & 1 & 0 & 0 \\ 1 & 1 & 0 & 0 \\ 0 & 0 & 0 & 0 \\ 0 & 0 & 0 & 0 \end{pmatrix} \cdot \begin{pmatrix} 1 \\ 0 \\ 0 \\ 0 \end{pmatrix} \tag{93c}$$

$$= \underline{R}(-\theta_G) \cdot \underline{M}_{\lambda/4} \cdot \underline{R}(\theta_G) \cdot \begin{pmatrix} 1 & 0 & 0 & 0 \\ 0 & \cos(-2\theta_P) & \sin(-2\theta_P) & 0 \\ 0 & -\sin(-2\theta_P) & \cos(-2\theta_P) & 0 \\ 0 & 0 & 0 & 1 \end{pmatrix} \cdot \frac{1}{2} \begin{pmatrix} 1 \\ 1 \\ 0 \\ 0 \end{pmatrix} \tag{93d}$$

$$= \underline{R}(-\theta_G) \cdot \underline{M}_{\lambda/4} \cdot \begin{pmatrix} 1 & 0 & 0 & 0 \\ 0 & \cos(2\theta_G) & \sin(2\theta_G) & 0 \\ 0 & -\sin(2\theta_G) & \cos(2\theta_G) & 0 \\ 0 & 0 & 0 & 1 \end{pmatrix} \cdot \frac{1}{2} \begin{pmatrix} \cos(2\theta_P) \\ \sin(2\theta_P) \\ 0 \\ 0 \end{pmatrix} \tag{93e}$$

$$= \underline{R}(-\theta_G) \cdot \begin{pmatrix} 1 & 0 & 0 & 0 \\ 0 & 1 & 0 & 0 \\ 0 & 0 & 0 & 1 \\ 0 & 0 & -1 & 0 \end{pmatrix} \cdot \frac{1}{2} \begin{pmatrix} \cos(2\theta_G) \cos(2\theta_P) + \sin(2\theta_G) \sin(2\theta_P) \\ -\sin(2\theta_G) \sin(2\theta_P) + \cos(2\theta_G) \cos(2\theta_P) \\ 0 \\ 0 \end{pmatrix} \tag{93f}$$

$$= \begin{pmatrix} 1 & 0 & 0 & 0 \\ 0 & \cos(-2\theta_G) & \sin(-2\theta_G) & 0 \\ 0 & -\sin(-2\theta_G) & \cos(-2\theta_G) & 0 \\ 0 & 0 & 0 & 1 \end{pmatrix} \cdot \frac{1}{2} \begin{pmatrix} \cos(2\theta_G) \cos(2\theta_P) + \sin(2\theta_G) \sin(2\theta_P) \\ 0 \\ \sin(2\theta_G) \cos(2\theta_P) - \cos(2\theta_G) \sin(2\theta_P) \\ 0 \end{pmatrix} \tag{93g}$$

$$= \frac{1}{2} \begin{pmatrix} 1 & & & \\ \cos^2(2\theta_G) \cos(2\theta_P) + \sin(2\theta_G) \cos(2\theta_G) \sin(2\theta_P) & & & \\ \sin(2\theta_G) \cos(2\theta_G) \cos(2\theta_P) + \sin^2(2\theta_G) \sin(2\theta_P) & & & \\ \sin(2\theta_G) \cos(2\theta_P) - \cos(2\theta_G) \sin(2\theta_P) & & & \end{pmatrix}, \tag{93h}$$

and:

$$\underline{M}_{\text{PSA}} = \underline{R}(-\theta_A) \cdot \underline{M}_{\text{pol}} \cdot \underline{R}(\theta_A) \tag{94a}$$

$$= \begin{pmatrix} 1 & 0 & 0 & 0 \\ 0 & \cos(-2\theta_A) & \sin(-2\theta_A) & 0 \\ 0 & -\sin(-2\theta_A) & \cos(-2\theta_A) & 0 \\ 0 & 0 & 0 & 1 \end{pmatrix} \cdot \frac{1}{2} \begin{pmatrix} 1 & 1 & 0 & 0 \\ 1 & 1 & 0 & 0 \\ 0 & 0 & 0 & 0 \\ 0 & 0 & 0 & 0 \end{pmatrix} \cdot \begin{pmatrix} 1 & 0 & 0 & 0 \\ 0 & \cos(2\theta_A) & \sin(2\theta_A) & 0 \\ 0 & -\sin(2\theta_A) & \cos(2\theta_A) & 0 \\ 0 & 0 & 0 & 1 \end{pmatrix} \tag{94b}$$

$$= \begin{pmatrix} 1 & 0 & 0 & 0 \\ 0 & \cos(-2\theta_A) & \sin(-2\theta_A) & 0 \\ 0 & -\sin(-2\theta_A) & \cos(-2\theta_A) & 0 \\ 0 & 0 & 0 & 1 \end{pmatrix} \cdot \frac{1}{2} \begin{pmatrix} 1 & \cos(2\theta_A) & \sin(2\theta_A) & 0 \\ 0 & \cos(2\theta_A) & \sin(2\theta_A) & 0 \\ 0 & 0 & 0 & 0 \\ 0 & 0 & 0 & 0 \end{pmatrix} \tag{94c}$$

$$= \frac{1}{2} \begin{pmatrix} 1 & \cos(2\theta_A) & \sin(2\theta_A) & 0 \\ \cos(2\theta_A) & \cos^2(2\theta_A) & \sin(2\theta_A) \cos(2\theta_A) & 0 \\ \sin(2\theta_A) & \sin(2\theta_A) \cos(2\theta_A) & \sin^2(2\theta_A) & 0 \\ 0 & 0 & 0 & 0 \end{pmatrix}. \tag{94d}$$

Again, we neglect the factors of $1/2$ and obtain the respective vectors of PSA and PSG:

$$\begin{pmatrix} m_{a,0} & m_{a,1} & m_{a,2} & m_{a,3} \end{pmatrix} = \begin{pmatrix} 1 & \cos(2\theta_A) & \sin(2\theta_A) & 0 \end{pmatrix}, \quad (95)$$

$$\begin{pmatrix} S_{g,0} \\ S_{g,1} \\ S_{g,2} \\ S_{g,3} \end{pmatrix} = \begin{pmatrix} 1 \\ \cos^2(2\theta_G) \cos(2\theta_P) + \sin(2\theta_G) \cos(2\theta_G) \sin(2\theta_P) \\ \sin(2\theta_G) \cos(2\theta_G) \cos(2\theta_P) + \sin^2(2\theta_G) \sin(2\theta_P) \\ \sin(2\theta_G) \cos(2\theta_P) - \cos(2\theta_G) \sin(2\theta_P) \end{pmatrix}. \quad (96)$$

From this, we obtain $\mu_{uv} = m_{a,u} S_{g,v}$ again and flatten them out in regard of θ_G , because it will be the rotating compensator that causes the intensity modulation:

$$\begin{aligned} \mu_{00} &= 1, \\ \mu_{01} &= \frac{1}{2} \cos(2\theta_P) + \frac{1}{2} \cos(2\theta_P) \cos(4\theta_G) + \frac{1}{2} \sin(2\theta_P) \sin(4\theta_G), \\ \mu_{02} &= \frac{1}{2} \cos(2\theta_P) \sin(4\theta_G) - \frac{1}{2} \sin(2\theta_P) \cos(4\theta_G) + \frac{1}{2} \sin(2\theta_P), \\ \mu_{03} &= \cos(2\theta_P) \sin(2\theta_G) - \sin(2\theta_P) \cos(2\theta_G), \\ \mu_{10} &= \cos(2\theta_A), \\ \mu_{11} &= \frac{1}{2} \cos(2\theta_A) \cos(2\theta_P) + \frac{1}{2} \cos(2\theta_A) \cos(2\theta_P) \cos(4\theta_G) + \frac{1}{2} \cos(2\theta_A) \sin(2\theta_P) \sin(4\theta_G), \\ \mu_{12} &= \frac{1}{2} \cos(2\theta_A) \cos(2\theta_P) \sin(4\theta_G) - \frac{1}{2} \cos(2\theta_A) \sin(2\theta_P) \cos(4\theta_G) + \frac{1}{2} \cos(2\theta_A) \sin(2\theta_P), \\ \mu_{13} &= \cos(2\theta_A) \cos(2\theta_P) \sin(2\theta_G) - \cos(2\theta_A) \sin(2\theta_P) \cos(2\theta_G), \\ \mu_{20} &= \sin(2\theta_A), \\ \mu_{21} &= \frac{1}{2} \sin(2\theta_A) \cos(2\theta_P) + \frac{1}{2} \sin(2\theta_A) \cos(2\theta_P) \cos(4\theta_G) + \frac{1}{2} \sin(2\theta_A) \sin(2\theta_P) \sin(4\theta_G), \\ \mu_{22} &= \frac{1}{2} \sin(2\theta_A) \cos(2\theta_P) \sin(4\theta_G) - \frac{1}{2} \sin(2\theta_A) \sin(2\theta_P) \cos(4\theta_G) + \frac{1}{2} \sin(2\theta_A) \sin(2\theta_P), \\ \mu_{23} &= \sin(2\theta_A) \cos(2\theta_P) \sin(2\theta_G) - \sin(2\theta_A) \sin(2\theta_P) \cos(2\theta_G), \\ \mu_{30} &= 0, \\ \mu_{31} &= 0, \\ \mu_{32} &= 0, \\ \mu_{33} &= 0. \end{aligned}$$

Here, we already see that we won't be able to measure the last row of the MUELLER matrix with this configuration. We continue by rearranging for the different harmonics again:

$$\begin{aligned}
I &= \sum_{u,v=0}^3 \mu_{uv} m_{uv} \\
&= \mu_{00} m_{00} + \mu_{01} m_{01} + \mu_{02} m_{02} + \mu_{03} m_{03} + \mu_{10} m_{10} + \mu_{11} m_{11} + \mu_{12} m_{12} + \mu_{13} m_{13} \\
&\quad + \mu_{20} m_{20} + \mu_{21} m_{21} + \mu_{22} m_{22} + \mu_{23} m_{23} + \mu_{30} m_{30} + \mu_{31} m_{31} + \mu_{32} m_{32} + \mu_{33} m_{33} \\
&= (m_{00} + \frac{1}{2} m_{01} \cos(2\theta_P) + \frac{1}{2} m_{02} \sin(2\theta_P) + m_{10} \cos(2\theta_A) + \frac{1}{2} m_{11} \cos(2\theta_A) \cos(2\theta_P) \\
&\quad + \frac{1}{2} m_{12} \cos(2\theta_A) \sin(2\theta_P) + m_{20} \sin(2\theta_A) + \frac{1}{2} m_{21} \sin(2\theta_A) \cos(2\theta_P) \\
&\quad + \frac{1}{2} m_{22} \sin(2\theta_A) \sin(2\theta_P)) - (m_{03} \sin(2\theta_P) + m_{13} \cos(2\theta_A) \sin(2\theta_P) \\
&\quad + m_{23} \sin(2\theta_A) \sin(2\theta_P)) \cdot \cos(2\theta_G) + (m_{03} \cos(2\theta_P) + m_{13} \cos(2\theta_A) \cos(2\theta_P) \\
&\quad + m_{23} \sin(2\theta_A) \cos(2\theta_P)) \cdot \sin(2\theta_G) + (\frac{1}{2} m_{01} \cos(2\theta_P) - \frac{1}{2} m_{02} \sin(2\theta_P) \\
&\quad + \frac{1}{2} m_{11} \cos(2\theta_A) \cos(2\theta_P) - \frac{1}{2} m_{12} \cos(2\theta_A) \sin(2\theta_P) + \frac{1}{2} m_{21} \sin(2\theta_A) \cos(2\theta_P) \\
&\quad - \frac{1}{2} m_{22} \sin(2\theta_A) \sin(2\theta_P)) \cdot \cos(4\theta_G) + (\frac{1}{2} m_{01} \sin(2\theta_P) + \frac{1}{2} m_{02} \cos(2\theta_P) \\
&\quad + \frac{1}{2} m_{11} \cos(2\theta_A) \sin(2\theta_P) + \frac{1}{2} m_{12} \cos(2\theta_A) \cos(2\theta_P) + \frac{1}{2} m_{21} \sin(2\theta_A) \sin(2\theta_P) \\
&\quad + \frac{1}{2} m_{22} \sin(2\theta_A) \sin(2\theta_P)) \cdot \sin(4\theta_G) \\
&= a_0 + a_1 \cos(2\theta_G) + b_1 \sin(2\theta_G) + a_2 \cos(4\theta_G) + b_2 \sin(4\theta_G) \\
&= a_0 + \sum_{j=1}^{12} (a_j \cos(2j\theta_G) + b_j \sin(2j\theta_G)) = I(\theta_G).
\end{aligned}$$

Like in the PCSCA configuration, we obtained expressions that connect MUELLER matrix elements and FOURIER coefficients. The FOURIER coefficients can be obtained from the intensity measurement as in Equation (53). However, in order to solve this system of equations for MUELLER matrix elements, we would have to perform at least four measurements at different combinations of polarizer and analyzer angles, e.g. for $\theta_P = 0^\circ$ and $\theta_A = [-45^\circ, 0^\circ, 45^\circ, 90^\circ]$.

A.3.2 Error Compensation

When performing the FOURIER transform for a dual-rotating retarder configuration under consideration of the misalignments of the optical elements as described in Section 3.1.4, we obtain the following FOURIER coefficients [70]:

$$\begin{aligned}
 a_0 &= \frac{1}{2}m_{00} + \frac{1}{4}\beta_3m_{01} + \frac{1}{4}\beta_4 \cos(2\varepsilon_5)m_{10} & b_0 &= 0 \\
 &+ \frac{1}{8}\beta_3\beta_4 \cos(2\varepsilon_5)m_{11} + \frac{1}{4}\beta_4 \sin(2\varepsilon_5)m_{20} \\
 &+ \frac{1}{8}\beta_3\beta_4 \sin(2\varepsilon_5)m_{21} \\
 a_1 &= \frac{1}{2} \sin(\delta_1) \sin(2\varepsilon_3)m_{03} & b_1 &= \frac{1}{2} \sin(\delta_1) \cos(2\varepsilon_3)m_{03} \\
 &+ \frac{1}{4}\beta_4 \sin(\delta_1) \sin(2\varepsilon_3) \cos(2\varepsilon_5)m_{13} & &+ \frac{1}{4}\beta_4 \sin(\delta_1) \cos(2\varepsilon_3) \cos(2\varepsilon_5)m_{13} \\
 &+ \frac{1}{4}\beta_4 \sin(\delta_1) \sin(2\varepsilon_3) \sin(2\varepsilon_5)m_{23} & &+ \frac{1}{4}\beta_4 \sin(\delta_1) \cos(2\varepsilon_3) \sin(2\varepsilon_5)m_{23} \\
 a_2 &= \frac{1}{4}\beta_1 (\cos(4\varepsilon_3)m_{01} + \sin(4\varepsilon_3)m_{02}) & b_2 &= \frac{1}{4}\beta_1 (-\sin(4\varepsilon_3)m_{01} + \cos(4\varepsilon_3)m_{02}) \\
 &+ \frac{1}{8}\beta_1\beta_4 (\cos(4\varepsilon_3) \cos(2\varepsilon_5)m_{11} & &+ \frac{1}{8}\beta_1\beta_4 (\cos(4\varepsilon_3) \cos(2\varepsilon_5)m_{12} \\
 &+ \sin(4\varepsilon_3) \cos(2\varepsilon_5)m_{12} & &- \sin(4\varepsilon_3) \cos(2\varepsilon_5)m_{11} \\
 a_3 &= -\frac{1}{8}\beta_1 \sin(2\delta_2) \sin(\alpha_3)m_{31} & b_3 &= -\frac{1}{8}\beta_1 \sin(\delta_2) \cos(\alpha_3)m_{31} \\
 &-\frac{1}{8}\beta_1 \sin(\delta_2) \cos(\alpha_3)m_{32} & &+ \frac{1}{8}\beta_1 \sin(\delta_2) \sin(\alpha_3)m_{32} \\
 a_4 &= -\frac{1}{4} \sin(\delta_1) \sin(\delta_2) \cos(\alpha_1)m_{33} & b_4 &= \frac{1}{4} \sin(\delta_1) \sin(\delta_2) \sin(\alpha_1)m_{33} \\
 a_5 &= \frac{1}{2} \sin(\delta_2) \sin(\alpha_5)m_{30} & b_5 &= -\frac{1}{2} \sin(\delta_2) \cos(\alpha_5)m_{30} \\
 &+ \frac{1}{4}\beta_3 \sin(\delta_2) \sin(\alpha_5)m_{31} & &- \frac{1}{4}\beta_3 \sin(\delta_2) \cos(\alpha_5)m_{31} \\
 a_6 &= \frac{1}{4} \sin(\delta_1) \sin(\delta_2) \cos(\alpha_2)m_{33} & b_6 &= -\frac{1}{4} \sin(\delta_1) \sin(\delta_2) \sin(\alpha_2)m_{33} \\
 a_7 &= -\frac{1}{8}\beta_1 \sin(\delta_2) \sin(\alpha_4)m_{31} & b_7 &= -\frac{1}{8}\beta_1 \sin(\delta_2) \cos(\alpha_4)m_{31} \\
 &+ \frac{1}{8}\beta_1 \sin(\delta_2) \cos(\alpha_4)m_{32} & &- \frac{1}{8}\beta_1 \sin(\delta_2) \sin(\alpha_4)m_{32} \\
 a_8 &= \frac{1}{16}\beta_1\beta_2 \cos(\alpha_9) (m_{11} + m_{22}) & b_8 &= -\frac{1}{16}\beta_1\beta_2 \sin(\alpha_9) (m_{11} + m_{22}) \\
 &+ \frac{1}{16}\beta_1\beta_2 \sin(\alpha_9) (m_{21} - m_{12}) & &- \frac{1}{16}\beta_1\beta_2 \cos(\alpha_9) (m_{12} - m_{21}) \\
 a_9 &= \frac{1}{8}\beta_2 \sin(\delta_1) \sin(\alpha_6)m_{13} & b_9 &= -\frac{1}{8}\beta_2 \sin(\delta_1) \cos(\alpha_6)m_{13} \\
 &+ \frac{1}{8}\beta_2 \sin(\delta_1) \cos(\alpha_6)m_{23} & &+ \frac{1}{8}\beta_2 \sin(\delta_1) \sin(\alpha_6)m_{23} \\
 a_{10} &= \frac{1}{4}\beta_2 \cos(\alpha_{11})m_{10} + \frac{1}{8}\beta_2\beta_3 \cos(\alpha_{11})m_{11} & b_{10} &= -\frac{1}{4}\beta_2 \sin(\alpha_{11})m_{10} - \frac{1}{8}\beta_2\beta_3 \sin(\alpha_{11})m_{11} \\
 &+ \frac{1}{4}\beta_2 \sin(\alpha_{11})m_{20} + \frac{1}{8}\beta_2\beta_3 \sin(\alpha_{11})m_{21} & &+ \frac{1}{4}\beta_2 \cos(\alpha_{11})m_{20} + \frac{1}{8}\beta_2\beta_3 \cos(\alpha_{11})m_{21} \\
 a_{11} &= -\frac{1}{8}\beta_2 \sin(\delta_1) \sin(\alpha_7)m_{13} & b_{11} &= \frac{1}{8}\beta_2 \sin(\delta_1) \cos(\alpha_7)m_{13} \\
 &-\frac{1}{8}\beta_2 \sin(\delta_1) \cos(\alpha_7)m_{23} & &- \frac{1}{8}\beta_2 \sin(\delta_1) \sin(\alpha_7)m_{23} \\
 a_{12} &= \frac{1}{16}\beta_1\beta_2 \cos(\alpha_{10}) (m_{11} - m_{22}) & b_{12} &= -\frac{1}{16}\beta_1\beta_2 \sin(\alpha_{10}) (m_{11} - m_{22}) \\
 &+ \frac{1}{16}\beta_1\beta_2 \sin(\alpha_{10}) (m_{12} + m_{21}) & &+ \frac{1}{16}\beta_1\beta_2 \cos(\alpha_{10}) (m_{12} + m_{21})
 \end{aligned}$$

These expressions use the following supporting parameters α and β :

$$\begin{aligned}\alpha_1 &= 2\varepsilon_4 - 2\varepsilon_3 - 2\varepsilon_5 & \alpha_2 &= 2\varepsilon_4 + 2\varepsilon_3 - 2\varepsilon_5 & \alpha_3 &= 2\varepsilon_4 - 4\varepsilon_3 - 2\varepsilon_5 \\ \alpha_4 &= 2\varepsilon_4 + 4\varepsilon_3 - 2\varepsilon_5 & \alpha_5 &= 2\varepsilon_5 - 2\varepsilon_4 & \alpha_6 &= 2\varepsilon_5 - 4\varepsilon_4 + 2\varepsilon_3\end{aligned}$$

$$\alpha_1 = 2\varepsilon_4 - 2\varepsilon_3 - 2\varepsilon_5$$

$$\alpha_2 = 2\varepsilon_4 + 2\varepsilon_3 - 2\varepsilon_5$$

$$\alpha_3 = 2\varepsilon_4 - 4\varepsilon_3 - 2\varepsilon_5$$

$$\alpha_4 = 2\varepsilon_4 + 4\varepsilon_3 - 2\varepsilon_5$$

$$\alpha_5 = 2\varepsilon_5 - 2\varepsilon_4$$

$$\alpha_6 = 2\varepsilon_5 - 4\varepsilon_4 + 2\varepsilon_3$$

$$\alpha_7 = 2\varepsilon_5 - 4\varepsilon_4 - 2\varepsilon_3$$

$$\alpha_8 = -2\varepsilon_5 + 4\varepsilon_4 - 2\varepsilon_3$$

$$\alpha_9 = 4\varepsilon_4 - 4\varepsilon_3 - 2\varepsilon_5$$

$$\alpha_{10} = 4\varepsilon_4 + 2\varepsilon_3 - 2\varepsilon_5$$

$$\alpha_{11} = 4\varepsilon_4 - 2\varepsilon_5$$

$$\beta_1 = 1 - \cos(\delta_1)$$

$$\beta_2 = 1 - \cos(\delta_2)$$

$$\beta_3 = 1 + \cos(\delta_1)$$

$$\beta_4 = 1 + \cos(\delta_2)$$

$$\delta_1 = \cos^{-1} \left(\frac{a_{10} \cos(\alpha_9) - a_8 \cos(\alpha_{11})}{a_{10} \cos(\alpha_9) + a_8 \cos(4\varepsilon_3 - 2\varepsilon_5)} \right)$$

$$\delta_2 = \cos^{-1} \left(\frac{a_2 \cos(\alpha_9) - a_8 \cos(\alpha_{11})}{a_2 \cos(\alpha_9) + a_8 \cos(4\varepsilon_3 - 2\varepsilon_5)} \right)$$

$$\varepsilon_1 = \delta_1 - 90^\circ$$

$$\varepsilon_2 = \delta_2 - 90^\circ$$

$$\varepsilon_3 = \frac{1}{4} \tan^{-1} \left(\frac{b_8}{a_8} \right) - \frac{1}{4} \tan^{-1} \left(\frac{b_{10}}{a_{10}} \right)$$

$$\varepsilon_4 = \frac{1}{2} \tan^{-1} \left(\frac{b_2}{a_2} \right) - \frac{1}{2} \tan^{-1} \left(\frac{b_6}{a_6} \right) + \frac{1}{4} \tan^{-1} \left(\frac{b_8}{a_8} \right) - \frac{1}{4} \tan^{-1} \left(\frac{b_{10}}{a_{10}} \right)$$

$$\varepsilon_5 = \frac{1}{2} \tan^{-1} \left(\frac{b_2}{a_2} \right) + \frac{1}{2} \tan^{-1} \left(\frac{b_8}{a_8} \right) - \frac{1}{2} \tan^{-1} \left(\frac{b_{10}}{a_{10}} \right)$$

For the MUELLER matrix elements follows:

$$\begin{aligned}
 m_{00} &= 4a_0 - \frac{1}{2}\beta_3 m_{01} - \frac{1}{2}\beta_4 \cos(2\varepsilon_5) m_{10} - \frac{1}{4}\beta_3 \beta_4 \cos(2\varepsilon_5) m_{11} - \frac{1}{2}\beta_4 \sin(2\varepsilon_5) m_{20} \\
 &\quad - \frac{1}{4}\beta_3 \beta_4 \sin(2\varepsilon_5) m_{21} \\
 m_{01} &= \frac{1}{2\beta_1} (16a_2 \cos(4\varepsilon_3) - 16b_2 \sin(4\varepsilon_3) - \beta_1 \beta_4 \cos(2\varepsilon_5) m_{11} - \beta_1 \beta_4 \sin(2\varepsilon_5) m_{21}) \\
 m_{02} &= \frac{1}{2\beta_1} (16a_2 \sin(4\varepsilon_3) + 16b_2 \cos(4\varepsilon_3) - \beta_1 \beta_4 \cos(2\varepsilon_5) m_{12} - \beta_1 \beta_4 \sin(2\varepsilon_5) m_{22}) \\
 m_{03} &= -\frac{1}{2}\beta_4 \cos(2\varepsilon_5) m_{13} + \frac{4b_1}{\cos(2\varepsilon_3) \sin(\delta_1)} - \frac{1}{2}\beta_4 \sin(2\varepsilon_5) m_{23} \\
 m_{10} &= \frac{1}{2\beta_2} (16a_{10} \cos(\alpha_{11}) - 16b_{10} \sin(\alpha_{11}) - \beta_1 \beta_3 m_{11}) \\
 m_{11} &= \frac{16}{\beta_1 \beta_2} (a_8 \cos(\alpha_9) + a_{12} \cos(\alpha_{10}) - b_8 \sin(\alpha_9) - b_{12} \sin(\alpha_{10})) \\
 m_{12} &= \frac{16}{\beta_1 \beta_2} (-a_8 \sin(\alpha_9) + a_{12} \sin(\alpha_{10}) - b_8 \cos(\alpha_9) + b_{12} \cos(\alpha_{10})) \\
 m_{13} &= \frac{8}{\beta_2 \sin(\delta_1)} (a_9 \sin(\alpha_6) - b_9 \cos(\alpha_6) - a_{11} \sin(\alpha_7) + b_{11} \cos(\alpha_7)) \\
 m_{20} &= -\frac{1}{2\beta_2} (\beta_2 \beta_3 m_{21} - 16b_{10} \cos(\alpha_{11}) - 16a_{10} \sin(\alpha_{11})) \\
 m_{21} &= \frac{16}{\beta_1 \beta_2} (a_8 \sin(\alpha_9) + a_{12} \sin(\alpha_{10}) + b_8 \cos(\alpha_9) + b_{12} \cos(\alpha_{10})) \\
 m_{22} &= \frac{16}{\beta_1 \beta_2} (a_8 \cos(\alpha_9) - a_{12} \cos(\alpha_{10}) - b_8 \sin(\alpha_9) + b_{12} \sin(\alpha_{10})) \\
 m_{23} &= \frac{8}{\beta_2 \sin(\delta_1)} (a_9 \cos(\alpha_6) + b_9 \sin(\alpha_6) - a_{11} \cos(\alpha_7) - b_{11} \sin(\alpha_7)) \\
 m_{30} &= -\frac{\beta_3 m_{31}}{2} - \frac{4b_5}{\cos(\alpha_5) \sin(\delta_2)} \\
 m_{31} &= -\frac{8}{\beta_1 \sin(\delta_2)} (a_3 \sin(\alpha_3) + b_3 \cos(\alpha_3) + a_7 \sin(\alpha_4) + b_7 \cos(\alpha_4)) \\
 m_{32} &= \frac{8}{\beta_1 \sin(\delta_2)} (-a_3 \cos(\alpha_3) + b_3 \sin(\alpha_3) + a_7 \cos(\alpha_4) - b_7 \sin(\alpha_4)) \\
 m_{33} &= \frac{4}{\sin(\delta_1) \sin(\delta_2)} \left(-\frac{a_4}{\cos(\alpha_1)} + \frac{a_6}{\cos(\alpha_2)} \right)
 \end{aligned}$$

A.4 Fit Parameters

Parameters for Chapter 3

Table A.2 – Fit parameters of Figure 3.14(a).

Eq.	Size = $A \cdot (\text{Dose Factor})^B$
A	4994.1 ± 2.3
B	0.0139 ± 0.0005
χ^2 (red.)	0.00494

Table A.4 – Fit parameters of Figure 3.14(b).

Eq.	Left Corner	Right Corner
	Deviation = $A + B \cdot e^{-\frac{t}{C}}$	
A	4.088 ± 0.527	4.892 ± 1.106
B	59.80 ± 15.38	160.2 ± 181.4
C	259.1 ± 50.36	97.06 ± 58.11
χ^2 (red.)	0.645	2.343

Table A.3 – Fit parameters of Figure 3.14(c).

Eq.	B	C
	Deviation = $A + B \cdot e^{-\frac{\text{Dose Factor}}{C}}$	
A	61.47 ± 9.86	7087.5 ± 793109
B	-81.04 ± 7.12	-7093.9 ± 793106
C	2.80 ± 0.68	660.75 ± 74118
χ^2 (red.)	0.0041	0.025

Table A.5 – Fit parameters of Figure 3.14(d).

Eq.	B	C
	Deviation = $A \cdot w^B$	
A	3265.1 ± 498.9	2473.5 ± 1851.1
B	-0.947 ± 0.026	-0.952 ± 0.126
χ^2 (red.)	0.035	0.804

Table A.6 – Fit parameters of Figure 3.25(a).

Eq.	$T = A + B \cdot e^{-\frac{t}{C}}$
A	21.993 ± 0.001
B	$(9.014 \pm 1.918) \cdot 10^{10}$
C	0.0626 ± 0.0005
χ^2 (red.)	$8.861 \cdot 10^{-4}$

Parameters for Chapter 4

Table A.7 – Fit parameters of Figure 4.28(b).

	One-Wavelength Lens Fit	Two-Wavelength Lens Fit
Equation	$f = A + B\lambda + C\lambda^2$	
A / μm	3.129 ± 0.081	1.479 ± 0.057
B / $\mu\text{m} / \text{nm}$	$(-61.70 \pm 2.339) \cdot 10^{-4}$	$(-16.70 \pm 1.645) \cdot 10^{-4}$
C / $\mu\text{m} / \text{nm}^2$	$(3.420 \pm 1.650) \cdot 10^{-7}$	$(6.011 \pm 1.160) \cdot 10^{-7}$
χ^2 (reduced)	$8.258 \cdot 10^{-5}$	$4.085 \cdot 10^{-5}$

A.5 Derivation of the Characteristic Equation for Surface Plasmon Polaritons

This section gives a detailed derivation of the characteristic Equation (61) for the propagation of SPPs in metal-dielectric waveguides [48, 61, 125].

We consider two opposing interfaces as depicted in Figure 4.1(b). In this configuration, we distinguish three regions. We can find the field components for these three regions for the TM case. For the outer regions ($z > w/2$ or $z < -w/2$):

$$\text{III: } E_x = iA \frac{1}{\omega \varepsilon_0 \varepsilon_3} k_3 e^{i\beta x} e^{-k_3 z}, \quad (98a) \quad \text{II: } E_x = -iB \frac{1}{\omega \varepsilon_0 \varepsilon_2} k_2 e^{i\beta x} e^{k_2 z}, \quad (98d)$$

$$H_y = A e^{i\beta x} e^{-k_3 z}, \quad (98b) \quad H_y = B e^{i\beta x} e^{k_2 z}, \quad (98e)$$

$$E_z = -A \frac{\beta}{\omega \varepsilon_0 \varepsilon_3} e^{i\beta x} e^{-k_3 z}, \quad (98c) \quad E_z = -B \frac{\beta}{\omega \varepsilon_0 \varepsilon_2} e^{i\beta x} e^{k_2 z}, \quad (98f)$$

and for the middle region ($-w/2 < z < w/2$):

$$\text{I: } E_x = -iC \frac{1}{\omega \varepsilon_0 \varepsilon_1} k_1 e^{i\beta x} e^{k_1 z} + iD \frac{1}{\omega \varepsilon_0 \varepsilon_1} k_1 e^{i\beta x} e^{-k_1 z}, \quad (99a)$$

$$H_y = C e^{i\beta x} e^{k_1 z} + D e^{i\beta x} e^{-k_1 z}, \quad (99b)$$

$$E_z = C \frac{\beta}{\omega \varepsilon_0 \varepsilon_1} e^{i\beta x} e^{k_1 z} + D \frac{\beta}{\omega \varepsilon_0 \varepsilon_1} e^{i\beta x} e^{-k_1 z}. \quad (99c)$$

H_y and E_x need to be continuous at the interfaces ($z = \pm w/2$). For H_y at the upper interface (III/I, $z = w/2$):

$$H_{y,3} = H_{y,1} \quad (100a)$$

$$A e^{i\beta x} e^{-k_3 z} = C e^{i\beta x} e^{k_1 z} + D e^{i\beta x} e^{-k_1 z} \quad (100b)$$

$$A e^{-k_3 z} = C e^{k_1 z} + D e^{-k_1 z} \quad (100c)$$

$$A e^{-k_3 \frac{w}{2}} = C e^{k_1 \frac{w}{2}} + D e^{-k_1 \frac{w}{2}} \quad (100d)$$

For H_y at the lower interface (II/I, $z = -w/2$):

$$H_{y,2} = H_{y,1} \quad (101a)$$

$$B e^{i\beta x} e^{k_2 z} = C e^{i\beta x} e^{k_1 z} + D e^{i\beta x} e^{-k_1 z} \quad (101b)$$

$$B e^{k_2 z} = C e^{k_1 z} + D e^{-k_1 z} \quad (101c)$$

$$B e^{-k_2 \frac{w}{2}} = C e^{-k_1 \frac{w}{2}} + D e^{k_1 \frac{w}{2}} \quad (101d)$$

For E_x at the upper interface (III/I, $z = w/2$):

$$E_{x,3} = E_{x,1} \tag{102a}$$

$$iA \frac{1}{\omega \epsilon_0 \epsilon_3} k_3 e^{i\beta x} e^{-k_3 z} = -iC \frac{1}{\omega \epsilon_0 \epsilon_1} k_1 e^{i\beta x} e^{k_1 z} + iD \frac{1}{\omega \epsilon_0 \epsilon_1} k_1 e^{i\beta x} e^{-k_1 z} \tag{102b}$$

$$A \frac{k_3}{\epsilon_3} e^{-k_3 z} = -C \frac{k_1}{\epsilon_1} e^{k_1 z} + D \frac{k_1}{\epsilon_1} e^{-k_1 z} \tag{102c}$$

$$A \frac{k_3}{\epsilon_3} e^{-k_3 \frac{w}{2}} = -C \frac{k_1}{\epsilon_1} e^{k_1 \frac{w}{2}} + D \frac{k_1}{\epsilon_1} e^{-k_1 \frac{w}{2}} \tag{102d}$$

For E_x at the lower interface (II/I, $z = -w/2$):

$$E_{x,2} = E_{x,1} \tag{103a}$$

$$-iB \frac{1}{\omega \epsilon_0 \epsilon_2} k_2 e^{i\beta x} e^{k_2 z} = -iC \frac{1}{\omega \epsilon_0 \epsilon_1} k_1 e^{i\beta x} e^{k_1 z} + iD \frac{1}{\omega \epsilon_0 \epsilon_1} k_1 e^{i\beta x} e^{-k_1 z} \tag{103b}$$

$$-B \frac{k_2}{\epsilon_2} e^{k_2 z} = -C \frac{k_1}{\epsilon_1} e^{k_1 z} + D \frac{k_1}{\epsilon_1} e^{-k_1 z} \tag{103c}$$

$$-B \frac{k_2}{\epsilon_2} e^{-k_2 \frac{w}{2}} = -C \frac{k_1}{\epsilon_1} e^{-k_1 \frac{w}{2}} + D \frac{k_1}{\epsilon_1} e^{k_1 \frac{w}{2}} \tag{103d}$$

These four conditions form a linear system which can be solved to obtain an implicit expression for the dispersion relation. Inserting Equation (100d) in (102d):

$$\frac{k_3}{\epsilon_3} \left(C e^{k_1 \frac{w}{2}} + D e^{-k_1 \frac{w}{2}} \right) = \frac{k_1}{\epsilon_1} \left(-C e^{k_1 \frac{w}{2}} + D e^{-k_1 \frac{w}{2}} \right) \tag{104a}$$

$$\frac{k_3}{\epsilon_3} C e^{k_1 \frac{w}{2}} + \frac{k_3}{\epsilon_3} D e^{-k_1 \frac{w}{2}} = -\frac{k_1}{\epsilon_1} C e^{k_1 \frac{w}{2}} + \frac{k_1}{\epsilon_1} D e^{-k_1 \frac{w}{2}} \tag{104b}$$

$$\frac{k_3}{\epsilon_3} C e^{k_1 \frac{w}{2}} + \frac{k_1}{\epsilon_1} C e^{k_1 \frac{w}{2}} = \frac{k_1}{\epsilon_1} D e^{-k_1 \frac{w}{2}} - \frac{k_3}{\epsilon_3} D e^{-k_1 \frac{w}{2}} \tag{104c}$$

$$C e^{k_1 \frac{w}{2}} \left(\frac{k_1}{\epsilon_1} + \frac{k_3}{\epsilon_3} \right) = D e^{-k_1 \frac{w}{2}} \left(\frac{k_1}{\epsilon_1} - \frac{k_3}{\epsilon_3} \right) \tag{104d}$$

$$\frac{\frac{k_1}{\epsilon_1} + \frac{k_3}{\epsilon_3}}{\frac{k_1}{\epsilon_1} - \frac{k_3}{\epsilon_3}} = \frac{D}{C} e^{-2k_1 \frac{w}{2}} \tag{104e}$$

Equation (101d) in (103d):

$$-\frac{k_2}{\varepsilon_2} \left(Ce^{-k_1 \frac{w}{2}} + De^{k_1 \frac{w}{2}} \right) = \frac{k_1}{\varepsilon_1} \left(-Ce^{-k_1 \frac{w}{2}} + De^{k_1 \frac{w}{2}} \right) \quad (105a)$$

$$-\frac{k_2}{\varepsilon_2} Ce^{-k_1 \frac{w}{2}} - \frac{k_2}{\varepsilon_2} De^{k_1 \frac{w}{2}} = -\frac{k_1}{\varepsilon_1} Ce^{-k_1 \frac{w}{2}} + \frac{k_1}{\varepsilon_1} De^{k_1 \frac{w}{2}} \quad (105b)$$

$$-\frac{k_2}{\varepsilon_2} Ce^{-k_1 \frac{w}{2}} + \frac{k_1}{\varepsilon_1} Ce^{-k_1 \frac{w}{2}} = \frac{k_2}{\varepsilon_2} De^{k_1 \frac{w}{2}} + \frac{k_1}{\varepsilon_1} De^{k_1 \frac{w}{2}} \quad (105c)$$

$$Ce^{-k_1 \frac{w}{2}} \left(\frac{k_1}{\varepsilon_1} - \frac{k_2}{\varepsilon_2} \right) = De^{k_1 \frac{w}{2}} \left(\frac{k_1}{\varepsilon_1} + \frac{k_2}{\varepsilon_2} \right) \quad (105d)$$

$$\frac{\frac{k_1}{\varepsilon_1} - \frac{k_2}{\varepsilon_2}}{\frac{k_1}{\varepsilon_1} + \frac{k_2}{\varepsilon_2}} = \frac{D}{C} e^{2k_1 \frac{w}{2}} \quad (105e)$$

Now we compare Equations (104e) and (105e) which yields:

$$e^{-4k_1 \frac{w}{2}} = \frac{\frac{k_1}{\varepsilon_1} + \frac{k_3}{\varepsilon_3} \frac{k_1}{\varepsilon_1} + \frac{k_2}{\varepsilon_2}}{\frac{k_1}{\varepsilon_1} - \frac{k_3}{\varepsilon_3} \frac{k_1}{\varepsilon_1} - \frac{k_2}{\varepsilon_2}} \quad (106)$$

Let's now consider the special case that regions 2 and 3 are of the same material. We assume these outer regions to be metal (index m) and the inner region to be dielectric (index d). This simplifies equation 106 to:

$$e^{-4k_d \frac{w}{2}} = \left(\frac{\frac{k_d}{\varepsilon_d} + \frac{k_m}{\varepsilon_m}}{\frac{k_d}{\varepsilon_d} - \frac{k_m}{\varepsilon_m}} \right)^2 \quad (107)$$

Taking the square root from this has two solutions:

$$e^{-2k_d \frac{w}{2}} = \frac{\frac{k_d}{\varepsilon_d} + \frac{k_m}{\varepsilon_m}}{\frac{k_d}{\varepsilon_d} - \frac{k_m}{\varepsilon_m}} \quad (108a)$$

$$e^{-2k_d \frac{w}{2}} = -\frac{\frac{k_d}{\varepsilon_d} + \frac{k_m}{\varepsilon_m}}{\frac{k_d}{\varepsilon_d} - \frac{k_m}{\varepsilon_m}} \quad (108b)$$

For the moment, let's just focus on the first one of these. The left part of the equation can be rewritten using hyperbolic identities:

$$\tanh(x) = 1 - \frac{2}{e^{2x} + 1} \Leftrightarrow e^{2x} = \frac{2}{1 - \tanh(x)} - 1 \quad (109a)$$

$$\Rightarrow e^{-2k_d \frac{w}{2}} = \frac{2}{1 + \tanh(k_d \frac{w}{2})} - 1 \quad (109b)$$

Together with the right part, this leads to:

$$\frac{2}{1 + \tanh(k_d \frac{w}{2})} - 1 = \frac{\frac{k_d}{\varepsilon_d} + \frac{k_m}{\varepsilon_m}}{\frac{k_d}{\varepsilon_d} - \frac{k_m}{\varepsilon_m}} \quad (110a)$$

$$= \frac{2\varepsilon_d k_m}{\varepsilon_m k_d - \varepsilon_d k_m} + 1 \quad (110b)$$

$$\frac{1}{1 + \tanh(k_d \frac{w}{2})} = \frac{\varepsilon_d k_m}{\varepsilon_m k_d - \varepsilon_d k_m} + 1 \quad (110c)$$

$$= \frac{\varepsilon_d k_m + \varepsilon_m k_d - \varepsilon_d k_m}{\varepsilon_m k_d - \varepsilon_d k_m} = \frac{\varepsilon_m k_d}{\varepsilon_m k_d - \varepsilon_d k_m} \quad (110d)$$

$$1 + \tanh\left(k_d \frac{w}{2}\right) = \frac{\varepsilon_m k_d - \varepsilon_d k_m}{\varepsilon_m k_d} = 1 - \frac{\varepsilon_d k_m}{\varepsilon_m k_d} \quad (110e)$$

$$\tanh\left(k_d \frac{w}{2}\right) = -\frac{\varepsilon_d k_m}{\varepsilon_m k_d} \quad (110f)$$

$$\tanh\left(\frac{w}{2} \sqrt{\beta^2 - k_0^2 \varepsilon_d}\right) = -\frac{\varepsilon_d \sqrt{\beta^2 - k_0^2 \varepsilon_m}}{\varepsilon_m \sqrt{\beta^2 - k_0^2 \varepsilon_d}}, \quad (110g)$$

which describes modes of even vector parity, with $k_d^2 = \beta^2 - k_0^2 \varepsilon_d$. The other solution is derived in a similar way and describes modes of odd vector parity [46, 48, 61, 83, 125].

A.6 Plasmonic Lens Parameters

Design parameters as well as ridge widths w_i and positions x_i of the fabricated inverted plasmonic lenses, for either lens design. Positions are relative to the central ridge.

Table A.8 – Design parameters of inverted plasmonic lenses

Label	Aperture a	(Thickness l)	# Ridges	Wavelength λ_0	Focal Length f
CP-00 / OP-00	50 μm	200 nm	71	455 nm	5 μm
CP-01 / OP-01	100 μm	200 nm	89	532 nm	5 μm
CP-02 / OP-02	100 μm	300 nm	77	632 nm	5 μm
CP-03 / OP-03	100 μm	400 nm	111	1064 nm	5 μm
CP-04 / OP-04	100 μm	600 nm	141	1550 nm	5 μm
CP-10 / OP-10	50 μm	200 nm	69	455 nm	10 μm
CP-11 / OP-11	100 μm	200 nm	89	532 nm	10 μm
CP-12 / OP-12	100 μm	200 nm	75	632 nm	10 μm
CP-13 / OP-13	100 μm	200 nm	117	1064 nm	10 μm
CP-14 / OP-14	100 μm	600 nm	147	1550 nm	10 μm
CS-00 / OS-00	50 μm	200 nm	93	455 nm	5 μm
CS-01 / OS-01	50 μm	200 nm	79	532 nm	5 μm
CS-02 / OS-02	50 μm	300 nm	67	632 nm	5 μm
CS-03 / OS-03	100 μm	400 nm	85	1064 nm	5 μm
CS-04 / OS-04	100 μm	600 nm	59	1550 nm	5 μm
CS-10 / OS-10	50 μm	200 nm	79	455 nm	10 μm
CS-11 / OS-11	50 μm	200 nm	67	532 nm	10 μm
CS-12 / OS-12	50 μm	200 nm	57	632 nm	10 μm
CS-13 / OS-13	100 μm	200 nm	79	1064 nm	10 μm
CS-14 / OS-14	100 μm	600 nm	55	1550 nm	10 μm
CS-20 / OS-20	100 μm	200 nm	65	455 nm	100 μm
CS-21 / OS-21	100 μm	200 nm	59	532 nm	100 μm
CS-22 / OS-22	100 μm	200 nm	49	632 nm	100 μm
CS-23 / OS-23	100 μm	300 nm	29	1064 nm	100 μm
CS-24 / OS-24	100 μm	500 nm	25	1550 nm	100 μm
CS-30 / OS-30	100 μm	200 nm	57	455 nm	1000 μm
CS-31 / OS-31	100 μm	200 nm	55	532 nm	1000 μm
CS-32 / OS-32	100 μm	200 nm	49	632 nm	1000 μm
CS-33 / OS-33	100 μm	300 nm	23	1064 nm	1000 μm
CS-34 / OS-34	100 μm	500 nm	33	1550 nm	1000 μm

Table A.9 – Periodic ridge arrangement, 5 μm focal length, part 1.

<i>i</i>	P-00		P-01		P-02		P-03		P-04	
	x_i / nm	w_i / nm								
0	0	40	0	44	0	55	0	40	0	34
1	200	41	200	45	200	57	200	40	200	34
2	400	47	400	51	400	63	400	42	400	35
3	600	59	600	63	600	77	600	45	600	37
4	800	89	800	91	800	109	800	51	800	39
5	1000	158	2400	50	2600	57	1000	60	1000	42
6	2200	43	4400	92	3800	63	1200	76	1200	48
7	2400	143	5200	134	4800	76	1400	108	1400	55
8	3200	52	6600	140	8000	60	3600	60	1600	67
9	4000	61	7200	67	8800	111	3800	133	1800	86
10	5400	128	7800	47	10200	80	5200	57	2000	123
11	6000	119	11400	44	11600	88	6600	57	4400	44
12	6600	151	12000	53	13000	141	7800	41	4600	65
13	7600	41	12600	69	13600	60	8000	97	4800	120
14	8200	76	13200	103	15000	115	9200	81	6400	35
15	9200	44	15400	53	15600	58	10400	83	6600	53
16	9800	133	16000	85	17000	141	11400	40	6800	97
17	10800	111	18200	68	17600	69	11600	101	8400	46
18	11800	120	18800	144	19600	103	12600	47	8600	80
19	12800	154	20400	69	20200	60	13800	61	10200	50
20	13200	46	22000	46	22200	104	15000	92	10400	96
21	14200	66	22600	84	22800	62	16000	50	11800	39
22	15200	121	24200	57	24800	129	17200	77	12000	67
23	15600	42	24800	127	25400	74	18200	47	13400	34
24	16600	73	25800	44	28000	102	19400	74	13600	55
25	17600	161	26400	83	28600	64	20400	47	13800	118
26	18000	56	28000	62	31200	96	21600	79	15200	49
27	19000	133	28600	157	31800	62	22600	50	15400	97
28	19400	48	29600	50	34400	100	23800	90	16800	46
29	20400	116	30200	110	35000	65	24800	56	17000	88
30	20800	45	31800	84	37600	114	25800	40	18400	45
31	21800	110	33400	69	38200	72	26000	112	18600	84
32	22200	44	35000	60	40800	144	27000	65	20000	44
33	23200	113	35600	156	41400	85	28000	45	20200	84
34	23600	46	36600	53	42000	59	29200	82	21600	45
35	24600	125	37200	126	44600	108	30200	54	21800	87
36			38200	48	45200	71	31400	111	23200	46
37			38800	106	48400	90	32400	67	23400	91
38			39800	44	49000	62	33400	47	24800	49
39			40400	92			34600	90	25000	99
40			42000	82			35600	59	26400	51
41			43600	75			36600	43	26600	110
42			45200	69			36800	136	28000	55
43			46800	65			37800	78	28200	126
44			48400	61			38800	53	29400	35

Table A.10 – Periodic ridge arrangement, 5 μm focal length, part 2.

<i>i</i>	P-00		P-01		P-02		P-03		P-04	
	x_i / nm	w_i / nm								
45							39800	40	29600	60
46							40000	114	31000	38
47							41000	70	31200	66
48							42000	50	32600	41
49							43200	101	32800	74
50							44200	65	34200	44
51							45200	47	34400	85
52							46400	93	35800	48
53							47400	61	36000	99
54							48400	45	37400	54
55							49600	87	37600	120
56									38800	35
57									39000	60
58									40400	38
59									40600	68
60									42000	42
61									42200	79
62									43600	47
63									43800	94
64									45200	52
65									45400	115
66									46600	35
67									46800	59
68									48200	38
69									48400	69
70									49800	43

Table A.11 – Periodic ridge arrangement, 10 μm focal length, part 1.

i	P-10		P-11		P-12		P-13		P-14	
	x_i / nm	w_i / nm								
0	0	40	0	44	0	55	0	40	0	34
1	200	40	200	45	200	56	200	40	200	34
2	400	43	400	47	400	59	400	41	400	34
3	600	48	600	52	600	64	600	42	600	35
4	800	56	800	60	800	74	800	45	800	36
5	1000	72	1000	75	1000	91	1000	48	1000	38
6	1200	102	1200	104	1200	123	1200	53	1200	40
7	1400	155	3400	59	3800	112	1400	60	1400	42
8	3200	66	4800	58	5200	58	1600	70	1600	46
9	4400	46	6000	94	7600	74	1800	86	1800	50
10	4600	155	7000	117	8600	72	2000	113	2000	56
11	5600	153	7800	54	9600	120	4800	44	2200	64
12	6400	75	9400	44	10400	57	5000	66	2400	76
13	7200	69	10200	58	13000	144	5200	123	2600	93
14	8000	111	11000	116	16000	66	7000	55	2800	122
15	8600	41	12400	115	16800	121	7200	110	5800	34
16	9400	128	13000	51	18200	67	8800	71	6000	44
17	10000	69	14400	128	20400	139	10200	44	6200	59
18	10600	50	15000	73	21800	141	10400	93	6400	89
19	11200	44	15600	52	23800	63	11800	79	8600	41
20	11800	43	22800	44	25200	88	13000	42	8800	60
21	12400	46	23400	52	27200	66	13200	95	9000	103
22	13000	56	24000	66	28600	127	14400	56	10800	39
23	13600	78	24600	90	29200	59	15600	42	11000	59
24	14200	135	25200	139	30600	124	15800	103	11200	109
25	15200	41	27400	51	31200	61	17000	79	12800	37
26	15800	76	28000	73	32600	149	18200	70	13000	57
27	17400	82	28600	124	33200	69	19400	68	13200	107
28	18400	50	30200	44	35200	90	20600	71	14800	44
29	19000	152	30800	65	37200	142	21800	81	15000	74
30	20000	109	31400	115	37800	71	22800	40	16600	40
31	21000	90	33000	48	39800	118	23000	101	16800	67
32	22000	85	33600	77	40400	65	24000	46	18400	42
33	23000	91	35800	65	42400	115	25200	57	18600	71
34	24000	108	36400	131	43000	65	26400	76	20200	47
35			38000	61	45000	127	27400	42	20400	88
36			38600	125	45600	71	27600	119	21800	36
37			40200	64	48200	83	28600	55	22000	59
38			40800	139			29800	82	22200	133
39			42400	72			30800	46	23600	46
40			44000	48			32000	67	23800	86
41			44600	91			33000	41	25200	39
42			46200	59			33200	116	25400	66
43			46800	130			34200	59	26800	34
44			48400	79			35400	102	27000	55

Table A.12 – Periodic ridge arrangement, 10 μm focal length, part 2.

<i>i</i>	P-10		P-11		P-12		P-13		P-14	
	x_i / nm	w_i / nm								
45							36400	56	27200	119
46							37600	98	28600	48
47							38600	56	28800	95
48							39800	99	30200	44
49							40800	57	30400	82
50							42000	106	31800	41
51							43000	60	32000	73
52							44000	41	33400	39
53							44200	120	33600	68
54							45200	66	35000	38
55							46200	44	35200	65
56							47400	75	36600	37
57							48400	49	36800	63
58							49600	89	38200	37
59									38400	62
60									39800	37
61									40000	62
62									41400	37
63									41600	63
64									43000	37
65									43200	65
66									44600	38
67									44800	67
68									46200	40
69									46400	71
70									47800	41
71									48000	75
72									49400	43
73									49600	80

Table A.13 – Successive ridge arrangement, 5 μm focal length.

<i>i</i>	S-00		S-01		S-02		S-03		S-04	
	x_i / nm	w_i / nm								
0	0	156	0	199	0	229	0	585	0	448
1	269	164	320	222	359	279	3440	646	4240	483
2	2185	158	2369	202	2594	234	5090	670	6379	484
3	3154	159	3435	205	3775	233	6490	593	8259	481
4	3939	157	4305	204	4750	232	7789	591	10029	493
5	4640	158	5085	208	5630	236	9030	607	11730	455
6	5285	157	5804	203	6449	233	10230	615	13399	463
7	5899	161	6489	201	7234	240	11400	588	15049	504
8	6485	161	7150	201	7990	235	12559	666	16669	470
9	7049	160	7790	201	8724	230	13700	681	18280	457
10	7599	159	8414	200	9450	242	14820	593	19889	504
11	8139	160	9029	204	10160	244	15939	606	21479	474
12	8670	160	9635	207	10859	244	17050	585	23070	482
13	9190	159	10229	206	11550	236	18159	630	24649	460
14	9705	159	10819	208	12234	234	19259	614	26230	462
15	10215	160	11400	200	12914	234	20359	645	27810	484
16	10720	161	11980	203	13590	232	21450	597	29380	462
17	11220	161	12555	204	14264	245	22550	703	30950	456
18	11715	159	13124	202	14929	233	23629	599	32520	461
19	12209	161	13695	207	15594	233	24720	641	34090	477
20	12700	161	14259	207	16260	243	25799	585	35660	504
21	13185	158	14820	201	16919	242	26890	669	37220	474
22	13670	157	15380	200	17574	231	27969	650	38780	454
23	14155	159	15939	204	18235	245	29049	647	40350	502
24	14635	157	16495	200	18890	247	30130	659	41910	493
25	15114	157	17049	199	19540	235	31210	682	43469	489
26	15594	159	17605	202	20195	248	32280	596	45030	490
27	16075	162	18160	209	20844	246	33360	641	46590	495
28	16550	161	18710	206	21490	229	34439	695	48150	504
29	17024	161	19260	205	22139	235	35510	637	49699	453
30	17494	157	19810	208	22790	245	36580	586		
31	17970	159	20355	199	23435	239	37659	664		
32	18440	157	20905	206	24079	236	38730	626		
33	18915	162	21450	202	24725	235	39800	595		
34	19385	161	21995	200			40879	690		
35	19849	156	22545	211			41950	669		
36	20320	158	23084	200			43020	653		
37	20790	160	23630	202			44090	641		
38	21255	156	24175	206			45160	633		
39	21725	160	24719	211			46230	628		
40	22190	158					47300	627		
41	22655	156					48370	630		
42	23125	161					49439	635		
43	23590	161								
44	24055	161								
45	24520	162								
46	24979	157								

Table A.14 – Successive ridge arrangement, 10 μm focal length.

<i>i</i>	S-10		S-11		S-12		S-13		S-14	
	x_i / nm	w_i / nm								
0	0	156	0	199	0	299	0	585	0	448
1	264	160	314	212	349	253	810	809	629	594
2	535	169	644	234	739	314	4739	615	5779	450
3	3055	158	3304	199	3614	235	6870	639	8469	478
4	4365	158	4734	200	5184	230	8610	632	10709	465
5	5405	159	5874	205	6445	233	10170	668	12750	471
6	6304	158	6864	203	7549	237	11609	620	14670	473
7	7119	157	7765	201	8554	230	12979	601	16509	462
8	7880	158	8605	201	9499	234	14300	604	18300	472
9	8594	158	9400	200	10395	230	15580	598	20049	481
10	9280	159	10164	208	11260	243	16829	593	21769	491
11	9935	158	10895	201	12089	236	18059	630	23460	462
12	10569	157	11610	207	12899	237	19270	660	25140	484
13	11189	159	12299	200	13690	235	20459	646	26799	478
14	11795	160	12979	203	14465	234	21639	668	28449	487
15	12385	160	13644	202	15229	243	22800	592	30090	499
16	12964	160	14299	203	15980	241	23960	622	31719	505
17	13535	160	14944	204	16720	238	25110	633	33339	494
18	14094	159	15580	202	17450	230	26249	612	34950	463
19	14650	159	16209	205	18174	231	27390	663	36559	466
20	15195	157	16829	201	18894	237	28519	662	38170	499
21	15739	160	17450	210	19605	230	29640	602	39770	498
22	16275	158	18059	209	20315	241	30760	593	41360	458
23	16805	156	18665	207	21014	233	31879	628	42960	502
24	17335	159	19265	204	21715	241	32990	588	44550	502
25	17860	161	19864	209	22410	245	34099	585	46130	457
26	18380	161	20454	201	23100	244	35210	615	47720	488
27	18894	160	21045	199	23785	236	36320	677	49300	472
28	19404	156	21635	205	24469	239	37420	647		
29	19920	161	22219	206			38520	644		
30	20425	158	22800	201			39620	664		
31	20930	158	23380	201			40710	587		
32	21434	160	23959	207			41810	649		
33	21935	159	24534	206			42900	610		
34	22435	160					43990	588		
35	22930	157					45090	702		
36	23424	156					46169	591		
37	23919	158					47260	613		
38	24415	160					48350	649		
39	24905	159					49439	697		

Table A.15 – Successive ridge arrangement, 100 μm focal length.

i	S-20		S-21		S-22		S-23		S-24	
	x_i / nm	w_i / nm								
0	0	156	0	199	0	229	0	585	0	448
1	269	157	309	200	340	232	709	615	560	457
2	539	158	619	204	690	239	1490	719	1139	488
3	810	160	940	210	1049	251	2369	816	1769	557
4	1079	163	1259	218	1419	269	14629	591	2529	738
5	1349	166	1589	226	1809	291	20740	586	3839	1653
6	1629	168	1929	233	2219	310	25470	592	17680	453
7	1910	170	2269	235	11269	233	29489	605	25099	460
8	9559	157	10329	200	15950	229	33050	585	30849	451
9	13529	158	14629	201	19569	233	36299	592	35760	457
10	16580	156	17940	200	22630	232	39309	596	40130	458
11	19170	157	20740	199	25340	232	42130	589	44120	451
12	21459	158	23220	200	27800	230	44800	592	47839	474
13	23529	157	25470	201	30080	237	47350	629		
14	25439	156	27550	203	32200	231	49779	599		
15	27230	157	29489	204	34209	236				
16	28910	156	31320	204	36119	242				
17	30509	157	33050	199	37940	242				
18	32040	159	34710	201	39679	233				
19	33499	159	36299	201	41370	243				
20	34900	156	37830	200	42990	234				
21	36260	157	39309	202	44569	240				
22	37579	160	40740	200	46100	239				
23	38850	158	42130	200	47590	240				
24	40090	158	43490	208	49040	235				
25	41299	160	44800	201						
26	42479	161	46089	205						
27	43629	160	47350	209						
28	44750	158	48580	208						
29	45850	156	49779	202						
30	46940	161								
31	47999	160								
32	49040	159								

Table A.16 – Successive ridge arrangement, 1000 μm focal length.

i	S-30		S-31		S-32		S-33		S-34	
	x_i / nm	w_i / nm								
0	0	156	0	199	0	229	0	585	0	448
1	269	156	309	199	340	230	699	588	560	449
2	539	156	619	200	680	230	1400	596	1119	452
3	810	157	929	200	1020	231	2109	611	1679	456
4	1079	157	1240	201	1360	233	2840	634	2250	463
5	1349	157	1549	202	1700	235	3599	664	2829	472
6	1620	158	1859	204	2049	238	4389	702	3419	484
7	1889	158	2170	205	2399	241	5220	746	4019	499
8	2159	159	2489	207	2749	244	6099	788	4639	518
9	2429	160	2810	209	3109	248	7009	813	5279	542
10	2699	161	3129	211	3469	253	7930	812	5949	575
11	2970	161	3449	214	3839	258	46150	589	6660	618
12	3239	162	3780	216	4210	264			7420	678
13	3509	163	4110	219	4590	271			8249	768
14	3780	164	4439	222	4970	277			9200	918
15	4049	165	4769	224	5359	284			10379	1219
16	4330	166	5109	227	5759	291			11920	1645
17	4609	167	5449	229	6169	298				
18	4889	167	5789	231	6580	305				
19	5170	168	6129	233	7000	310				
20	5449	169	6469	234	7420	314				
21	5730	169	6809	235	7850	317				
22	6009	170	7159	235	35560	230				
23	6289	170	32629	200	35920	279				
24	30169	156	32949	223	36329	314				
25	30439	165	33289	234						
26	30719	169	46150	200						
27	42680	157	46479	230						
28	42949	167								

Table A.17 – Proof-of-concept merged plasmonic lens parameters. Lens thickness $l = 200 \text{ nm}$.

i	532 nm	532 nm	632 nm	632 nm
	x_i / nm	w_i / nm	x_i / nm	w_i / nm
0	0	22	0	13
1	127	23	118	13
2	260	29	238	15
3	406	51	361	19
4	1040	22	491	29
5	1191	69	666	109
6	1652	22	1161	13
7	2223	22	1284	22
8			1869	13
9			1993	24



Further Figures

MUELLER matrix images tend to need a lot of memory. For example, the measurement of Figure 5.1 alone used up 17.1 GB of hard drive space. The measurements of MUELLER matrix images at different focus positions from Section 5.1.2 even used up more than 250 GB. Boiling this information down to one image of 300 dpi resolution still ends up as a file with about 100 KB per matrix image, albeit at the cost of several pixels of the original images. Therefore, it should be self-evident that not each and every MUELLER matrix image measured for this thesis can be visualized here. In this part of the Appendix, however, a few matrix images that might be helpful for the comprehensibility of this work are collected.

B.1 MUELLER Matrix Images of the Nanoform Sample

B.1.1 Row A, without drift correction

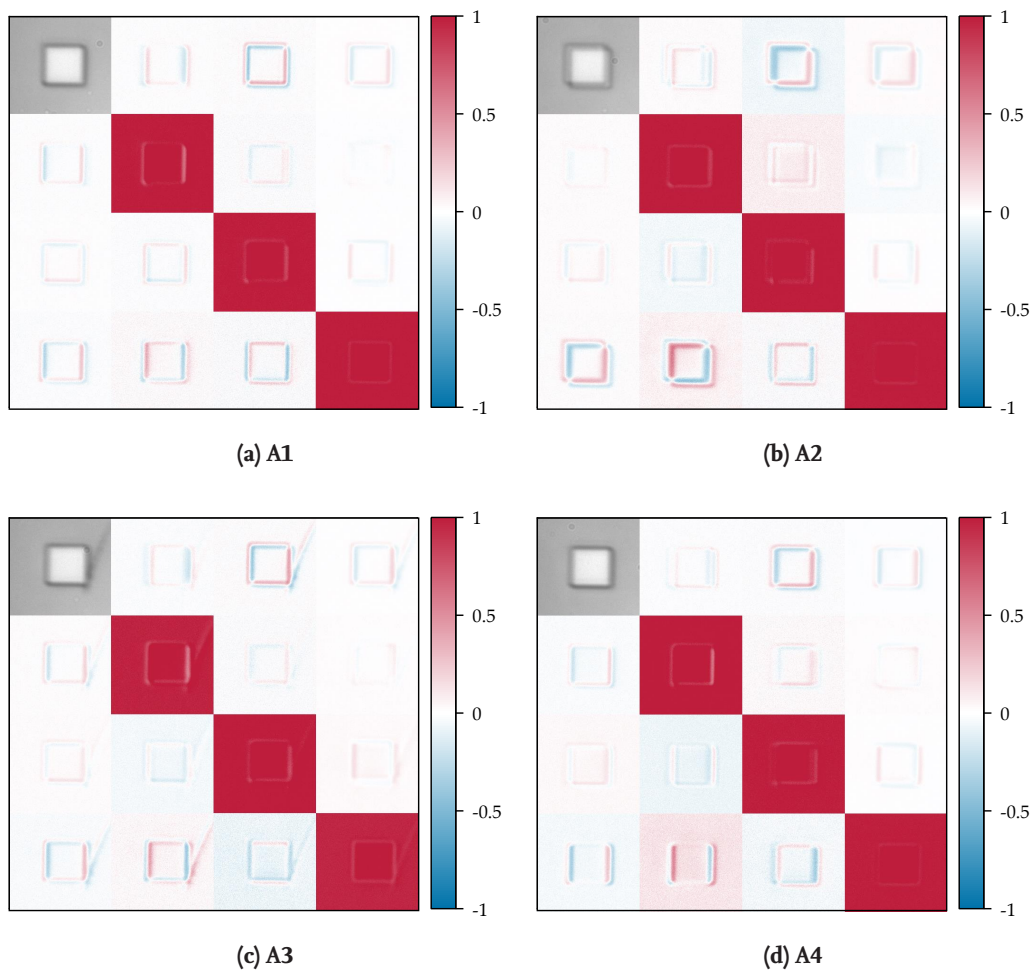


Figure B.1 – Measured MUELLER matrix images of row A at MUELLER matrix microscope without drift correction, part 1.

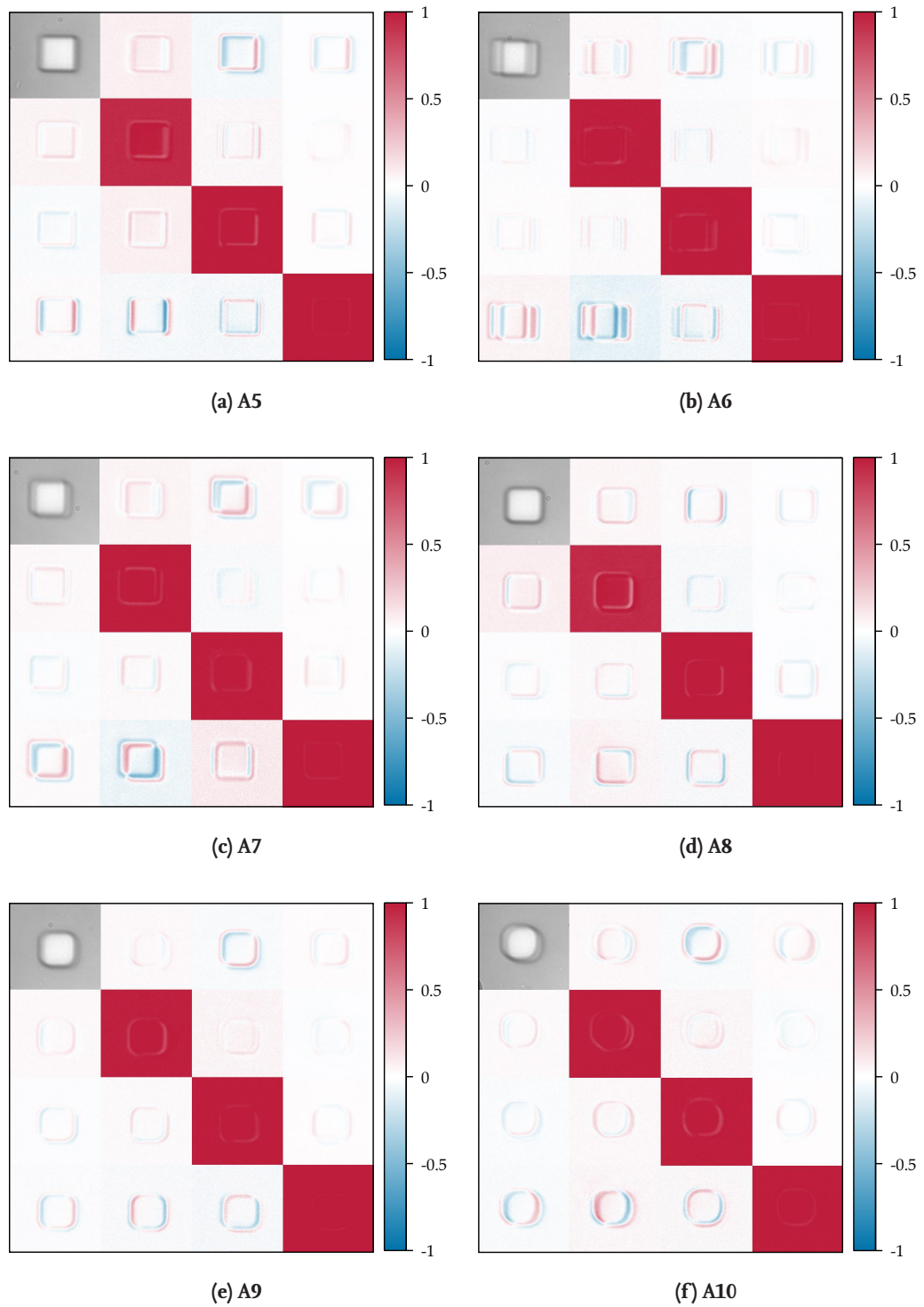


Figure B.2 – Measured MUELLER matrix images of row A at MUELLER matrix microscope without drift correction, part 2.

B.1.2 Row A, with drift correction

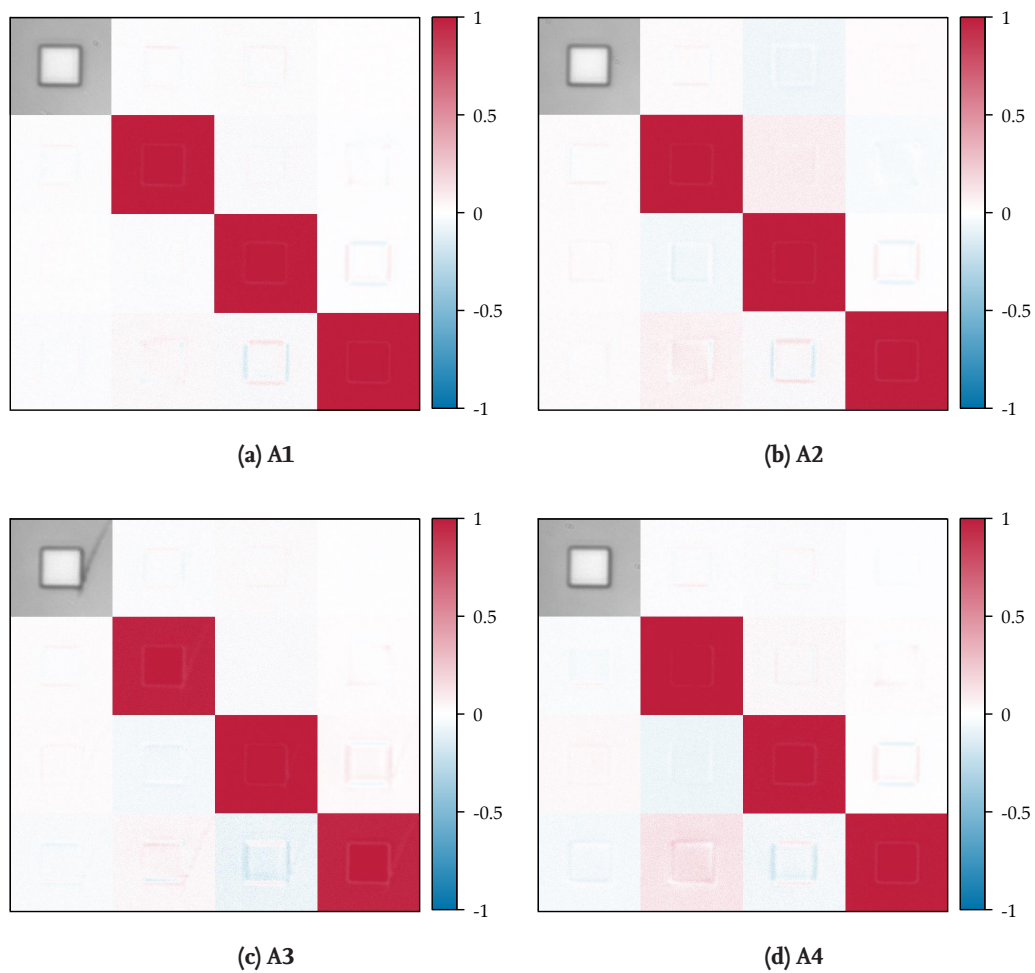


Figure B.3 – Measured MUELLER matrix images of row A at MUELLER matrix microscope with drift correction, part 1.

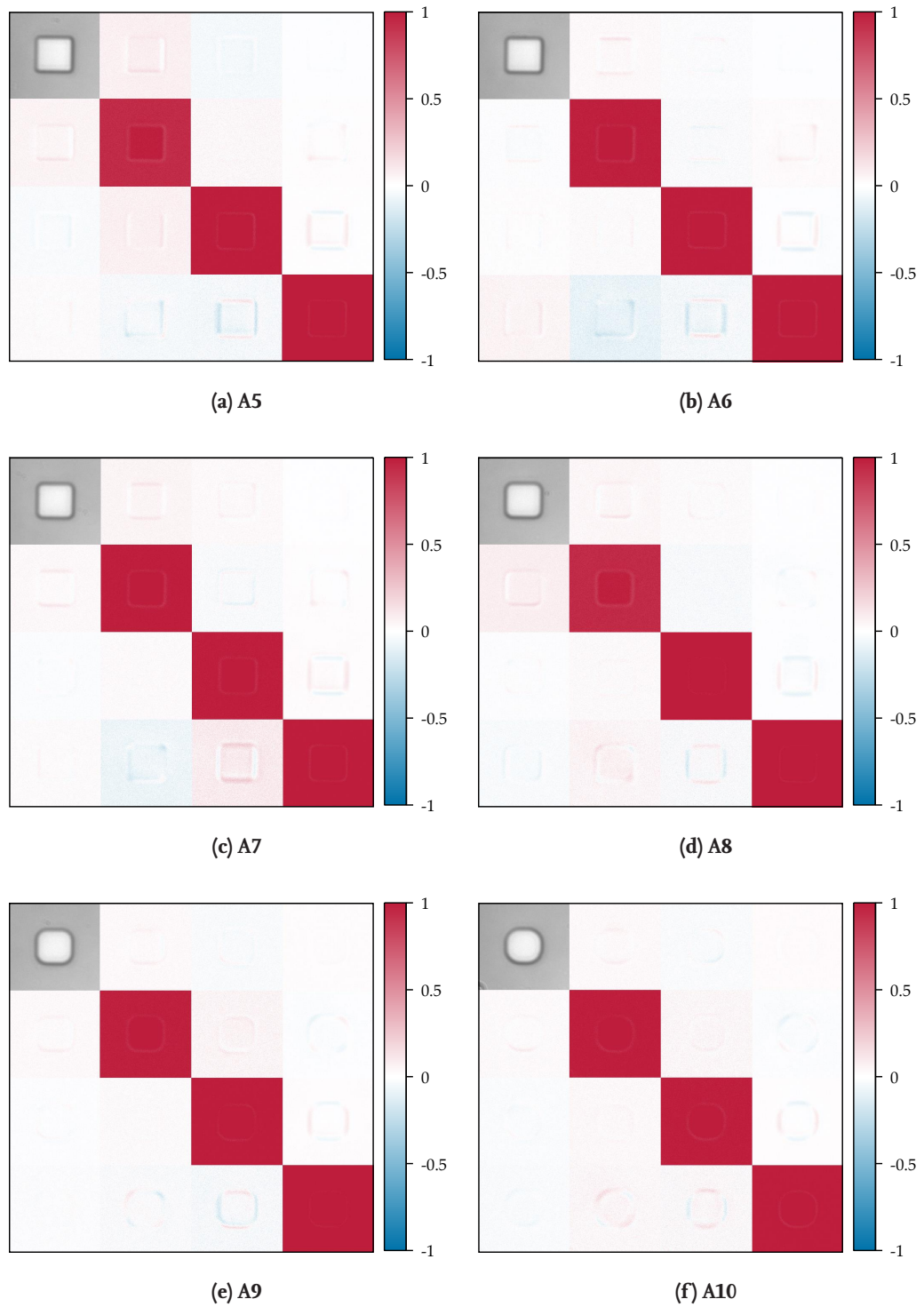


Figure B.4 – Measured MUELLER matrix images of row A at MUELLER matrix microscope with drift correction, part 2.

B.1.3 Row A, simulated

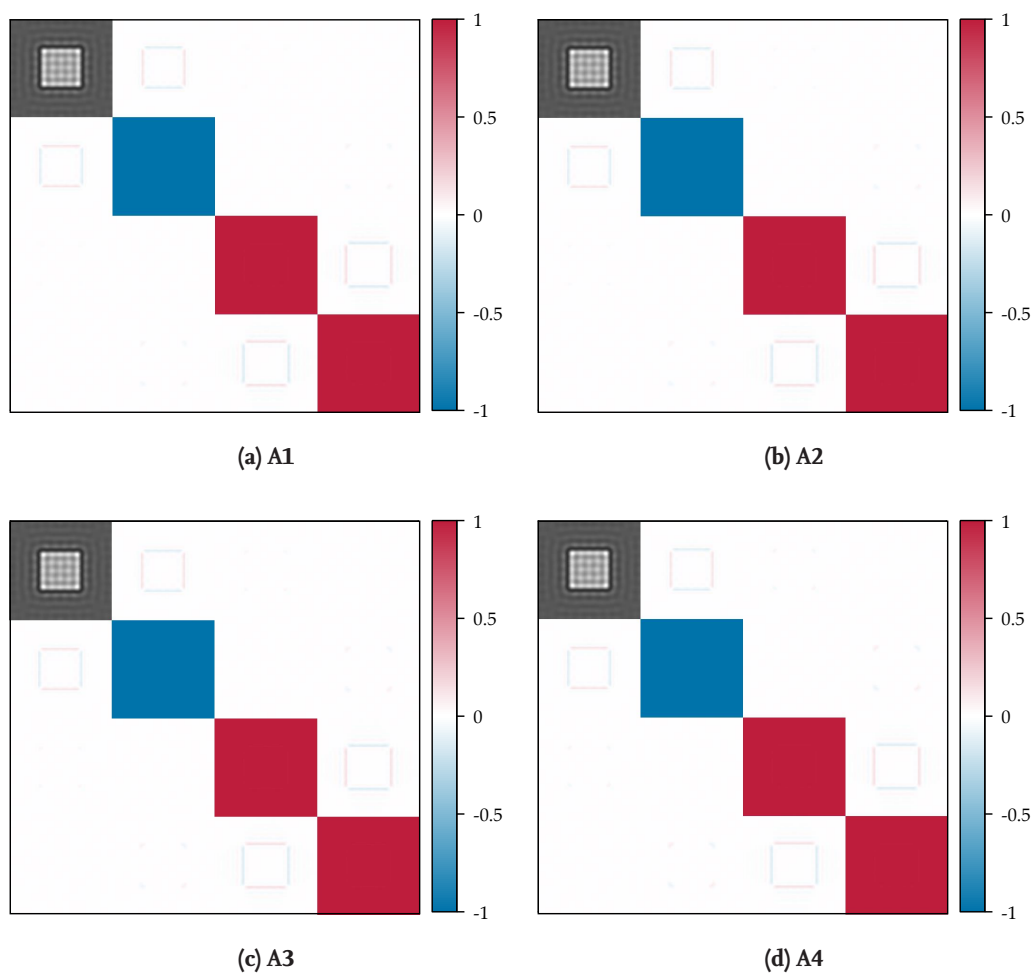


Figure B.5 – Simulated MUELLER matrix images of row A, part 1.

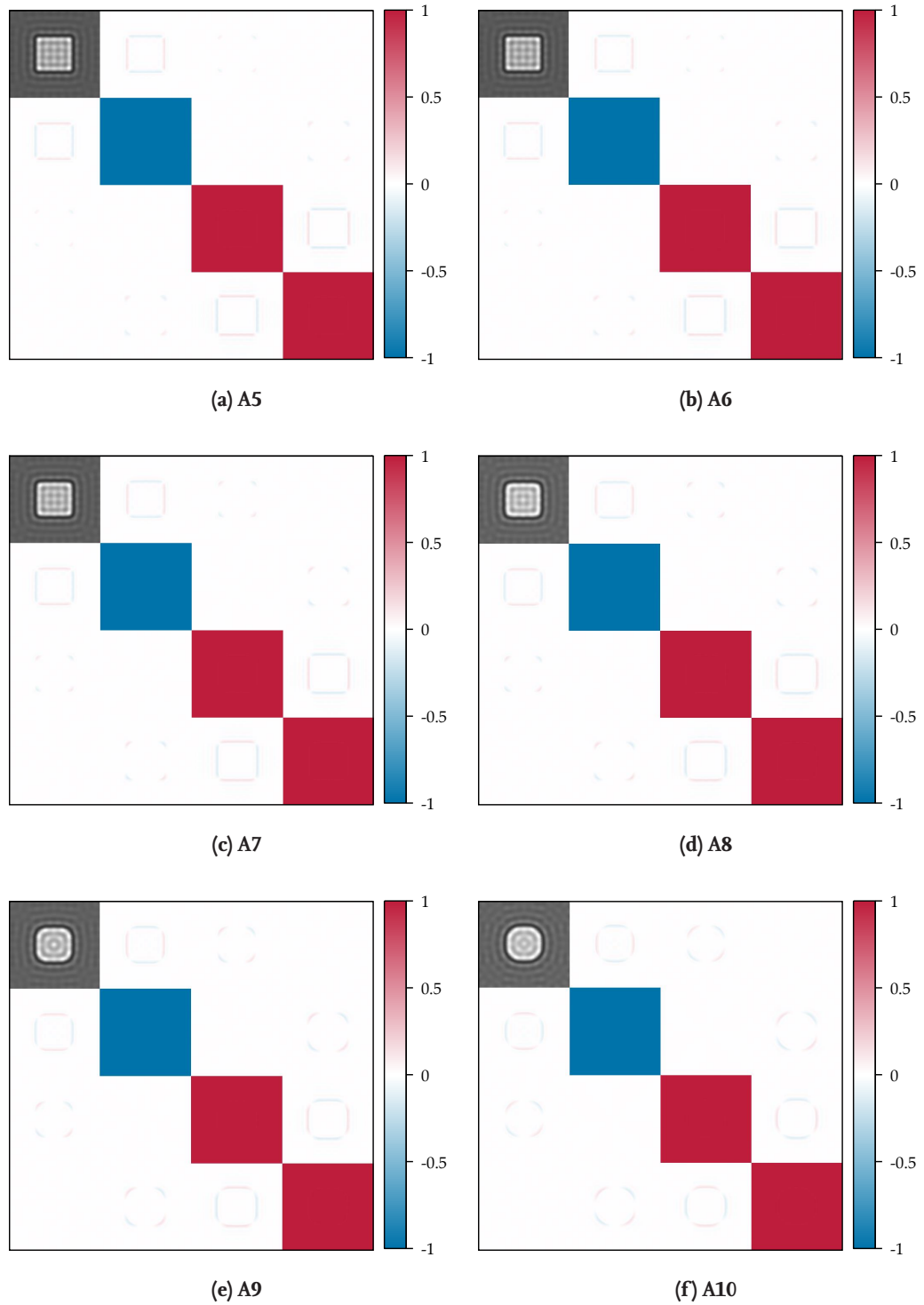


Figure B.6 – Simulated MUELLER matrix images of row A, part 2.

B.1.4 Row C

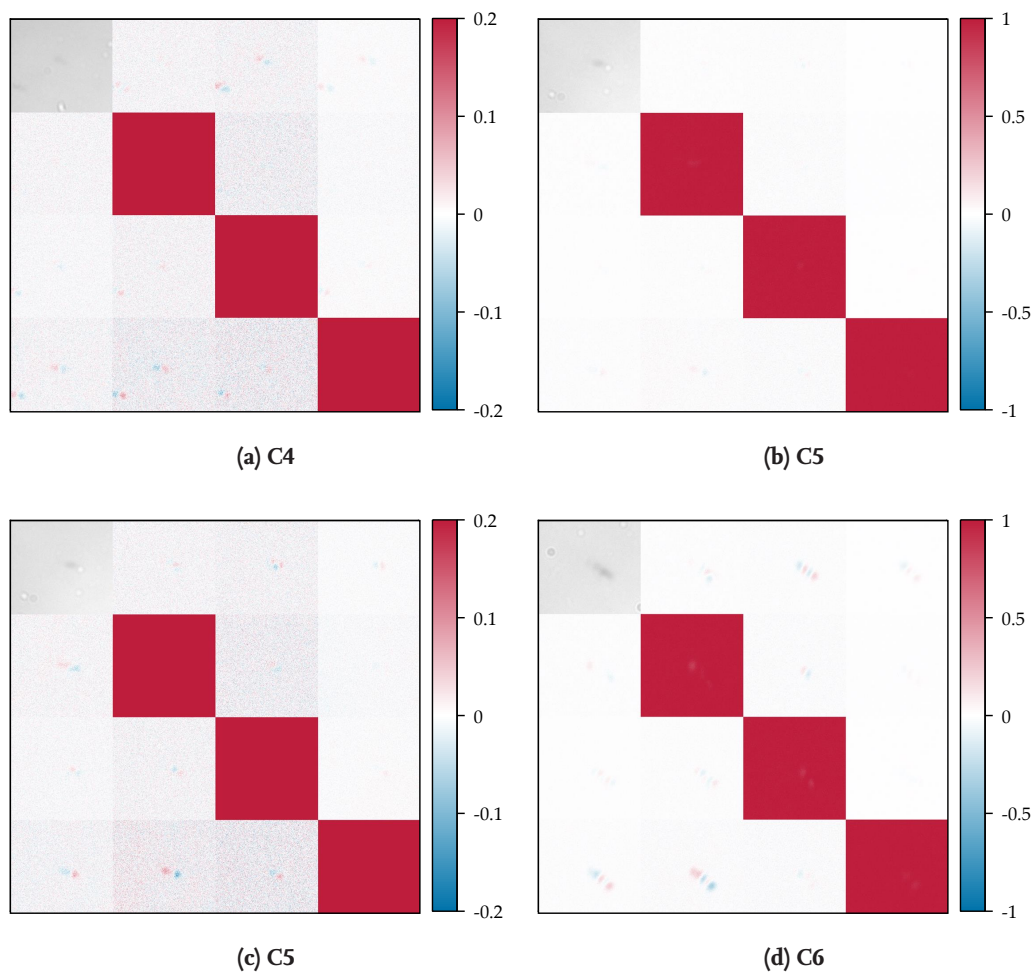


Figure B.7 – Measured MUELLER matrix images of row C without drift correction, part 1.

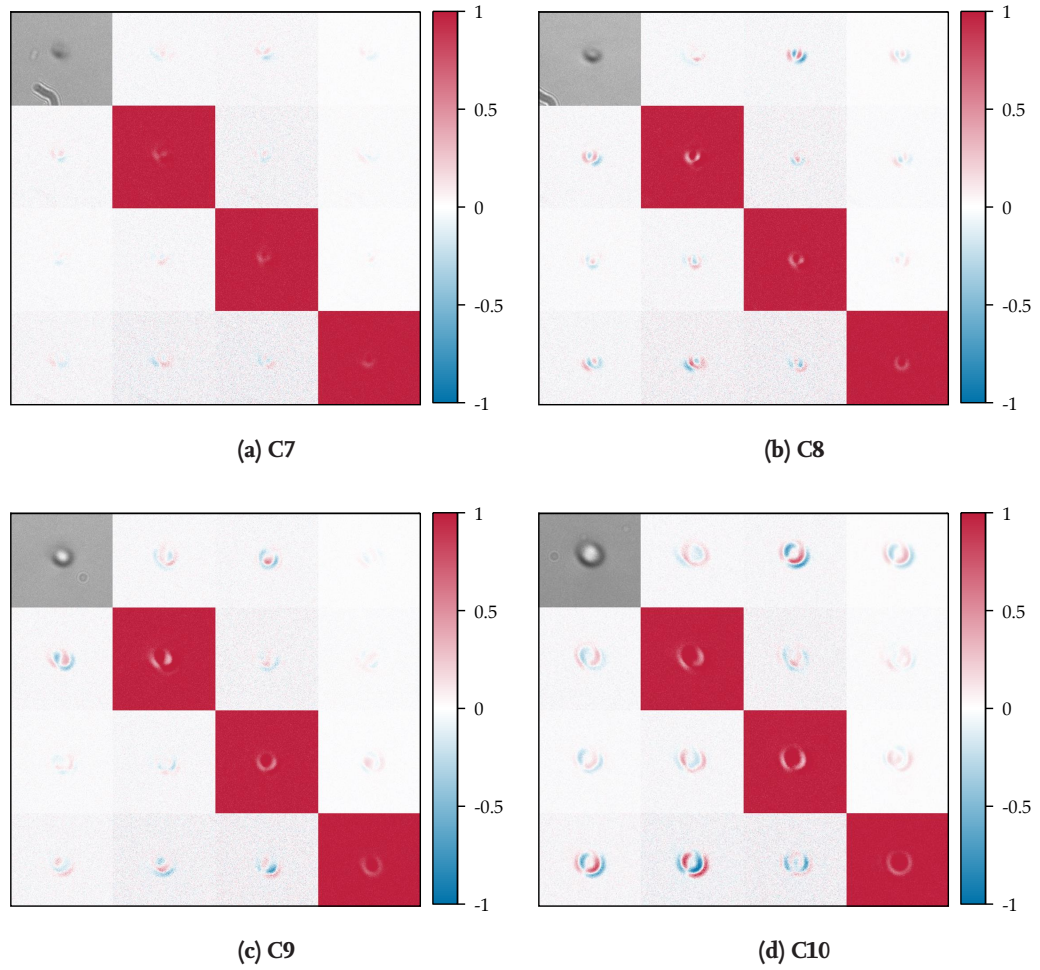


Figure B.8 – Measured MUELLER matrix images of row C without drift correction, part 2.

B.2 MUELLER Matrix Images of Plasmonic Lenses

B.2.1 OS-00, Measurement at EP4, PCSA

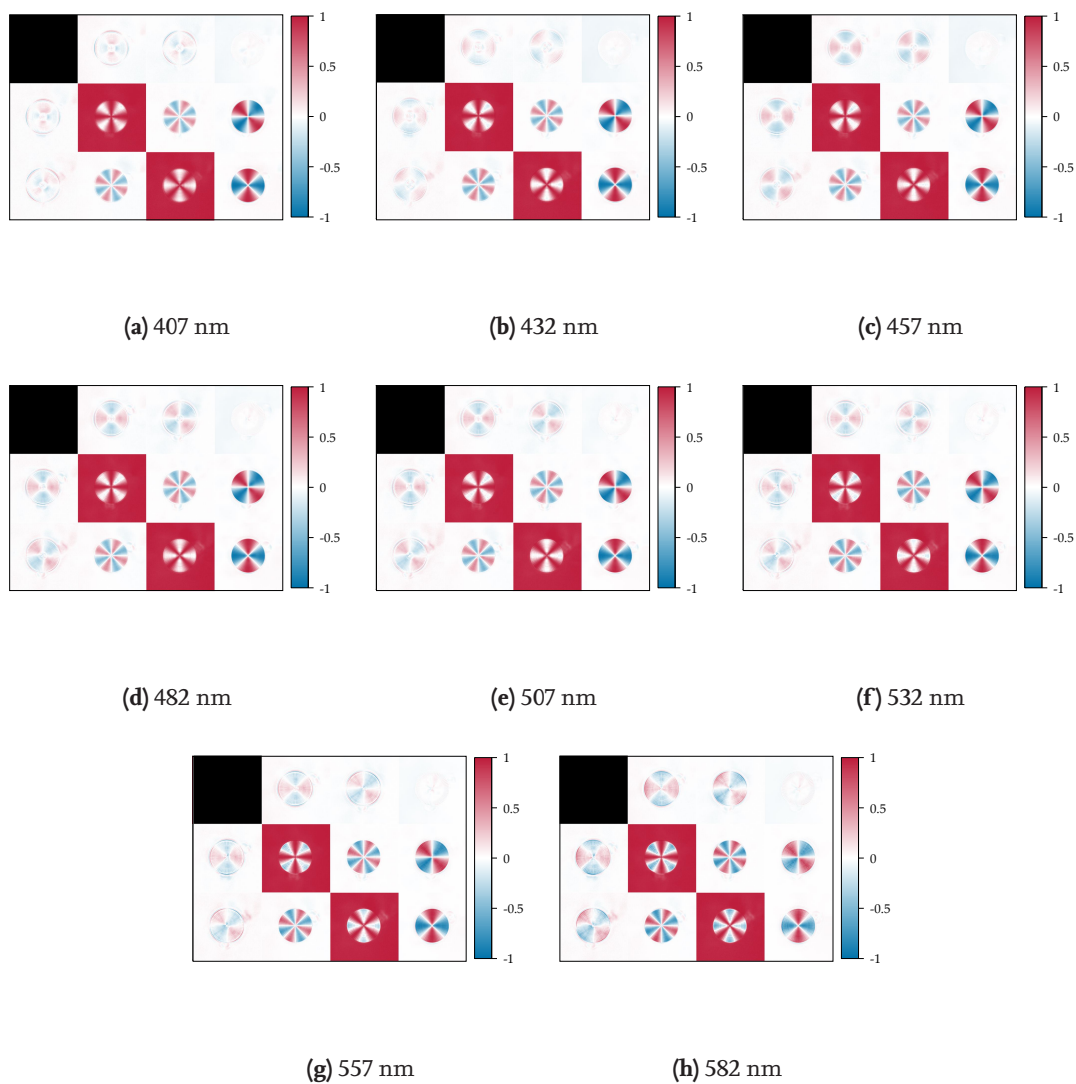


Figure B.9 – Measured MUELLER matrix images at different wavelengths, part 1.

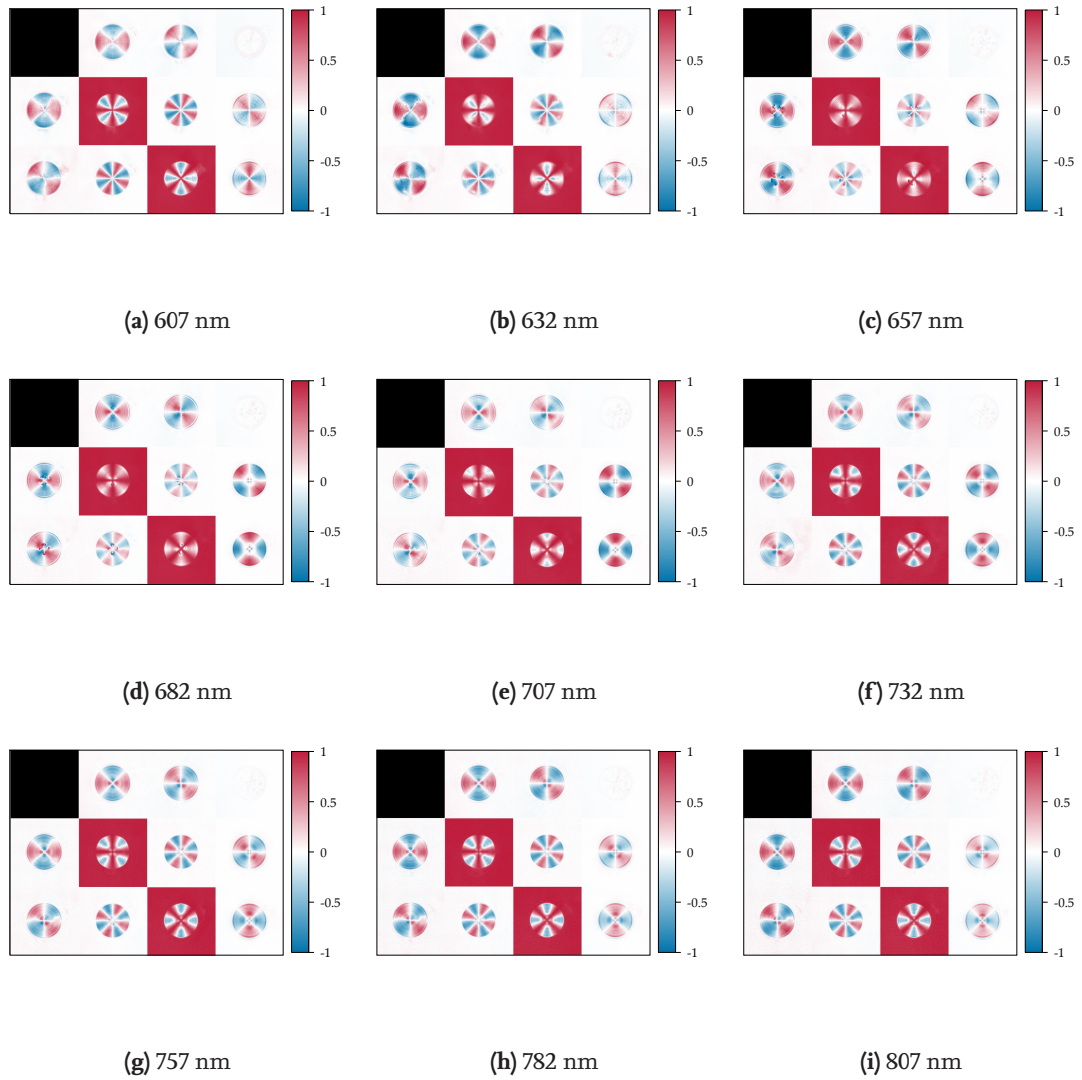


Figure B.10 – Measured MUELLER matrix images at different wavelengths, part 2.

B.2.2 OS-00, Measurement at EP4, PCSCA

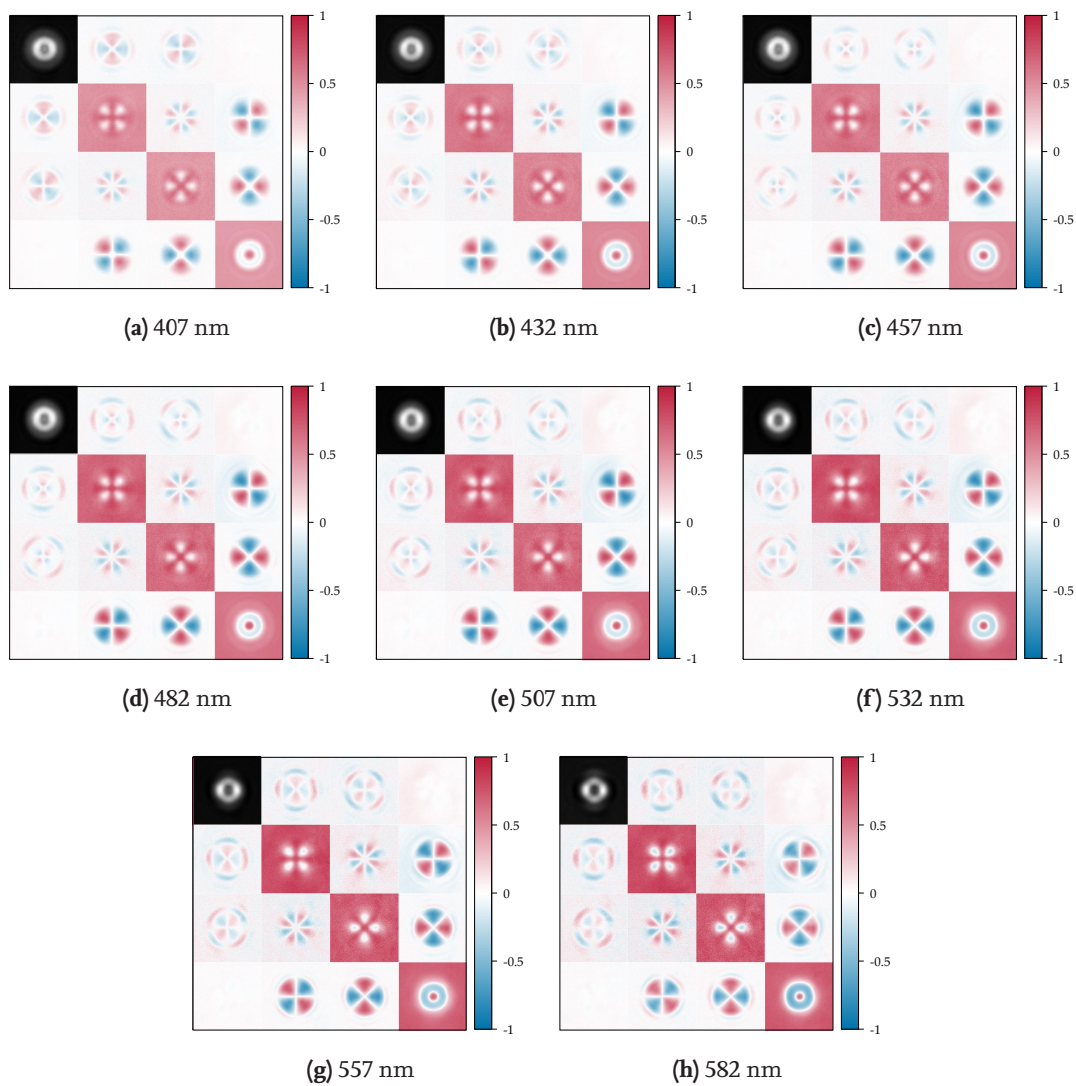


Figure B.11 – Measured MUELLER matrix images at different wavelengths, part 1.



Figure B.12 – Measured MUELLER matrix images at different wavelengths, part 2.

Acknowledgments

Danksagungen

„Tell me... If you had the strength to take another step, could you do it?“

Ardbert – Final Fantasy XIV

Die Fertigstellung dieser Arbeit war ein anspruchsvoller Weg. Die Kraft, diesen Weg zu gehen, wurde mir durch die Ermutigung und Unterstützung vieler Menschen zuteil. Ihnen möchte ich an dieser Stelle meine aufrichtige Dankbarkeit ausdrücken.

Allen voran danke ich Stefanie KROKER herzlich für die universitäre Betreuung dieser Arbeit. Deine stetige Hilfsbereitschaft, deine Geduld und dein Engagement sind ohne Gleichen, und so danke ich nicht nur für die wertvollen fachlichen Einblicke, sondern auch für deine inspirierende und wegweisende Begleitung. Für die Übernahme des Zweitgutachtens spreche ich zudem meinen herzlichen Dank an Uwe ZEITNER aus. Des Weiteren danke ich Bernd BODERMANN, meinem Betreuer und Mentor an der PTB, für die fachkundige Anleitung. Du hattest stets ein offenes Ohr bei Problemen aller Art und ich danke von Herzen für die vielen konstruktiven Ratschläge und die vorbildhafte Unterstützung während der gesamten Promotionszeit.

Mein tiefster Dank gebührt natürlich beiden Arbeitsgruppen, deren Gemeinschaft ich während meiner Zeit an der PTB wie auch an der TU Braunschweig Anteil haben durfte. Ihr alle gabt mir immer ein Gefühl von Zugehörigkeit und Rückhalt. Insbesondere möchte ich meinen Bürokolleg*innen Jana GRUNDMANN und Jan KRÜGER danken. Ohne euch wäre die Zeit an der PTB nicht halb so spaßig gewesen. Seien es knifflige Aufbauten im Labor, tückische Simulationen die einfach nicht laufen wollten, Dienstreisen quer durch Europa, oder einfach nur das Bemalen kleiner Plastikfiguren. Unzählige Stunden haben wir uns gegenseitig in unseren Bemühungen unterstützt, und diese Zeit werde ich nie vergessen. Natürliche danke ich auch den weiteren Mitgliedern der AG 4.23 „Optische Nanometrologie“: Detlef BERGMANN für Unterstützung bei Messungen am Axio-phot, Alexander DIENER für Untersuchungen am Scatterometer sowie für den IT-Support, Martina KEMLITZ für Eingangsprüfungen an so mancher Probe, Matthias WURM für fachliche Unterstützung in allem was Ellipsometrie, Scatterometrie und lineare Algebra betrifft, Marcel JANIK für die Herstellung von wichtigen Bauteilen und den mechanischen Support, Manuela SCHIEK für spannende Diskussionen über abbildende Ellipsometrie,

und selbstverständlich auch an Matthias STURM, Sven TEICHERT, Sven DOPSLAFF sowie allen, die während meiner Zeit kamen und gingen. Ein besonderer Dank auch an Iris HOPERT für Hilfe, wann immer die Bürokratie Überhand zu nehmen drohte, sowie an Egbert BUHR für die stetige Ermutigung. Selbstverständlich gilt mein Dank auch allen Mitglieder*innen der Arbeitsgruppe „Metrologie funktionaler Nanosysteme“, die oft genug Versuchskandidat*innen für meine Experimente in PowerPoint waren. Insbesondere danke ich Johannes DICKMANN für den reibungslosen Start meiner Promotionszeit.

Vielen Dank auch an Thomas SIEFKE, nicht nur für die unablässige Versorgung mit Proben, sondern auch für so manch spannende fachliche Diskussion. Des Weiteren danke ich Miroslav VALTR und Petr Klapetek für Unterstützung mit AFM-Messungen, sowie Poul-Erik HANSEN für fachliche Diskussionen zum Thema Ellipsometrie. Darüber hinaus möchte ich meinen Dank allen Mitglieder*innen der Konsortien der Projekte *BeCOME* und *POLight* aussprechen. Die Mitarbeit in diesen Projekten war für mich eine wertvolle und lehrreiche Erfahrung und ich bin froh, diese Zeit mit einem so kompetenten wie auch gemeinschaftlichen Team verbracht zu haben.

An dieser Stelle danke ich auch noch einmal besonders allen, die diese Arbeit zum Korrekturlesen auseinander genommen haben. Ich bin mir sicher, dass ihr alle Fehler findet. Ich möchte außerdem meinen aufrichtigen Dank meiner Familie aussprechen, deren anhaltende Unterstützung mir die Verwirklichung dieses Ziels erst ermöglicht hat. Auch meinen Freunden danke ich von Herzen für all die Geduld und die aufmunternden Gespräche, die mir die Kraft gaben, nicht aufzugeben. Und zu guter Letzt danke ich natürlich Sandro EISNER, meinem Freund, Verlobten, Ehemann – was auch immer wir sind wenn dies endlich gedruckt wird. Du hast mich über die gesamte Promotionszeit begleitet und unterstützt und ich möchte dich in meinem Leben nicht mehr missen. Ich liebe dich ♡

Figure 1.1(a) is licensed under the Creative Commons Attribution-Share Alike 3.0 Unported License. Figure 3.7(a) was created using the ComponentLibrary by Alexander Franzen, which is licensed under a Creative Commons Attribution-NonCommercial 3.0 Unported License.

This work is funded through the project 17FUN01 “BeCOME” within the Programme EMPIR. The EMPIR initiative is cofounded by the European Union’s Horizon 2020 research and innovation program and the EMPIR Participating Countries.

This project (20FUN02 “POLight”) has received funding from the EMPIR programme co-financed by the Participating States and from the European Union’s Horizon 2020 research and innovation programme.

List of Publications

Liste wissenschaftlicher Veröffentlichungen und Vorträge als Erstautor

Peer-Reviewed Papers

T. Käseberg, J. Grundmann, T. Siefke, S. Kroker, and B. Bodermann. „Abbildende Müller-Matrix-Ellipsometrie für die Charakterisierung vereinzelter Nanostrukturen“. In: *tm – Technisches Messen* 89.6 (2022), pp. 438–446. DOI: 10.1515/teme-2021-0133.

T. Käseberg, J. Grundmann, T. Siefke, P. Klapetek, M. Valtr, S. Kroker, and B. Bodermann. „MUELLER Matrix Ellipsometric Approach on the Imaging of Sub-Wavelength Nanostructures“. In: *Frontiers in Physics* 9 (2022). DOI: 10.3389/fphy.2021.814559.

T. Käseberg, T. Siefke, S. Kroker, and B. Bodermann. „Inverted plasmonic lens design for nanometrology applications“. In: *Measurement Science and Technology* 31.7 (2020). DOI: 10.1088/1361-6501/ab7e6b.

Proceedings

T. Käseberg, J. Grundmann, S. Kroker, and B. Bodermann. „Nanoform evaluation approach using MUELLER matrix microscopy and machine learning concepts“. In: *EPJ Web of Conferences* 266 (2022). EOS Annual Meeting, 2022, Porto, Portugal. DOI: 10.1051/epjconf/202226610007.

T. Käseberg, J. Grundmann, S. Teichert, M. Wurm, T. Siefke, S. Kroker, and B. Bodermann. „Ellipsometric characterizations of individual nanoform structures“. In: *Proceedings of SPIE* 11927 (2021). SPIE Technologies and Applications of Structured Light, 2021, Online, Japan. DOI: 10.1117/12.2616273.

T. Käseberg, J. Grundmann, J. Dickmann, S. Kroker, and B. Bodermann. „Imaging MUELLER matrix ellipsometry setup for optical nanoform metrology“. In: *EPJ Web of Conferences* 238 (2020). EOS Annual Meeting, 2020, Online. DOI: 10.1051/epjconf/202023806006.

T. Käseberg, J. Dickmann, T. Siefke, M. Wurm, S. Kroker, and B. Bodermann. „MUELLER matrix ellipsometry for enhanced optical form metrology of sub-lambda structures“. In: *Proceedings of SPIE* 11057 (2019). SPIE Optical Metrology, 2019, Munich, Germany. DOI: 10.1117/12.2527419.

T. Käseberg, T. Siefke, M. Wurm, S. Kroker, and B. Bodermann. „Sub-Wavelength Features in Spectroscopic MUELLER Matrix Ellipsometry“. In: *DGaO Proceedings (2019)*. 120. Jahrestagung der Deutschen Gesellschaft für angewandte Optik, 2019, Darmstadt, Germany. ISSN: 1614-8436.

Talks and Posters

T. Käseberg, S. Kroker, and B. Bodermann. „Simulating Achromatic Plasmonic Lenses with Inverted Design for Improved Nano-Optics“. Talk. SPIE Optical Metrology, 2023, Munich, Germany.

T. Käseberg, T. Siefke, S. Kroker, and B. Bodermann. „Konzepte für invertierte, achromatische plasmonische Linsen für nanooptische Systeme im sichtbaren und nahinfraroten Bereich“. Poster. 124. Jahrestagung der Deutschen Gesellschaft für angewandte Optik, 2023, Berlin, Germany.

T. Käseberg, J. Grundmann, S. Kroker, and B. Bodermann. „Nanoform evaluation approach using MUELLER matrix microscopy and machine learning concepts“. Talk. European Optical Society Annual Meeting, 2022, Porto, Portugal.

T. Käseberg, J. Grundmann, S. Kroker, and B. Bodermann. „MUELLER matrix microscopy with machine learning inspired nanoform evaluation“. Talk. 25th Congress of the International Commission for Optics & 16th International Conference on Optics Within Life Sciences, 2022, Dresden, Germany.

T. Käseberg, J. Grundmann, T. Siefke, S. Kroker, and B. Bodermann. „Einzelstrukturcharakterisierung mittels abbildender Müller-Matrix-Ellipsometrie“. Poster. 122. Jahrestagung der Deutschen Gesellschaft für angewandte Optik, 2021, Bremen, Germany.

T. Käseberg, J. Grundmann, T. Siefke, S. Kroker, and B. Bodermann. „Optical nanoform characterization by imaging MUELLER matrix ellipsometry“. Talk. SPIE Optical Systems Design, 2021, Online. DOI: 10.1117/12.2599853.

T. Käseberg, J. Grundmann, T. Siefke, S. Kroker, and B. Bodermann. „MUELLER Matrix Imaging Simulations with Inverted Plasmonic Lenses“. Poster. 11th Workshop Ellipsometry, 2021, Steyr, Austria.

T. Käseberg, T. Siefke, J. Grundmann, S. Kroker, and B. Bodermann. „Applicability simulations of inverted plasmonic lenses“. Talk. SPIE Optical Metrology, 2021, Online. DOI: 10.1117/12.2591098.

T. Käseberg, J. Grundmann, S. Teichert, M. Wurm, T. Siefke, S. Kroker, and B. Bodermann. „Ellipsometric characterizations of individual nanoform structures“. Talk. SPIE Technologies and Applications of Structured Light, 2021, Online, Japan. DOI: 10.1117/12.2616273.

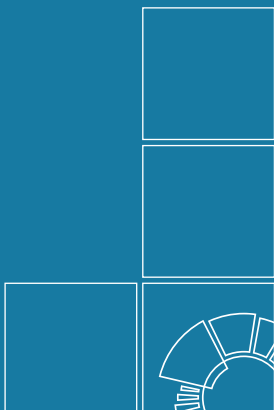
- T. Käseberg, J. Grundmann, J. Dickmann, S. Kroker, and B. Bodermann. „Imaging MUELLER matrix ellipsometry setup for optical nanoform metrology“. Talk. EOS Annual Meeting, 2020, Online. DOI: 10.1051/epjconf/202023806006.
- T. Käseberg. „Enhanced nanoform metrology by imaging MUELLER matrix ellipsometry combined with plasmonic support structures“. Talk. SPIE Photonics Europe, 2020, Online. DOI: 10.1117/12.2556146.
- T. Käseberg, J. Grundmann, T. Siefke, S. Kroker, and B. Bodermann. „Finite Element Simulation and Optimization of Inverted Plasmonic Lenses“. Poster. Workshop on Theoretical and Numerical Tools for Nanophotonics, 2020, Berlin, Germany.
- T. Käseberg, T. Siefke, S. Kroker, and B. Bodermann. „Design Study for the Application of Plasmonic Lenses in MUELLER Matrix Ellipsometry“. Poster. 12th Seminar on Quantitative Microscopy and 8th Seminar on Nanoscale Calibration, Standards and Methods, 2019, Braunschweig, Germany.
- T. Käseberg, J. Dickmann, T. Siefke, M. Wurm, S. Kroker, and B. Bodermann. „MUELLER matrix ellipsometry for enhanced optical form metrology of sub-lambda structures“. Talk. SPIE Optical Metrology, 2019, Munich, Germany. DOI: 10.1117/12.2527419.
- T. Käseberg, T. Siefke, B. Bodermann, and S. Kroker. „Concepts for Nanoscale form Evaluation by Off-diagonal MUELLER Matrix Element Interpretation“. Poster. 41st Photonics & Electromagnetics Research Symposium, 2019, Rome, Italy.
- T. Käseberg, T. Siefke, M. Wurm, S. Kroker, and B. Bodermann. „Sub-Wavelength Features in Spectroscopic MUELLER Matrix Ellipsometry“. Poster. 120. Jahrestagung der Deutschen Gesellschaft für angewandte Optik, 2019, Darmstadt, Germany.
- T. Käseberg, T. Siefke, S. Kroker, and B. Bodermann. „Reference Structure Design for Nanometrology by enhanced MUELLER Matrix Ellipsometry“. Poster. 8th International Conference on Spectroscopic Ellipsometry, 2019, Barcelona, Spain.
- T. Käseberg, J. Dickmann, T. Siefke, M. Wurm, S. Kroker, and B. Bodermann. „Spectroscopic MUELLER Matrix Ellipsometry for Advanced Nanoform Metrology“. Talk. DPG Spring Meeting, 2019, Rostock, Germany.
- T. Käseberg. „Design concepts for sensing of nanoscale features by enhanced near-field to far-field coupling“. Talk. 12th Annual Meeting Photonic Devices, 2019, Berlin, Germany.

Awards

Best Student Presentation Award for „Nanoform evaluation approach using MUELLER matrix microscopy and machine learning concepts“ at the European Optical Society Annual Meeting, 2022, Porto, Portugal.

SPIE Student Paper Prize for „MUELLER matrix microscopy with machine learning inspired nanoform evaluation“ at the 25th Congress of the International Commission for Optics, 2022, Dresden, Germany.

Best Poster Award for „Einzelstrukturcharakterisierung mittels abbildender Müller-Matrix-Ellipsometrie“ at the 122. Jahrestagung der Deutschen Gesellschaft für angewandte Optik, 2021, Bremen, Germany.



Herausgeber:

Physikalisch-Technische Bundesanstalt
ISNI: 0000 0001 2186 1887

Presse und Öffentlichkeitsarbeit

Bundesallee 100
38116 Braunschweig

Telefon: (05 31) 592-93 21
Telefax: (05 31) 592-92 92
www.ptb.de